Faculdade de Engenharia da Universidade do Porto
Departamento de Engenharia Mecânica e Gestão Industrial

Biomechanics of the Pelvic Floor during Vaginal delivery

by

Marco Paulo Lages Parente

A thesis submitted in conformity with the requirements for the
Doctoral Degree in Mechanical Engineering

Supervisor:
Renato Manuel Natal Jorge
Auxiliary Professor, Faculty of Engineering, University of Porto

Co-Supervisors:
João Arménio Correia Martins
Full Professor, Instituto Superior Técnico, Technical University of Lisbon

Maria Teresa da Quinta e Costa de Mascarenhas Saraiva
Associate Professor, Faculty of Medicine, University of Porto

June 2008

À Cecília e ao nosso filho, Pedro

"o caminho faz-se caminhando"

A. Machado

Agradecimentos

Longe de ser um trabalho puramente individual, o processo de investigação e desenvolvimento que uma tese de Doutoramento envolve depende de todo um sentido e espírito de grupo, sem o qual a discussão e questionamento científico simplesmente não existem.

Em primeiro lugar desejo exprimir ao Professor Doutor Renato Manuel Natal Jorge, meu orientador, os meus mais sinceros agradecimentos pelo empenho, amizade e acompanhamento constante e incondicional proporcionado durante todo o Doutoramento. A sua disponibilidade incondicional e esforço para proporcionar as melhores condições de trabalho, bem como o alento e motivação nos momentos mais difíceis, foram decisivos para a qualidade do trabalho final.

Quero também expressar os meus agradecimentos aos meus co-orientadores, o Professor Doutor João Martins e Professora Doutora Teresa Mascarenhas, pelas suas valorosas contribuições durante diferentes fases deste trabalho.

Ao Instituto de Engenharia Mecânica (IDMEC, Unidade de Concepção e Validação Experimental), na pessoa do Professor Doutor António Augusto Fernandes, bem como à Faculdade de Engenharia da Universidade do Porto e ao Departamento de Engenharia Mecânica e Gestão Industrial, agradeço as condições e os meios informáticos dispensados. Estendo ainda estes agradecimentos ao seu secretariado, em especial à Sr.ª Júlia Meira e à Sr.ª Fernanda Grandão.

Cumpre-me também referir a importância do apoio financeiro proporcionado pela Fundação para a Ciência e a Tecnologia, através da Bolsa de Doutoramento SFRH/BD/13013/2003, sem a qual este trabalho não seria possível.

Aos colegas bolseiros de investigação do Departamento de Engenharia Mecânica e Gestão Industrial Cassilda Tavares, Pedro Moreira, Pedro Martins, Carla Roque, Paulo Matos, Jorge Belinha e restantes colegas o meu agradecimento pela amizade e excelente ambiente de investigação proporcionado.

À Cecília, e à minha família, pela forma incondicional e constante com que sempre acreditaram e me apoiaram nesta longa caminhada, vão os meus maiores agradecimentos. Sem o seu incentivo este trabalho certamente não teria sequer começado.

Abstract

Pelvic floor dysfunctions represent an extensive problem with a magnitude unknown to many. A study conducted by Olsen et al., based on a population under one health care system, showed that 11% of women had surgery for urinary incontinence or pelvic organ prolapse during their lifetime. Furthermore, statistics show that 30 to 40% of women will suffer from some degree of incontinence in their lifetime. Other study, conducted by Rortveit et al showed that the prevalence of this problem among nulliparous women ranged from 8% to 32%, increasing with age. They also showed that parity was associated with incontinence, the first delivery being the most significant.

Several studies have shown that pelvic floor injuries during a vaginal delivery can be considered a significant factor in the development of urinary incontinence, fecal incontinence and pelvic organ prolapse. During delivery, the pelvic floor experiences several changes, which cannot be measured in vivo due to clinical, technical and ethical reasons.

This work presents a biomechanical method of modeling a biologic process, the delivery in this case, in order to estimate biomechanical changes (stretch, strain, stresses, etc.) on tissues. Knowledge of these biomechanical changes might help to explain known phenomena associated with delivery and pregnancy, like damage to the pelvic floor tissues, including the levator ani muscle. The purpose of the vaginal childbirth simulation presented is to determine the stretches and stresses induced in the pelvic floor muscles by the passage of a fetus.

The purpose of the presented vaginal childbirth simulation is to contribute to the clarification of the mechanisms behind pelvic floor disorders related to a vaginal delivery. For this purpose a numerical simulation based on the Finite Element Method was carried out. The Finite Element Model aims at representing the effects that the passage of a fetal head can induce on the muscles of the pelvic floor, from a mechanical point of view. The model used for the simulation represents the pelvic bones, with the attached pelvic floor muscles and the fetus. In this work, the movements of the fetus during birth, in vertex position are simulated. The different simulations conducted are divided into two groups, in the first group of simulations the fetus presents in occipito-anterior position and in the second group the fetus

presents in occipito-posterior position.

As investigation progresses, clinicians will eventually shift from a condition-based approach to an injury-based approach, radically transforming both clinical research and patient care. An enhanced precision in defining pelvic floor disorders will revolutionize the ability to define and implement appropriate treatment, as well as to conduct focused clinical research.

The computer model presented in this work is a first step in understanding how obstetrical factors and interventions might influence the risk for levator ani injury, because experimental measurements of the elevator muscle stretch in laboring women are not currently feasible for many clinical, technical and ethical reasons. The use of precise numerical models of the female pelvic cavity will, in the future, provide the tools to simulate, in a realistic manner, the pelvic floor function and the effects of its dysfunctions. And, in this manner, provide tools that will allow surgeons to plan the surgery and perform it in a more controlled and reliable way.

Résumé

Les dysfonctions du plancher pelvien représentent un grave problème avec une ampleur méconnu de beaucoup. Une étude réalisée par Olsen et al., basée sur une population déterminée d'un système de santé, a démontré qu'environ 11% de la population féminine, pendant leur vie, a été soumise a des chirurgies pour résoudre des problèmes d'incontinence urinaire ou prolapsus des organes de la cavité pelvienne. Par ailleurs, les statistiques montrent que 30 a 40% des femmes vont souffrir d'un type de dysfonction du plancher pelvien pendant leur vie. Une autre étude réalisée par Rortveit et al. a démontré que la prévalence de ce problème parmi les femmes nullipares varie entre 8 et 32%, et que ce nombre augmente avec l'âge. Cette étude a aussi démontré que la parité était associée avec l'incontinence, étant le premier accouchement le plus significatif.

Plusieurs études ont montrés que les dommages du plancher pelvien pendant un accouchement peuvent être considérés un facteur important pour le développement d'incontinence urinaire, incontinence fécale ou prolapsus des organes de la cavité pelvienne. Pendant l'accouchement, le plancher pelvien est soumis à plusieurs altérations qui ne sont pas mesurées in vivo pour des raisons cliniques, techniques e éthiques.

Ce travail présente une méthode biomécanique de modélisation d'un processus biologique, l'accouchement, de manière à prévoir les altérations biomécaniques (allongement, déformation, contrainte, etc.) des tissus du plancher pelvien. La connaissance de ces altérations biomécaniques pourra aider à expliquer des phénomènes connus associés avec l'accouchement et à la grossesse, comme les dommages des tissus du plancher pelvien, y compris le muscle élévateur de l'anus. L'objectif de la simulation de l'accouchement vaginal présenté dans ce travail est de déterminer les allongements et les contraintes induits sur le plancher pelvien par le passage du foetus.

L'objectif de ce travail est de contribuer à la clarification des mécanismes qui justifient l'apparition de dysfonctions du plancher pelvien liés à un accouchement vaginal. Dans ce but, des simulations numériques ont été effectuées basées sur la Méthode des Éléments Finis. La méthode des éléments finis permet de représenter les effets mécaniques du passage du foetus sur les muscles du plancher pelvien. Le

modèle des éléments finis utilisé dans les simulations représente le foetus, les os pelviens et les muscles du plancher pelvien fixés aux os. Les mouvements du foetus pendant l'accouchement en présentation céphalique ont été simulés. Les différentes simulations réalisées ont été divisées en deux groupes. Dans le premier groupe de simulations, le foetus se trouve avec une présentation occipito-antérieur et dans le deuxième groupe en position occipito-postérieur.

Au fur et à mesure que la recherche progresse, les médecins iront éventuellement passer d'une évaluation du patient, basée sur ses symptômes, à une évaluation basée sur les dommages que le plancher pelvien d'une femme présente, transformant radicalement non seulement l'investigation clinique comme les soins médicaux. Une plus grande précision dans la définition des dysfonctions du plancher pelvien iront révolutionner la capacité de définir et d'introduire un traitement approprié, ainsi que de réaliser une investigation clinique ciblée sur le problème.

Le modèle computationnel présenté dans ce travail est un premier pas pour comprendre la façon dont les facteurs obstétriques peuvent influencer le risque de dommage du muscle élévateur de l'anus, dans la mesure ou des mesures expérimentales de l'allongement du muscle élévateur pendant l'accouchement ne sont pas possibles actuellement du a des raisons cliniques, techniques et éthiques. L'utilisation de modèles numériques précis de la cavité pelvienne de la femme ira dans le futur fournir des outils pour simuler d'une façon réaliste la cavité pelvienne et l'effet de ses dysfonctions. De cette manière, il sera possible de produire des outils qui permettront aux chirurgiens de planifier la chirurgie et de la réaliser de façon plus contrôlée et avec plus de confiance dans le résultat final.

Resumo

As disfunções do pavimento pélvico representam um problema vasto, com uma amplitude desconhecida por muitos. Um estudo realizado por Olsen et al., baseado na população de um determinado sistema de saúde, demonstrou que cerca de 11% da população feminina, durante a sua vida, foram sujeitas a cirurgias para resolver problemas de incontinência urinária ou prolapso dos órgãos da cavidade pélvica. Além disso, as estatísticas mostram que 30 a 40% das mulheres vão sofrer de algum tipo de disfunção do pavimento pélvico durante a sua vida. Um outro estudo, realizado por Rortveit et al., demonstrou que a prevalência deste problema em mulheres nulíparas, variava entre 8 e 32%, aumentando com a idade. Esse estudo também demonstrou que a paridade estava associada com a incontinência, sendo o primeiro parto o mais significativo.

Vários estudos têm mostrado que os danos no pavimento pélvico durante um parto vaginal podem ser considerados um factor importante para o desenvolvimento de incontinência urinária, incontinência fecal ou prolapso dos órgãos da cavidade pélvica. Durante o parto, o pavimento pélvico sofre várias alterações, que não podem ser medidas in vivo por motivos clínicos, técnicos e éticos.

Este trabalho apresenta um método biomecânico de modelação de um processo biológico, o parto, de forma a estimar as alterações biomecânicas (alongamento, deformação, tensão, etc.) nos tecidos do pavimento pélvico. O conhecimento destas alterações biomecânicas poderá ajudar a explicar fenómenos conhecidos associados com o parto e gravidez, tais como os danos nos tecidos do pavimento pélvico, incluindo o músculo elevador do ânus. O objectivo da simulação de um parto vaginal, apresentada neste trabalho, é determinar os alongamentos e as tensões induzidas no pavimento pélvico, pela passagem do feto.

O objectivo do presente trabalho é contribuir para a clarificação dos mecanismos que justificam o aparecimento de disfunções do pavimento pélvico, relacionadas com um parto vaginal. Com esse fim efectuaram-se simulações numéricas baseadas no Método dos Elementos Finitos. O método dos elementos finitos pretende representar os efeitos mecânicos da passagem do feto nos músculos do pavimento pélvico. O modelo de elementos finitos utilizado nas simulações representa o feto, os ossos pélvicos e os músculos do pavimento pélvico, fixados aos ossos. Neste trabalho

foram simulados os movimentos do feto durante o parto, em apresentação cefálica. As diferentes simulações realizadas foram divididas em dois grupos, no primeiro grupo de simulações, o feto encontra-se com uma apresentação occipito-anterior e no segundo grupo com uma apresentação occipito-posterior.

À medida que a investigação progredir, os clínicos irão eventualmente passar de uma avaliação do paciente, baseada nos seus sintomas, para uma avaliação baseada nos danos que o pavimento pélvico dessa pessoa apresenta, transformando radicalmente não só a investigação clínica como os cuidados médicos. Uma maior precisão na definição das disfunções do pavimento pélvico irá revolucionar a capacidade de definir e implementar um tratamento apropriado, assim como realizar investigação clínica de uma forma focalizada no problema.

O modelo computacional apresentado neste trabalho é um primeiro passo para se compreender a forma como os factores obstétricos podem influenciar o risco de dano para o músculo elevador do ânus, uma vez que medições experimentais do alongamento do musculo elevador, durante o parto, presentemente não são possíveis, devido a motivos clínicos, técnicos e éticos. A utilização de modelos numéricos precisos da cavidade pélvica da mulher irá, no futuro, fornecer ferramentas para simular, de uma forma realista, a cavidade pélvica e o efeito das suas disfunções. Desta forma será possível produzir ferramentas que irão permitir aos cirurgiões planear a cirurgia e realizá-la de uma forma mais controlada e com mais confiança nos resultados finais.

Contents

List of Figures

List of Tables

Nomenclature

$\bar{\lambda}_f$	Fiber stretch ratio in the direction $\mathbf{N}$ of the undeformed fiber.
$\bar{\mathbf{C}}$	Distortional component of the right Cauchy-Green deformation tensor.
$\bar{\mathbf{E}}$	Distortional component of the Green-Lagrange strain tensor.
$\bar{\mathbf{F}}$	Distortional component of the deformation gradient $\mathbf{F}$.
$\bar{\mathbf{F}}$	Distortional component of the deformation gradient.
$\bar{\boldsymbol{K}}^{M}_{T_{IK}}$	Tangent matrix with respect to the current configuration.
$\bar{\boldsymbol{K}}_{T_{IK}}$	Tangent matrix to the deformation at $\bar{\boldsymbol{\varphi}}$.
$\bar{I}_1^C$	First invariant of $\bar{\mathbf{C}}$.
$\bigcup$	Assembly operator.
$\boldsymbol{\eta}$	Virtual displacement or test function.
$\boldsymbol{\varphi}$	A configuration of a body $\mathcal{B}$.
$\boldsymbol{\varphi}_t$	Motion of a body $\mathcal{B}$.
$\boldsymbol{\sigma}$	Cauchy stress tensor.
$\boldsymbol{\tau}$	Kirchhoff stress tensor.
$\delta\mathbf{C}$	Variation of the Right Cauchy-Green deformation tensor.
$\delta\mathbf{E}$	Variation of the Green-Lagrangian strain tensor.
$\delta\mathbf{F}$	Virtual variation of the deformation gradient.
δ_{AB}	Kronecker delta.
$\dot{\mathbf{C}}$	Time derivative of the right Cauchy-Green tensor.

$\dot{\mathbf{E}}$ time derivative of the Green-Lagrangian strain tensor.

$\dot{\mathbf{F}}$ Time derivative of the deformation gradient.

$\dot{\mathbf{S}}$ Rate of the second Piola-Kirchhoff stress tensor.

$\dot{\boldsymbol{v}}$ Acceleration vector after assembly of the global structure.

$\mathbb{C}$ Fourth order incremental constitutive tensor.

$\mathbb{C}_0$ incremental constitutive tensor evaluated at the undeformed state.

$\mathbb{I}$ Fourth order unit tensor.

$\mathbb{I}_{C^{-1}}$ Fourth order tensor.

$\mathbf{1}$ Second order unit tensor.

$\mathbf{b}$ Left Cauchy-Green or Finger deformation tensor.

$\mathbf{C}$ Right Cauchy-Green deformation tensor.

$\mathbf{d}$ Symmetrical spatial velocity gradient.

$\mathbf{E}$ Green-Lagrange strain tensor.

$\mathbf{e}$ Eulerian or Almansi strain tensor.

$\mathbf{F}$ Deformation gradient tensor.

$\mathbf{G}$ C^1-mapping.

$\mathbf{H}$ Displacement gradient with respect to $\mathbf{X}$.

$\mathbf{H}$ Material version of the tangent operator.

$\mathbf{h}$ Spatial version of the tangent operator.

$\mathbf{L}$ Linear part of a mapping.

$\mathbf{l}$ Spatial velocity gradient.

$\mathbf{N}$ Direction of the undeformed fiber.

$\mathbf{N}$ Normal to the surface of $\mathcal{B}$.

$\mathbf{n}$ Current muscle fiber direction.

$\mathbf{n}$ Normal to the surface of $\boldsymbol{\varphi}(\mathcal{B})$.

$\mathbf{P}$	First Piola-Kirchhoff stress tensor.
$\mathbf{S}$	Second Piola-Kirchhoff stress tensor.
$\mathbf{t}$	Normal Stress vector.
$\mathbf{u}$	Displacement vector.
$\mathbf{x}$	Position of a particle X of $\mathcal{B}$ in the configuration $\boldsymbol{\varphi}$.
$\mathcal{B}$	A body.
$\mathcal{B}^h$	Finite element discretization of $\mathcal{B}$.
$\mathcal{L}_v$	Lie-derivative.
$\Delta\bar{\mathbf{G}}$	directional derivative of a C^1-mapping $\mathbf{G}$.
Λ	Lamé constant.
$\Omega_\square$	Finite element in the reference configuration.
Π	Total elastic potential.
B	A body.
$\mathfrak{c}$	Spatial incremental constitutive tensor.
DEV	Operator deviator in the reference configuration.
dev	Operator deviator in the spatial configuration.
$\boldsymbol{D}_0$	Elasticity tensor of the geometrical linear theory of elasticity.
$\boldsymbol{J}_e$	The Jacobi matrix of an element Ω_e.
$\boldsymbol{M}$	Mass matrix after assembly of the global structure.
$\boldsymbol{u}_I$	Unknown nodal variables.
μ	Lamé constant.
Ω_e	Finite element.
$\otimes$	Tensor product.
$\partial\mathcal{B}$	Boundary of $\mathcal{B}$.
$\partial\mathcal{B}^h$	Boundary of the finite element discretization of $\mathcal{B}$.

ρ Density in the current configuration.

ρ_0 Density in the initial configuration.

D Derivative operator.

$d\mathbf{X}$ Material line element.

$d\mathbf{x}$ Spatial line element.

dA Surface element in the reference configuration.

da Surface element in the spatial configuration.

dV Volume element in the reference configuration.

dv Volume element in the spatial configuration.

I_b First invariant of the left Cauchy-Green train tensor.

I_C First invariant of the right Cauchy-Green train tensor.

II_b Second invariant of the left Cauchy-Green train tensor.

II_C Second invariant of the right Cauchy-Green train tensor.

III_b Third invariant of the left Cauchy-Green train tensor.

III_C Third invariant of the right Cauchy-Green train tensor.

J Jacobian determinant.

m Mass of a body $\mathcal{B}$.

N Number of nodes of an element.

$N_I(\boldsymbol{\xi})$ Interpolation functions in the reference configuration.

$N_I(\mathbf{X})$ Interpolation or basis functions.

p Pressure loading.

t Time.

U_f Strain energy stored in the various muscle fibers families.

U_J Strain energy associated with the volume change.

W Strain energy function.

X A particle belonging to the body $\mathcal{B}$.

x_i Components of $\mathbf{x}$.

$\boldsymbol{P}$ Loads acting on the structure.

Chapter 1

Introduction

1.1 Introduction

Pelvic floor dysfunction represents an extensive problem with unknown dimensions. The term pelvic floor dysfunction refers to a group of clinical conditions that include problems like urinary incontinence, fecal incontinence, pelvic organ prolapse and any other sensory and emptying abnormalities of the lower urinary and gastrointestinal tracts [Weber et al., 2004]. The three most common and clinically definable conditions encountered are urinary incontinence, anal incontinence and pelvic organ prolapse [Davila et al., 2006].

It is estimated that one or more of these conditions affects up to one-third of adult women. A study conducted by Olsen et al., based on a population under one health care system, showed that 11% of women had surgery for urinary incontinence or pelvic organ prolapse during their lifetime [Olsen et al., 1997]. Furthermore, statistics show that 30 to 40% of women suffer from some degree of incontinence in their lifetime [Lien et al., 2005; Kenton and Mueller, 2006].

A real understanding of the pathophysiology of pelvic floor disorders is still nonexistent. Development of a clinical condition is the result of the combination of multiple factors. One can easily presume a genetic predisposition overlaid by critical life events (acquired risk factors, such as childbirth, hormonal changes, and aging) although strong evidence does not yet exist for these hypotheses [Weber et al., 2004].

The pelvic organ support system comprises muscles, ligaments, and nerves arranged in a complex tension-based apparatus. Therefore, understanding function of this apparatus must include biomechanical analysis of the overall support mechanisms, targeting research into the biology of muscle, ligament, nerve components, and their complex interactions in women with normal pelvic floor function and in symptomatic patients.

It remains unclear whether muscle damage or neuropathy is the primary mech-

anism for the development of pelvic floor disorders, but some authors believe that the dysfunctions are largely caused by damage of connective tissues (ligaments and fascia) and muscles of the pelvic floor [Papa Petros, 2004]. Pregnancy and childbirth are considered particularly traumatic events leading to mechanical injury of the anal sphincter and levator ani muscles and to neuropathy of the pudendal nerves[Gregory and Nygaard, 2004]. The combined action of ligaments, fascia, and muscles keeps in place and strengthens the pelvic organs, and the urethra, vagina, and rectum [Papa Petros, 2004]. The normal function of the pelvic organs is thus dependent on the integrity of the pelvic floor structure. Modern reconstructive pelvic floor surgery uses polymeric or biologic tapes or meshes to reconstruct damaged suspensor ligaments or reinforce fascia tissue [Leval, 2003; Delome, 2001].

Clinical aspects of pelvic floor disorders have been extensively studied, in particular the effect of pregnancy and childbirth, as shown for example in the following studies [Dimpfl et al., 1998; Gregory and Nygaard, 2004]. However, it is widely recognized that the understanding of the mechanism of damage to the pelvic floor components (muscles, nerves, fascia) is still very limited. In particular, a global perspective of the function of the pelvic floor and its anomalies is completely lacking [Gregory and Nygaard, 2004].

This work presents a biomechanical method of modeling a biologic process, the delivery in this case, in order to estimate biomechanical changes (stretch, strain, stresses, etc.) on tissues. Knowledge of these biomechanical changes might help to explain known phenomena associated with delivery and pregnancy, like damage to the pelvic floor tissues, including the elevator ani muscle. The purpose of the presented vaginal childbirth simulation is to determine the stretches and stresses induced in the pelvic floor muscles by the passage of a fetus.

The objective of the present work is to contribute to the clarification of the mechanisms behind pelvic floor disorders related to a vaginal delivery. For this purpose a numerical simulation based on the Finite Element Method was carried out. The Finite Element Model aims at representing the effects that the passage of a fetal head can induce on the muscles of the pelvic floor, from a mechanical point of view. The model used for the simulation represents the pelvic bones, with the attached pelvic floor muscles and the fetus. In this work, the movements of the fetus during birth, in vertex position were simulated. The different simulations conducted here are divided into two groups, in the first group of simulations the fetus presents in occipito-anterior position and in the second group the fetus presents in occipito-posterior position.

To achieve these goals it is necessary to have a good geometrical description of the anatomy of the pelvic region, as well as good models of the complex mechanical behavior of the muscles and supporting structures in presence. These topics will be addressed in the following Chapters.

This study improves previous work in this area [Lien et al., 2004; Lien et al., 2005]

by using a realistic model of the fetus body to better simulate vaginal childbirth and thus obtain the stretches induced in the pelvic floor muscles.

The use of precise numerical models of the female pelvic cavity will, in the future, provide the tools to simulate, in a realistic manner, the pelvic floor function and the effects of its dysfunctions. And, in this manner, provide tools that will allow surgeons to plan the surgery and perform it in a more controlled and reliable way.

Chapter 2

Anatomy of the Female Pelvis and Perineum

2.1 Introduction

This chapter first make a presentation of the organization of the human body, its main structures and functions. After this first presentation, the main objective of this chapter will be treated, the study of the structures and processes involved in the anatomy of the female pelvic floor. The anatomy of the female pelvis and perineum described on this chapter is already very well established on the literature, and is presented here only briefly. This Chapter is based on the following works of [Moore and Dalley, 2006], [DeCherney and Nathan, 2003], [Seeley et al., 2004], [Mader, 2004], [Kent, 2001], [Standring, 2004], [Netter, 2006], [Scanlon and Sanders, 2007], [Ellis, 2006] and [Sobotta et al., 2001], which should be consulted for more details on this subject.

The human body is complex, like a highly technical and sophisticated machine. It operates as a single entity, but is made up of a number of operational parts that work interdependently. Each part is associated with a specific, and sometimes related, function that is essential for the well-being of the individual. The component parts do not operate independently, but rather in conjunction with all the others. Should one part fail, the consequences are likely to extend to other parts, and may reduce the ability of the body to function normally. Integrated working of the body parts ensures the ability of the individual to survive. The human body is therefore complex in both its structure and function.

2.2 The Human Body

Anatomy and physiology is the study of the human body. Anatomy is the study of the structure of the body and the physical relationships involved between body parts. Although historically and strictly speaking the primary concern of anatomy is structure, true understanding results when structure and function are considered together. Physiology is the study of how the parts of the body work, and the ways in which they cooperate together to maintain the life and health of the individual. Anatomy and physiology are closely connected in that the structure of an organ suits its function. For example, the stomach's pouch like shape and ability to expand are suitable to its function of storing food. In addition, the microscopic structure of the stomach wall is suitable to its secretion of digestive juices. Pathology is the study of abnormalities and how they affect body functions, often causing illness.

2.2.1 Organization of body parts

The human body is organized into structural and functional levels of increasing complexity. Each higher level incorporates the structures and functions of the previous level. Conceptually, the body has six structural levels: the chemical, cell, tissue, organ, organ system, and complete organism. All the levels of organization are depicted in Figure 2.1.

2.2.1.1 Cellular Level

The cell is the basic structural and functional component of life. Humans are multicellular organisms composed of nearly 60 to 100 trillion cells. It is at the microscopic cellular level that the vital functions of life such as metabolism, growth, irritability (responsiveness to stimuli), repair, and replication are carried on.

All substances, including body parts, are composed of chemicals made up of submicroscopic particles, atoms (Figure 2.1). Atoms join to form molecules, which can in turn join to form macromolecules. For example, molecules called amino acids join to form a macromolecule called protein, which makes up the bulk of our muscles. Macromolecules are found in all cells, the basic units of all living things. Within cells are organelles, small functional structures called that perform cellular functions. For example, the organelle called the nucleus is especially concerned with cell reproduction, another organelle, called the mitochondrion, supplies the cell with energy.

2.2.1.2 Tissue Level

Tissues are the next level of organization. Tissues are layers or groups of similar cells that perform a common function. The entire body is composed of four kinds

of tissues: epithelial, connective, muscular, and nervous tissue. The muscle within the heart is an example of a tissue, whose function it is to pump the blood through the body. The outer layer of skin (epidermis) is a tissue because it is composed of similar cells that together serve as a protective shield for the body. The science concerned with the microscopic study of tissues is named histology.

2.2.1.3 Organ Level

An organ is composed of several types of tissues that performs a particular function within an organ system. Organs vary greatly in size and function and occur throughout the body. Each organ usually has one or more primary tissues and several secondary tissues. In the stomach, for example, the inside epithelial lining is considered the primary tissue because the basic functions of secretion and absorption occur within this layer. Secondary tissues of the stomach are the connective, nervous, and muscle tissues.

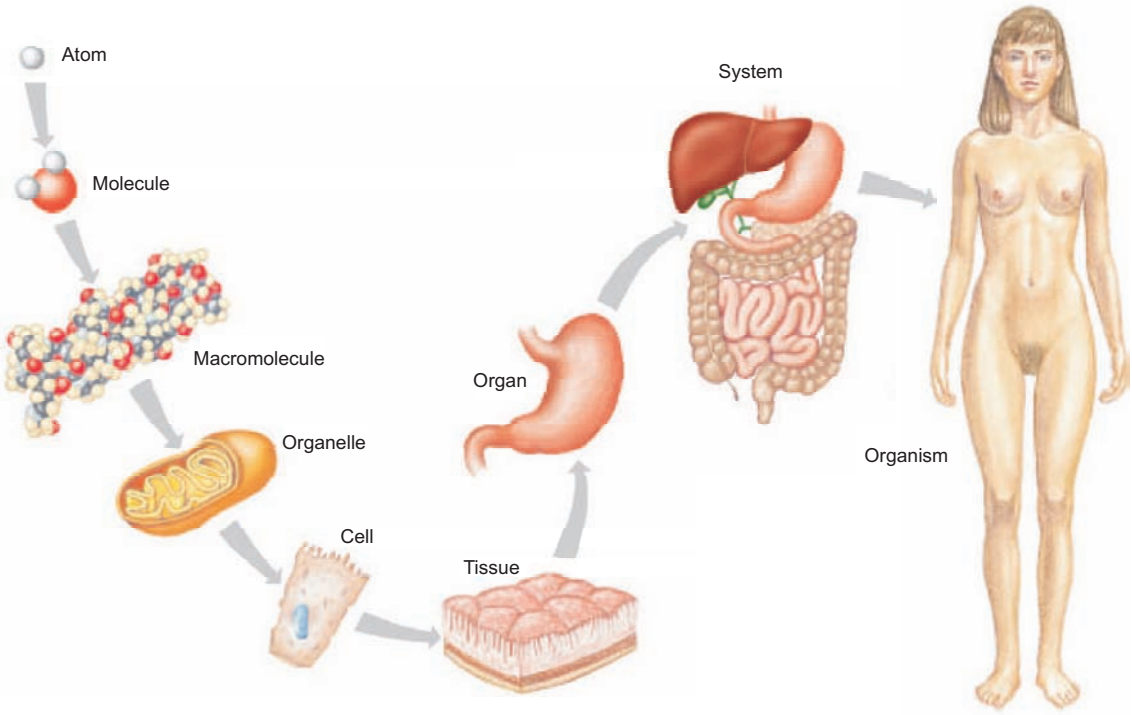

Figure 2.1: Levels of structural organization of the human body, depicted from the simplest (chemical) to the most complex (organism) (adapted from [Mader, 2004]).

2.2.1.4 System Level

The different systems of the body constitute the next level of structural organization. A body system consists of various organs that have similar or related functions. Certain organs may serve two systems. For example, the pancreas functions with both the endocrine and digestive systems and the pharynx serves both the respiratory and digestive systems. In the Human body, all the systems are interrelated and function together, making up the organism.

A systematic approach to study anatomy emphasizes the purposes of the various organs within a system. For example, the functional role of the digestive system can be best understood if the different organs of that system are studied together. In a regional approach, all of the organs and structures in one particular region are examined at the same time. The regional approach has merit in graduate professional schools because the structural relationships of portions of several systems can be observed simultaneously. Dissections of cadavers are usually conducted on a regional basis. Trauma or injury usually affects a region of the body, whereas a disease that affects a region may also involve an entire system.

All of the body systems together make up the organism, a human being for example. Human beings are complex animals, but this complexity can be broken down and studied at simpler levels.

2.2.2 Anatomical terms

The terminology presented here will allow to describe the location of body parts, regions of the body, and imaginary planes by which the body can be sectioned. This knowledge is essential to enable an effective communication.

2.2.2.1 Anatomical Position

Anatomical terms are useful only if everyone has in mind the same position of the body and is using the same reference points. Therefore, it is assumed that the body is in the anatomical position.

This position provides a precise and standard frame of reference for anatomical description and dissection. The anatomic position refers to a person standing erect with the face directed forward, the upper limbs hanging to the sides, and the palms of the hands facing forward (Figure 2.2). Without such a frame of reference, to say that a structure such as the sternum, thymus, or aorta is "above the heart" would be vague, since it would depend on whether the subject was standing, lying face down, or lying face up.

By using this position and appropriate terminology, any part of the body can be related precisely to any other part. Although gravity causes a downward shift

of internal organs when the upright position is assumed, it is often necessary to describe the position of organs in the supine position (lying down, face upward) or prone position (lying down, face downward) because this is the posture in which people are typically examined. In the anatomic position, the elbow is above the hand, but in the supine or prone position, the elbow and hand are at the same level. To avoid confusion, relational descriptions are always based on the anatomic position, no matter the actual position of the body. Thus, the elbow is always described as being above the wrist, whether the person is lying down or is even upside down. Therefore, unless stated otherwise, it is assumed that all anatomical descriptions refer to the anatomical position.

It is important to bear in mind that when a subject in anatomical position is facing the observer, the subject's left will be on the observer's right and vice versa. In most anatomical illustrations, for example, the left atrium of the heart appears toward the right side of the page, and while the appendix is located in the right lower quadrant of the abdomen, it appears on the left side of most illustrations.

2.2.2.2 Planes and Sections of the Body

In order to visualize and study the structural arrangements of various organs, it is customary to use imaginary "slices" called sections or planes. "Section" implies an actual cut or slice to reveal the internal anatomy, whereas "plane" implies an imaginary flat surface passing through the body. The three major anatomical planes are the sagittal, frontal, and transverse plane (Figure 2.2).

The sagittal plane extends vertically through the body or an organ and divides it into right and left portions. A midsagittal (median) plane is a sagittal plane that passes lengthwise through the midplane of the body, dividing it equally into right and left halves. The head and pelvic organs are commonly illustrated on the median plane.

The frontal (coronal) plane also extends vertically, but it is perpendicular to the sagittal plane and divides the body into anterior (front) and posterior (back) portions. A frontal section of the head, for example, would divide it into one portion bearing the face and another bearing the back of the head. Contents of the thoracic and abdominal cavities are most commonly shown in frontal sections.

A transverse (horizontal) plane is perpendicular to the body's long axis and therefore divides the body horizontally to produce a cross section. A transverse cut divides the body or an organ into superior and inferior portions. The terms longitudinal section and cross section are often applied to body parts that have been removed and cut either lengthwise or straight across, respectively. Typically, CT scans are transverse sections.

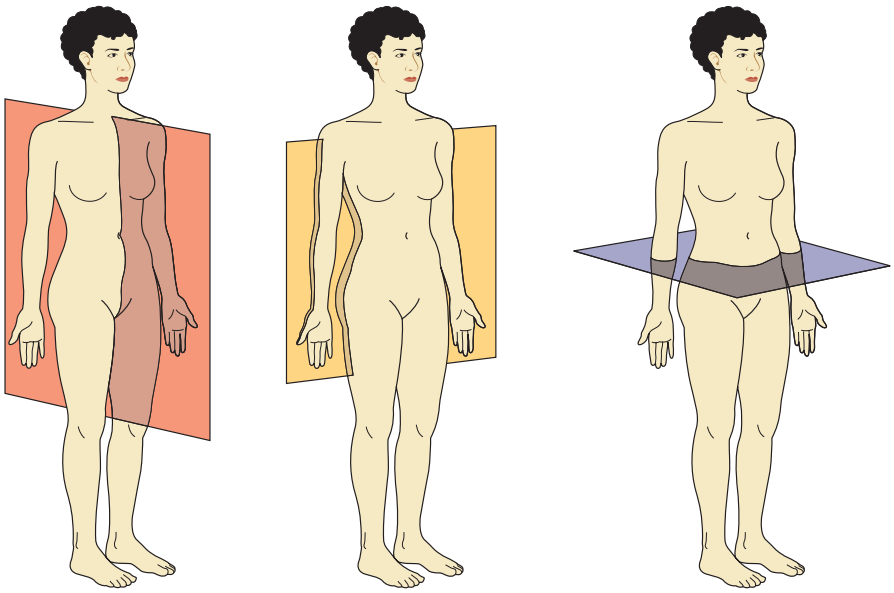

(a) Sagittal plane (b) Frontal plane (c) Transverse plane

Figure 2.2: Anatomical Planes of Reference (adapted from [Mader, 2004]).

2.2.2.3 Directional terms

Directional terms are used to describe the location of one body part in relation to another. Important directional terms are illustrated in Figure 2.3 and summarized in Table 2.1.

Right and left are retained as directional terms in anatomic terminology. Up is replaced by superior, down by inferior, front by anterior, and back by posterior.

In humans, superior is synonymous with cephalic, which means toward the head, because in the anatomic position, the head is the highest point. In humans, the term inferior is synonymous with caudal, which means toward the tail, represented in humans by the coccyx, the small bone at the inferior (caudal) end of the vertebral column.

The word anterior, denotes the region of the body that leads the way in normal locomotion, for a human, it is the area of the chest and abdomen. The anterior surface of the human body is therefore the ventral surface, or belly, because the belly "goes first" when walking. The word posterior means that which follows and dorsal means back. The posterior surface of the body is the dorsal surface, or back, which follows when walking.

Proximal means nearest, whereas distal means distant. These terms are used to refer to linear structures, such as the limbs, in which one end is near some other structure and the other end is farther away. Each limb is attached at its proximal

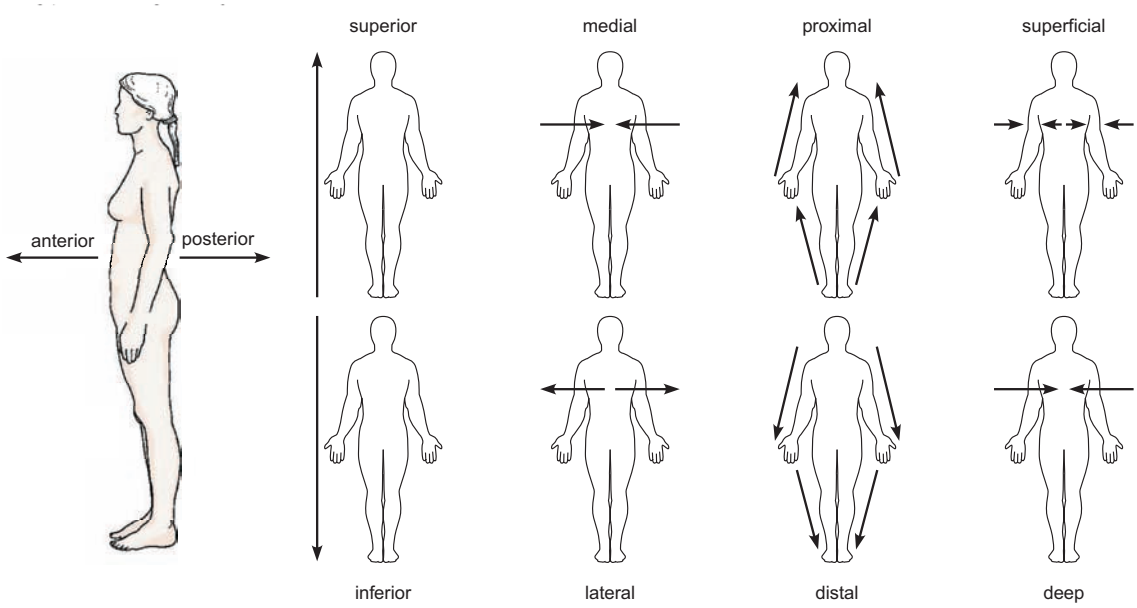

Figure 2.3: Directional terms used to describe the position of one structure relative to another, with the body in the anatomical position (adapted from [Mader, 2004])

Term	**Definition**	**Example**
Right	Toward the right side of the body	The right ear.
Left	Toward the left side of the body	The left eye.
Superior	A structure above another	The heart is superior to the diaphragm.
Inferior	A structure below another	The liver is inferior to the diaphragm.
Cephalic	Closer to the head	The chin is cephalic to the navel.
Caudal	Closer to the tail	The navel is caudal to the chin.
Anterior	Toward the ventral side	The sternum is anterior to the heart.
Posterior	Toward the dorsal side	The esophagus is posterior to the trachea.
Ventral	Toward the front or belly	The navel is ventral to the spine.
Dorsal	Toward the back or spine	The spine is dorsal to the breastbone.
Proximal	Closer to the point of origin	The elbow is proximal to the wrist.
Distal	Farther from the point of origin	The hand is distal to the elbow.
Lateral	Away from the median plane	The eyes are lateral to the nose.
Medial	Toward the median plane	The heart is medial to the lungs.
Superficial	Closer to the body surface	The skin is superficial to the muscles.
Deep	Farther from the body surface	The bones are deep to the muscles.

Table 2.1: Directional Terms for the Human Body

end to the body, and the distal end, such as the hand, is farther away.

Medial means toward the midline, and lateral means away from the midline. The nose is located in a medial position in the face, and the eyes are lateral to the nose. The term superficial refers to a structure close to the surface of the body, and deep is toward the interior of the body. The skin is superficial to the muscles and bones.

2.2.2.4 Body Parts and Regions

Knowledge of the external anatomy and landmarks of the body is important in performing a physical examination and many other clinical procedures. The human body can be divided into two major regions called the axial and appendicular regions. Smaller areas within the major regions are described in the following paragraphs and illustrated in Figure 2.4. The labels in Figure 2.4 do not include the word "region". The scientific name for each region is followed by the common name for that region. For example, the cephalic region is commonly called the head.

The axial region consists of the head, neck (cervical region), and trunk. The trunk can be divided into the thorax, abdomen, and pelvis. The pelvis is that part of the trunk associated with the hips.

One way of referring to the locations of abdominal structures is to divide the region into quadrants. Two perpendicular lines intersecting at the umbilicus (navel) divide the abdomen into a right upper quadrant, right lower quadrant, left upper quadrant, and left lower quadrant (Figure 2.5a). The quadrant scheme is often used to describe the site of an abdominal pain or abnormality. In addition to these quadrants, the abdomen is sometimes subdivided into nine regions by four imaginary lines: two horizontal and two vertical, resulting in nine regions: epigastric, right and left hypochondriac, umbilical, right and left lumbar, hypogastric, and right and left iliac (Figure 2.5b). Clinicians use the quadrants or regions as reference points for locating underlying organs.

The appendicular region of the body consists of the appendages (also called limbs or extremities): the upper limbs and the lower limbs. The upper limb includes the brachium (arm), antebrachium (forearm), carpus (wrist), manus (hand), and digits (fingers). The arm extends from the shoulder to the elbow, and the forearm extends from the elbow to the wrist. The lower limb includes the thigh, crus (leg), tarsus (ankle), pes (foot), and digits (toes). The thigh extends from the hip to the knee, and the leg extends from the knee to the ankle. Note that the terms "arm" and "leg" refer to only a part of the respective limb.

2.2.3 Body Cavities and Membranes

The body contains many cavities, among which are the nasal, cranial, and abdominal cavities. Some of these open to the outside of the body, and some do not. Internally,

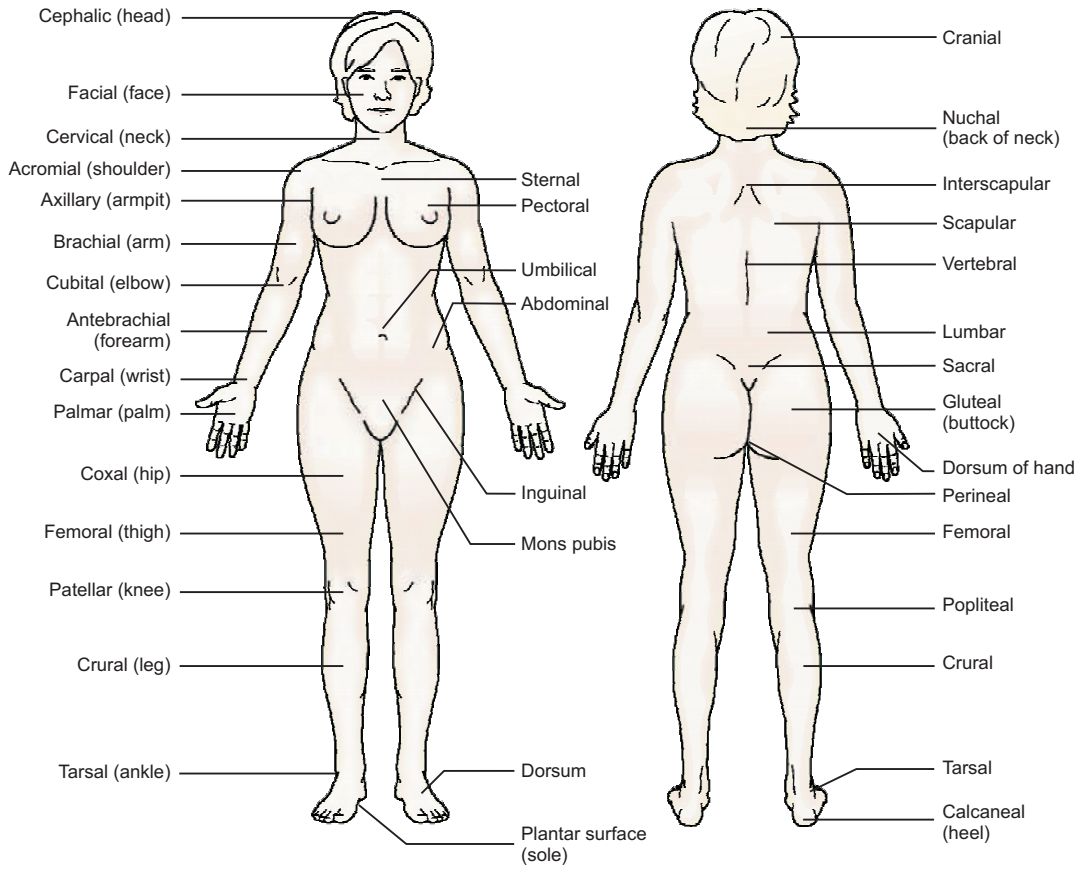

Figure 2.4: Terms for body parts and areas.

the body is divided into two major body cavities, dorsal and ventral (Figure 2.6). The organs within them are called the viscera. Various membranes line the cavities, cover the viscera, and hold the viscera in place (Table 2.2).

2.2.3.1 Posterior Body Cavity

The posterior body cavity has two subdivisions: the cranial cavity, which is enclosed by the bony cranium (braincase) and contains the brain, and the vertebral canal, which is enclosed by the vertebral column (backbone) and contains the spinal cord.

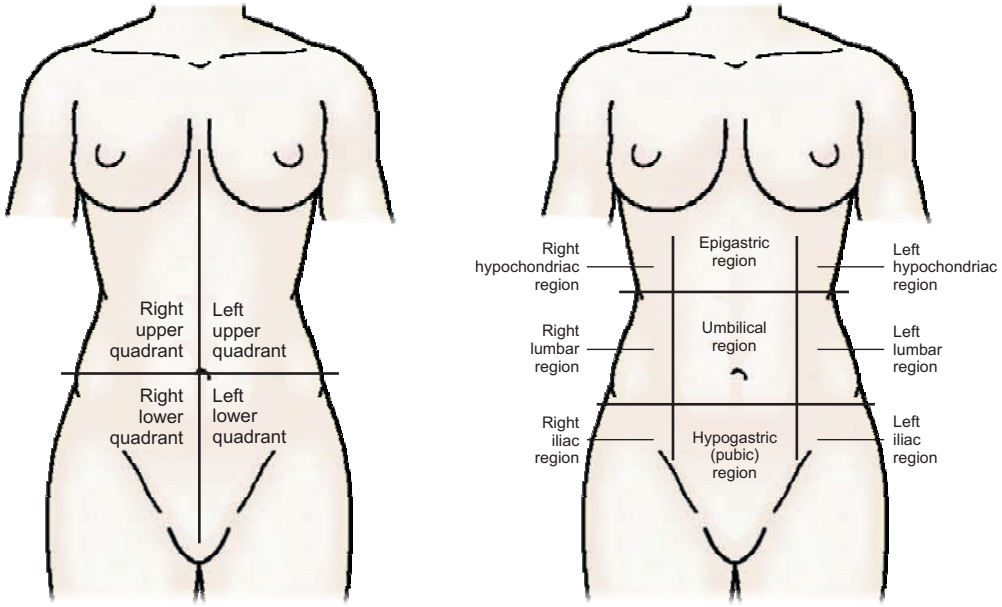

(a) Abdominal quadrants consist of four subdivisions.

(b) Abdominal regions consist of nine subdivisions.

Figure 2.5: Subdivisions of the Abdomen.

The posterior body cavity is lined by three membranous layers, called the meninges. Among other functions, the meninges protect the delicate nervous tissue from the hard protective bone that encloses it. The most inner of the meninges is tightly bound to the surface of the brain and the spinal cord. The space between this layer and the next layer is filled with cerebrospinal fluid. Spinal meningitis, a serious condition, is an inflammation of the meninges usually caused by an infection.

2.2.3.2 Anterior Body Cavity

The large anterior body cavity is subdivided into the thoracic, abdominal, and pelvic cavities (Figure 2.6). The rib cage surrounds the thoracic cavity, and a muscular

partition, called the diaphragm separates it from the abdominal cavity.

Abdominal muscles primarily enclose the abdominal cavity and the pelvic bones encase the small space known as the pelvic cavity. The abdominal and pelvic cavities are not physically separated and sometimes are called the abdominopelvic cavity.

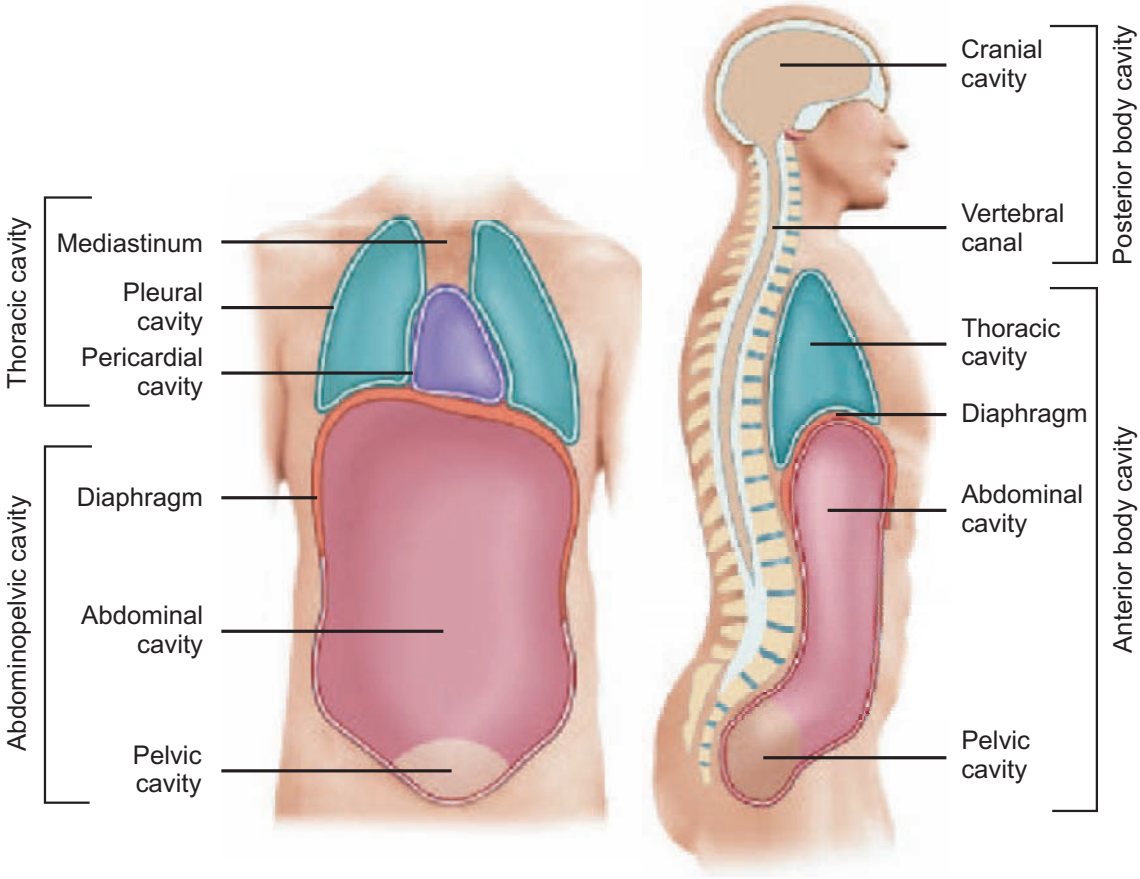

Figure 2.6: The two major body cavities and their subdivisions (adapted from [Mader, 2004]).

The membranes that cover the organs of the trunk cavities and line the trunk cavities are called serous membranes. They are named this way because they secrete a fluid that has just about the same composition as serum. The serous fluid between the smooth serous membranes reduces friction as the viscera rub against each other or against the body wall. To understand the relationship between serous membranes and an organ, imagine an inflated balloon into which a fist has been pushed (Figure 2.7). The fist represents an organ, the inner balloon wall in contact with the fist represents the visceral serous membrane covering the organ, and the outer part

of the balloon wall represents the parietal serous membrane. The cavity or space between the visceral and parietal serous membranes is normally filled with a thin, lubricating film of serous fluid produced by the membranes. As organs rub against the body wall or against another organ, the combination of serous fluid and smooth serous membranes reduces friction.

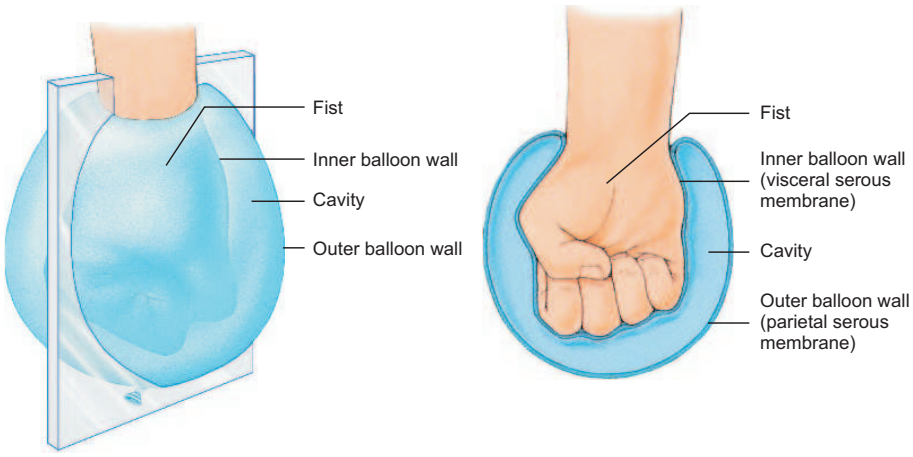

Figure 2.7: Relationship between serous membranes and an organ (adapted from [Seeley et al., 2004]).

The thoracic cavity – The thoracic cavity is enclosed by the rib cage and contains three serous membrane-lined cavities: a pericardial cavity and two pleural cavities. It is divided into right, left, and medial portions by a partition called the mediastinum. The right and left sides contain the lungs. and are lined by a two-layered membrane called the pleura. The outer layer, or parietal pleura, lines the inner surface of the thoracic wall against the inside of the rib cage, the lateral surfaces of the mediastinum, and the superior surface of the diaphragm; the inner layer, or visceral pleura, forms the external surface of the lung. The narrow, moist space between the visceral and parietal pleurae is called the pleural cavity. It is lubricated by the pleural fluid.

The medial portion, or mediastinum, is occupied by the esophagus and trachea, a gland called the thymus, the heart and the major blood vessels connected to it. The heart is enclosed by a two-layered membrane called the pericardium. The visceral pericardium forms the heart surface, while the parietal pericardium is separated from it by a space called the pericardial cavity. This space is lubricated by pericardial fluid.

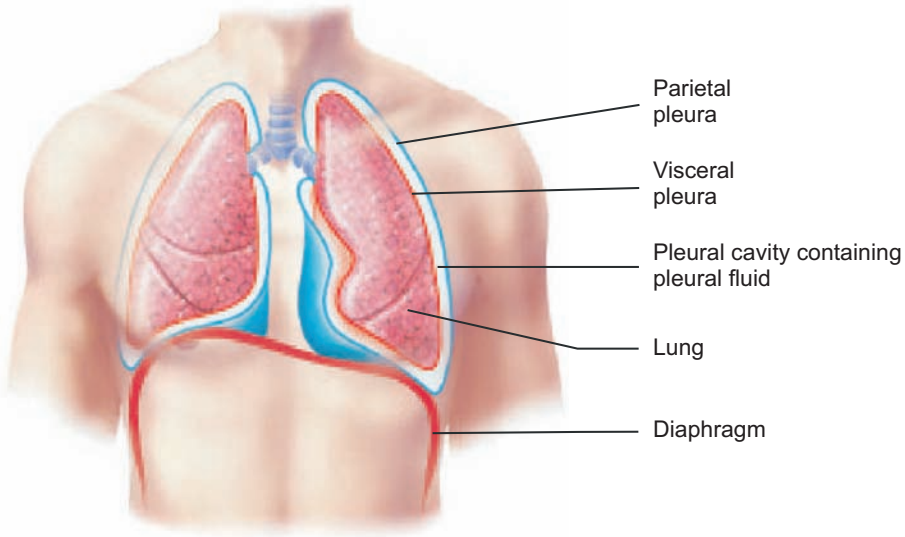

(a) Parietal pleura, visceral pleura, and pleural cavity.

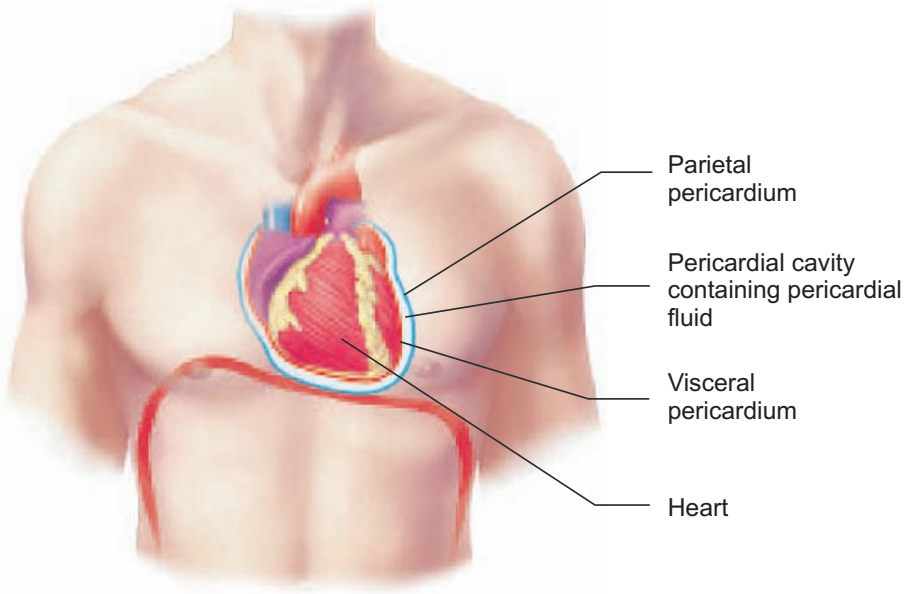

(b) Parietal pericardium, visceral pericardium, and pericardial cavity.

Figure 2.8: Location of Serous Membranes (adapted from [Seeley et al., 2004]).

The Abdominopelvic Cavity – The abdominopelvic cavity consists of the abdominal cavity above the brim of the pelvis and the pelvic cavity below the brim. Abdominal muscles primarily enclose the abdominal cavity, which contains the stomach, intestines, liver, spleen, pancreas, and kidneys. Pelvic bones encase the small space known as the pelvic cavity, where the urinary bladder, part of the large intestine, and the internal reproductive organs are housed. The abdominal and pelvic cavities are not physically separated and are called the abdominopelvic cavity.

The abdominopelvic cavity contains a moist serous membrane called the peritoneum. The parietal peritoneum lines the wall of the abdominopelvic cavity and the inferior surface of the diaphragm, while the visceral peritoneum covers the external surfaces of most digestive organs. The peritoneal cavity is the space between the parietal and visceral layers. It is lubricated by peritoneal fluid.

Some organs of the abdominal cavity lie between the peritoneum and dorsal body wall (outside of the peritoneal cavity), so they are said to have a retroperitoneal position. These include the kidneys, ureters, adrenal glands, most of the pancreas, and abdominal portions of two major blood vessels, the aorta and inferior vena cava.

Mesenteries, which consist of two layers of peritoneum fused together, connect the visceral peritoneum of some abdominopelvic organs to the parietal peritoneum on the body wall or to the visceral peritoneum of other abdominopelvic organs (Figure 2.9). The mesenteries anchor the organs to the body wall and provide a pathway for nerves and blood vessels to reach the organs. Other abdominopelvic organs are more closely attached to the body wall and do not have mesenteries.

The mesentery gives support to the intestines from the dorsal abdominal wall. The membrane then wraps around the intestines and some other viscera, forming a moist membrane called the serosa on their outer surfaces. The mesentery of the large intestine is called the mesocolon. The visceral peritoneum consists of the mesenteries and serosae.

A fatty membrane called the greater omentum hangs like an apron from the inferolateral margin of the stomach and overlies the intestines. It is unattached at its inferior border and can be lifted to reveal the intestines. A smaller lesser omentum extends from the superomedial border of the stomach to the liver.

The table 2.2 summarizes the presentation of the body cavities and membranes.

2.2.4 Organ Systems

The organs of the body work together in systems. The human body has 11 organ systems and an immune system, which is better described as a population of cells than as an organ system. These systems are classified in the following list by their principal functions.

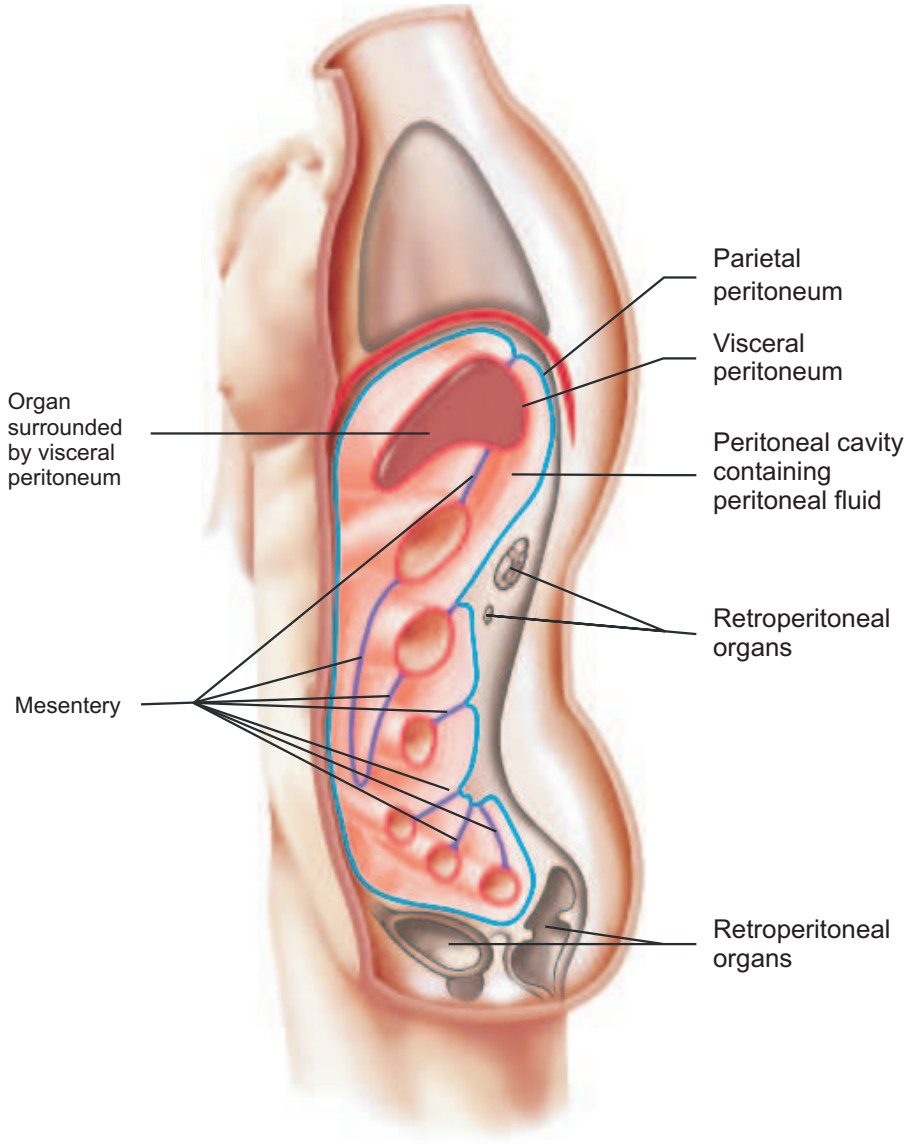

Figure 2.9: Sagittal section through the abdominopelvic cavity showing the parietal peritoneum (blue), visceral peritoneum (red), peritoneal cavity, mesenteries (purple), and retroperitoneal organs (adapted from [Seeley et al., 2004]).

Name of Cavity	Associated Viscera	Membranous Lining
Dorsal Body Cavity		
Cranial cavity	Brain	Meninges
Vertebral canal	Spinal coord	Meninges
Ventral Body Cavity		
Thoracic Cavity		
Pleural cavaties (2)	Lungs	Pleurae
Pericardial cavity	Heart	Pericarduim
Abdominopelvic Cavity		
Abdominal cavity	Digestive organs, spleen, kidneys	Peritoneum
Pelvic cavity	Bladder, rectum, reproductive organs	Peritoneum

Table 2.2: Body Cavities and Membranes

2.2.4.1 Support, Movement, and Protection

Integumentary system The integumentary system, includes the skin and accessory organs, such as the hair, nails, sweat glands, and sebaceous glands. The skin protects underlying tissues, contains sense organs, helps regulate body temperature and even synthesizes certain chemicals that affect the rest of the body.

Skeletal system The skeletal system and the muscular system give the body support and are involved in the ability of the body and its parts to move. The skeletal system, consists of the bones of the skeleton and associated cartilage, as well as the ligaments that bind these structures together. The skeleton protects body parts. For example, the skull forms a protective encasement for the brain, as does the rib cage for the heart and lungs. Some bones produce blood cells, and all bones are a storage area for calcium and phosphorus salts. The skeleton as a whole serves as a place of attachment for the muscles.

Muscular system Contraction of skeletal muscles, accounts for the ability of the body to move voluntarily and to respond to outside stimuli. These muscles also maintain posture and are responsible for the production of body heat. Cardiac muscle and smooth muscle are called involuntary muscles because they contract automatically. Cardiac muscle makes up the heart, and smooth muscle is found within the walls of internal organs.

2.2.4.2 Integration and Coordination

Nervous system The nervous system, consists of the brain, spinal cord, and associated nerves. The nerves conduct nerve impulses from the sense organs to the brain and spinal cord. They also conduct nerve impulses from the brain and spinal cord to the muscles and glands. The sense organs provide us with information about the outside environment. This information is then processed by the brain and spinal cord.

Endocrine system The endocrine system, consists of the hormonal glands that secrete chemicals that serve as messengers between body parts. Both the nervous and endocrine systems help maintain a relatively constant internal environment by coordinating and regulating the functions of the body's other systems. The nervous system acts quickly but has a short-lived effect; the endocrine system acts more slowly but has a more sustained effect on body parts. The endocrine system also helps maintain the proper functioning of the reproductive organs.

2.2.4.3 Maintenance of the Body

The internal environment of the body is maintained by the blood within the blood vessels and the tissue fluid that surrounds the cells. Five systems add substances to and/or remove substances from the blood: the cardiovascular, lymphatic, respiratory, digestive, and urinary systems.

Cardiovascular system The cardiovascular system, consists of the heart and the blood vessels that carry blood through the body. Blood transports nutrients and oxygen to the cells, and removes waste molecules to be excreted from the body. Blood also contains cells produced by the lymphatic system.

Lymphatic system The lymphatic system protects the body from disease.

Respiratory system The respiratory system, consists of the lungs and the tubes that take air to and from the lungs. The respiratory system brings oxygen into the lungs and takes carbon dioxide out of the lungs.

Digestive system The digestive system, consists of the mouth, esophagus, stomach, small intestine, and large intestine (colon), along with the accessory organs: teeth, tongue, salivary glands, liver, gallbladder, and pancreas.

Urinary system The urinary system, contains the kidneys and the urinary bladder. This system eliminates the nitrogenous wastes and helps regulate the fluid level and chemical content of the blood.

2.2.4.4 Reproduction and Development

The male and female reproductive systems, contain different organs.

Reproductive system The male reproductive system consists of the testes, other glands, and various ducts that conduct semen to and through the penis. The female reproductive system consists of the ovaries, uterine tubes, uterus, vagina, and external genitalia.

2.3 The Female Pelvis and Perineum

2.3.1 Introduction to the Pelvis and Perineum

The term *pelvis* is used to denote a variety of structures: a region, the pelvic girdle, and the pelvic cavity.

In common usage, the pelvis is the part of the trunk inferoposterior to the abdomen and is the area of transition between the trunk and the lower limbs. Anatomically, the pelvis is the space or compartment surrounded by the pelvic girdle (bony pelvis), part of the appendicular skeleton of the lower limb.

The pelvis is subdivided into greater and lesser pelves. The greater pelvis consists primarily of the space superior to the iliopectineal line, including the two iliac fossae and the region between them. The lesser pelvis, located below the iliopectineal line, is bounded anteriorly by the pubic bones, posteriorly by the sacrum and coccyx, and laterally by the ischium and a small segment of the ilium.

The greater pelvis affords protection to inferior abdominal viscera similar to the way the inferior thoracic cage protects superior abdominal viscera. The lesser pelvis provides the skeletal framework for both the pelvic cavity and the perineum compartments of the trunk separated by the musculofascial pelvic diaphragm.

Externally, the pelvis is covered or overlapped by the inferior anterolateral abdominal wall anteriorly, the gluteal region of the lower limb posterolaterally, and the perineum inferiorly.

The perineum refers both to the area of the surface of the trunk between the thighs and the buttocks, extending from the coccyx to the pubis, and to the shallow compartment lying deep to this area and inferior to the pelvic diaphragm. The perineum includes the anus and external genitalia.

2.3.2 The Pelvic Girdle

The pelvic girdle (Figure 2.11) is a basin-shaped ring of bones that marks the distal margin of the trunk and connects the vertebral column to the two femurs. The pelvis rests upon the lower extremities and supports the spinal column. It is composed of

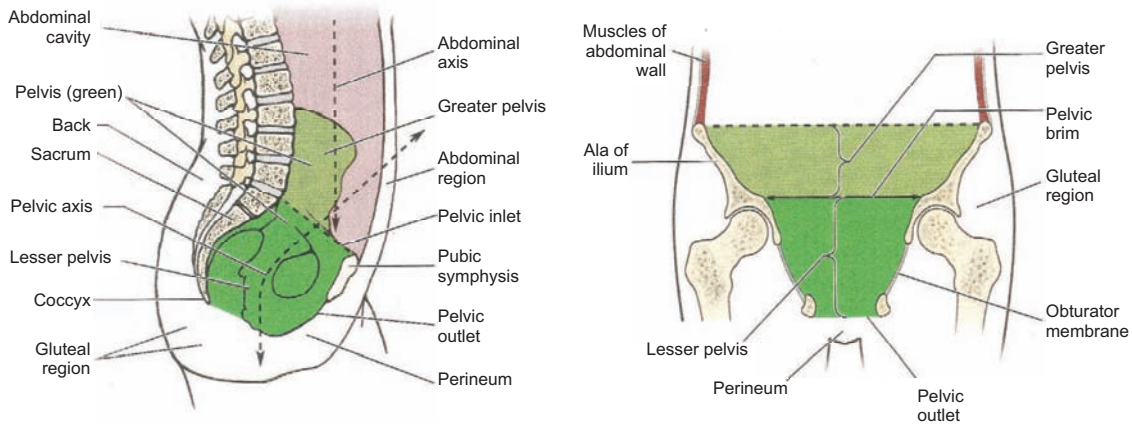

Figure 2.10: Pelvis and perineum (adapted from [Moore and Dalley, 2006])

two innominate bones (coxal bones, hipbones), one on each side, joined anteriorly and articulated with the sacrum posteriorly. The bones of the pelvic girdle are firmly attached to one another and bear the weight of the body.

The primary functions of the pelvic girdle is to bear the weight of the upper body when sitting and standing and transfer that weight from the axial to the lower appendicular skeleton. The pelvic girdle also provides attachment for the powerful muscles of locomotion and posture, as well as those of the abdominal wall, withstanding the forces generated by their actions. Consequently, the pelvic girdle is quite strong and rigid, especially compared to the pectoral (shoulder) girdle.

The pelvic girdle, contains and protect the pelvic viscera (inferior parts of the urinary tracts and the internal reproductive organs) especially but also the inferior abdominal viscera (intestines), while permitting passage of their terminal parts via the perineum. In the females the pelvic girdle also as to allow for the passage of a full-term fetus (see Chapter 4). The pelvic girdle provides support for the abdominopelvic viscera and gravid (pregnant) uterus and provides attachment for the muscles and membranes that assist in these functions by forming the pelvic floor and filling gaps that exist in or around it.

2.3.2.1 Bones and Features of the Pelvic Girdle

In a mature individual, the pelvic girdle is formed by three bones, the two hip bones bones (coxal bones, pelvic bones) and the sacrum, bound to each other by dense ligaments.

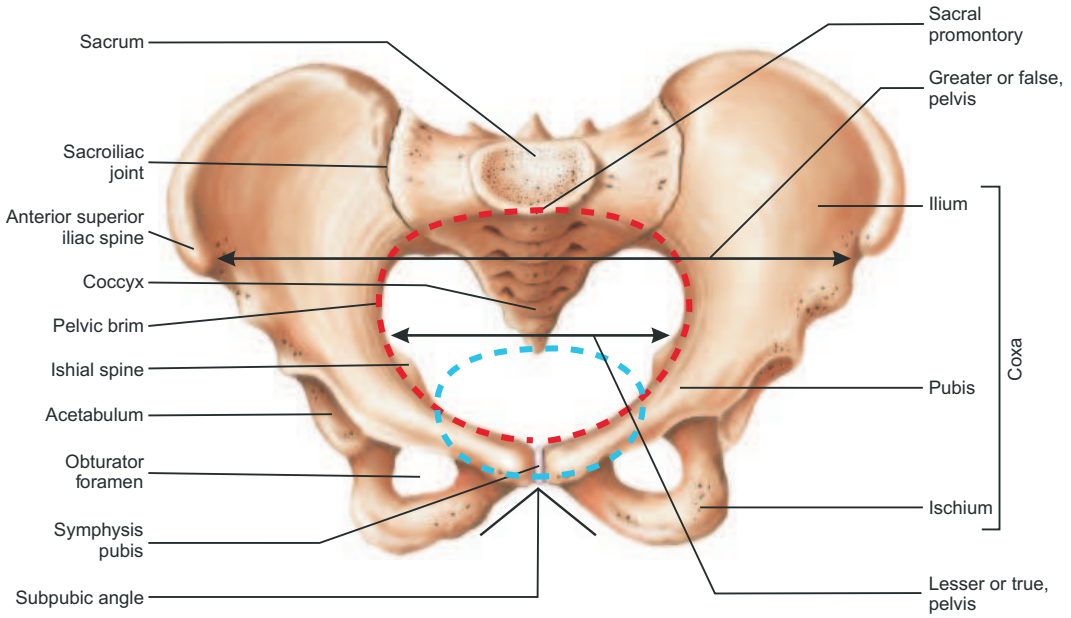

Figure 2.11: Anterior view of the pelvic girdle (adapted from [Seeley et al., 2004])

The hip bone In infants and children, the hip bones consist of three separate bones that are united by a triradiate cartilage at the acetabulum (Figure 2.12), the cup-like depression in the lateral surface of the hip bone, which articulates with the head of the femur. After puberty, the ilium, ischium, and pubis fuse to form the hip bone. The two hip bones are joined anteriorly at the pubic symphysis and articulate posteriorly with the sacrum at the sacroiliac joints to form the pelvic girdle. The internal (medial or pelvic) aspects of the hip bones bound the pelvis, forming its lateral walls. Their external aspects is primarily involved in providing attachment for the lower limb muscles.

The ilium is formed by a fan-shaped upper part or ala (wing) and a thicker, lower part called the body. The body participates in formation of the upper portion of the acetabulum and unites with the bodies of the ischium and pubis. The medial surface of the ilium presents as a large concave area: the anterior portion is the iliac fossa; the smaller posterior portion is composed of a rough upper part, the iliac tuberosity; and the lower part contains a large surface for articulation with the sacrum. At the inferior medial margin of the iliac fossa, a rounded ridge, the arcuate line, ends anteriorly in the iliopectineal eminence. Posteriorly, the arcuate line is continuous with the anterior margin of the ala of the sacrum across the anterior aspect of the sacroiliac joint. Anteriorly, it is continuous with the ridge or pecten on the superior ramus of the pubis. The lateral surface or dorsum of the ilium

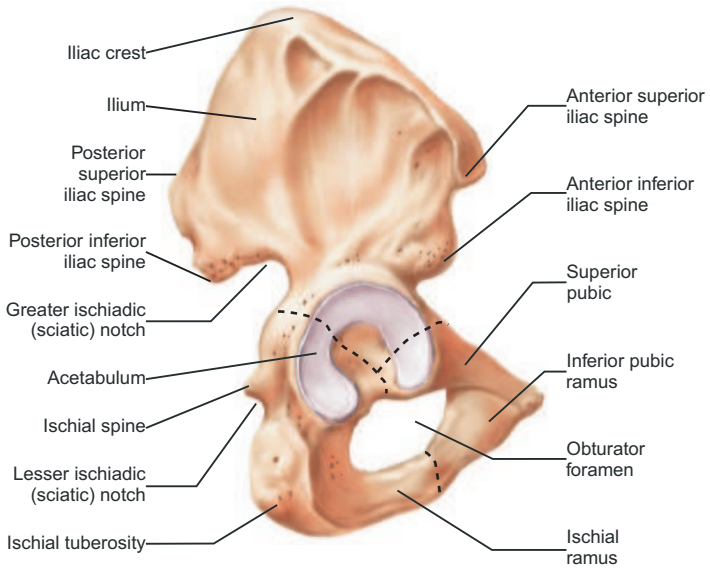

Figure 2.12: Lateral view of the right hip bone (adapted from [Seeley et al., 2004]).

is traversed by three ridges, the posterior, anterior, and the inferior gluteal lines. The superior border is called the crest, and at its extremities are the anterior and posterior superior iliac spines. The principal feature of the anterior border of the ilium is the heavy anterior inferior iliac spine. Important aspects of the posterior border are the posterior superior and the inferior iliac spines and, below the latter, the greater sciatic notch, the inferior part of which is bounded by the ischium.

The ischium is composed of a body, superior and inferior rami, and a tuberosity. The body is the heaviest part of the bone and joins with the ilium and pubis to form the acetabulum. The ischium presents three surfaces, a smooth internal surface, continuous above with the body of the ilium and below with the inner surface of the superior ramus of the ischium, forming the posterior portion of the lateral wall of the lesser pelvis. The external surface of the ischium is the portion that enters into the formation of the acetabulum and the posterior surface is the area between the acetabular rim and the posterior border. The posterior border, with the ilium, forms the bony margin of the greater sciatic notch. The superior ramus of the ischium descends from the body of the bone to join the inferior ramus at an angle of approximately 90 degrees. The large ischial tuberosity and its inferior portion are situated on the convexity of this angle. The inferior portion of the tuberosity forms the point of support in the sitting position. The posterior surface is divided into two areas by an oblique line. The lesser sciatic notch occupies the posterior border of the superior ramus between the spine and the tuberosity. The inferior ramus, as

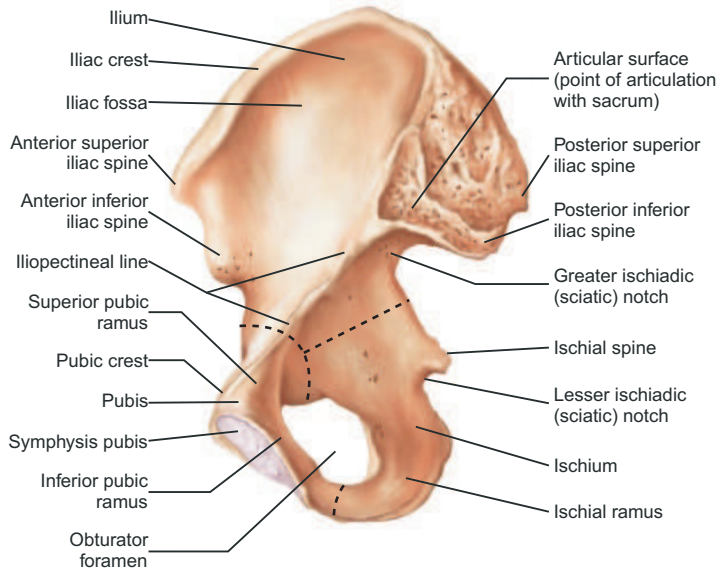

Figure 2.13: Medial view of the right hip bone (adapted from [Seeley et al., 2004]).

it is traced forward, joins the inferior ramus of the pubis to form the arcus pubis (ischiopubic arch).

The pubis is composed of a body and two rami, superior and inferior. The body contributes to the formation of the acetabulum, joining with the body of the ilium at the iliopectineal eminence and with the body of the ischium in the region of the acetabular notch. The superior ramus passes medially and forward from the body to meet the corresponding ramus of the opposite side at the symphysis pubica. The medial or fore portion of the superior ramus is broad and flattened anteroposteriorly and presents an outer and an inner surface, the symphyseal area, and an upper border or "crest". Approximately two cm from the medial edge of the ramus and in line with the upper border is the prominent pubic tubercle, an important landmark.

Below the crest is the anterior surface and the posterior or deep surface. The medial portion of the superior ramus is continuous below with the inferior ramus, and the lateral part presents a wide, smooth area anterosuperiorly, behind which is an irregular ridge, the pecten ossis pubis. The pecten pubis forms the anterior part of the linea terminalis. In front of and below the pectineal area is the obturator crest, passing from the tubercle to the acetabular notch. On the inferior aspect of the superior ramus is the obturator sulcus. The inferior ramus is continuous with the superior ramus and passes downward and backward to join the inferior ramus of the ischium, forming the "ischiopubic arch".

The sacrum The sacrum is formed in the adult by the union of 5 or 6 sacral vertebrae. Occasionally, the fifth lumbar vertebra is partly fused with it. The process of union is known as "sacralization" in the vertebral column. The sacrum constitutes the base of the vertebral column. As a single bone, it is considered to have a base, an apex, two surfaces (pelvic and dorsal), and two lateral portions. The base faces upward and is composed principally of a central part, formed by the upper surface of the body of the first sacral vertebra, and 2 lateral areas of alae. The body articulates by means of a fibrocartilage disk with the body of the fifth lumbar vertebra. The alae represents the heavy transverse processes of the first sacral vertebra that articulate with the two iliac bones. The anterior margin of the body is called the promontory and forms the sacrovertebral angle with the fifth lumbar vertebra. The rounded anterior margin of each ala constitutes the posterior part of the linea terminalis. The pelvic surface of the sacrum is rough and convex. In the midline is the median sacral crest (fused spinal processes), and on either side is a flattened area formed by the fused laminae of the sacral vertebrae.

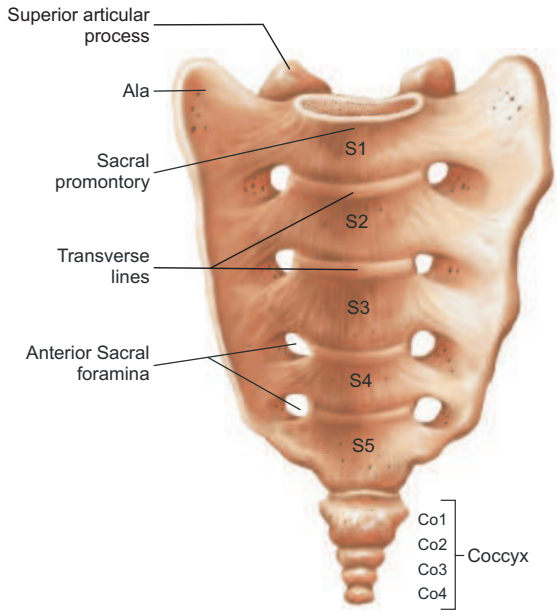

Figure 2.14: Sacrum, anterior view (adapted from [Seeley et al., 2004]).

The laminae of the fifth vertebra and, in many cases, those of the fourth and occasionally of the third are incomplete (the spines also are absent), thus leaving a wide opening to the dorsal wall of the sacral canal known as the sacral hiatus. Lateral to the laminae are the articular crests (right and left), which are in line with the paired superior articular processes above. The lateral processes articulate with

the inferior articular processes of the fifth lumbar vertebra. The inferior extensions of the articular crests form the sacral cornua that bind the sacral hiatus laterally and are attached to the cornua of the coccyx. The cornua can be palpated in life and are important landmarks indicating the inferior opening of the sacral canal (for sacral-caudal anesthesia). The lateral portions of the sacrum are formed by the fusion of the transverse processes of the sacral vertebrae. They form dorsally a line of elevations called the lateral sacral crests. The parts corresponding to the first three vertebrae are particularly massive and present a large area facing laterally called the articular surface, which articulates with the sacrum. Posterior to the articular area, the rough bone is called the sacral tuberosity. It faces the tuberosity of the ilium. The apex is the small area formed by the lower surface of the body of the fifth part of the sacrum.

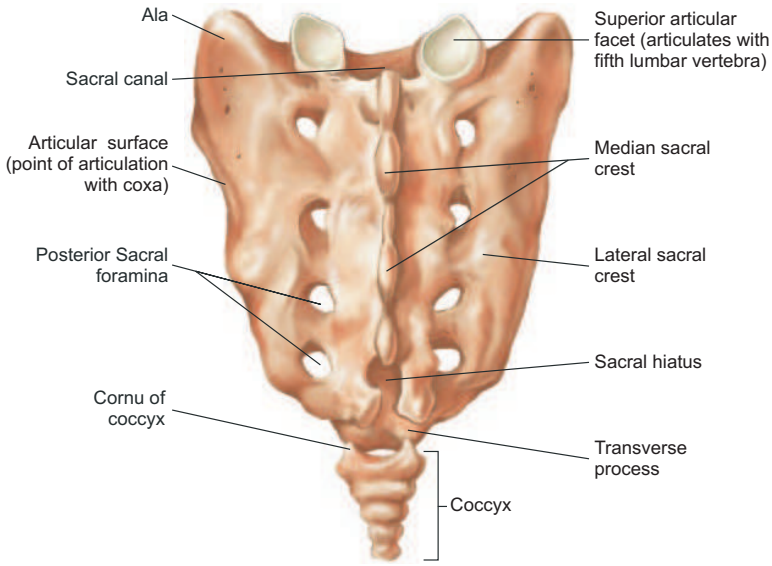

Figure 2.15: Sacrum, posterior view (adapted from [Seeley et al., 2004]).

The coccyx is formed by 4 (occasionally 3 or 5) caudal or coccygeal vertebrae. The second, third, and fourth parts are frequently fused into a single bone that articulates with the first by means of a fibrocartilage. The entire coccyx may become ossified and fused with the sacrum.

2.3.2.2 Joints and Ligaments of the Pelvic Girdle

The sacroiliac joints and the pubic symphysis are the primary joints of the pelvic girdle (Fig 2.16). The sacroiliac joints link the axial skeleton (the skeleton of the trunk, composed of the vertebral column at this level) and the inferior appendicular

skeleton (skeleton of the lower limb). The lumbosacral and sacrococcygeal joints, although joints of the axial skeleton, are directly related to the pelvic girdle. Strong ligaments support and strengthen these joints.

Sacroiliac Joints The sacroiliac joints are strong, weight-bearing compound joints, consisting of an anterior synovial joint (between the ear-shaped auricular surfaces of the sacrum and ilium, covered with articular cartilage) and a posterior syndesmosis (between the tuberosities of the same bones). The articular (auricular) surfaces of the synovial joint have irregular but congruent elevations and depressions that interlock. The sacroiliac joints differ from most synovial joints in that limited mobility is allowed, a consequence of their role in transmitting the weight of most of the body to the hip bones. Weight is transferred from the axial skeleton to the ilia and then to the femurs during standing and to the ischial tuberosities during sitting. As long as tight apposition is maintained between the articular surfaces, the sacroiliac joints remain stable.

The sacrum is suspended between the iliac bones and is firmly attached to them by posterior and interosseous sacroiliac ligaments. The thin anterior sacroiliac ligaments are merely the anterior part of the fibrous capsule of the synovial part of the joint. The abundant interosseous sacroiliac ligaments (lying deep between the tuberosities of the sacrum and ilium and occupying an area of approximately 10 cm^2) are the primary structures involved in transferring the weight of the upper body from the axial skeleton to the two ilia of the appendicular skeleton. The posterior sacroiliac ligaments are the posterior external continuation of the same mass of fibrous tissue. Because the fibers of the interosseous and posterior sacroiliac ligaments run obliquely upward and outward from the sacrum, the axial weight pushing down on the sacrum actually pulls the ilia inward (medially) so that they compress the sacrum between them, locking the irregular but congruent surfaces of the sacroiliac joints together. The iliolumbar ligaments are accessory ligaments to this mechanism.

Inferiorly, the posterior sacroiliac ligaments are joined by fibers extending from the posterior margin of the ilium (between the posterior superior and posterior inferior iliac spines) and the base of the coccyx to form the sacrotuberous ligament. This massive ligament passes from the posterior ilium and lateral sacrum and coccyx to the ischial tuberosity, transforming the sciatic notch of the hip bone into a large sciatic foramen. The sacrospinous ligament, passing from lateral sacrum and coccyx to the ischial spine, further subdivides this foramen into greater and lesser sciatic foramina.

Pubic Symphysis The pubic symphysis joint consists of a fibrocartilaginous interpubic disc and surrounding ligaments uniting the bodies of the pubic bones in

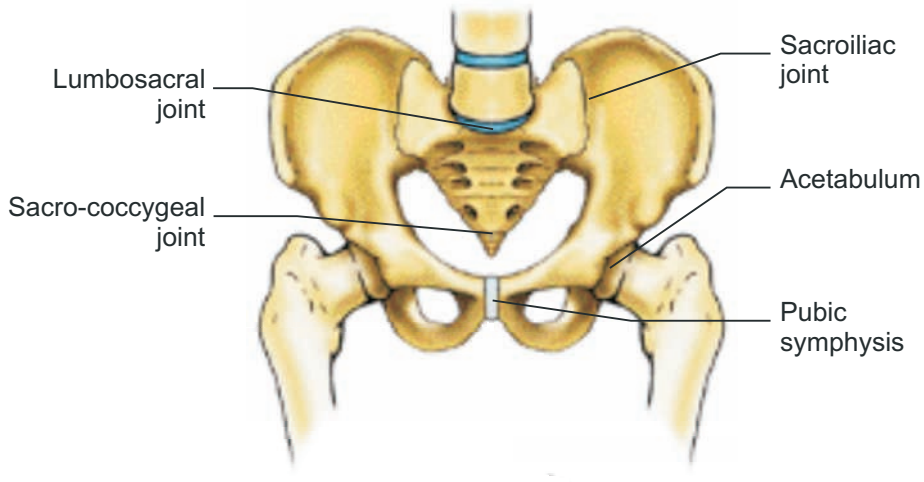

Figure 2.16: Anterior view of the pelvic girdle joins (adapted from the reference [Moore and Dalley, 2006])

the median plane (Figures 2.16 and 2.17). The interpubic fibrocartilage is generally wider in women and is thicker in front than behind, projecting beyond the edges of the bones, especially on the posterior aspect, blending intimately with the ligaments at its margins. Sometimes it is woven throughout, but often the interpubic fibrocartilage presents an elongated, narrow fissure with fluid in the interspace, partially dividing the cartilage into two plates. The interpubic cartilage is intimately adherent to the layer of hyaline cartilage that covers the symphyseal surface of each pubic bone.

The ligaments joining the bones are thickened at the superior and inferior margins of the symphysis, forming the superior and inferior pubic ligaments. The superior pubic ligament connects the superior aspects of the pubic bodies and interpubic disc, extending as far laterally as the pubic tubercles. The inferior (arcuate) pubic ligament is a thick band of closely connected fibers that fills the angle between the pubic rami to form a smooth, rounded top to the pubic arch (Figure 2.11). On the anterior and posterior aspects of the joint, the ligament gives off decussating fibers that, interlacing with one another, strengthen the joint.

Lumbosacral Joints In the lumbosacral joint, the L5 and S1 vertebrae articulate at the anterior intervertebral joint formed by the intervertebral disc between their bodies (Figure 2.16) and at two posterior zygapophysial joints (facet joints) between the articular processes of these vertebrae. The facets on the S1 vertebra face posteromedially, interlocking with the anterolaterally facing inferior articular facets of the L5 vertebra, preventing the lumbar vertebra from sliding anteriorly

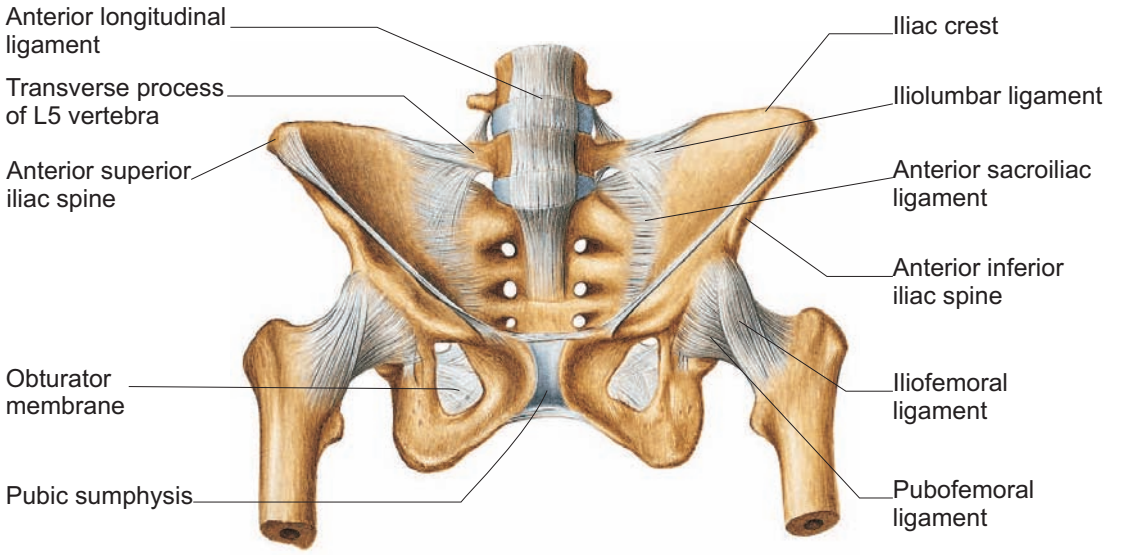

(a) Ventral view.

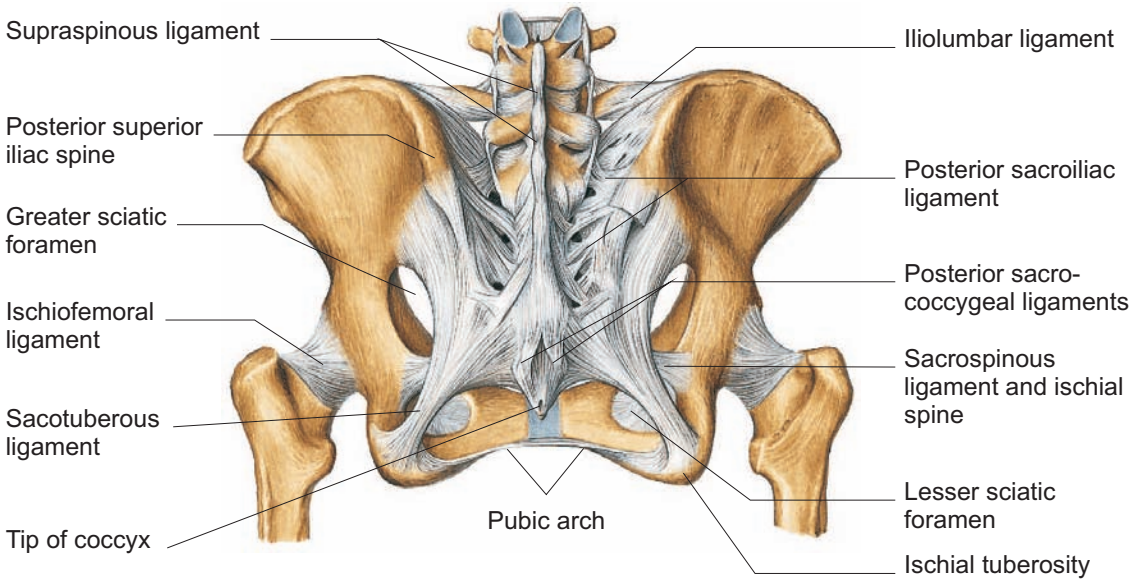

(b) Dorsal view.

Figure 2.17: Articulations of the pelvic girdle and the lumbosacral joint (adapted from the reference [Sobotta et al., 2001]).

down the incline of the sacrum. These joints are further strengthened by fan-like iliolumbar ligaments radiating from the transverse processes of the L5 vertebra to the ilia.

Sacrococcygeal Joint The sacrococcygeal joint is a secondary cartilaginous joint with an intervertebral disc (Figure 2.16). The apex of the sacrum is joined to the base of the coccyx by fibrocartilage and ligaments. The anterior and posterior sacrococcygeal ligaments are long strands that reinforce the joint, much like the anterior and posterior longitudinal ligaments do for the superior vertebrae.

2.3.3 Pelvic Cavity

The abdominopelvic cavity extends inferiorly into the pelvis and superiorly into the thoracic cage, so that its inferior and superior parts are relatively protected (Figure 2.10). A perforating wound in either the thorax or the pelvis could therefore involve the abdominopelvic cavity and its contents. The space bounded peripherally by the bony, ligamentous, muscular pelvic walls and floor is the inferoposterior part of the abdominopelvic cavity, continuous with the abdominal cavity at the pelvic inlet but angulated posteriorly from it (Figure 2.10). The abdominal and pelvic cavities are described separately, although continuous, for descriptive purposes, facilitating the regional approach.

The pelvic cavity contains the terminal parts of the ureters and the urinary bladder, rectum, pelvic genital organs, blood vessels, lymphatics, and nerves. In addition to these distinctly pelvic viscera, it also contains what might be considered an overflow of abdominal viscera: loops of small intestine (mainly ileum) and, frequently, large intestine (appendix and transverse and/or sigmoid colon). The pelvic cavity is limited inferiorly by the musculofascial pelvic diaphragm, which is suspended above the pelvic outlet, forming a bowl-like pelvic floor.

The pelvic cavity is bounded posteriorly by the coccyx and inferiormost sacrum, with the superior part of the sacrum forming a roof over the posterior half of the cavity (Figure 2.10). The bodies of the pubic bones and the pubic symphysis uniting them form an anteroinferior wall that is much shallower than the posterosuperior wall and ceiling formed by sacrum and coccyx. Consequently, the axis of the pelvis is curved, pivoting around the pubic symphysis. The curving form of the axis and the disparity in depth between the anterior and the posterior walls of the cavity are important factors in the mechanism of fetal passage through the pelvic canal.

2.3.3.1 Walls and Floor of the Pelvic Cavity

The pelvic cavity has two lateral walls, a posterior wall, an anteroinferior wall and a floor (Figures 2.18 to 2.20).

Anteroinferior Pelvic Wall The anteroinferior pelvic wall (more of a weight-bearing floor than an anterior wall in the anatomical position) is formed primarily by the bodies and rami of the pubic bones and the pubic symphysis (Figure 2.16). It participates in bearing the weight of the urinary bladder.

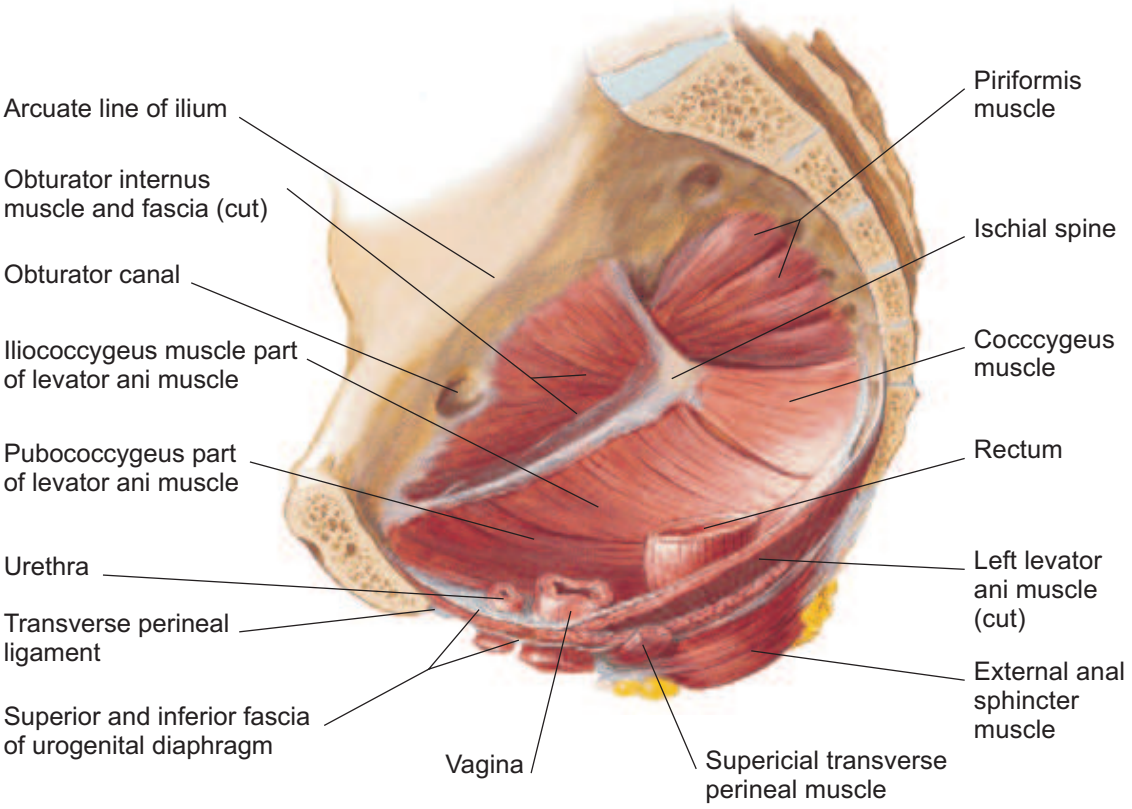

Figure 2.18: Medial view of the Pelvic floor diaphragm (adapted from the reference [Netter, 2006]).

Lateral Pelvic Walls The lateral pelvic walls are formed by the right and left hip bones, each of which includes an obturator foramen closed by an obturator membrane (Figure 2.17). The fleshy attachments of the obturator internus muscles cover most of the lateral pelvic walls (Figure 2.18). The fleshy fibers of each obturator internus converge posteriorly, become tendinous, and turn sharply laterally to pass from the lesser pelvis through the lesser sciatic foramen to attach to the greater trochanter of the femur. The medial surfaces of these muscles are covered by obturator fascia, thickened centrally as a tendinous arch that provides attachment for the pelvic diaphragm (Figure 2.18). The pelvic diaphragm is the boundary between

the pelvis and the perineum, forming the floor of the pelvic cavity and the roof of the perineum (Figure 2.20), this attachment divides the muscle into a superior pelvic portion and an inferior perineal portion. Medial to the pelvic portions of these muscles are the obturator nerves, vessels and other branches of the internal iliac vessels.

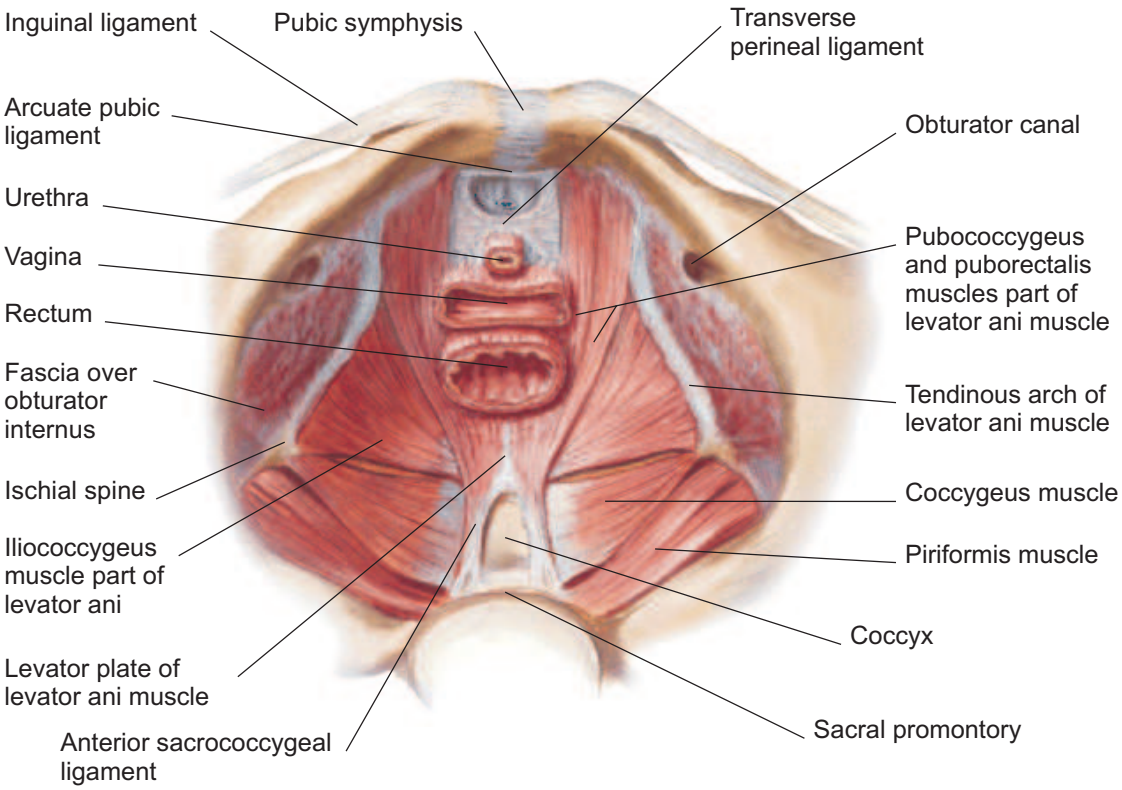

Figure 2.19: Pelvic floor diaphragm viewed from above (adapted from the reference [Netter, 2006]).

Posterior Wall (Posterolateral Wall and Roof) When in the anatomical position, the posterior pelvic wall consists of a bony wall and roof in the midline (formed by the sacrum and coccyx) and musculoligamentous posterolateral walls, formed by the ligaments associated with the sacroiliac joints and piriformis muscles (Figure 2.19). The different ligaments include the anterior sacroiliac, sacrospinous, and sacrotuberous ligaments. The piriformis muscles arise from the superior sacrum, lateral to its pelvic foramina. These muscles pass laterally, leaving the lesser pelvis through the greater sciatic foramen to attach to the superior border of the greater

trochanter of the femur. Much of the greater sciatic foramen is occupied by these muscles, forming the posterolateral walls of the pelvic cavity (Figure 2.18). The nerves of the sacral plexus are immediately deep (anteromedial) to these muscles (often embedded in the fleshy fibers). A gap at the inferior border of the piriformis allows for the passage of neurovascular structures between the pelvis and the lower limbs.

Pelvic Floor The pelvic floor is formed by the bowl or funnel-shaped pelvic diaphragm, which consists of the coccygeus and levator ani muscles and the fascias covering the superior and inferior aspects of these muscles (Figure 2.18 and 2.19). The pelvic diaphragm separates the pelvic cavity from the perineum within the lesser pelvis.

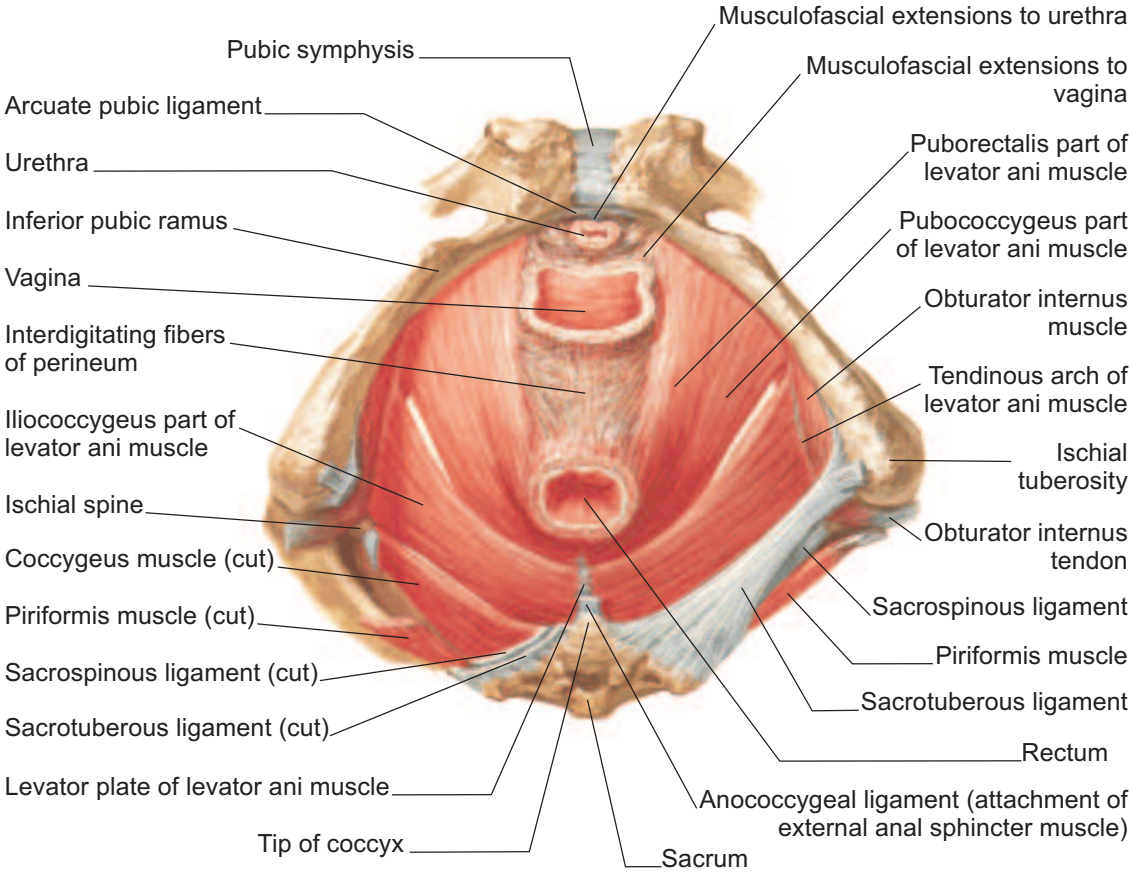

Figure 2.20: Pelvic floor diaphragm viewed from bellow (adapted from the reference [Netter, 2006]).

The coccygeus muscles departs from the lateral aspects of the inferior sacrum

and coccyx, with their fleshy fibers underlying the deep surface of the sacrospinous ligament (Figure 2.17). The levator ani is the larger and more important part of the pelvic floor. It is attached to the bodies of the pubic bones anteriorly, to the ischial spines posteriorly, and to a thickening in the obturator fascia (the tendinous arch of the levator ani) between the two bony sites on each side. The pelvic diaphragm thus stretches between the anterior, the lateral, and the posterior walls of the lesser pelvis, giving it the appearance of a hammock suspended from these attachments, closing much of the ring of the pelvic girdle. An anterior gap between the medial borders of the levator ani muscles of each side the urogenital hiatus gives passage to the urethra and the vagina.

The levator ani muscle is formed by three parts, designated according the attachment and course of its fibers (Figures 2.18 to 2.20):

- Puborectalis. The puborectalis is the thicker, narrower, medial part of the levator ani, consisting of muscle fibers that are continuous between the posterior aspects of the right and left pubic bodies. It forms a U-shaped muscular sling (puborectal sling) that passes posterior to the anorectal junction (Figure 2.20), bounding the urogenital hiatus. This part plays a major role in maintaining fecal continence.
- Pubococcygeus. The pubococcygeus is the wider but thinner intermediate part of the levator ani, which arises lateral to the puborectalis from the posterior aspect of the body of the pubis and anterior tendinous arch. It passes posteriorly in a nearly horizontal plane. The pubococcygeus lateral fibers attach to the coccyx and its medial fibers merge with those of the contralateral muscle to form a fibrous raphe or tendinous plate, part of the anococcygeal body or ligament between the anus and the coccyx.
- Iliococcygeus. The iliococcygeus is the posterolateral part of the levator ani, which arises from the posterior tendinous arch and ischial spine. It is thin and often poorly developed and also blends with the anococcygeal body posteriorly.

The levator ani acts as a dynamic floor, supporting the abdominopelvic viscera. Most of the time it is tonically contracted to support the abdominopelvic viscera and to assist in maintaining urinary and fecal continence. It is actively contracted during activities such as forced expiration, coughing, sneezing, vomiting, and fixation of the trunk during strong movements of the upper limbs (when lifting heavy objects for example), primarily to increase support of the viscera during periods of increased intra-abdominal pressure (resisting forces that would push it through the pelvic outlet).

Active contraction of the (voluntary) puborectalis portion is important in maintaining fecal continence immediately after rectal filling or during peristalsis when the

rectum is full and the involuntary sphincter muscle is relaxed. The levator ani must relax in order to allow urination and defecation. The increased intra-abdominal pressure for defecation is provided by contraction of the (thoracic) diaphragm and muscles of the anterolateral abdominal wall. The ability of the musculofascial pelvic floor to relax and distend is critical to the functions of defecation and parturition.

2.3.3.2 Peritoneum and Peritoneal Cavity of the Pelvis

The parietal peritoneum lining the abdominal cavity continues inferiorly into the pelvic cavity. The pelvic viscera (onto which it is reflected) and the pelvic fascia in which the viscera are embedded, separates the parietal peritoneum from the pelvic floor (Table 2.3). Except for the ovaries and uterine tubes, the pelvic viscera are not completely ensheathed by the peritoneum, mainly lying inferior to it. Only the uterine tubes (except for their ostia, which are open) are intraperitoneal and suspended by a mesentery. The ovaries, although suspended in the peritoneal cavity by a mesentery, are covered with a special, relatively-dull epithelium of cuboidal cells.

The existence of a loose areolar layer between the transversalis fascia and the parietal peritoneum of the inferior part of the anterior abdominal wall allows the bladder to expand between these layers as it becomes distended with urine. The region superior to the bladder (1 in Table 2.3) is the only site where the parietal peritoneum is not firmly bound to the underlying structures. Consequently, the level at which the peritoneum reflects onto the superior surface of the bladder, creating the supravesical fossa (2 in Table 2.3) is variable, depending on the fullness of the bladder. When the peritoneum reflects from the abdominopelvic wall onto the pelvic viscera and fascia, a series of folds and fossae are created (2 to 7 in Table 2.3).

The inferior third of the rectum is subperitoneal, because it is below the inferior limits of the peritoneum. The middle third is covered with peritoneum only on its anterior surface, and the superior third is covered on both its anterior and its lateral surfaces. The rectosigmoid junction, near the pelvic brim, is intraperitoneal.

2.3.3.3 Pelvic Fascia

The space between the membranous peritoneum and the muscular pelvic walls and floor not occupied by the pelvic viscera is occupied by a connective tissue, the pelvic fascia. This "layer" is a continuation of the comparatively thin endoabdominal fascia that lies between the muscular abdominal walls and the peritoneum superiorly. Traditionally, the pelvic fascia has been described as having parietal and visceral components (Figure 2.21).

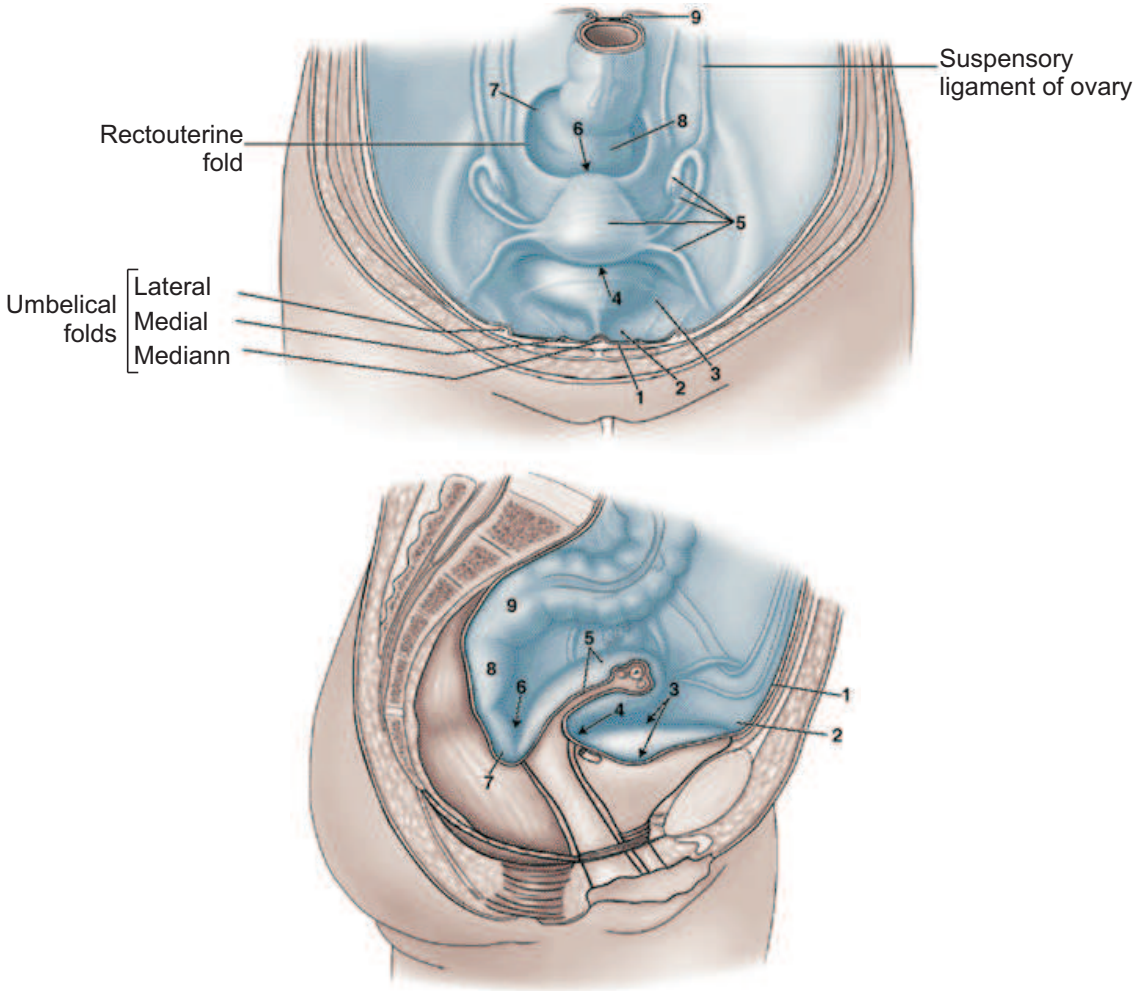

1. Descends anterior abdominal wall (loose attachment allows insertion of bladder as it fills)
2. Reflects onto superior surface of bladder, creating supravesical fossa
3. Covers convex superior surface (roof) of bladder and slopes down sides of roof to ascend lateral wall of pelvis, creating paravesical fossae on each side
4. Reflects from bladder roof onto body of uterus forming vesicouterine pouch
5. Covers body and fundus of uterus and posterior fornix of vagina; extends laterally from uterus as double fold or mesentery - broad ligament that engulfs uterine tubes, ovaries, and round ligaments of uterus
6. Reflects from vagina onto rectum, forming rectouterine pouch
7. Rectouterine pouch extends laterally and posteriorly to form pararectal fossae on each side of rectum
8. Ascends rectum; from inferior to superior, rectum is subperitoneal and then retroperitoneal.
9. Engulfs sigmoid colon beginning at rectosigmoid junction

Table 2.3: Peritoneal reflections in the pelvis (from [Moore and Dalley, 2006]).

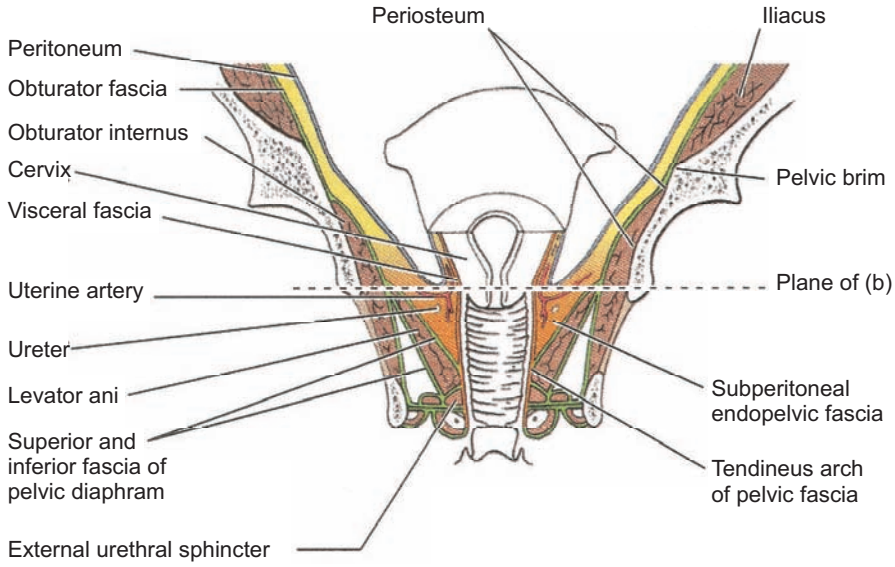

(a) Anterior view of coronal section.

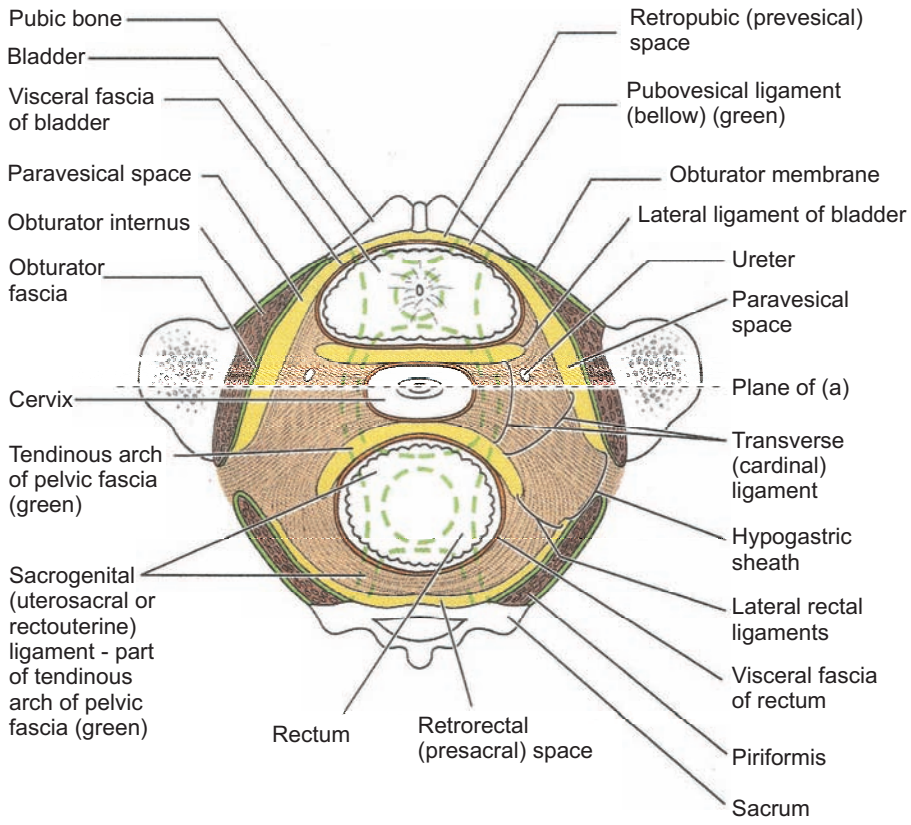

(b) Superior view of transverse section.

Figure 2.21: Pelvic fascia, endopelvic fascia and fascial ligaments (adapted from [Moore and Dalley, 2006]).

Membranous Pelvic Fascia: Parietal and Visceral The parietal pelvic fascia is a membranous layer of variable thickness that lines the inner aspect of the muscles forming the walls and floor of the pelvis (Figure 2.21). The parietal pelvic fascia covers the pelvic surfaces of the obturator internus, piriformis, coccygeus, levator ani, and part of the urethral sphincter muscles. Specific parts of the parietal fascia are named for the muscle they cover.

The visceral pelvic fascia includes the membranous fascia that directly ensheathes the pelvic organs. The membranous parietal and visceral layers become continuous where the organs penetrate the pelvic floor (Figure 2.21a). The tendinous arch of pelvic fascia, a thickening of the parietal fascia, forms a continuous bilateral band running from the pubis to the sacrum along the pelvic floor adjacent to the viscera (Figure 2.21b). The anteriormost part of this tendinous arch, the pubovesical ligament, connects the fundus of the bladder to the pubis. The posteriormost part of the band runs as the sacrogenital ligaments from the sacrum around the side of the rectum to attach to the vagina.

Endopelvic Fascia: Loose and Condensed The abundant connective tissue remaining between the parietal and the visceral membranous layers is usually considered part of the visceral fascia, but various authors label parts of it as parietal. It is probably more realistic to consider this remaining fascia simply as extraperitoneal or subperitoneal endopelvic fascia (Figure 2.21a), which is continuous with both the parietal and the visceral membranous fascias [Moore and Dalley, 2006]. This fascia forms a connective tissue matrix or packing material for the pelvic viscera (Figure 2.21). It varies markedly in density and content. Part of it is extremely loose areolar (fatty) tissue, relatively devoid of all but minor lymphatics and nutrient vessels.

Although these types of endopelvic fascia do not differ much in their gross appearance, other parts of the endopelvic fascia have a much more fibrous consistency, containing an abundance of collagen and elastic fibers and, according to some authors, a scattering of smooth muscle fibers. These parts are often described as "fascial condensations" or "pelvic ligaments". This fascial condensation gives passage to essentially all the vessels and nerves passing from the lateral wall of the pelvis to the pelvic viscera, along with the ureters. The hypogastric sheath divides into three laminae (leaflets or wings) that pass to or between the pelvic organs, as it extends medially from the lateral wall, conveying neurovascular structures and providing support. They are also referred to as ligaments because of the latter function. The anteriormost lamina, the lateral ligament of the bladder, passes to the bladder, conveying the superior vesical arteries and veins. The posteriormost lamina passes to the rectum, conveying the middle rectal artery and vein.

The middle lamina is more substantial than the other two lamina, passing medi-

ally to the uterine cervix and vagina as the transverse cervical ligament, also known clinically as the lateral cervical or Mackenrodt ligament (Figure 2.21). At the base of the peritoneal broad ligament, the uterine artery runs transversely toward the cervix while the ureters pass immediately inferior to them as they pass on each side of the cervix heading anteriorly toward the bladder. The main passive support for the uterus is provided by the transverse cervical ligament and the way in which the uterus normally "rests" on top of the bladder. The perineal muscles provide dynamic support for the uterus by contracting during moments of increased intra-abdominal pressure (sneezing, coughing, etc.). Passive and dynamic supports together resist the tendency for the uterus to fall or be pushed through the hollow tube formed by the vagina (uterine prolapse).

2.3.4 Neurovascular Structures of the Pelvis

The major neurovascular structures of the pelvis lie extraperitoneally against the posterolateral walls. The nerves lie most external or superficial (adjacent to the walls), with the vascular structures internal or deep (medial) to them. Generally, the veins are external (lateral) to the arteries.

2.3.4.1 Pelvic Nerves

The pelvis is innervated mainly by the sacral and coccygeal spinal nerves and the pelvic part of the autonomic nervous system. The piriformis and coccygeus muscles form a bed for the sacral and coccygeal nerve plexuses. The anterior rami of the S2 and S3 nerves emerge between the digitations of these muscles. At or immediately superior to the pelvic brim, the descending part of the L4 nerve unites with the anterior ramus of the L5 nerve to form the thick, cord-like lumbosacral trunk. The trunk passes inferiorly, on the anterior surface of the ala of the sacrum, and joins the sacral plexus (Figure 2.22).

2.3.4.2 Pelvic Arteries

The pelvis is richly supplied with arteries, among which multiple anastomoses occur, providing an extensive collateral circulation. Six main arteries enter the lesser pelvis of females, the internal iliac and ovarian arteries are paired, and the median sacral and superior rectal arteries are unpaired.

A collateral circulatory system is formed by multiple anastomosing arteries, providing an adequate blood supply to the greater and lesser pelves. Most arterial blood is delivered to the lesser pelvis by the internal iliac arteries, which commonly bifurcate into an anterior division (providing all the visceral branches) and a posterior division (usually exclusively parietal).

2.3.4.3 Pelvic Veins

The pelvic venous plexuses are formed by the interjoining veins surrounding the pelvic viscera (Figure 2.22). The various plexuses within the lesser pelvis (rectal, vesical, prostatic, uterine, and vaginal) unite and are drained mainly by the internal iliac veins, but some of them drain through the superior rectal vein into the inferior mesenteric vein or through lateral sacral veins into the internal vertebral venous plexus. Additional paths of venous drainage from the lesser pelvis include the parietal median sacral vein, the superior rectal vein and the ovarian veins.

The internal iliac veins merge with the external iliac veins to form the common iliac veins, which unite at the level of vertebra L4 or L5 to form the inferior vena cava (Figure 2.22).

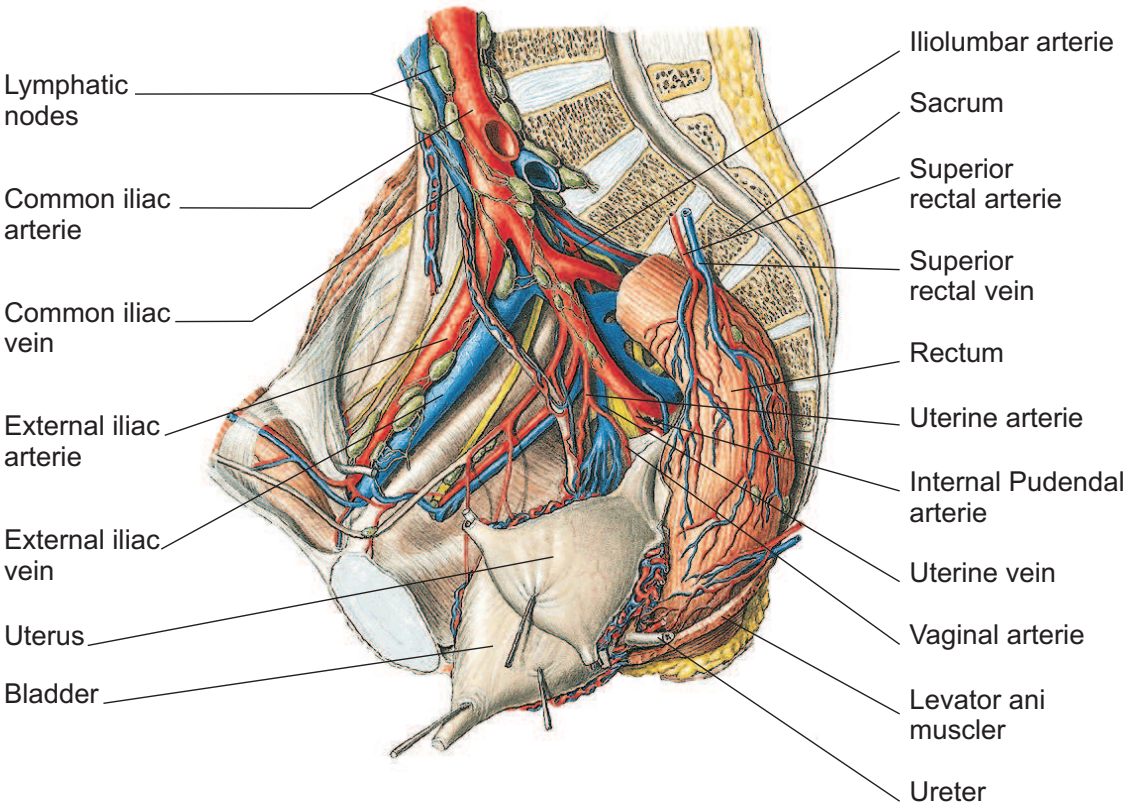

Figure 2.22: Neurovascular structures of the pelvis ([Sobotta et al., 2001]).

2.3.4.4 Lymph Nodes of the Pelvis

The lymph nodes receiving lymph drainage from pelvic organs are variable in number, size, and location and division into definite groups is often somewhat arbitrary. Four primary groups of nodes are located in or adjacent to the pelvis, named for the blood vessels with which they are associated:

External iliac lymph nodes These nodes lie above the pelvic brim, along the external iliac vessels. They receive lymph mainly from the inguinal lymph nodes and from the pelvic viscera, especially the superior parts of the middle to anterior pelvic organs.

Internal iliac lymph nodes These nodes are clustered around the anterior and posterior divisions of the internal iliac artery and the origins of the gluteal arteries. They receive drainage from the inferior pelvic viscera, deep perineum, and gluteal region and drain into the common iliac nodes.

Sacral lymph nodes These nodes lie in the concavity of the sacrum, adjacent to the median sacral vessels. They receive lymph from posteroinferior pelvic viscera and drain either to internal or common iliac nodes.

Common iliac lymph nodes These nodes lie superior to the pelvis and receive drainage from the three main groups listed above, beginning a common route for drainage from the pelvis that passes next to the lumbar nodes.

Additional minor groups of nodes occupy the connective tissue along the branches of the internal iliac vessels. In females, lymphatic drainage from the ovaries and uterine tubes follows the ovarian veins to the lumbar nodes.

2.3.5 Pelvic Viscera

The pelvic viscera include the urinary bladder and parts of the ureters, the reproductive system, and the rectum, the distal part of the alimentary tract. Although the sigmoid colon and parts of the small bowel extend into the pelvic cavity, they are abdominal rather than pelvic viscera. The sigmoid colon is continuous with the rectum anterior to S3 vertebra.

2.3.5.1 Urinary Organs

The pelvic urinary organs (Figure 2.23) are: Ureters, which carry urine from the kidneys, Urinary bladder, which temporarily stores urine and the Urethra, which conducts urine from the bladder to the exterior.

Ureters The ureters are muscular tubes, 25 to 30 cm long, that connect the kidneys to the urinary bladder (Figure 2.23). The ureters are retroperitoneal and their superior halves are in the abdomen and their inferior halves lie in the pelvis. As the ureters cross the bifurcation of the common iliac artery or the beginning of the external iliac artery they pass over the pelvic brim, thus leaving the abdomen and entering the lesser pelvis. In females, the ureter passes medial to the origin of the uterine artery and continues to the level of the ischial spine, where it is crossed superiorly by the uterine artery. It then passes close to the lateral part of the fornix of the vagina and enters the posterosuperior angle of the bladder.

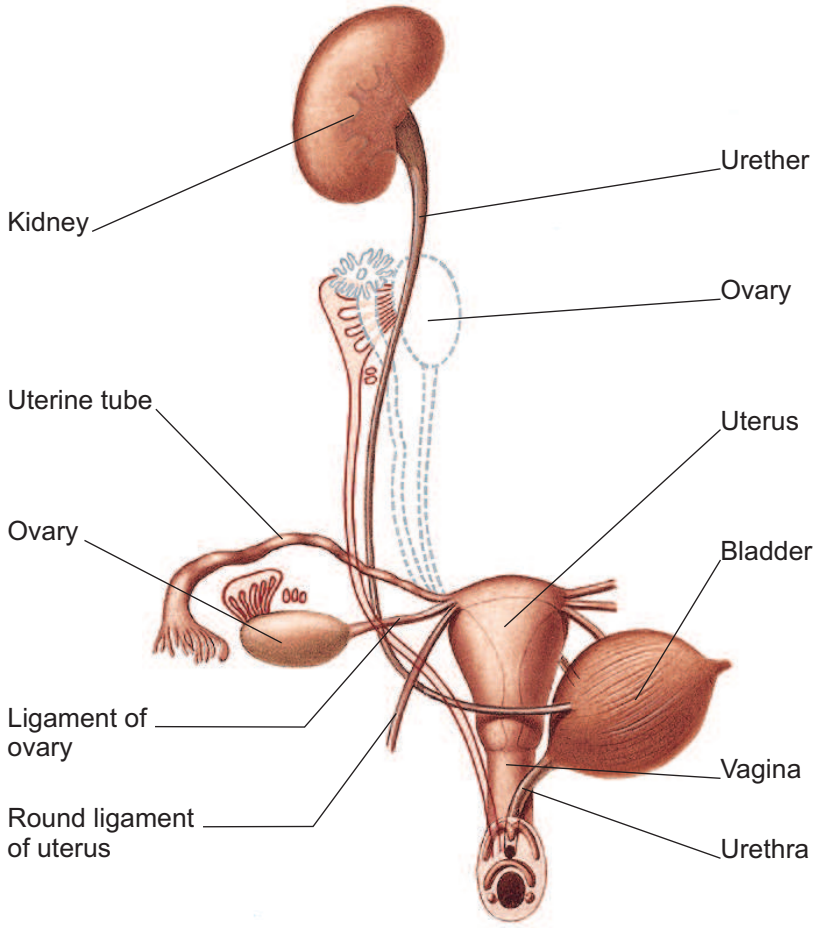

Figure 2.23: Urogenital viscera, the broken lines represent the position of the organs before descending, the bladder has been pulled to the left, ventral view (adapted from [Sobotta et al., 2001]).

Urinary Bladder The urinary bladder is a hollow viscus with strong muscular walls, characterized by its distensibility (Figure 2.24). The urinary bladder is a temporary reservoir for urine and varies in size, shape, position, and relationships according to its content and the state of the neighboring viscera. When empty, the adult urinary bladder is located in the lesser pelvis, lying partially superior to and partially posterior to the pubic bones. It is separated from these bones by the potential retropubic space and lies mostly inferior to the peritoneum, resting on the pubic bones and pubic symphysis anteriorly and the pelvic floor posteriorly. The bladder is relatively free within the extraperitoneal subcutaneous fatty tissue, except for its neck, which is held firmly by the lateral ligaments of bladder and the tendinous arch of the pelvic fascia, especially its anterior components, the pubovesical ligament (Figure 2.21b).

Urethra The female urethra (approximately 4 cm long and 6 mm in diameter) passes anteroinferiorly from the internal urethral orifice of the urinary bladder (Figure 2.23), posterior and then inferior to the pubic symphysis, to the external urethral orifice. The musculature surrounding the internal urethral orifice of the female bladder is not organized into an internal sphincter. In females, the external urethral orifice is located in the vestibule, directly anterior to the vaginal orifice. The urethra lies anterior to the vagina (forming an elevation in the anterior vaginal wall) (Figure 2.24). The axis of the urethra is parallel to that of the vagina. The urethra passes with the vagina through the pelvic diaphragm, external urethral sphincter, and perineal membrane.

2.3.5.2 Internal Genital Organs

The female internal genital organs include the vagina, uterus, uterine tubes, and ovaries.

Vagina The vagina is a musculomembranous tube (7 to 9 cm long), extending from the cervix of the uterus to the vestibule, the cleft between the labia minora. It contains the vaginal and external urethral orifices and the openings of the two greater vestibular glands (Figure 2.24). The superior end of the vagina surrounds the cervix.

The vagina has the following functions in the body:

- Serves as a canal for menstrual fluid.
- Forms the inferior part of the pelvic (birth) canal.
- Receives the penis and ejaculate during sexual intercourse.
- Communicates superiorly with the cervical canal and inferiorly with the vestibule.

The vagina is usually collapsed (H-shaped in cross section) so that its anterior and posterior walls are in contact, except at its superior end where the cervix holds them apart. The vagina lies posterior to the urethra, which projects into its inferior anterior wall, and urinary bladder, and it lies anterior to the rectum, passing between the medial margins of the levator ani muscles. The vaginal fornix, the recess around the cervix, has anterior, posterior, and lateral parts. The posterior vaginal fornix is the deepest part and is closely related to the rectouterine pouch. Four muscles compress the vagina and act as sphincters: pubovaginalis, external urethral sphincter, urethrovaginal sphincter, and bulbospongiosus. The relations of the vagina are the following:

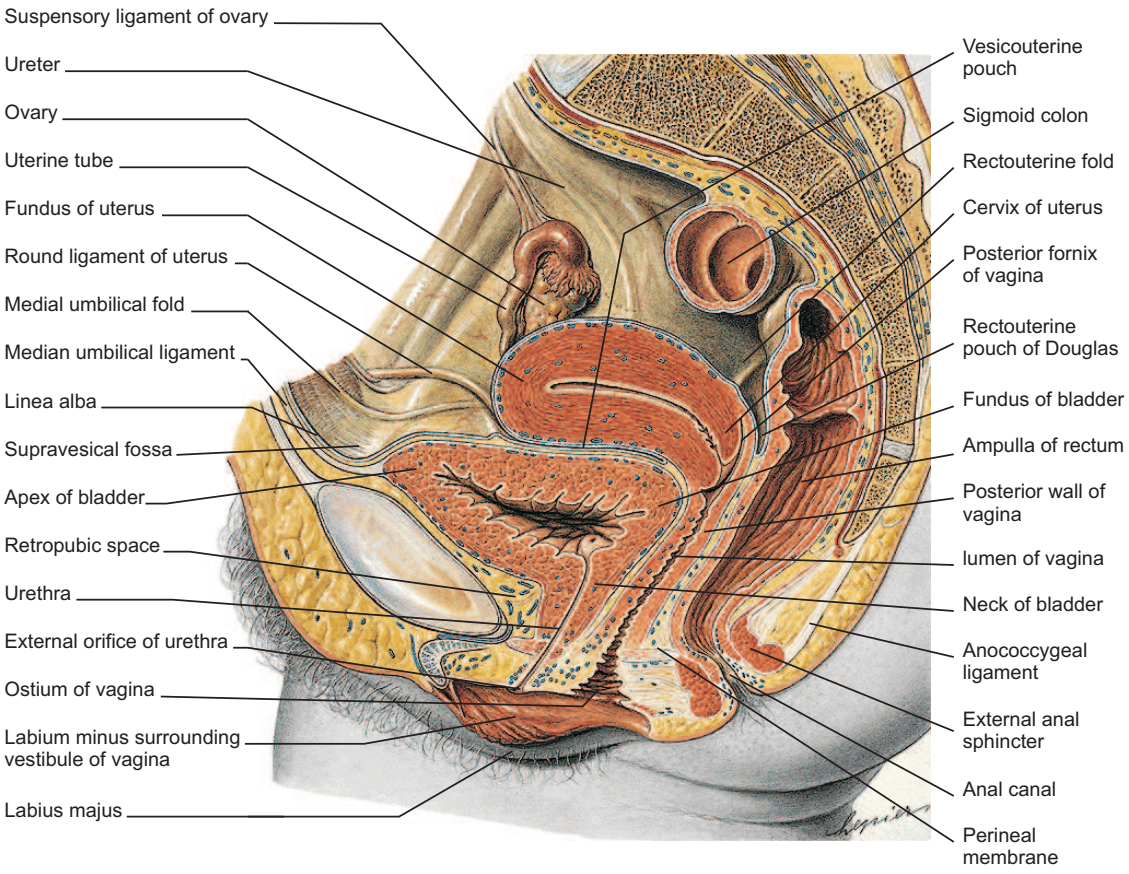

Figure 2.24: Female genital viscera (adapted from [Sobotta et al., 2001])

- Anteriorly: the fundus of the urinary bladder and urethra.
- Laterally: the levator ani, visceral pelvic fascia, and ureters.

- Posteriorly (inferior to superior): the anal canal, rectum, and rectouterine pouch.

Uterus The uterus is a pear-shaped, thick-walled, hollow muscular organ. Its muscular walls adapt to the growth of the fetus and then provide the power for its expulsion during childbirth. The non-gravid (non-pregnant) uterus usually lies in the lesser pelvis, with its body lying on the urinary bladder and its cervix between the urinary bladder and the rectum. The position of the uterus varies with the degree of fullness of the bladder and rectum. Although its size changes considerably, the uterus is approximately 7.5 cm long, 5 cm wide, and 2 cm thick and weighs approximately 90g. The uterus is divisible into two main parts: the body and cervix.

The body of the uterus forms the superior two thirds of the organ and includes the fundus of the uterus, the rounded part that lies superior to the orifices of the uterine tubes. The body lies between the layers of the broad ligament and is freely movable. It has two surfaces: vesical (related to the bladder) and intestinal. The body is demarcated from the cervix by the isthmus of the uterus, a relatively constricted segment, approximately 1 cm long.

The cervix of the uterus is the cylindrical, relatively narrow inferior third of the uterus, approximately 2.5 cm long in an adult non-pregnant woman. The rounded vaginal part surrounds the external os of the uterus and is surrounded in turn by a narrow space, the vaginal fornix. The supra-vaginal part is separated from the bladder anteriorly by loose connective tissue and from the rectum posteriorly by the rectouterine pouch.

The wall of the body of the uterus consists of three coats, or layers:

- Perimetrium. The perimetrium is the serosa or outer serous coat, consisting of peritoneum supported by a thin layer of connective tissue.
- Myometrium. The myometrium is the middle coat of smooth muscle. This layer becomes greatly distended during pregnancy. The main branches of the blood vessels and nerves of the uterus are located in this coat. During childbirth, contraction of the myometrium is hormonally stimulated at intervals of decreasing length to dilate the cervical os and expel the fetus and placenta.
- Endometrium. The endometrium is the inner mucous coat and is firmly adhered to the underlying myometrium. The endometrium is actively involved in the menstrual cycle, differing in structure with each stage of the cycle.

The cervix is mostly fibrous and is composed mainly of collagen with a small amount of smooth muscle and elastin. The amount of muscular tissue in the cervix is markedly less than in the body of the uterus.

Uterine Tubes The uterine tubes conduct the oocyte (ovum), discharged monthly from an ovary during child-bearing years, from the periovarian peritoneal cavity to the uterine cavity. They also provide the usual site of fertilization. They extend laterally from the uterine horns and open into the peritoneal cavity near the ovaries. The uterine tubes (approximately 10 cm long) lie in the mesosalpinx in the free edges of the broad ligaments.

Ovaries The ovaries are almond-shaped and -sized female gonads in which the ova develop. They are also endocrine glands that produce reproductive hormones. The ovaries are typically located near the attachment of the broad ligament to the lateral pelvic walls, suspended from both by peritoneal folds: from the posterosuperior aspect of the broad ligament by the mesovarium and from the lateral pelvic walls by the suspensory ligaments of the ovaries (Figure 2.24).

2.3.5.3 Rectum

The main function of the rectum is to accumulate and temporarily stores feces. It begins at the rectosigmoid junction as the teniae of the sigmoid colon spread and unite into a continuous longitudinal layer of smooth muscle and the omental appendices cease. It ends with the anorectal flexure as the gut penetrates the pelvic diaphragm, becoming the anal canal. The rectum is concave anteriorly as the sacral flexure and has three lateral flexures formed in relation to the internal transverse rectal folds. The rectum enlarges into the rectal ampulla directly above the pelvic floor. Its superior, middle, and inferior parts are, respectively, intraperitoneal, retroperitoneal, and subperitoneal.

2.3.6 Perineum

The perineum includes the external genitalia, perineal muscles, and anal canal. The perineum refers to both an external surface area and a shallow compartment of the body. The perineum is bounded by the pelvic outlet and is separated from the pelvic cavity by the pelvic diaphragm, which is formed by the levator ani and coccygeus muscles. In the anatomical position, the surface of the perineum is the narrow region between the proximal parts of the thighs. When the lower limbs are abducted, it is a diamond-shaped area extending from the mons pubis anteriorly, the medial surfaces of the thighs laterally, and the gluteal folds and superior end of the intergluteal cleft posteriorly (Figure 2.25).

The osseofibrous structures marking the boundaries of the perineum (perineal compartment) are the following:

- Pubic symphysis, anteriorly.

- Inferior pubic rami and ischial rami, anterolaterally.
- Ischial tuberosities, laterally.
- Sacrotuberous ligaments, posterolaterally.
- Inferiormost sacrum and coccyx, posteriorly.

An imaginary transverse line joining the anterior ends of the ischial tuberosities divides the diamond-shaped perineum into two triangles, the oblique planes of which intersect at the transverse line (Figure 2.25). The anal triangle lies posterior to this line. The anal canal and its orifice, the anus, constitute the major deep and superficial features of the triangle, lying centrally surrounded by ischioanal fat. The urogenital triangle is anterior to this line. In contrast to the open anal triangle, the urogenital triangle is closed by a thin sheet of tough, deep fascia, the perineal membrane, which stretches between the two sides of the pubic arch, covering the anterior part of the pelvic outlet (Figure 2.26). The perineal membrane fills the anterior gap in the pelvic diaphragm but is perforated by the urethra and by the vagina. The membrane and the ischiopubic rami to which it attaches provide a foundation for the vulva, which is the superficial feature of the triangle (Figure 2.27).

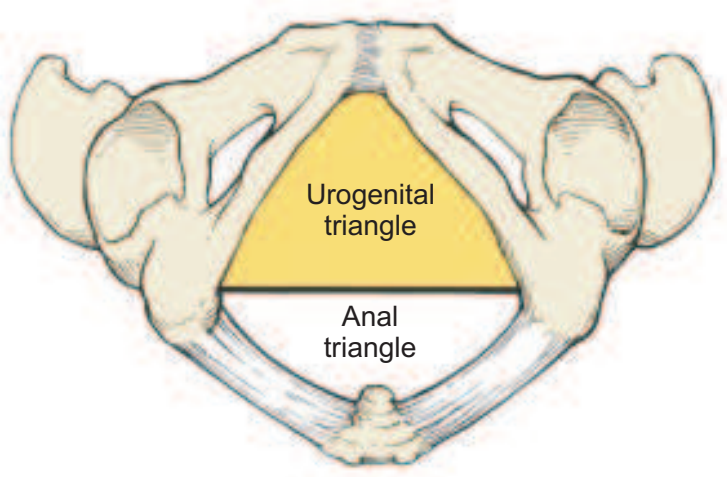

Figure 2.25: Boundaries of the perineum (adapted from [Gabbe et al., 2007]).

The midpoint of the line joining the ischial tuberosities gives the central point of the perineum (Figure 2.26). This is the location of the perineal body, which is an irregular mass, variable in size and consistency and containing collagenous and elastic fibers and both skeletal and smooth muscle (Figure 2.27). The perineal body

lies deep to the skin, with relatively little overlying subcutaneous tissue, posterior to the vestibule and anterior to the anus and anal canal. The perineal body is the site of convergence and interlacing of fibers of several muscles, including the:

- Bulbospongiosus.
- External anal sphincter.
- Superficial and deep transverse perineal muscles.
- Smooth and voluntary slips of muscle from the external urethral sphincter, levator ani, and muscular coats of the rectum.

Superiorly, the perineal body blends with the rectovesical or rectovaginal septum and anteriorly, with the posterior border of the perineal membrane (Figure 2.27).

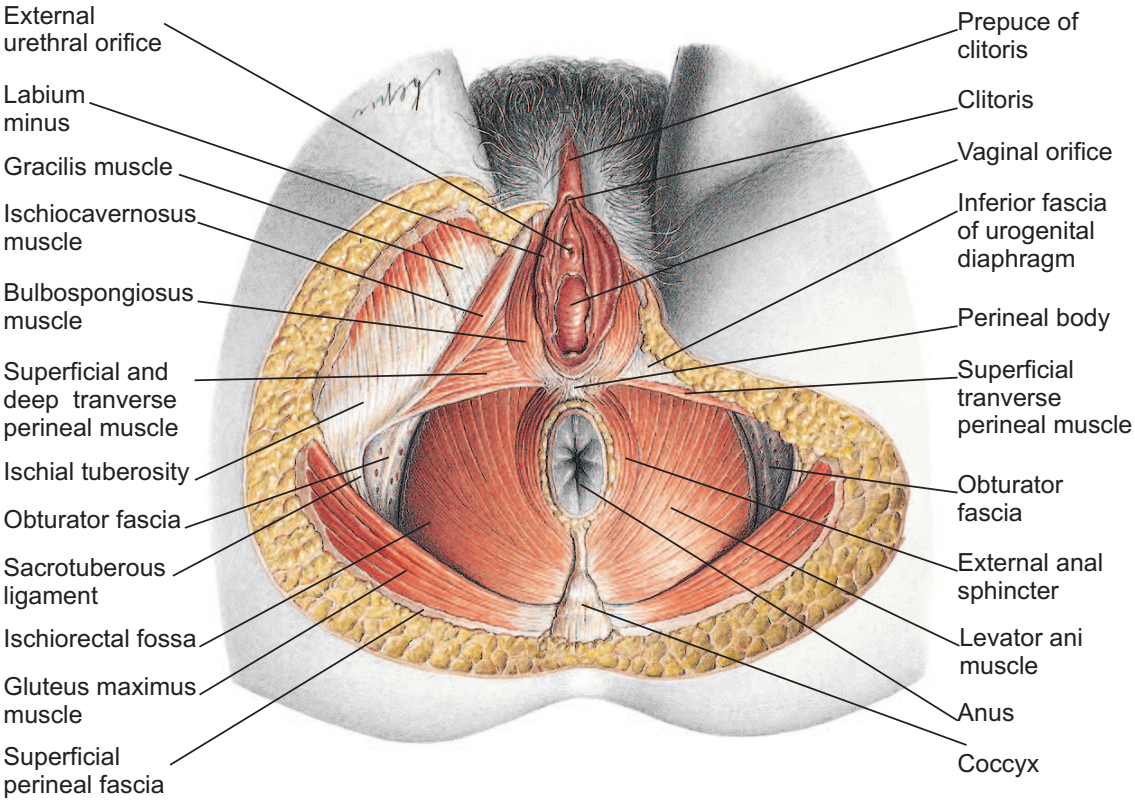

Figure 2.26: The perineum, pelvic diaphragm, and external female genital organs, viewed from below (adapted from [Sobotta et al., 2001]).

2.3.6.1 Fasciae and Pouches of the Urogenital Triangle

Perineal Fasciae The perineal fascia consists of superficial and deep layers. The subcutaneous tissue of the perineum, or superficial perineal fascia, consists of a superficial fatty layer and a deep membranous layer. The fatty layer makes up the substance of the labia majora and mons pubis and is continuous anteriorly and superiorly with the fatty layer of subcutaneous tissue of the abdomen. The fatty layer of subcutaneous tissue of the perineum is continuous posteriorly with the ischioanal fat pad in the anal region.

The membranous layer of subcutaneous tissue of the perineum does not extend into the anal triangle, being attached posteriorly to the posterior margin of the perineal membrane and the perineal body. Laterally it is attached to the fascia lata of the superiormost medial aspect of the thigh. The membranous layer passes superior to the fatty layer forming the labia majora and becomes continuous with the membranous layer of subcutaneous tissue of the abdomen.

The perineal fascia intimately invests the ischiocavernosus, bulbospongiosus, and superficial transverse perineal muscles (Figure 2.27). It is also attached laterally to the ischiopubic rami. The perineal fascia is fused with the suspensory ligament of the clitoris and with the deep fascia of the abdomen.

Superficial Perineal Pouch The superficial perineal pouch is a potential space between the membranous layer of subcutaneous tissue and the perineal membrane. It is bounded laterally by the ischiopubic rami (Figure 2.26).

The superficial perineal pouch contains the:

- Clitoris and associated muscles (ischiocavernosus).
- Bulbs of the vestibule and surrounding muscle (bulbospongiosus).
- Greater vestibular glands.
- Superficial transverse perineal muscles.
- Related vessels and nerves (deep perineal branches of the internal pudendal vessels and pudendal nerves).

Deep Perineal Pouch The deep perineal pouch is bounded inferiorly by the perineal membrane, superiorly by the inferior fascia of the pelvic diaphragm, and laterally by the inferior portion of the obturator fascia (Figure 2.21a). It includes the fat-filled anterior recesses of the ischioanal fossa. The superior boundary in the region of the urogenital hiatus is indistinct.

The deep perineal pouch contains the following:

- Part of the urethra, centrally.

- The inferior part of the external urethral sphincter muscle, above the center of the perineal membrane, surrounding the urethra.
- Anterior extensions of the ischioanal fat pads.
- Proximal part of the urethra.
- A mass of smooth muscle in the place of deep transverse perineal muscles on the posterior edge of the perineal membrane, associated with the perineal body.
- Dorsal neurovasculature of the clitoris.

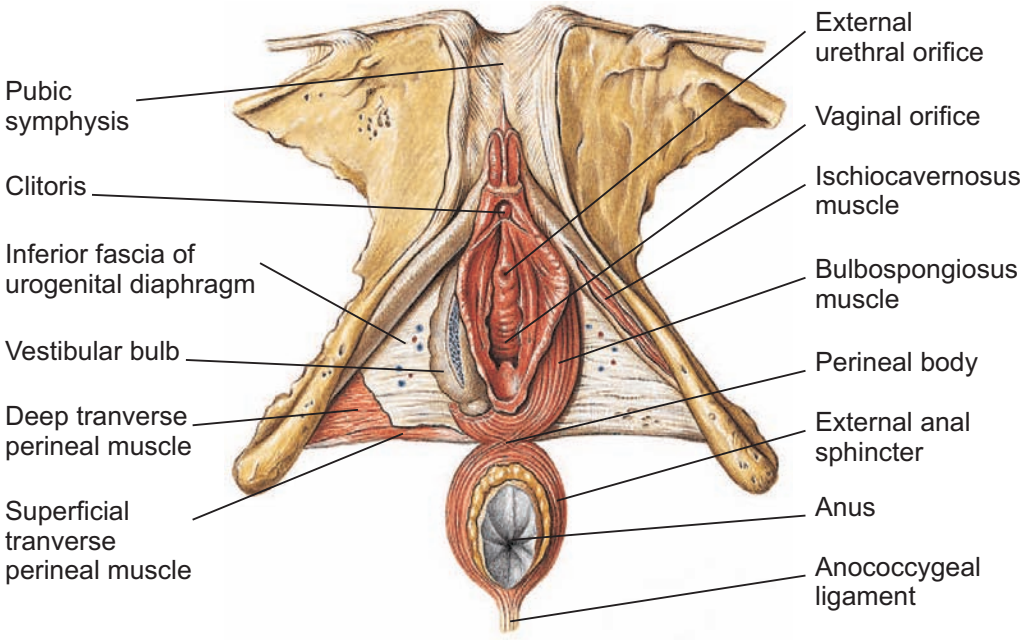

Figure 2.27: The external genital organs of the female and parts of the urogenital diaphragm, ventral view from below (adapted from the reference [Sobotta et al., 2001]).

2.3.6.2 Features of the Anal Triangle

Ischioanal Fossae The ischioanal fossae on each side of the anal canal are large fascia-lined, wedge-shaped spaces between the skin of the anal region and the pelvic diaphragm. The apex of each fossa lies superiorly where the levator ani muscle arises from the obturator fascia. The ischioanal fossae, wide inferiorly and narrow

superiorly, are filled with fat and loose connective tissue. The two ischioanal fossae communicate by means of the deep postanal space over the anococcygeal ligament (body), a fibrous mass located between the anal canal and the tip of the coccyx (Figure 2.26).

Each ischioanal fossa is bounded by the following:

- Laterally by the ischium and overlapping inferior part of the obturator internus, covered with obturator fascia.
- Medially by the external anal sphincter, with a sloping superior medial wall or roof formed by the levator ani as it descends to blend with the sphincter.
- Posteriorly by the sacrotuberous ligament and gluteus maximus.
- Anteriorly by the bodies of the pubic bones, inferior to the origin of the puborectalis.

Each ischioanal fossa is filled with a fat body of the ischioanal fossa. These fat bodies support the anal canal but they are readily displaced to permit descent and expansion of the anal canal during the passage of feces. The fat bodies are traversed by tough, fibrous bands, as well as by several neurovascular structures, including the inferior anal/rectal vessels and nerves and two other cutaneous nerves, the perforating branch of S2 and S3 and the perineal branch of S4 nerve.

Pudendal Canal The pudendal canal is an essentially horizontal passageway within the obturator fascia that covers the medial aspect of the obturator internus and lines the lateral wall of the ischioanal fossa.

Anal Canal The anal canal is the terminal part of both the large intestine and the alimentary tract, the anus being the external outlet. Fecal continence is maintained by the coordinated action of the involuntary internal and voluntary external anal sphincters. The sympathetically stimulated tonus of the internal sphincter maintains closure, except during filling of the rectal ampulla and when inhibited during a parasympathetically stimulated peristaltic contraction of the rectum. During these moments, closure is maintained by voluntary contraction of the puborectalis and external anal sphincter.

2.3.6.3 External Genitalia

The external genitalia (Figure 2.28) include the mons pubis and labia majora, labia minora, clitoris, bulbs of the vestibule, and greater and lesser vestibular glands. The synonymous terms vulva and pudendum include all these parts. The vulva has the following functions:

- Serves as sensory and erectile tissue for sexual arousal and intercourse.
- Directs the flow of urine.
- Prevents entry of foreign material into the urogenital tract.

Mons Pubis The mons pubis is the rounded, fatty eminence anterior to the pubic symphysis, pubic tubercles, and superior pubic rami (Figure 2.28). The eminence is formed by a mass of fatty subcutaneous tissue. The amount of fat increases at puberty and decreases after menopause. The surface of the mons is continuous with the anterior abdominal wall. After puberty, the mons pubis is covered with coarse pubic hairs.

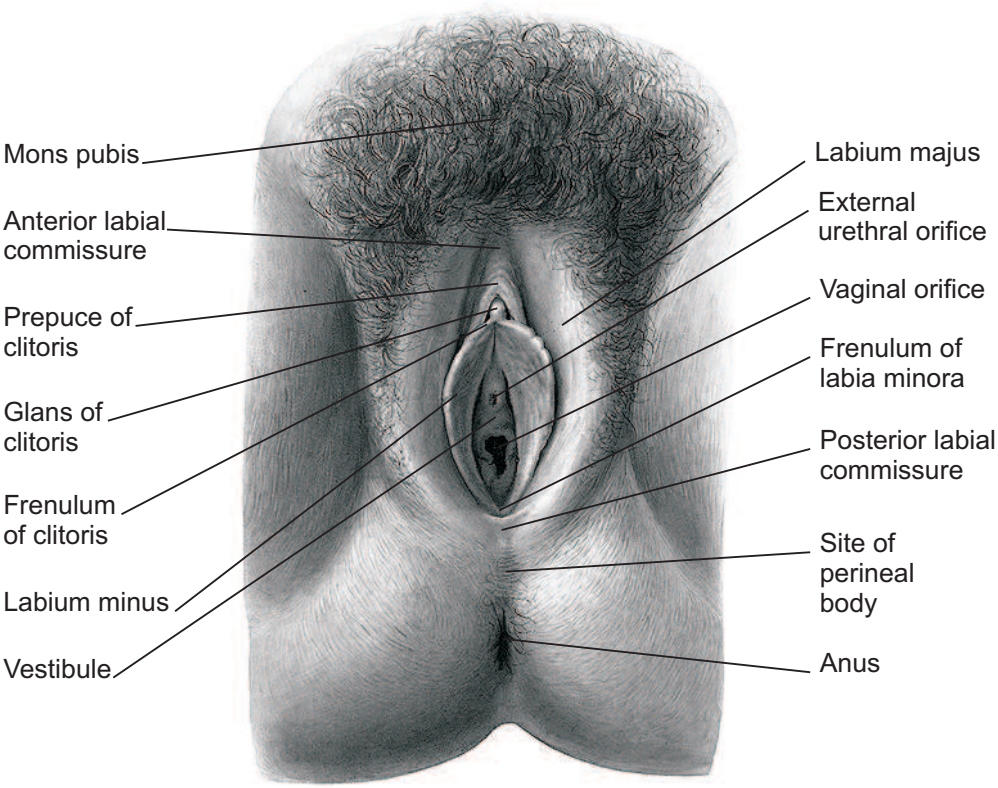

Figure 2.28: Female external genitalia. The labia majora and minora are separated to show the vestibule, into which the external urethral orifice and the vaginal orifice open (adapted from [Sobotta et al., 2001]).

Labia Majora The labia majora are prominent folds of skin that indirectly provide protection for the urethral and vaginal orifices. The labia majora lie on the sides of a central depression, the pudendal cleft, within which are the labia minora and vestibule (Figure 2.28).

Labia Minora The labia minora are rounded folds of fat-free, hairless skin. They are enclosed in the pudendal cleft and immediately surround the vestibule into which both the external urethral and the vaginal orifices open. They have a core of spongy connective tissue containing erectile tissue at their base and many small blood vessels. Anteriorly, the labia minora form two laminae. The medial laminae of each side unite as the frenulum of the clitoris. The lateral laminae unite anterior to the glans of the clitoris, forming the prepuce of the clitoris.

Clitoris The clitoris is an erectile organ located where the labia minora meet anteriorly. The clitoris consists of a root and a body. Together, the body and glans of the clitoris are approximately 2 cm in length and < 1 cm in diameter. In contrast to the penis, the clitoris is not functionally related to the urethra or to urination. It functions solely as an organ of sexual arousal. The clitoris is highly sensitive and enlarges on tactile stimulation. The glans of the clitoris is the most highly innervated part of the clitoris and is densely supplied with sensory endings.

Vestibule The vestibule is the space surrounded by the labia minora into which the orifices of the urethra and vagina and the ducts of the greater and lesser vestibular glands open (Figures 2.26 and 2.28). The external urethral orifice is located 2 to 3 cm posteroinferior to the glans of the clitoris and anterior to the vaginal orifice (Figures 2.26 and 2.28).

Bulbs of the Vestibule The bulbs of the vestibule are paired masses of elongated erectile tissue, approximately 3 cm in length (Figure 2.27). The bulbs lie along the sides of the vaginal orifice, superior or deep to the labia minora, immediately inferior to the perineal membrane. They are covered inferiorly and laterally by the bulbospongiosus muscles extending along their length.

Vestibular Glands Located on each side of the vestibule, posterolateral to the vaginal orifice and inferior to the perineal membrane, the greater vestibular glands, approximately 0.5 cm in diameter, are found. The greater vestibular glands are round or oval and are partly overlapped posteriorly by the bulbs of the vestibule, and like the bulbs, are partially surrounded by the bulbospongiosus muscles. These glands secrete mucus into the vestibule during sexual arousal.

Chapter 3

Pelvic Floor Dysfunctions

3.1 Introduction

Female pelvic floor dysfunctions form an extensive, if well hidden problem. Urinary incontinence is perhaps the best known of these dysfunctions but prolapses, faecal incontinence and pelvic pain affect a significant number of women [Papa Petros, 2004].

With the life expectancy continuously increasing on developed countries, the expectations for a high quality of life, has led to a greater public awareness and helpseeking behavior regarding symptomatic dysfunction of the organs found within the pelvic cavity in women. Women are increasingly less willing to simply accept incontinence or prolapse as a normal part of the aging process. New technologies and a greater understanding of the pathophysiology underlying these dysfunctions have provided clinicians with a number of effective tools for treatment of these patients. Unfortunately, the traditional fragmentation of health care duties among specialists has led to significant gaps in the treatment of pelvic floor dysfunctions. The concept of the female pelvic cavity and its contents, as a single functional unit has not yet gained wide acceptance [Davila et al., 2006].

It is estimated that one or more of these conditions affects up to one-third of adult women. On recent studies, based on a population under one health care system, 11% of women had surgery for urinary incontinence or pelvic organ prolapse during their lifetime [Olsen et al., 1997]. Although the magnitude of this public health problem is unknown to many, gynecologists know that 1 in every 10 women will have a pelvic floor dysfunction so severe that it will require surgery [Olsen et al., 1997].

It is estimated that at least one-third of adult women are affected by at least one of these conditions. Furthermore, statistics show that 30 to 40% of women suffer from some degree of incontinence in their lifetime, and that almost 10% of women will undergo surgery for urinary incontinence or pelvic organ prolapse.

In the United States, pelvic floor dysfunction affects each year between 300,000

to 400,000 women so severely that they require surgery [Lien et al., 2005]. The American population is experiencing a steady increase of older women, which is the fastest growing segment of the population, therefore, the national cost burden related to pelvic floor disorders is huge in terms of direct health care costs, lost productivity, and decreased quality of life [Weber et al., 2004].

A real understanding of the pathophysiology of pelvic floor disorders is still inexistent. Developing a clinical condition is the result of the combination of multiple factors. One can easily presuppose a genetic predisposition overlaid by critical life events (acquired risk factors, such as childbirth, hormonal changes, and aging) although strong evidence does not yet exist for these hypotheses [Weber et al., 2004].

Without a real understanding of the true causes of pelvic floor disorders, efforts at prevention are fruitless and therapy can only be empiric, rather than directed at specific injuries or deficits in function. Surgery for pelvic floor disorders often fails and unfortunately, 30% of women undergoing surgery for prolapse or urinary incontinence have had one or more previous procedures [Olsen et al., 1997; Weber et al., 2004].

Efforts at prevention and treatment improvement will only be possible if research clarifies causative mechanisms and scientifically valid studies discover why operations fail. Specific events or behaviors in a woman's life that lead to these problems and that are subjectable to preventive strategies must be discovered. In addition, the specific biologic and behavioral factors that explain why certain women have recurrence after surgery must be defined.

The pelvic organ support system is comprised of muscles, ligaments, and nerves arranged in a complex tension-based apparatus, therefore, the basic nature of this work must include biomechanical analysis of the overall mechanism and targeted research into the biology of muscle, ligament, nerve, and their complex interactions in normal pelvic floor function and in symptomatic patient. A joint effort of scientists in this different areas, that are becoming well developed, will result in a move forward that will bring predictably important results.

3.2 Concept of the Pelvic Cavity and its contents as a Unit

Disorders of urinary and fecal continence, as well as genital and rectal support, are common in adult women. Clinicians who address these problems include urologists, gynecologists, and colorectal surgeons. There has been little overlap in the verticalized spectrum of care provided by urologists (kidneys, ureters, bladder, urethra), gynecologists (uterus, vagina, perineum), and colorectal surgeons (colon, rectum, anus). Coexistence of dysfunction of urinary and bowel control is high and is al-

ready well established [Swash et al., 1985].

Clinicians who address pelvic floor dysfunction syndromes have been slow to adapt their practice styles to address all pelvic floor dysfunctions in one setting [Davila et al., 2006]. The concept used by clinician of an horizontal integration of pelvic floor dysfunction evaluation and management is already well established [Davila and Ghoniem, 2003]. This concept is expanding as clinicians realize the importance of a team approach to evaluation and treatment of pelvic floor dysfunction.

The dysfunction of the pelvic floor muscles can result from stretch or tear injuries to the pelvic floor muscles. However, the most common etiology for muscular dysfunction is a denervation injury from childbirth or lower back trauma. A denervation injury will result in partial paralysis of the supplied muscle groups. As a consequence, any lower back injury can result in weakness of pelvic floor support. This is especially true for the lower components of the pelvic floor. Injury to the pudendal nerve can result in dysfunction of the urethral sphincter, anal sphincter, and motor or sensory dysfunction of the perineum. Significant injury to the pudendal innervation will typically result in multisystem dysfunction, such as urinary and fecal incontinence.

The organ systems of the pelvic cavity are enveloped in moderately thick layers of connective neuromuscular tissue, the endopelvic fascia (see Figure 2.21). This neuromuscular tissue provides circumferential support to the three cavities that cross the pelvic floor muscles. The lack of integrity of the fibromuscular layer between two organ systems will result in the herniation of one organ system into another. The resultant cystocele, enterocele, or rectocele (Figure 3.1) may then result in dysfunction of the underlying visceral organ including disorders of urinary continence and storage, or dysfunction of fecal continence or storage. Frequently, multiple sites of fibromuscular layer damage are found. This is represented by the frequent coexistence of prolapse of the anterior and posterior vaginal walls requiring repair of both [Davila et al., 2006].

3.3 Epidemiology and Prevalence of the different Pelvic Floor Dysfunctions

The term pelvic floor dysfunction refers to a group of clinical conditions that includes problems like urinary incontinence, fecal incontinence, pelvic organ prolapse and any other sensory and emptying abnormalities of the lower urinary and gastrointestinal tracts. The three most common and definable conditions encountered clinically are urinary incontinence, anal incontinence and pelvic organ prolapse.

3.3.1 Obstetric Factors

Many pelvic floor dysfunction symptoms have a common denominator, a vaginal birth process. The understanding of the neuromuscular damage, which occurs during a vaginal birth process, has been enhanced with the use of procedures like neurophysiologic testing and endoanal ultrasound. Endoanal ultrasound is an essential investigation tool in the management of faecal incontinence, consisting of a probe, typically, with a diameter of 1.7 cm, that can be moved freely within the anal canal, causing minimal discomfort or image distortion [Wright, 2005].

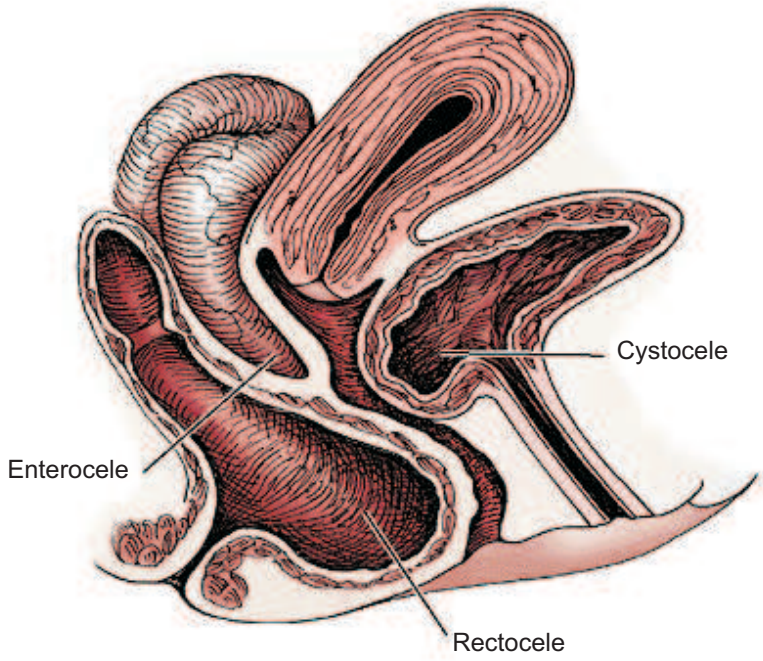

Figure 3.1: Pelvic floor dysfunctions (adapted from [Moore and Dalley, 2006]).

A vaginal birth results not only in significant stretching of the levator musculatures in a vertical direction, but, more importantly, in stretching of the pudendal nerves in the vertical direction. Any stretch of a somatic nerve of more than 12% has been reported to lead to a degree of permanent injury to that nerve [Davila et al., 2006]. During the vaginal birth process, perineal descent stretches the pudendal nerve to such a degree that permanent injury can result. Beyond direct injury to muscles and nerves of the pelvic floor, the vaginal birth process also results in significant symptomatic as well as occult injury to the anal sphincteric mechanism. Many anal sphincter tears are symptomatic. However, it is unknown whether

occult anal tears will result in subsequent fecal incontinence a few years postpartum [Sultan et al., 1993]. It is thus not surprising that there is a high incidence of postpartum gas and fecal incontinence.

The increased understanding of the neuromuscular consequences of the vaginal delivery process has been the subject of much debate, especially as relating to the acceptance of elective, on-demand cesarean delivery [Davila et al., 2006]. As the clinicians increase their understanding of the neuromuscular consequences of a vaginal delivery process, much debate among obstetricians and gynecologists as taken place in relation to the acceptance of elective, on-demand cesarean delivery. Many cultures around the world have already debated and accepted this concept for various reasons, including resultant pelvic floor dysfunction. The urogynecologic position on this subject has been one of providing patients information regarding potential consequences of pelvic floor dysfunction and allowing patients to make a decision whether they wish to undergo an elective cesarean delivery [Davila, 2001].

According to a survey conducted to pregnant women, it seems that providing women with information regarding potential pelvic floor consequences of a vaginal delivery does not alter their decision-making process significantly. Nevertheless, providing patients information regarding the risks and benefits of the vaginal delivery process, as in informed-consent processes for other invasive procedures, will likely become a part of antepartum obstetric care [Pollak et al., 2003].

3.3.2 Coexistence of Pelvic Floor Dysfunction Symptoms

Different studies have been conducted in order to obtain a better understanding of the coexistence of symptoms of urinary, genital, and fecal dysfunction. The common conclusion is that there is a high incidence of coexistence of incontinence and support defects. It has been reported that in patients with fecal incontinence, 24% to 53% also complained of urinary incontinence, and 7% to 22% complained of genital prolapse. From the patients who presented with rectal prolapse, 66% also complained of urinary incontinence and 34% complained of genital prolapse [Gonzalez-Argente et al., 2001; Khullar et al., 1998; Meschia et al., 2002].

The coexistence of symptoms of urinary and colorectal dysfunction, verified frequently, provides further emphasis on the need for a team approach to the evaluation and management of women with any of these conditions. Additionally, the fact that rectal prolapse patients have a higher incidence of urinary incontinence and genital prolapse suggests that rectal prolapse may represent a more advanced degree of pelvic floor dysfunction [Davila et al., 2006].

3.3.3 Urinary Dysfunction

Bladder dysfunction is a problem that affects millions of people, particularly women and the elderly. Although most studies have mainly focused on incontinence, more recently, attention has also included overactive bladder. Therefore, this Section will be focused on urinary incontinence and overactive bladder, because both of them constitute the most common causes of urinary dysfunction.

Urinary incontinence was defined in 1988 by the International Continence Society defined as the involuntary loss of urine that is objectively demonstrable and is a social or hygienic problem. Recently, the urinary incontinence has been redefined as the complaint of any involuntary leakage of urine [Abrams et al., 2002]. This new definition results in more cases of urinary incontinence being discovered and hopefully treated.

3.3.3.1 Urinary Incontinence

Urinary incontinence symptoms are mainly stress urinary incontinence, which is leakage with physical exertion, urge urinary incontinence, which is leakage with a strong desire to void, and mixed, which is a combination of both. When stress urinary incontinence is urodynamically proven, it is also called genuine stress incontinence. Urinary urgency and frequency with urge incontinence has recently been defined as overactive bladder with incontinence. There are other types of incontinence, although less frequent, including overflow incontinence, functional, and extra-urethral incontinence.

Different epidemiologic studies conducted in various populations revealed that a number of variables are related to the development of urinary incontinence including several possible risk factors:

Age It is a common result between the different studies that the prevalence of urinary incontinence tends to increase with advancing age as shown in the following references [Chiarelli et al., 1999; Nygaard and Lemke, 1996]. Institutionalized adults also show higher prevalence, because residents in institutions tend to be older and more impaired. According to a survey conducted to young and middle-aged women, it is suggested that pure stress incontinence predominates in that age group [Davila et al., 2006]. Other studies by [Diokno et al., 1986], [Peet and Castleden, 1995] and [Cheater and Castleden, 2000] suggested that urge and mixed incontinence predominate in older women.

Race There are several studies showing that ethnicity may be associated with urinary incontinence. There are several studies of non-Caucasians showing a wide variation in prevalence. In these studies different methods and definitions have

been used, therefore, a comparison between the results is difficult to obtain [Lara and Nacey, 1994; Brieger et al., 1997; Nakanishi et al., 1997].

Another study, conducted on more than 4000 women 70 years of age and older showed that the prevalence of involuntary urine loss was significantly higher in white women (23%) than in black women (16%) [Fultz et al., 1999]. There are reports stating that black South Africans rarely develop stress incontinence, and they develop the related disorder of genital prolapse at a rate 80 times lower than whites. The rarity of stress incontinence among blacks was explained by the authors as a function of differing urethral pressures and length as well as pubococcygeal muscle strength [Davila et al., 2006].

Sex The prevalence rates of urinary incontinence are higher in women than in men. The prevalence range for urinary incontinence is 4.5% to 53% in women and 1.6% to 24% in men, according to [Davila and Neimark, 2002].

The effects of pregnancy and childbirth are often assumed to be the main cause of urinary incontinence in women. The literature shows that urinary incontinence is a more common occurrence among pregnant women compared with other groups of women [Burgio et al., 1996; D'Alfonso et al., 2006].

During pregnancy, urinary incontinence is a self-limited condition. In a study by Viktrup [Viktrup et al., 1992] a prevalence rate of stress urinary incontinence during pregnancy of 28% was found, with 16% becoming free of symptoms in the puerperium. It is still questionable whether pregnancy itself is a risk factor for urinary incontinence in later life or if it is the vaginal delivery that is the main risk factor. The authors also compared continent women having delivered vaginally with women who underwent a cesarean delivery and found a difference in favor of cesarean delivery. However, 3 months after delivery, the difference became statistically insignificant.

Several explanations have been offered to explain the link existing between urinary incontinence and parity. Childbirth may result in pelvic floor laxity as a consequence of weakening and stretching of the muscles and connective tissue during delivery. Damage may occur as a result of spontaneous lacerations and episiotomies during delivery. Both may result in impairment of the position and support of the pelvic organs. The stretching of the pelvic tissues during vaginal delivery may damage the pudendal and pelvic nerves, as well as the muscles and connective tissue of the pelvic floor [Foldspang et al., 1992].

Menopause Studies have shown that postmenopausal women are more likely to have urinary incontinence than premenopausal women. The evidence that atrophy of the urogenital mucosa can be reversed with estrogen suggests that

estrogen loss contributes to the problem. However, the literature is inconsistent in describing the role of menopause and estrogen loss as significant contributors.

In a study comparing postmenopausal women with premenopausal women found that the differences between the prevalence of urinary incontinence between the two groups were not significant [Rekers et al., 1992].

In another study it was found that women who experienced surgical menopause had a higher rate of urinary incontinence (36%) compared with those who experienced natural menopause (22%) [Milsom et al., 1993].

Hysterectomy Some studies have shown significant association between urinary incontinence and hysterectomy, as well as oophorectomy, nevertheless, the role of hysterectomy is controversial. This association is due to the fact that hysterectomy may disturb the musculofascial attachments of the bladder to the surrounding pelvic wall, and oophorectomy results in surgical menopause [Brown et al., 2000].

Obesity Studies have shown that obesity and increased body mass index is frequently associated with urinary incontinence. Obesity may cause stretching and weakening of the muscles, nerves, and other structures of the pelvic floor. There is clear epidemiologic support for the role of obesity in urinary incontinence [Mommsen and Foldspang, 1994].

Many other risk factors may contribute to the development of urinary incontinence. Patients with dementia, Parkinson's disease, multiple sclerosis, and stroke are at a higher risk of manifesting bladder dysfunction during the course of their disease. Patients lacking mental orientation have a greater risk of being incontinent than those with normal mental status. Studies conducted in nursing homes have suggested a link between dementia and urinary incontinence [Aggazzotti et al., 2000].

There are other factors correlated with the urinary dysfunction problem, including chronic obstructive lung diseases, smoking, diabetes, constipation, fecal incontinence, impaired function of levator muscles, genital prolapse, previous gynecologic surgery, perineal suturing, and history of childhood enuresis [Davila et al., 2006].

3.3.3.2 Overactive Bladder

Overactive bladder is defined by the International Continence Society as a medical condition referring to the urinary symptoms of frequency and urgency, with or without urge incontinence, when appearing in the absence of local pathologic factors [Abrams et al., 2002].

Patients with overactive bladder experience a wide range of symptoms, including frequency, both daytime and nighttime (nocturia), as well as urgency. A continuum of symptomatology is necessary to accurately describe overactive bladder. Approximately one-third of patients with overactive bladder have urge incontinence [Stewart et al., 2001].

A study conducted on the United States found that overactive bladder without incontinence was more prevalent in men, whereas overactive bladder with incontinence was more prevalent in women. Thirty-seven percent of people with overactive bladder have overactive bladder with incontinence; the remaining 63% have overactive bladder without incontinence. The same study assessed the prevalence of the individual bothersome symptoms that characterize overactive bladder. The prevalence of urge incontinence was 6%, frequency was 15%, urgency was 22%, and nocturia was 29% [Stewart et al., 2001].

The total economic costs of overactive bladder in the United States in the year 2000 were 18.2 million dollars [Stewart et al., 2001]. This estimate includes direct and indirect costs at the community and institutional levels but does not consider intangible costs; therefore, although this current cost of overactive bladder is higher than the cost of disease states such as osteoporosis and Parkinson's disease, the economic burden of overactive bladder in the United States may be underestimated.

3.3.4 Bowel Dysfunction

Pelvic floor disorders involving bowel dysfunction include several different clinical problems such as constipation, prolapse of the rectum and fecal incontinence. These disorders are often complex, involving the functions of smooth and skeletal muscles, their nerves, and connective tissues. Etiologies of these disorders are either posttraumatic (such as from vaginal birth or prior anorectal surgery) or acquired, developing from chronic evacuation problems or with age. In some cases, the cause is idiopathic. Management strategies for the treatment of these disorders have evolved and continue to evolve as the clinicians better understand the nature of these problems.

3.3.4.1 Evacuation Disorders

Constipation is one of the most common complaints of patients seeing colorectal surgeons. The prevalence of chronic constipation in the United States varies from 2% to 34% [Talley et al., 1993]. Constipation is caused by several etiologies. Pelvic outlet obstruction is a common cause of constipation and is attributed to muscular dysfunction of the pelvic floor. Population studies have demonstrated the prevalence of pelvic outlet obstruction in the elderly (age 65 years and older) as 20% [Talley et al., 1996]. In a population study performed by Talley [Talley et al., 1993], the prevalence of pelvic outlet obstruction was 16.5% in females and 5.2% in males.

In another study that compared age-related prevalence in the same community of patients, aged less than 60 to more than 65 years, there was an increasing prevalence of pelvic outlet obstruction with increasing age [Talley et al., 1993; Talley et al., 1996].

From the multiple risk factors suspected to be associated with pelvic outlet obstruction, gender is one such risk factor. Constipation in young and middle-aged adults is approximately three times more prevalent in women, and the prevalence increases in both genders with age [Johnson et al., 1989]. Nonsteroidal antiinflammatory drug usage has also been shown to be associated with pelvic outlet obstruction in some studies but not in others[Talley et al., 1993; Talley et al., 1996].

Among patients with pelvic outlet obstruction, there are several neuromuscular-associated or etiologic syndromes, including:

- Nonrelaxing puborectalis syndrome
- Rectocele
- Descending perineum syndrome

Nonrelaxing puborectalis syndrome occurs when there is failure of relaxation or paradoxical contraction of the puborectalis muscle at the time of the defecatory effort. The nonrelaxation of the puborectalis muscle is the cause in 31% to 42% of patients with pelvic outlet obstruction constipation [Glia et al., 1998]. As a result of the chronic straining associated with this syndrome, many other associated disorders may develop including rectal prolapse and rectocele.

The descending perineum syndrome occurs as a result of either injury of the sacral or pudendal nerves or damage to the pelvic floor muscles. Most often, this injury occurs secondary to childbirth or chronic straining at stool. The descending perineum syndrome is frequently associated with constipation and, later, development of fecal incontinence. Its incidence increases with age and it is more common in women than men [Bannister et al., 1997].

A rectocele is defined as a herniation or protrusion of the anterior rectal wall into the vagina and is associated with pelvic laxity. In patients presenting to specialists with complaints of chronic constipation, rectoceles are found in 1% of them [Surrenti et al., 1995]. Rectoceles are very common and not often symptomatic, and so they stay vastly underreported. Many rectoceles will remain asymptomatic until the fourth or fifth decade of life [Davila et al., 2006]. The majority of patients with rectoceles are multiparous and/or have chronic constipation with a history of straining. The damage to the rectovaginal septum, pelvic floor muscles, and the pudendal nerves, during vaginal delivery or chronic straining can be related to rectocele development. The association of rectoceles with hysterectomies has also been verified [Felt-Bersma and Cuesta, 2001].

3.3.4.2 Prolapse Syndromes

Rectal prolapse occurs when the full thickness of the rectal wall protrudes through the anus. Rectal prolapse is the most common type of distal digestive tract prolapse. In mucosal prolapse, only the mucosa of the rectal wall protrudes through the anus. In contrast, internal intussusception, where a part of the small intestine has invaginated into another section of intestine, can occur in full or partial thickness but the prolapse does not pass beyond the anus. Intussusception is common in normal, healthy volunteers (up to 50%) and may be normal. It rarely leads to full prolapse [Felt-Bersma and Cuesta, 2001].

The true incidence of rectal prolapse (mucosal or complete) is unknown mostly because of underreporting. It is associated with long-standing constipation, chronic straining, pregnancy, prior surgery, female gender, aging, neurologic disease, mental illness (up to 53% in a study by Vongsangnak), and other pelvic floor disorders [Vongsangnak et al., 1985].

It is in the fourth and seventh decades of life that the peak incidence of prolapse is seen, and women are affected more often, outnumbering men in a relation of 10 to 1 [Davila et al., 2006]. In fact, the incidence increases with age in women, but not in men. Approximately two-thirds of women with rectal prolapse have neurogenic weakness of the pelvic floor, which is usually a consequence of childbirth [Neil et al., 1981]. However. In nulliparous women, the incidence of prolapse does not seem to be lower, although they are less likely to have associated fecal incontinence [Neil et al., 1981]. Other associated conditions with rectal prolapse include rectosigmoid cancer, systemic sclerosis, laxative abuse, malnutrition, and increased intraabdominal pressure. Up to 40% of patients with rectal prolapse have fecal incontinence, and up to 60% have constipation [Rashid and Basson, 1996].

3.3.4.3 Continence Abnormalities

Fecal incontinence, similar to other pelvic floor disorders, is vastly underreported by patients, and thus the true prevalence is unknown. In a study, based on a telephone survey, 2.2% of the population reported incontinence, half of whom were incontinent to solid or liquid stool [Nelson et al., 1995]. The studies conducted by using anonymous questionnaires have shown higher rates, with 4.8% having incontinence to solid stool and 6.7% with incontinence to liquid stool. Women are 50% more likely to report incontinence than men [Giebel et al., 1998].

The most important etiologic factor in the pathogenesis of fecal incontinence in women is the obstetric trauma. There is evidence that hormonal changes during pregnancy lead to smooth muscle relaxation attributed to progesterone. The connective tissue remodeling in the pelvic floor is due to relaxin, an ovarian hormone that peaks late during pregnancy [Lepert, 1995]. With parturition, there is stretch-

ing of the levators, stretching and tearing of the rectovaginal septum, stretching of the vaginal wall, and compression of the pudendal nerves against the pelvic side wall. All these factors may contribute to fecal incontinence.

In a study published by Sultan [Sultan et al., 1993] a percentage of 30% to 40% was obtained for anal sphincter defects in asymptomatic postpartum females. However, these patients may become symptomatic later in life or with subsequent vaginal deliveries. In addition, pudendal nerve injury documented by electromyography has been demonstrated in 42% of postpartum females [Snooks et al., 1990]. In these patients, 60% recovered nerve function 2 months after delivery, but 40% did not. From a group of 906 postpartum women in a study by MacArthur [MacArthur et al., 1997], 4% reported new symptoms of incontinence after childbirth. A study conducted by Sultan [Sultan et al., 1993] showed 1% incidence of frank fecal incontinence and 25% incidence of decreased flatal control, 9 months after vaginal delivery.

The incidence of sphincter injury is higher in patients with perineal tears. In a study conducted by Wood [Wood et al., 1998], up to 25% of patients developed fecal incontinence symptoms after a third degree perineal tear. Third degree tears, involving the sphincter muscle, occur in approximately 0.6% of all vaginal deliveries [Sultan et al., 1994].

Episiotomies, similar to tears, are associated with incontinence. Episiotomy has been found to be associated with an increased risk of sphincter injury. A threefold increase in fecal incontinence after midline episiotomy as been verified, when compared with spontaneous laceration; therefore, a mediolateral episiotomy is recommended [Davila et al., 2006].

Regardless of the etiology, the prevalence of bowel dysfunction in pelvic floor disorders can be significant. For many of these problems, treatment is available but not always satisfactory. As the understanding of these disorders improves, more successful and more durable treatments will likely develop. Patient and physician education, as well as early intervention, can often make a sizable difference in outcome resulting in a true understanding of the incidence of these problems as well as improved results of therapy.

3.3.5 Genital Prolapse, Sexual Dysfunction and Urogenital Atrophy

This section presents the epidemiology, incidence, prevalence, and risk factors involved with genital prolapse. The urogenital atrophy and sexual dysfunction related to prolapse and its incidence after pelvic reconstructive are also discussed.

3.3.5.1 Genital Prolapse

Genital prolapse is a general term for the weakening or loss of support to the pelvic organs (bladder, vagina,uterus,and rectum) that results in a herniation of those pelvic organs. It is a common condition that can affect women of all ages. Multiple risk factors have been identified and studied that are thought to contribute to the development of genital prolapse, including age, parity, menopausal status, body mass index (>30kg/m2), race, genetics, connective tissue disease, tobacco use, chronic lung disease, chronic constipation, occupational straining, and previous surgery. The different types of genital prolapse include:

Vaginal vault prolapse A vaginal vault prolapse is a herniation of the vaginal vault caused by loss of support or weakening of the uterosacral ligaments, cardinal ligaments, and loss of attachment of the endopelvic fascia to the white line at the level of the sacrospinous ligament, or a combination of the above mentioned.

Uterine prolapse A uterine prolapse is a herniation of the uterus caused by the loss of support from the uterosacral and/or cardinal ligaments.

Cystocele A cystocele is a herniation of the anterior vaginal wall and bladder caused by tearing, stretching, or a combination of the two, of the anterior wall endopelvic fascia. The insult may either be midline, resulting in a central cystocele, or a lateral insult resulting in a paravaginal defect.

Enterocele A enterocele is a herniation of the superior portion of the posterior vaginal wall caused by tearing, stretching, or a combination of the two, of the posterior vaginal wall endopelvic fascia.

Rectocele A rectocele is a herniation of the inferior portion of the posterior vaginal wall and rectum caused by tearing, stretching, or a combination of the two, of the posterior vaginal wall endopelvic fascia.

Epidemiology The incidence of genital prolapse is largely underestimated because of limited patient access to medical care, limited number of clinicians trained to recognize prolapse, mild cases of prolapse that may be asymptomatic and therefore unknown to the patient and ignored by the physician, as well as the patient's desire to not disclose her problem to the clinician. Typically, patients with genital prolapse have more than one area of weakness, with more severe prolapse in some areas, depending on the initial damage to the pelvic floor as well as the length of time the prolapse has gone untreated.

Surgery for Prolapse Pelvic organ prolapse is one of the most common indications for gynecologic surgery and despite this fact, there is little epidemiologic information regarding surgical procedures for prolapse. In the United States, approximately 226 000 women underwent surgery for pelvic organ prolapse during 1997, according to a survey conducted, making prolapse one of the most common indications for gynecologic surgery [Brown et al., 2002]. The average age of women undergoing prolapse surgery was 55 years. The overall rate of pelvic organ prolapse surgery was 22.7 per 10 000 women in the United States. The rate of pelvic organ prolapse surgery increased with age, arising to a peak rate of 42.1 per 10 000 women aged 60 to 69 years. Vaginal hysterectomy with rectocele and cystocele repair was the most common surgery performed.

Age and Menopause The incidence of prolapse increases with age, as does the rate of surgery for prolapse. It has been demonstrated that the rate of pelvic organ prolapse surgery increases with age, peaking in the sixth decade. The lifetime risk of undergoing a single operation for pelvic organ prolapse by the age of 80 is 11.1%. This incidence will be influenced by variables including access to a health care provider trained to treat these problems, financial concerns, and overall medical care access. Surgically managed patients represent only a small fraction of those affected, because many women, especially the elderly, are managed conservatively or never present for evaluation [Olsen et al., 1997].

Because age has been shown to be a strong risk factor in the development of prolapse, it can be assumed that estrogen deficiency, which will occur in all women in the menopausal years, may contribute to weakening of the supports (epithelium, connective tissue, muscle) [Davila et al., 2006]. This may be a key factor in the development and progression of prolapse, explaining the increased incidence of prolapse in the postmenopausal years. Estrogen receptors have been identified throughout the nuclei of the connective tissue and smooth muscle cells of the bladder trigone, urethra, vaginal mucosa, levator ani muscle stroma, arcus tendineus, and the uterosacral ligaments. The collagen content of the pelvic floor is also estrogen dependent. In biochemical analysis of pelvic floor tissue, when the estrogen concentrations decrease it has been demonstrated that there is a reduction in the total collagen content. In addition, there is a reduction in collagen content in genitourinary tissue of patients with genital prolapse when compared with patients without prolapse, regardless of the menopausal states [Jackson et al., 1996].

Previous Surgery Reoperation rates for recurrent prolapse have been estimated to be approximately 30%. The time interval between repeat procedures for recurrent prolapse has been shown to decrease with each successive repair [Olsen et al., 1997]. Theoretically, previous surgical treatment will cause further damage to the nerves

and surrounding support systems and is thus increasing potential risks for recurrent prolapse. For example, after an abdominal or vaginal hysterectomy, a vaginal vault prolapse is a late and common complication, with a reported incidence as high as 43% [Virtanen and Makinen, 1993].

Development of prolapse after retropubic urethropexy has been described in the literature with a reported occurrence rate of anywhere from 4% to 26%, depending on the surgical technique used, severity of prolapse and duration of follow-up [Langer et al., 2003]. The risk of development of a cystocele after a sacrospinous ligament fixation is up to 20% [Smilen et al., 1998; Meschia et al., 1999].

Obstetric Factors Obstetric injury is thought to be a principal factor contributing to the development of pelvic floor dysfunction (prolapse, urinary and fecal incontinence). This is attributed to direct muscular and connective tissue injury or to denervation injury to the pudendal nerve. There is question as to whether the mode of obstetric delivery, or just the event of being pregnant, has a role in developing prolapse.

In a case-control study, patients who delivered their first child before the age of 25 years had an almost fourfold increase of developing prolapse [Moalli et al., 2003]. Up to 50% of all parous women have some degree of prolapse, with 10% to 20% being symptomatic [Bidmead and Cardozo, 1998]. Elective cesarean delivery in a nonlabored patient has been speculated to protect the pelvic floor from damage leading to prolapse; however, to date there are no prospective randomized studies to support this theory [Davila et al., 2006]. It has been well established that vaginal parity, notably the first, is an independent risk factor for the future development of genital prolapse. It was demonstrated that the odds ratio was 3.0 for women who had one vaginal delivery and 4.5 for women with a history of two or more vaginal deliveries [Chiaffarino et al., 1999]. In a study by Mant [Mant et al., 1997], the risk factors for genital prolapse in 17 032 women were analyzed. In those patients who were diagnosed with prolapse, parity was shown to have the strongest relationship to the development of prolapse.

Race and Genetics Different studies have shown that prolapse is more common in whites, less common in Asians, and uncommon in blacks. Differences in the incidence of prolapse between racial groups suggest congenital and cultural factors. Genetics may also have a role in those women who have collagen or connective tissue diseases contributing to the development of prolapse.

3.3.5.2 Female Sexual Dysfunction

Female sexual dysfunction is a generalized term for abnormalities in the normal female sexual cycle. It is a highly prevalent problem affecting anywhere from 30%

to 50% of women in all age groups. Only recently have the problems involved with female sexuality gained recognition by clinicians. There are risk factors associated with female sexual dysfunction including age, menopause, previous surgery, mental and physical health, and availability of a partner.

Sexual Function after Pelvic Surgery Pelvic surgery to correct prolapse may affect sexual function for a number of reasons including narrowed vaginal canal, poor lubrication, and fear of urinary incontinence. Some studies suggest that sexual dysfunction can occur up to 20% of the time after surgery for prolapse or incontinence. It is thought that the vaginal dissection may lead to pelvic floor neuropathy affecting the pudendal nerve, which subsequently affects vaginal sensation and orgasm. Hysterectomy has been associated with sexual dysfunction. It is thought that removal of the cervix alters the upper portion of the vaginal canal and causes a neuropathy, which is the source for dyspareunia (painful sexual intercourse), as well as anorgasmia. However, studies in the literature are conflicting as to the exact cause of sexual dysfunction after hysterectomy [Rhodes et al., 1999].

Prolapse Problems with sexual function have been reported to occur in women with urinary incontinence and uterovaginal prolapse. However, the precise relationship between prolapse and sexual function has not been well documented. In a study that compared sexual dysfunction in women with and without uterovaginal prolapse, the authors found that overall sexual dysfunction in women without prolapse did not differ from women who had prolapse. In addition, the degree of prolapse did not have a role in whether sexual dysfunction occurred among those with prolapse. Psychological and relationship conflicts tended to have a greater impact on sexual function for both groups of women [Weber et al., 1995].

Menopause Several menopause-related changes in sexual function are well described in the literature: diminished sexual responsiveness, dyspareunia, decreased sexual activity, decrease in sexual desire, and a dysfunctional male partner. In a study by Sarrel [Sarrel, 1990], it is described that the underlying cause of biological changes that occurred with sexual dysfunction is the estrogen deficiency. The postmenopausal ovary has been shown to be responsible for up to 50% of the testosterone believed to be associated with libido. Many clinicians believe that a combination of both estrogen and testosterone is required to improve female sexual function.

The effect of menopause on vaginal physiology has been described. There is a pronounced decrease in pelvic blood flow. This in turn results in a thinning of the vaginal mucosa and loss of the normal microbial environment. With the loss of estrogen, there is change in the integrity of the vaginal tube, making it less compliant for coitus. Lubrication is also compromised because of loss of estrogen.

3.3.5.3 Atrophy

As modern medicine continues to improve, life expectancy will continue to increase. It has been estimated that, in the United States there are currently more than 25 million women who will live 30 years beyond menopause. Menopause by definition is an estrogen-deficient state resulting in physiological changes to many female organs. The urogenital organs, including the urethra, bladder, vagina, and vulva, are highly estrogen dependent. Blood flow to the pelvis is also estrogen dependent. Without an appropriate estrogen level, urogenital atrophy will develop. This means that 100% of women who enter into the menopausal state will develop atrophy of the urogenital system [Davila et al., 2006].

3.3.6 Current Needs and Future Perspectives

A very strong case can be made for a multidisciplinary approach to treatment of pelvic floor dysfunction. Certainly, the concept of serial surgeries in a patient with pelvic floor dysfunction cannot be beneficial to the patient. Therefore, correction of all pelvic floor defects at one setting and postoperative physiotherapeutic pelvic floor rehabilitation may represent the most desirable means of treating asymptomatic patients. Less-severe degrees of pelvic floor dysfunction and syndromes not associated with anatomic alterations are amenable to pelvic floor rehabilitative interventions. An emphasis must be made on the fact that pelvic floor physiotherapy will benefit both urinary and fecal continence disorders. In fact, patients with urinary and fecal incontinence, especially associated with urgency symptoms, are optimal candidates for pelvic floor physiotherapy/rehabilitation. Physiotherapy must be considered an integral part of the treatment plan for many patients with pelvic floor dysfunction [Davila et al., 2006].

Chapter 4

The Course and Conduct of Labor and Delivery

4.1 Normal Labor and Delivery

4.1.1 Introduction

Labor is a sequence of uterine contractions that results in effacement and dilatation of the cervix and voluntary bearing-down efforts leading to the expulsion per vagina of the products of conception. Delivery is the mode of expulsion of the fetus and placenta. Labor and delivery is a normal physiologic process that most women experience without complications. The goal of the management of this process is to foster a safe birth for mothers and their newborns [DeCherney and Nathan, 2003].

This chapter briefly introduces the course and conduct of labor and delivery. This subject is already very well established on the literature, and is presented here only briefly. This Chapter is based on the works of [DeCherney and Nathan, 2003], [Gabbe et al., 2007], [Cunningham et al., 2005] and [Hanretty, 2003], which should be consulted, among many others, for more details on this subject.

4.1.2 Physiologic preparation for labor

Prior to the onset of true labor, several preparatory physiologic changes commonly occur. The settling of the fetal head into the brim of the pelvis, known as lightening, usually occurs 2 or more weeks before labor in first pregnancies. In women who have had a previous delivery, lightening often does not occur until early labor. Clinically, the mother may notice a flattening of the upper abdomen and increased pressure in the pelvis. This descent of the fetus is often accompanied by a decrease in discomfort associated with crowding of the abdominal organs under the diaphragm, while increasing pelvic discomfort and frequency of urination.

During the last 4-8 weeks of pregnancy irregular, generally painless uterine contractions occur with slowly increasing frequency. These contractions, known as Braxton Hicks contractions, may occur more frequently, sometimes every 10-20 minutes, and with greater intensity during the last weeks of pregnancy. When these contractions occur early in the third trimester, they must be distinguished from true preterm labor. Later, they are a common cause of "false labor," which is distinguished by the lack of cervical change in response to the contractions.

During the course of several days to several weeks before the onset of true labor, the cervix begins to soften, efface, and dilate. In many cases, when labor starts, the cervix is already dilated 1-3 cm in diameter. This is usually more pronounced in the multiparous patient, the cervix being relatively more firm and closed in nulliparous women. With cervical effacement, the mucus plug within the cervical canal may be released. When this occurs, the onset of labor is sometimes marked by the passage of a small amount of blood-tinged mucus from the vagina.

In true labor, the woman is usually aware of her contractions during the first stage. The intensity of pain depends on the fetopelvic relationships, the quality and strength of uterine contractions, and the emotional and physical status of the patient. Very few women experience no discomfort during the first stage of labor. With the beginning of true normal labor, some women describe slight low back pain that radiates around to the lower abdomen. Each contraction starts with a gradual build-up of intensity, and dissipation of discomfort promptly follows the climax. Normally, the contraction will be at its height well before discomfort is reported. Dilatation of the lower birth canal and distention of the perineum during the second stage of labor will almost always cause discomfort.

4.1.3 Characteristics of normal labor

Normal labor is a continuous process which has been divided into three stages, with the first stage further subdivided into two phases. The first stage of labor is the interval between the onset of labor and full cervical dilatation. The second stage is the interval between full cervical dilatation and delivery of the infant. The third stage of labor is the period between the delivery of the infant and the delivery of the placenta.

In his classic studies of labor in 1967, Friedman presented data describing the process of spontaneous labor over time [Friedman, 1967]. The duration of the first stage of labor in primipara patients is noted to range from 6-18 hours, while in multiparous patients the range is reported to be 2-10 hours. The lower limit of normal for the rate of cervical dilatation during the active phase is 1.2 cm per hour in first pregnancies and 1.5 cm per hour in subsequent pregnancies. The duration of the second stage in the primipara is 30 minutes to 3 hours, and is 5-30 minutes for multiparas. For both, the duration of the third stage was reported to be 0-30

minutes for all pregnancies.

4.1.3.1 Evaluation of Labor Progress

The first stage of labor is evaluated by the rate of change of cervical effacement, cervical dilatation, and descent of the fetal head. The frequency and duration of uterine contractions alone is not an adequate measure of labor progress. The second stage of labor begins after full cervical dilatation. The progress of this stage is measure by the descent, flexion, and rotation of the presenting part.

4.1.4 Clinical management of normal labor

Women most likely to have a normal labor and delivery have had adequate prenatal care without significant maternal or fetal complications and are at 36 weeks' gestation or beyond. If no complications are detected during the initial assessment and the patient is found to be in prodromal labor, admission for labor and delivery may be deferred.

4.1.4.1 The First Stage of Labor

During the first stage, the progress of labor is monitored by examination of the cervix. During the latent phase, especially when the membranes are ruptured, vaginal examinations should be done sparingly to decrease the risk of an intrauterine infection. In the active phase the cervix should be assessed approximately every 2 hours. The cervical effacement and dilatation, and the station and position of the fetal head should be recorded (Figure 4.1). Additional examinations to determine if full dilation has occurred may be required if the patient reports the urge to push, or to search for prolapse of the umbilical cord or perform fetal scalp stimulation if a significant fetal heart rate deceleration is detected.

4.1.4.2 Second Stage of Labor

At the beginning of the second stage of labor the mother usually feels a desire to bear down with each contraction. This abdominal pressure, together with the force of the uterine contractions, expels the fetus. During the second stage of labor the descent of the fetal head is measured to assess the progress of labor. The descent of the fetus is evaluated by measuring the relationship of the bony portion of the fetal head to the level of the maternal ischial spines (station) (Figure 4.1). When the bony portion of the fetal head is at the level of the ischial spines, the station is "0".

The second stage generally takes from 30 minutes to 3 hours in primigravid women and from 5-30 minutes in multigravid women. The median duration is 50

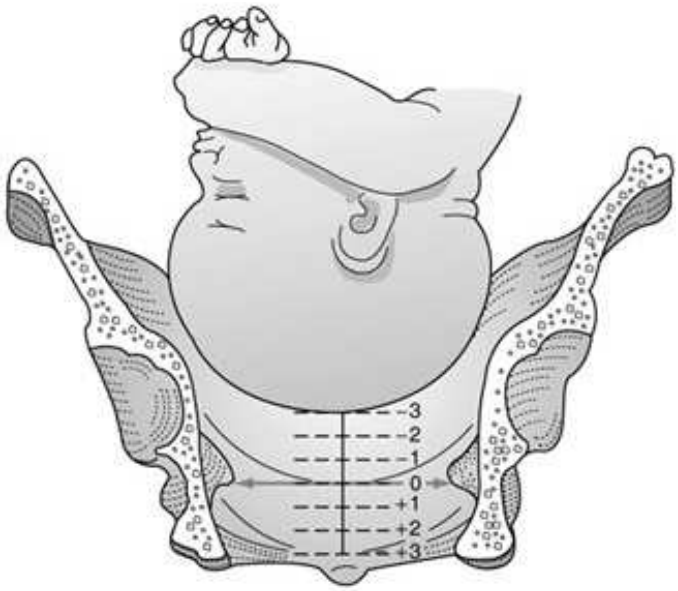

Figure 4.1: Stations of the fetal head ([DeCherney and Nathan, 2003]).

minutes in a primipara and 20 minutes in a multipara. These times may vary depending on the pushing efforts of the mother, the quality of the uterine contractions, and the type of analgesia.

4.1.4.3 Third Stage of Labor

Immediately after the baby is delivered, the cervix and vagina should be thoroughly inspected for lacerations and surgical repair should be performed as needed. Repair of vaginal lacerations should be performed using absorbable suture material. The inspection and repair of the cervix, vagina, and perineum is often easier prior to the separation of the placenta before uterine bleeding obscures visualization.

Separation of the placenta generally occurs within 2-10 minutes of the end of the second stage, but it may take 30 minutes or more to spontaneously separate.

After the delivery of the placenta, attention is turned to prevention of excessive postpartum bleeding. Uterine contractions which reduce this bleeding may be enhanced with uterine massage and/or the infusion of a dilute solution of oxytocin. The placenta should be examined to ensure complete removal and to detect placental abnormalities.

4.1.4.4 Puerperium

The puerperium consists of the period following the delivery of the baby and placenta to approximately 6 weeks postpartum. The immediate postpartum period (within the first hour of delivery) is a critical time for both maternal and neonatal physiologic and emotional adjustment. During that hour, the maternal blood pressure, pulse rate, and uterine blood loss must be monitored closely. It is during this time that most postpartum hemorrhage usually occurs, largely due to uterine relaxation, retained placental fragments, or unrepaired lacerations. Occult bleeding may manifest as increasing pelvic pain.

4.1.5 Mechanics Of Labor

Labor and delivery are not passive processes in which uterine contractions push a rigid object through a fixed aperture. The ability of the fetus to successfully negotiate the pelvis during labor and delivery is dependent on the complex interaction of three variables: uterine activity, the fetus, and the maternal pelvis.

4.1.5.1 Uterine Activity

Uterine activity is characterized by the frequency, amplitude (intensity), and duration of contractions. Assessment of uterine activity may include simple observation, manual palpation, external objective assessment techniques (such as external tocodynamometry), and direct measurement via an internal uterine pressure catheter. External tocodynamometry measures the change in shape of the abdominal wall as a function of uterine contractions and, as such, is qualitative rather than quantitative. Although it permits graphic display of uterine activity and allows for accurate correlation of fetal heart rate patterns with uterine activity, external tocodynamometry does not allow measurement of contraction intensity or basal intrauterine tone. The most precise method for determination of uterine activity is the direct measurement of intrauterine pressure. However, this procedure should not be performed unless indicated given the small but finite associated risks of uterine perforation, placental disruption and intrauterine infection.

Despite technologic improvements, the definition of "adequate" uterine activity during labor remains unclear. Classically, three to five contractions per 10 minutes has been used to define adequate labor; this pattern has been observed in approximately 95 percent of women in spontaneous labor. In labor, patients usually contract every 2 to 5 minutes, with contractions becoming as frequent as every 2 to 3 minutes in late active labor and during the second stage. Abnormal uterine activity can also be observed either spontaneously or resulting from iatrogenic interventions [Howarth and Botha, 2005]

Although it is generally believed that optimal uterine contractions are associated with an increased likelihood of vaginal delivery, there are limited data to support this assumption. If uterine contractions are "adequate" to effect vaginal delivery, one of two things will happen: either the cervix will efface and dilate, and the fetal head will descend, or there will be worsening caput succedaneum (scalp edema) and molding of the fetal head (overlapping of the skull bones) without cervical effacement and dilatation. The latter situation suggests the presence of cephalopelvic disproportion, which can be either absolute (in which a given fetus is simply too large to negotiate a given pelvis) or relative (in which delivery of a given fetus through a given pelvis would be possible under optimal conditions but is precluded by malposition or abnormal attitude of the fetal head).

4.1.5.2 The Fetus

There are several fetal variables that influence the course of labor and delivery [Gabbe et al., 2007]. These are summarized below.

Fetal size The fetus size can be estimated clinically by abdominal palpation or with ultrasound, but both are subject to a large degree of error. Fetal macrosomia is associated with an increased likelihood of failed trial of labor [Spellacy et al., 1985].

Lie The position of the longitudinal axis of the fetus relative to the longitudinal axis of the uterus is known as lie. Fetal lie can be either longitudinal, transverse, or oblique (Figure 4.2). In a singleton pregnancy, only fetuses in a longitudinal lie can be safely delivered vaginally.

Presentation Presentation refers to the fetal part that directly overlies the pelvic inlet. In a fetus presenting in the longitudinal lie, the presentation can be cephalic (vertex) or breech. Compound presentation refers to the presence of more than one fetal part overlying the pelvic inlet. Funic presentation refers to presentation of the umbilical cord and is rare at term. In a cephalic fetus, the presentation is classified according to the leading bony landmark of the skull, which can be either the occiput (vertex), the chin (mentum), or the brow (Figure 4.3). Malpresentation, referring to any presentation other than vertex, is seen in approximately 5 percent of all term labors.

Attitude Attitude refers to the position of the head with regard to the fetal spine (the degree of flexion and/or extension of the fetal head). Flexion of the head is important to facilitate engagement of the head in the maternal pelvis. When the fetal chin is optimally flexed onto the chest, the suboccipitobregmatic diameter (9.5

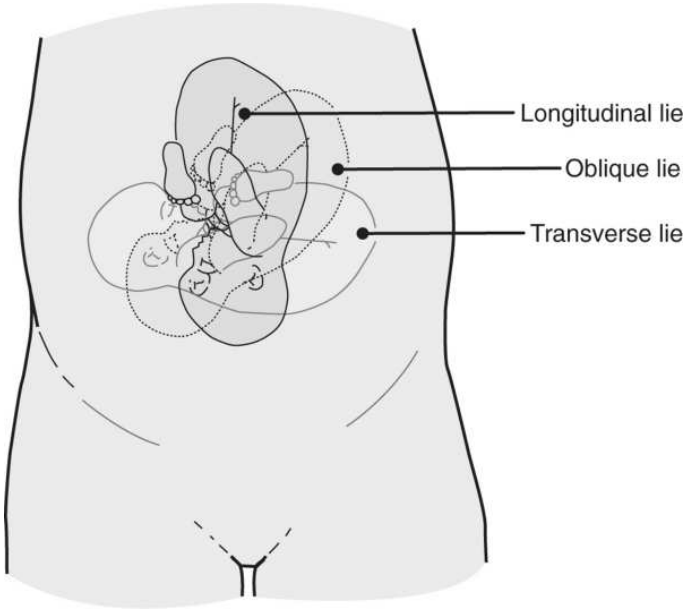

Figure 4.2: Examples of different fetal lie (adapted from [Gabbe et al., 2007]).

cm) presents at the pelvic inlet (Figure 4.4). This is the smallest possible presenting diameter in the cephalic presentation. As the head deflexes (extends), the diameter presenting to the pelvic inlet progressively increases even before the malpresentations of brow and face are encountered (see Figure 4.4), and may contribute to failure to progress in labor. The architecture of the pelvic floor along with increased uterine activity may correct deflexion in the early stages of labor.

Position Position of the fetus refers to the relationship of the fetal presenting part to the maternal pelvis, and it can be assessed most accurately on vaginal examination. For cephalic presentations, the fetal occiput is the reference. If the occiput is directly anterior, the position is occiput anterior. If the occiput is turned toward the mother's right side, the position is right occiput anterior. In the breech presentation, the sacrum is the reference (right sacrum anterior). The various positions of a cephalic presentation are illustrated in Figure 4.5. In a vertex presentation, position can be determined by palpation of the fetal sutures. The sagittal suture is the easiest to palpate. Palpation of the distinctive lamdoid sutures should identify the position of the fetal occiput. The frontal suture can also be used to determine the position of the front of the vertex. Most commonly, the fetal head enters the pelvis in a transverse position and, then as a normal part of labor, rotates to an occiput anterior position. Most fetuses deliver in the occiput anterior, left occiput

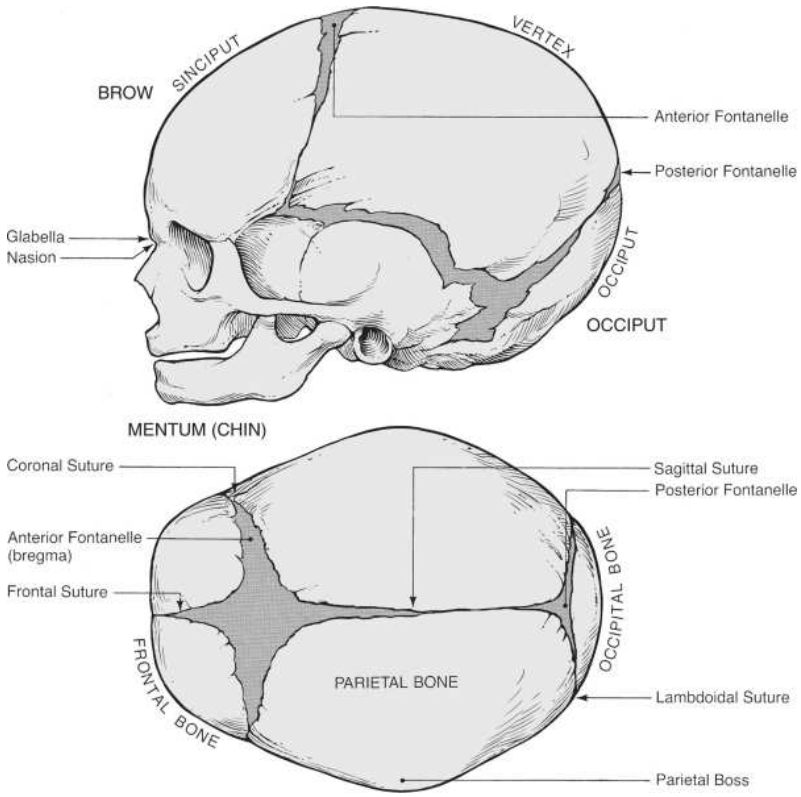

Figure 4.3: Landmarks of fetal skull for determination of fetal position (adapted from [Gabbe et al., 2007]).

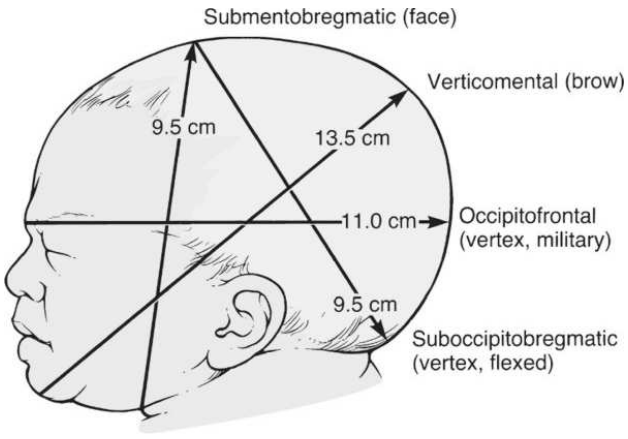

Figure 4.4: Presenting diameters of the average term fetal skull (adapted from [Gabbe et al., 2007]).

anterior, or right occiput anterior position. In the past, less than 10 percent of presentations were occiput posterior at delivery [Gabbe et al., 2007]. However epidural analgesia is associated with an increased risk of occiput posterior presentation (observed in 12.9 percent of women with epidural analgesia) [Lieberman et al., 2005]. Asynclitism occurs when the sagittal suture is not directly central relative to the maternal pelvis. If the fetal head is turned such that more parietal bone is present posteriorly, the sagittal suture is more anterior and this is referred to as posterior asynclitism. Anterior asynclitism occurs when there is more parietal bone presenting anteriorly. The occiput transverse and occiput posterior positions are less common at delivery and more difficult to deliver. Malposition refers to any position in labor that is not right occiput anterior, occiput anterior, or left occiput anterior.

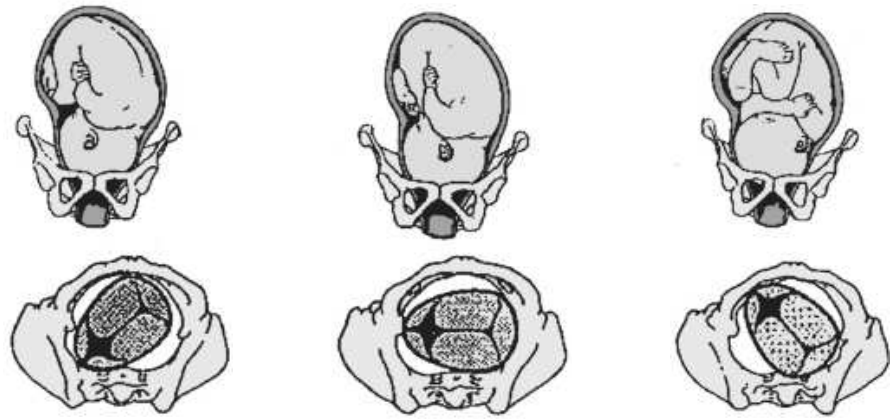

(a) Left occiput anterior.

(b) Left occiput transverse.

(c) Left occiput posterior.

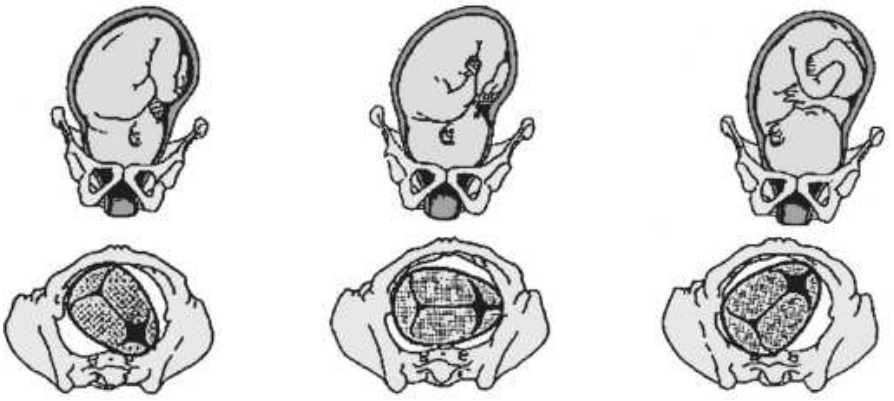

(d) Right occiput anterior.

(e) Right occiput transverse.

(f) right occiput posterior.

Figure 4.5: Fetal presentations and positions in labor ([Gabbe et al., 2007]).

Station Station is a measure of descent of the bony presenting part of the fetus through the birth canal (Figure 4.1). The current standard classification is based on a quantitative measure in centimeters of the distance of the leading bony edge from the ischial spines. The midpoint (0 station) is defined as the plane of the maternal ischial spines. The ischial spines can be palpated on vaginal examination. For the right-handed person, they are most easily felt on the maternal right.

An abnormality in any of the above-mentioned fetal variables may affect both the course of and the likelihood of vaginal delivery. Failure to progress in labor should prompt a careful reevaluation of the above-mentioned fetal parameters to exclude absolute or relative cephalopelvic disproportion.

4.1.5.3 The Maternal Pelvis

The birth canal consists of the bony pelvis (composed of the sacrum, ilium, ischium, and pubis) and the resistance provided by the soft tissues. The bony pelvis is divided into the false (greater) and true (lesser) pelvis by the pelvic brim, which is demarcated by the sacral promontory, the anterior ala of the sacrum, the arcuate line of the ilium, the pectineal line of the pubis, and the pubic crest culminating in the symphysis (Figure 2.11). Measurements of the various parameters of the bony female pelvis have been made with great precision, directly in cadavers and using radiographic imaging in living women. Such measurements have divided the true pelvis into a series of planes that must be negotiated by the fetus during passage through the birth canal, which can be broadly classified into the pelvic inlet, midpelvis and pelvic outlet.

Clinical pelvimetry is currently the only method of assessing the shape and dimensions of the bony pelvis in labor. The inlet of the true pelvis is largest in its transverse diameter (usually >12.0 cm). The diagonal conjugate (the distance from the sacral promontory to the inferior margin of the symphysis pubis as assessed on vaginal examination) (Figure 4.6) is a clinical representation of the anteroposterior diameter of the pelvic inlet. The true conjugate (or obstetric conjugate) of the pelvic inlet is the distance from the sacral promontory to the superior aspect of the symphysis pubis (Figure 4.7). This measurement cannot be made clinically but can be estimated by subtracting 1.5 to 2.0 cm from the diagonal conjugate . This is the smallest diameter of the inlet, and it usually measures approximately 10 to 11 cm. The limiting factor in the midpelvis is the interspinous diameter (the measurement between the ischial spines), which is usually the smallest diameter of the pelvis but should be greater than 10 cm. The pelvic outlet is rarely of clinical significance. The anteroposterior diameter from the coccyx to the symphysis pubis is approximately 13 cm in most cases, and the transverse diameter between the ischial tuberosities is approximately 8 cm.

The shape of the female bony pelvis can be classified into four broad categories:

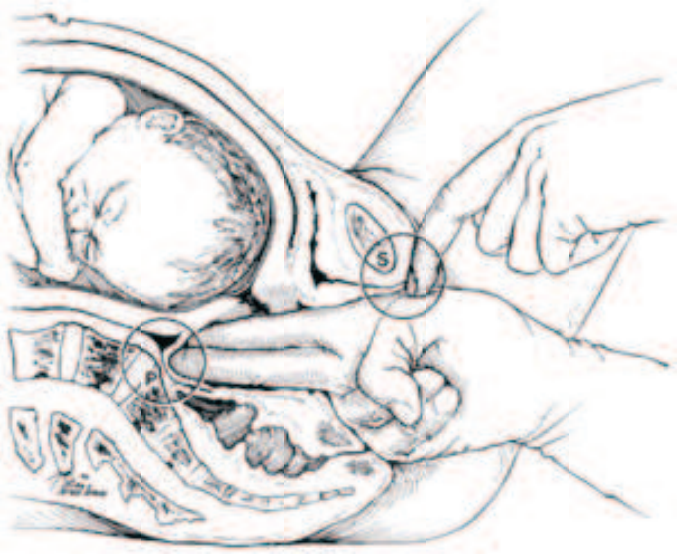

Figure 4.6: Diagonal conjugate (P = sacral promontory; S = symphysis pubis) (adapted from [Cunningham et al., 2005]).

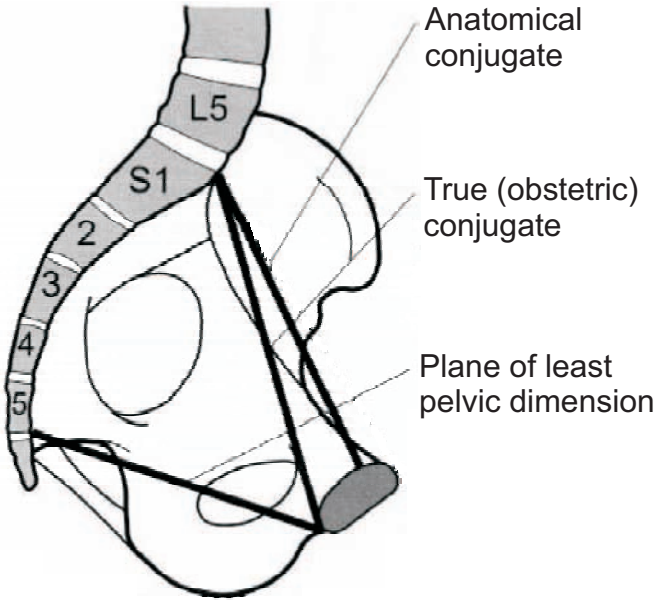

Figure 4.7: Pelvic Diameters (Conjugates) (adapted from [Hanretty, 2003]).

gynecoid, anthropoid, android, and platypelloid (Figure 4.8). This classification, based on the radiographic studies of Caldwell and Moloy, separates those with favorable characteristics (gynecoid, anthropoid) from those that are less favorable for vaginal delivery (android, platypelloid) [Caldwell and Moloy, 1933]. In reality, however, many women fall into intermediate classes, and the distinctions become arbitrary. The gynecoid pelvis is the classic female shape with an oval-shaped inlet, diverging midpelvic sidewalls, and far-spaced ischial spines. The anthropoid pelvis has an exaggerated oval shape to the inlet, with the largest diameter being anteroposterior, and with limited anterior capacity to the pelvis. Such pelves are more often associated with delivery in the occiput posterior position. The android pelvis is male in pattern, with a heart-shaped inlet, prominent sacral promontory and ischial spines, shallow sacrum, and converging midpelvic sidewalls theoretically increasing the risk of cephalopelvic disproportion. The platypelloid pelvis is a broad, flat pelvis with an exaggerated oval-shaped inlet, but with the largest diameter being the transverse diameter theoretically predisposing to transverse arrest. Although the assessment of fetal size along with pelvic shape and capacity is still of clinical utility, it is a very inexact science. An adequate trial of labor is the only definitive method to determine whether a given fetus will be able to safely negotiate a given pelvis.

Pelvic soft tissues may provide resistance in both the first and second stages of labor. In the first stage, resistance is offered primarily by the cervix; whereas in the second stage, it is by the muscles of the pelvic floor. It has been proposed that rapid labors result from low pelvic resistance rather than from high myometrial activity [Crawford, 1975]. In the second stage of labor, the resistance of the pelvic musculature is believed to play an important role in the rotation and movement of the presenting part through the pelvis.

4.1.5.4 Cardinal Movements in Labor

The mechanisms of labor in the vertex position, also known as the cardinal movements, refer to the changes in position of fetal head during its passage through the birth canal. Because of the asymmetry of the shape of both the fetal head and the maternal bony pelvis, such rotations are required for the fetus to successfully negotiate the birth canal. Although labor and birth is a continuous process, seven discrete cardinal movements of the fetus are described: engagement, descent, flexion, internal rotation, extension, external rotation or restitution, and expulsion (Figure 4.10).

The progress of labor is dictated by the pelvic dimensions and configuration, the size of the fetus, and the strength of the contractions. In essence, delivery proceeds along the line of least resistance, ie, by adaptation of the smallest achievable diameters of the presenting part to the most favorable dimensions and contours of

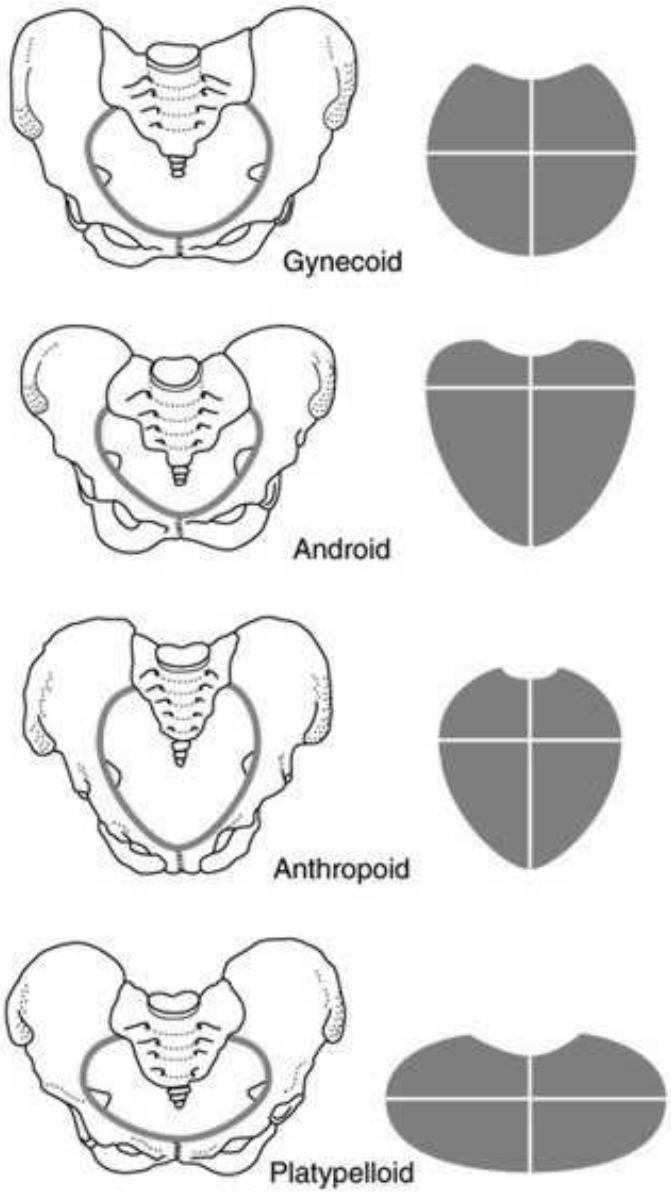

Figure 4.8: Types of pelves. The white lines in the diagrams at right show the greatest diameters of the pelves at left (adapted from the reference [DeCherney and Nathan, 2003]).

the birth canal. The sequence of events in vertex presentation is as follows:

Engagement Engagement refers to passage of the widest diameter of the presenting part to a level below the plane of the pelvic inlet (Figure 4.9). In the cephalic presentation with a well-flexed head, the largest transverse diameter of the fetal head is the biparietal diameter (9.5 cm). In the breech, the widest diameter is the bitrochanteric diameter. Clinically, engagement can be confirmed by palpation of the presenting part both abdominally and vaginally. With a cephalic presentation, engagement is achieved when the presenting part is at 0 station (at the level of the maternal ischial spines) on vaginal examination. Engagement is considered an important clinical prognostic sign because it demonstrates that, at least at the level of the pelvic inlet, the maternal bony pelvis is sufficiently large to allow descent of the fetal head. In 70% of women with a gynecoid pelvis (Figure 4.8), the head enters the superior strait in the occiput transverse position. In nulliparas, engagement of the fetal head usually occurs by 36 weeks' gestation. In multiparas, however, engagement can occur later in gestation or even during the course of labor.

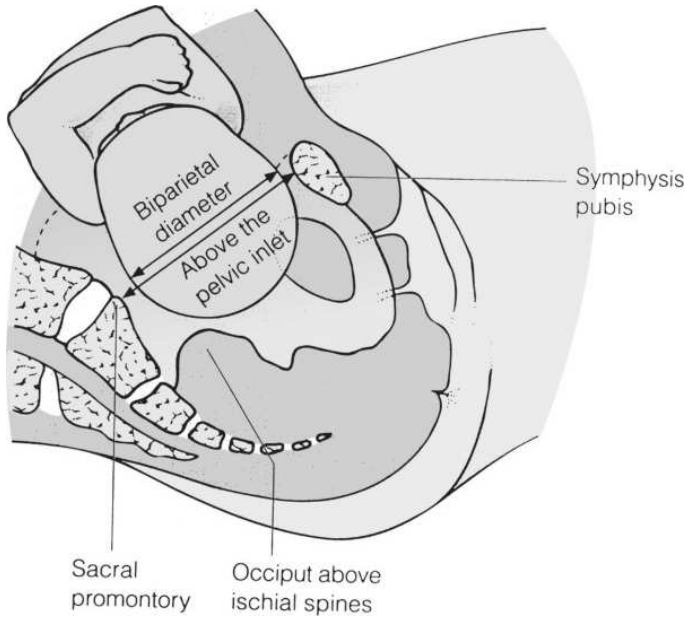

Figure 4.9: Engagement of the fetal head (adapted from [Gabbe et al., 2007]).

Descent Descent refers to the downward passage of the presenting part through the pelvis. Descent of the fetus is not continuous; the greatest rates of descent occur during the deceleration phase of the first stage of labor and during the second stage of labor.

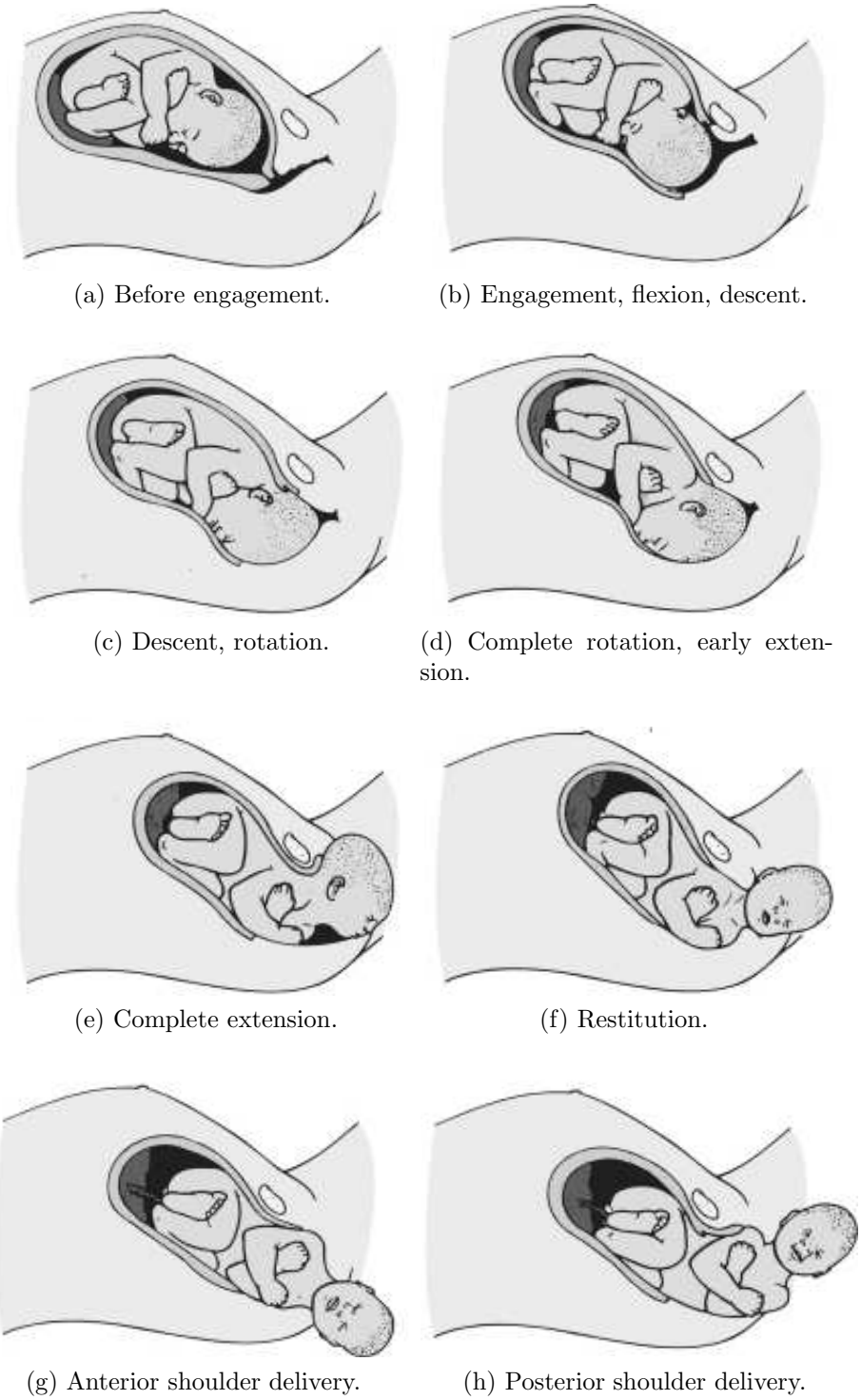

(a) Before engagement.

(b) Engagement, flexion, descent.

(c) Descent, rotation.

(d) Complete rotation, early extension.

(e) Complete extension.

(f) Restitution.

(g) Anterior shoulder delivery.

(h) Posterior shoulder delivery.

Figure 4.10: Cardinal movements during labor (adapted from [Gabbe et al., 2007]).

Flexion Flexion of the fetal head occurs passively as the head descends owing to the shape of the bony pelvis and the resistance offered by the soft tissues of the pelvic floor. Although flexion of the fetal head onto the chest is present to some degree in most fetuses before labor, complete flexion usually occurs only during the course of labor. The result of complete flexion is to present the smallest diameter of the fetal head (the suboccipitobregmatic diameter) for optimal passage through the pelvis.

Internal Rotation Internal rotation refers to rotation of the presenting part from its original position as it enters the pelvic inlet (usually occiput transverse) to the anteroposterior position as it passes through the pelvis. As with flexion, internal rotation is a passive movement resulting from the shape of the pelvis and the pelvic floor musculature. The pelvic floor musculature, including the coccygeus and ileococcygeus muscles, forms a V-shaped hammock that diverges anteriorly. As the head descends, the occiput of the fetus rotates towards the symphysis pubis (or, less commonly, towards the hollow of the sacrum), thereby allowing the widest portion of the fetus to negotiate the pelvis at its widest dimension. Owing to the angle of inclination between the maternal lumbar spine and pelvic inlet, the fetal head engages in an asynclitic fashion (i.e., with one parietal eminence lower than the other). With uterine contractions, the leading parietal eminence descends and is first to engage the pelvic floor. As the uterus relaxes, the pelvic floor musculature causes the fetal head to rotate until it is no longer asynclitic.

Extension Because the vaginal outlet is directed upward and forward, extension must occur before the head can pass through it. As the head continues its descent, there is a bulging of the perineum followed by crowning. Crowning occurs when the largest diameter of the fetal head is encircled by the vulvar ring. At this time spontaneous delivery is imminent and careful management by the practitioner with controlled efforts of the mother will minimize perineal trauma. Routine episiotomy is not necessary, and has been conclusively associated with increased maternal blood loss, increased risk of disruption of the anal sphincter (third-degree extension) and rectal mucosa (fourth-degree extension), as well as delay in the patient's resumption of sexual activity. Further extension follows extrusion of the head beyond the introitus. Once the head is delivered, the airway is cleared of blood and amniotic fluid using a bulb suction device. The oral cavity is cleared initially, followed by clearing of the nares.

External Rotation External rotation, also known as restitution, follows delivery of the head when it rotates to the position it occupied at engagement. Following this, the shoulders descend in a path similar to that traced by the head.

The anterior shoulder rotates internally about 45 degrees to come under the pubic arch for delivery. As this occurs, the head swings back to its position at birth. Delivery of the anterior shoulder is aided by gentle downward traction on the externally rotated head. The posterior shoulder is then delivered by gentle upward traction on the head. The brachial plexus may be injured if excessive force is used. Following these maneuvers, the body, legs, and feet are delivered with gentle traction on the shoulders. After the airway is cleared, an index finger is used to check whether the umbilical cord encircles the neck. If so, the cord can usually be slipped over the infant's head. If the cord is too tight, it can be cut between two clamps.

Expulsion Expulsion refers to delivery of the rest of the fetus. After delivery of the head and external rotation, further descent brings the anterior shoulder to the level of the symphysis pubis. The anterior shoulder is delivered in much the same manner as the head, with rotation of the shoulder under the symphysis pubis. After the shoulder, the rest of the body is usually delivered without difficulty.

After delivery, blood will be infused from the placenta into the newborn if the baby is held below the mother's introitus. Delayed cord clamping can result in neonatal hyperbilirubinemia as additional blood is transferred to the newborn infant.

4.1.6 Episiotomy, perineal injury, and perineal repair

Following delivery of the placenta, the cervix, vagina, and perineum should be carefully examined for evidence of injury. If a laceration is seen, its length and position should be noted and repair initiated. Adequate analgesia (either regional or local) is essential for repair. Special attention should be paid to repair of the perineal body, the external anal sphincter, and the rectal mucosa. Failure to recognize and repair rectal injury can lead to serious long-term morbidity, most notably fecal incontinence.

Perineal injuries, either spontaneous or with episiotomy, are the most common complications of spontaneous or operative vaginal deliveries. A first-degree tear is defined as a superficial tear confined to the epithelial layer. Second-degree tears extend into the perineal body but not into the external anal sphincter. Third-degree tears involve superficial or deep injury to the external anal sphincter, whereas a fourth-degree tear extends completely through the rectal mucosa. Significant morbidity is associated with third and fourth-degree tears, including risk of flatus and stool incontinence, rectal vaginal fistula, infection, and pain. Primary approximation of perineal laceration affords the best opportunity for functional repair, especially if there is evidence of rectal sphincter injury. The external anal sphincter should be

repaired by direct apposition or overlapping the cut ends and securing them using interrupted sutures.

Episiotomy is an incision into the perineal body made during the second stage of labor to facilitate delivery. It is by definition a second-degree tear. Because such incisions appear to be moderately protective against severe perineal trauma, they are the procedure of choice for women with inflammatory bowel disease because of the critical need to prevent rectal injury.

Chapter 5

Computational Solid Mechanics

5.1 Introduction

In this chapter, the fundamentals of the finite element method are presented. This chapter presents the finite element concept, the approximations involved, the construction of the finite element equations and the use of an incremental approach to solve nonlinear problems.

The finite element method is one of the most important developments in numerical analysis. The method was developed in the 1950's by engineers for systematically analyzing complex structures containing a large number of components [Argyris and Kelsey, 1960]. Over the years, the finite element method has spread to applications in all fields of engineering and science.

5.2 Kinematics of Deformation and Motion

Kinematics is the study of motion and deformation without reference to the cause. The deformation of solids is generally described by the kinematic relations, the equations of balance and the constitutive equations. This section summarizes the main equations which govern the deformation of solids. For a detailed treatment of this subject, the books of Eringen [Eringen, 1962], Malvern [Malvern, 1969], Ogden [Ogden, 1984] or Chadwick [Chadwick, 1999], for example, should be consulted. As shown in the following pages, consideration of finite deformation enables alternative coordinate systems to be employed, namely, material and spatial descriptions associated with the names of Lagrange and Euler respectively, see [Wriggers, 2006], [Bonet and Wood, 1997], [Belytschko et al., 2000] or [Doghri, 2000], for example.

Although inertial effects are not of primary concern, time derivatives of various kinematic quantities enrich our understanding and also provide the basis for the formulation of the virtual power expression of equilibrium, which uses the notion of

virtual velocity and associated kinematic quantities. Therefor, the time derivatives of the different kinematic quantities are presented on the following sections.

The different nonlinear kinematic quantities are linearized in preparation for inclusion in the linearized equilibrium equations that form the basis of the Newton-Raphson solution to the finite element equilibrium equations.

5.2.1 The Motion

Figure 5.1 shows the general motion of a deformable body. A given body $\mathcal{B}$ can be described by a set of points which are in a region of the Euclidean space $\mathbb{E}^3$. A configuration of the body $\mathcal{B}$ is then a one-to-one mapping $\boldsymbol{\varphi} : B \rightarrow \mathbb{E}^3$, which places all the particles of $\mathcal{B}$ in $\mathbb{E}^3$. The position of a particle X of $\mathcal{B}$ in the deformed configuration $\boldsymbol{\varphi}$ is defined by $\mathbf{x} = \boldsymbol{\varphi}(X)$. The placement of the body $\mathcal{B}$ is described by $\boldsymbol{\varphi}(B) = \{\boldsymbol{\varphi}(X) \,|X \in B\}$ and in the following sections is denoted as configuration $\boldsymbol{\varphi}(\mathcal{B})$ of body $\mathcal{B}$.

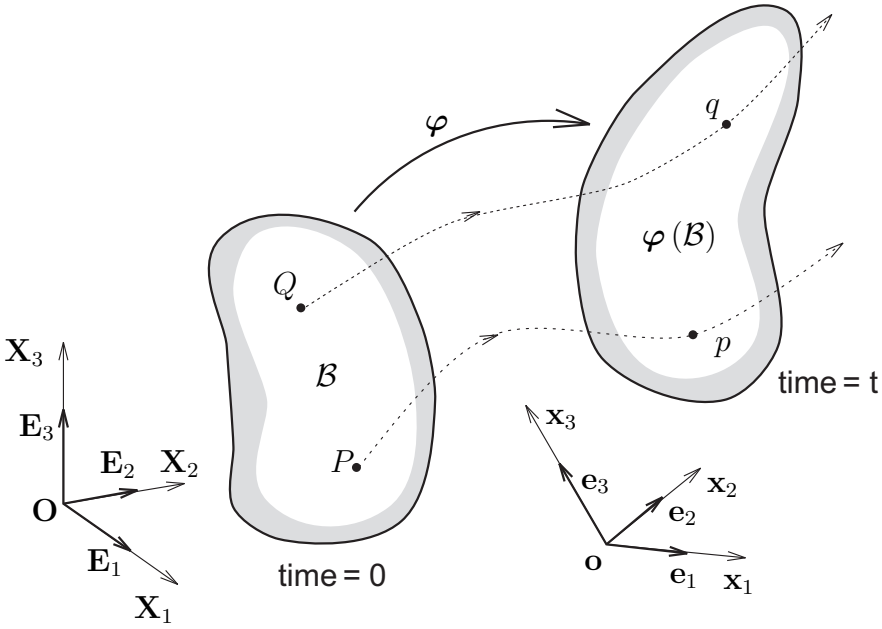

Figure 5.1: General motion of a deformable body, showing the trajectory of two points P and Q.

The motion of a body $\mathcal{B}$ is then a temporally parametric series of configurations $\boldsymbol{\varphi}_t : B \rightarrow \mathbb{E}^3$. For the position of a given particle X at time $t \in \mathbb{R}^+$ the following is obtained

$$\mathbf{x} = \boldsymbol{\varphi}_t(X) = \boldsymbol{\varphi}(X, t)\,. \tag{5.1}$$

In (5.1) $\boldsymbol{\varphi}$ is a vector field that defines the new location $\mathbf{x}$ of a particle X for a fixed t and is called the motion of the body $\mathcal{B}$. The motion $\boldsymbol{\varphi}$ is suitably regular and carries points X belonging to the body $\mathcal{B}$ to the current configuration $\boldsymbol{\varphi}(\mathcal{B})$. It is assumed that $\boldsymbol{\varphi}$ possesses continuous derivatives with respect to position and time. The parametric equation (5.1) defines successive positions $\mathbf{x}$ of a particle X in space. All successive points together form a curve in the Euclidian space $\mathbb{E}^3$ which is called the path line (or trajectory) of the particle X, as shown in Figure 5.1, with points P and Q.

The motion $\boldsymbol{\varphi}$ is assumed to be uniquely invertible. Consider that a given particle occupies the position $(\mathbf{x}, t)$, in a given time instance. The position of the particle X, which is associated with the place $\mathbf{x}$ at time t is given uniquely by Equation (5.1) as

$$\mathbf{X} = \boldsymbol{\varphi}^{-1}(\mathbf{x}) . \tag{5.2}$$

In (5.2) $\boldsymbol{\varphi}^{-1}$ is the inverse motion of the mapping $\boldsymbol{\varphi}$, as defined in (5.1). The position of this particle on the reference configuration of the body $\mathcal{B}$ is given by $\mathbf{X} = \boldsymbol{\varphi}_0(X)$, where $\mathbf{X}$ is the position of a particle X in this configuration. Using Equation (5.1), it is possible to obtain

$$\mathbf{x} = \boldsymbol{\varphi}\left(\boldsymbol{\varphi}_0^{-1}(\mathbf{X}), t\right) . \tag{5.3}$$

For practical applications there is no need to differentiate between $\mathbf{X}$ and X. This simplifies the notation, and Equation (5.3) can be written as

$$\mathbf{x} = \boldsymbol{\varphi}(\mathbf{X}, t) , \tag{5.4}$$

where $\mathbf{X}$ depicts the position of particle X in the reference configuration $\mathcal{B}$. With this, the positions $\mathbf{x}$ and $\mathbf{X}$ are described as vectors in $\mathbb{E}^3$ with respect to the origin $\mathbf{O}$. The point X is denoted in the reference configuration by the position vector $\mathbf{X} = X_A \mathbf{E}_A$. Here $\mathbf{E}_A$ defines a Cartesian basis in the reference configuration with origin $\mathbf{O}$. Therefore (5.4) can be written in components:

$$x_i = \varphi_i(X_A, t) . \tag{5.5}$$

In the following, when the indices are in capital letters they will denote components of vectors and tensors refering to the basis $\mathbf{E}_A$ of the reference configuration. X_A are the Lagrange coordinates of the particle X. Lower case letters are used for indices which refer to the basis $\mathbf{e}_i$ of the spatial or current configuration. The quantities x_i denote the spatial coordinates of X. To simplify notation, a Cartesian basis is employed. This coincides with the finite element method, since isoparametric interpolations are always defined in a Cartesian basis. The change to arbitrary curvilinear coordinates is a purely technical matter.

5.2.2 Material and Spatial Descriptions

In finite deformation analysis a careful distinction has to be made between the coordinate systems that can be chosen to describe the behavior of the body whose motion is under consideration. The so-called material description is a characterization of the motion (or any other quantity) with respect to the material coordinates (X_1, X_2, X_3) and time t, given by (5.2). In the material description, attention is paid to a particle, and what appends to the particle as it moves is observed. Traditionally the material description is often referred to as the Lagrangian description.

The so-called Eulerian (or spatial) description is a characterization of the motion (or any other quantity) with respect to the spatial coordinates (x_1, x_2, x_3) and time t, given by (5.4). In the spatial description attention is paid to a point in space, and what appends to that point as time changes is studied.

Fluid mechanicians almost exclusively work in terms of a spatial description because it is not appropriate to describe the behavior of a material particle in, for example, a steady-state flow situation.

In solid mechanics, material descriptions are most popular. Their attractiveness stems from the ease with which they handle complicated boundaries and their ability to follow material points, so that history dependent materials can be treated accurately. In the development of Lagrangian finite elements, two approaches are commonly taken:

- formulations in terms of the Lagrangian measures of stress and strain in which derivatives and integrals are taken with respect to the Lagrangian (material) coordinates $\mathbf{X}$, called total Lagrangian formulations.

- formulations expressed in terms of Eulerian measures of stress and strain in which derivatives and integrals are taken with respect to the Eulerian (spatial) coordinates $\mathbf{x}$, often called updated Lagrangian formulations.

Although the total and updated Lagrangian formulations are superficially quite different, it will be shown that the underlying mechanics of the two formulations is identical; furthermore, expressions in the total Lagrangian formulation can be transformed to updated Lagrangian expressions and vice versa. The major difference between the two formulations is in the point of view: the total Lagrangian formulation refers quantities to the original configuration, the updated Lagrangian formulation to the current configuration, often called the deformed configuration. There are also differences in the stress and deformation measures which are typically used in these two formulations. For example, the total Lagrangian formulation customarily uses a total measure of strain, whereas the updated Lagrangian formulation often uses a rate measure of strain. However these are not inherent characteristics

of the formulations, for it is possible to use total measures of strain in updated Lagrangian formulations, and rate measures in total Lagrangian formulation.

From the theoretical standpoint, there is no difference whether the equations refer to the current or the reference configuration of the body. When formulating numerical methods for continua, considerable differences in efficiency can occur when the equations are related to either the spatial or the reference configuration. Thus, strain measures with respect to both configurations will defined. On the following presentation, small letters will denote tensors which refer to the current configuration $\boldsymbol{\varphi}(\mathcal{B})$, and capital letters will denote tensors which refer to the reference configuration $\mathcal{B}$.

5.2.3 Deformation Gradient

The deformation gradient $\mathbf{F}$ is a key quantity in finite deformation analysis. It is involved in all equations relating quantities before deformation to corresponding quantities after (or during) deformation. The deformation gradient tensor allows to describe the relative spatial position of two neighboring particles after deformation in terms of their relative material position before deformation. The deformation gradient is central to the description of deformation and and therefor central to the description of strain [Lai et al., 1993].

The deformation gradient $\mathbf{F}$ maps elemental vectors of the reference configuration to elemental vectors in the spatial configuration. It is a tensor which associates to a material line element $d\mathbf{X}$ in $\mathcal{B}$ the spatial line element $d\mathbf{x}$ in $\boldsymbol{\varphi}(\mathcal{B})$:

$$d\mathbf{x} = \mathbf{F}\, d\mathbf{X}. \tag{5.6}$$

The different components of the deformation gradient follow from the direct notation $\mathbf{F} = \partial\mathbf{x}/\partial\mathbf{X}$ as partial derivatives $\partial x_i/\partial X_A = x_{i,A}$. Using (5.4) and (5.5) it is possible to obtain

$$\mathbf{F} = \operatorname{Grad}\boldsymbol{\varphi}(\mathbf{X}, t) = F_{iA}\,\mathbf{e}_i \otimes \mathbf{E}_A = \frac{\partial x_i}{\partial X_A}\,\mathbf{e}_i \otimes \mathbf{E}_A. \tag{5.7}$$

Since the gradient (5.7) is a linear operator, the local transformation (5.6) is also linear. To preserve the continuous structure in $\mathcal{B}$ during the deformation, the mapping (5.6) has to be one-to-one, which is equivalent to say that $\mathbf{F}$ cannot be singular. This is equivalent to the condition

$$J = \det\mathbf{F} \neq 0, \tag{5.8}$$

where J defines the Jacobian determinant. In order to exclude self-penetration of the body, and the disappearing of mass, J has to be greater than 0. If $\mathbf{F}$ cannot be

singular, it means its inverse exists, which is denoted by $\mathbf{F}^{-1}$. With this it is now possible to invert equation (5.6):

$$d\mathbf{X} = \mathbf{F}^{-1} d\mathbf{x}. \tag{5.9}$$

The inverse of the deformation gradient has the following form:

$$\mathbf{F}^{-1} = (F_{iA})^{-1}\, \mathbf{E}_A \otimes \mathbf{e}_i \qquad \text{with} \qquad (F_{iA})^{-1} = \left(\frac{\partial x_i}{\partial X_A} \right)^{-1} = \frac{\partial X_A}{\partial x_i}, \tag{5.10}$$

were $\mathbf{X} = \boldsymbol{\varphi}^{-1}(\mathbf{x})$.

Once the deformation gradient $\mathbf{F}$ is known, transformations of area and volume elements between $\mathcal{B}$ and $\boldsymbol{\varphi}(\mathcal{B})$ can be obtained. The transformation of area elements between $\mathcal{B}$ and $\boldsymbol{\varphi}(\mathcal{B})$ is given by [Ogden, 1984]:

$$d\mathbf{a} = \mathbf{n}\, da = J\, \mathbf{F}^{-T} \mathbf{N} dA = J\, \mathbf{F}^{-T} d\mathbf{A}. \tag{5.11}$$

In this equation $\mathbf{n}$ is the normal to the surface of $\boldsymbol{\varphi}(\mathcal{B})$ and $\mathbf{N}$ denotes the normal

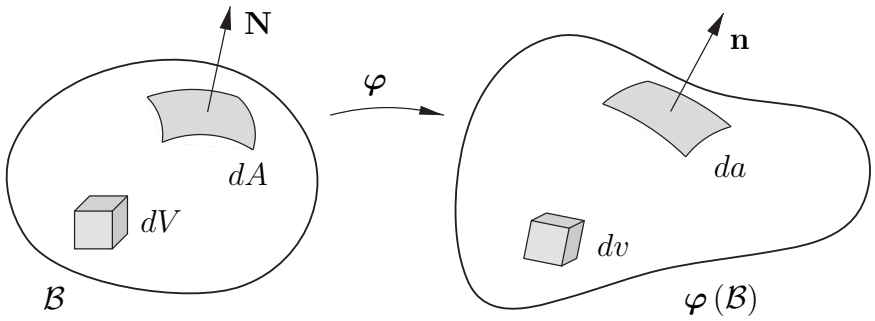

Figure 5.2: Transformation between area and volume elements.

to the surface of $\mathcal{B}$ (see Figure 5.2). J is the Jacobi determinant defined in (5.8), dA is the surface element in the reference configuration and da the surface element in the spatial configuration. For the transformation of volume elements from the reference to the spatial configuration, it is possible to obtain

$$dv = J dV. \tag{5.12}$$

With the introduction of a displacement vector $\mathbf{u}(\mathbf{X}, t)$ as the difference in position vectors of a point in the reference and current configurations,

$$\mathbf{u}(\mathbf{X}, t) = \boldsymbol{\varphi}(\mathbf{X}, t) - \mathbf{X} \tag{5.13}$$

it is possible to write the deformation gradient (5.7) as

$$\mathbf{F} = \operatorname{Grad}[\mathbf{X} + \mathbf{u}(\mathbf{X}, t)] = \mathbf{1} + \operatorname{Grad} \mathbf{u} = \mathbf{1} + \mathbf{H}, \tag{5.14}$$

where $\mathbf{H} = \operatorname{Grad} \mathbf{u}$ is the displacement gradient with respect to $\mathbf{X}$.

5.2.4 Strain measures

Section 5.2.3 presents the deformation gradient as the fundamental kinematic (second-order) tensor in finite deformation kinematics that characterizes changes of material elements during motion. The aim of this section is to determine these changes in the form of (second-order) strain tensors related either to the reference or current configuration.

In this section the most common definitions of strain tensors established in non-linear continuum mechanics are presented.

As a general measure of deformation, consider the change in the scalar product of two elemental vectors $d\mathbf{X}_1$ and $d\mathbf{X}_2$ as they deform to $d\mathbf{x}_1$ and $d\mathbf{x}_2$. This change will involve both the stretching (that is, change in length) and changes in the enclosed angle between the two vectors. Recalling (5.6), the spatial scalar product $d\mathbf{x}_1 \cdot d\mathbf{x}_2$ can be found in terms of the material vectors $d\mathbf{X}_1$ and $d\mathbf{X}_2$ as,

$$d\mathbf{x}_1 \cdot d\mathbf{x}_2 = d\mathbf{X}_1 \cdot \mathbf{C}\, d\mathbf{X}_2 \tag{5.15}$$

where $\mathbf{C}$ is the right Cauchy-Green deformation tensor, which is given in terms of the deformation gradient as $\mathbf{F}$ as,

$$\mathbf{C} = \mathbf{F}^T \mathbf{F} \tag{5.16}$$

Note that in (5.15) the tensor $\mathbf{C}$ operates on the material vectors $d\mathbf{X}_1$ and $d\mathbf{X}_2$ and consequently $\mathbf{C}$ is called a material tensor quantity. Also note that this strain measure is not zero at the initial state, were $\mathbf{F} = \mathbf{1} \Rightarrow \mathbf{C} = \mathbf{1}$ is obtained.

Alternatively the initial material scalar product $d\mathbf{X}_1 \cdot d\mathbf{X}_2$ can be obtained in terms of the spatial vectors $d\mathbf{x}_1$ and $d\mathbf{x}_2$ via the left Cauchy-Green or Finger deformation tensor $\mathbf{b}$ as,

$$d\mathbf{X}_1 \cdot d\mathbf{X}_2 = d\mathbf{x}_1 \cdot \mathbf{b}^{-1} d\mathbf{x}_2 \tag{5.17}$$

where $\mathbf{b}$ is,

$$\mathbf{b} = \mathbf{F}\, \mathbf{F}^T \tag{5.18}$$

Observe that in (5.17) the tensor $\mathbf{b}^{-1}$ operates on the spatial vectors $d\mathbf{x}_1$ and $d\mathbf{x}_2$, and consequently $\mathbf{b}^{-1}$, or indeed $\mathbf{b}$ itself, is a spatial tensor quantity.

The change in scalar product can now be found in terms of the material vectors $d\mathbf{X}_1$ and $d\mathbf{X}_2$ as

$$\frac{1}{2}\left(d\mathbf{x}_1 \cdot d\mathbf{x}_2 - d\mathbf{X}_1 \cdot d\mathbf{X}_2\right) = d\mathbf{X}_1 \cdot \mathbf{E}\, d\mathbf{X}_2 \tag{5.19}$$

where the material tensor $\mathbf{E}$ is the Green-Lagrange strain tensor,

$$\mathbf{E} = \frac{1}{2}\left(\mathbf{F}^T\mathbf{F} - \mathbf{1}\right) = \frac{1}{2}\left(\mathbf{C} - \mathbf{1}\right), \qquad E_{AB} = \frac{1}{2}\left(F_{iA}F_{iB} - \delta_{AB}\right). \tag{5.20}$$

Note that contrary to the Cauchy-Green deformation tensor, the Green-Lagrange deformation tensor is zero for the initial, undeformed configuration.

The same change in the scalar product can be expressed with reference to the spatial elemental vectors $d\mathbf{X}_1$ and $d\mathbf{X}_2$ and the Eulerian or Almansi strain tensor $\mathbf{e}$ as,

$$\frac{1}{2}\left(d\mathbf{x}_1 \cdot d\mathbf{x}_2 - d\mathbf{X}_1 \cdot d\mathbf{X}_2\right) = d\mathbf{x}_1 \cdot \mathbf{e}\, d\mathbf{x}_2 \tag{5.21}$$

where the spatial tensor $\mathbf{e}$ is,

$$\mathbf{e} = \frac{1}{2}\left(\mathbf{1} - \mathbf{b}^{-1}\right). \tag{5.22}$$

The Almansi strain tensor is connected to the Green-Lagrange strain tensor via the following transformation:

$$\mathbf{E} = \mathbf{F}^T \mathbf{e}\, \mathbf{F}, \tag{5.23}$$

which can easily be verified with (5.22).

5.2.5 Transformation of vectors and tensors

Once the transformation between differential elements in the reference and current configuration is known, it is now possible to transform vectors or tensors from the reference to the current configuration, and vice versa. This stems from the fact that the base vectors can be viewed as differential line elements.

If a quantity from the current configuration is transformed to the initial configuration, this transformation is called a *pull back* operation, see for example [Marsden and Hughes, 1983]. A transformation in the other direction is considered as a *push forward* operation.

For the gradient of a scalar field $G(\mathbf{X}) = g(\mathbf{x}) = g[\boldsymbol{\varphi}(\mathbf{X})]$, the following is obtained

$$\operatorname{Grad} G = \mathbf{F}^T \operatorname{grad} g \quad \Longleftrightarrow \quad \frac{\partial G}{\partial X_A} = \frac{\partial g}{\partial x_i}\frac{\partial x_i}{\partial X_A}, \tag{5.24}$$

$$\operatorname{grad} g = \mathbf{F}^{-T} \operatorname{Grad} G. \tag{5.25}$$

In a similar way, for the gradient of a vector field $\mathbf{W}(\mathbf{X}) = \mathbf{w}(\mathbf{x}) = \mathbf{w}[\boldsymbol{\varphi}(\mathbf{X})]$ the following is obtained

$$\operatorname{Grad} \mathbf{W} = \operatorname{grad} \mathbf{w}\, \mathbf{F} \quad \Longleftrightarrow \quad \operatorname{grad} \mathbf{w} = \operatorname{Grad} \mathbf{W}\, \mathbf{F}^{-1}. \tag{5.26}$$

Applying these results to the computation of the deformation gradient in terms of the displacement field $\mathbf{u}[\boldsymbol{\varphi}(\mathbf{X})]$ and using (5.14) and (5.26), it is possible to

obtain

$$\begin{aligned} \mathbf{F} &= \mathbf{1} + \operatorname{Grad}\mathbf{u}, \\ \mathbf{1} &= \mathbf{F}^{-1} + \operatorname{Grad}\mathbf{u}\,\mathbf{F}^{-1}, \\ \Longrightarrow \mathbf{F}^{-1} &= \mathbf{1} - \operatorname{grad}\mathbf{u}. \end{aligned} \tag{5.27}$$

Thus the inverse of the deformation gradient can be computed from the displacements that refers to the current configuration.

5.2.6 Distortional Component of the Deformation Gradient

When dealing with incompressible and nearly incompressible materials it is necessary to separate the volumetric from the distortional (or isochoric) components of the deformation. Such a separation must ensure that the distortional component, namely $\bar{\mathbf{F}}$, does not imply any change in volume. Noting that the determinant of the deformation gradient gives the volume ratio, the determinant of $\bar{\mathbf{F}}$ must therefore satisfy [Bonet and Wood, 1997],

$$\det \bar{\mathbf{F}} = 1 \tag{5.28}$$

This condition can be achieved by choosing $\bar{\mathbf{F}}$ as

$$\bar{\mathbf{F}} = J^{-\frac{1}{3}}\,\mathbf{F} \tag{5.29}$$

The deformation gradient $\mathbf{F}$ can now be expressed in terms of the volumetric and distortional components, J and , $\bar{\mathbf{F}}$ respectively, as,

$$\mathbf{F} = J^{\frac{1}{3}}\,\bar{\mathbf{F}} \tag{5.30}$$

Similar decompositions can be obtained for other strain-based tensors such as the right Cauchy-Green deformation tensor $\mathbf{C}$ by defining its distortional component $\bar{\mathbf{C}}$ as,

$$\bar{\mathbf{C}} = \bar{\mathbf{F}}^T\,\bar{\mathbf{F}} \tag{5.31}$$

Substituting for $\bar{\mathbf{F}}$ from Equation (5.29) gives an alternative expression for $\bar{\mathbf{C}}$ as,

$$\bar{\mathbf{C}} = (\det \mathbf{C})^{-\frac{1}{3}}\,\mathbf{C}; \qquad \det \mathbf{C} = J^2 \tag{5.32}$$

5.2.7 Time derivatives

Many nonlinear processes are time-dependent and as a consequence it is necessary to consider velocity and material time derivatives of various quantities. However, even if the process is not rate-dependant it is nevertheless convenient to establish

the equilibrium equations in terms of virtual velocities and associated virtual time-dependant quantities.

The time derivative of the deformation gradient $\mathbf{F}$, is defined as

$$\dot{\mathbf{F}} = \operatorname{Grad} \dot{\boldsymbol{\varphi}}\,(\mathbf{X}, t) = \operatorname{Grad} \mathbf{v} = \operatorname{grad} \hat{\mathbf{v}}\, \mathbf{F}. \tag{5.33}$$

The spatial velocity gradient ($\operatorname{grad} \hat{\mathbf{v}}$) in (5.33) is often described by $\mathbf{l}$. With (5.33) it is possible to define the spatial velocity gradient as:

$$\mathbf{l} = \dot{\mathbf{F}}\, \mathbf{F}^{-1} \tag{5.34}$$

Using Equation (5.33) to compute the time derivative of the Green-Lagrangian strain tensor (5.20) yields:

$$\dot{\mathbf{E}} = \frac{1}{2} \left(\dot{\mathbf{F}}^T \mathbf{F} + \mathbf{F}^T \dot{\mathbf{F}} \right). \tag{5.35}$$

The time derivative of $\mathbf{E}$ can be rewritten with the last relation in (5.33):

$$\dot{\mathbf{E}} = \frac{1}{2}\, \mathbf{F}^T \left(\mathbf{l} + \mathbf{l}^T \right) \mathbf{F} = \mathbf{F}^T \mathbf{d}\, \mathbf{F}. \tag{5.36}$$

This equation has a structure similar to (5.23), and hence it denotes a *pull back* of the symmetrical spatial velocity gradient

$$\mathbf{d} = \frac{1}{2} \left(\mathbf{l} + \mathbf{l}^T \right) \tag{5.37}$$

to the initial configuration.

5.3 Balance Principles

This section summarizes the partial differential equations which represent the local balance laws of continuum mechanics. More detail about the derivation of these equations can be consulted for example on the references [Malvern, 1969] or [Marsden and Hughes, 1983].

5.3.1 Balance of mass

The balance of mass m of a body $\mathcal{B}$ is given by the following relation

$$m = \int_{\mathcal{B}} \rho_0 \, dV = \int_{\varphi(\mathcal{B})} \rho \, dv = const., \tag{5.38}$$

where ρ_0 is the density in the initial configuration and ρ the density in the current configuration. Within the Lagrange description of motion, it can be concluded,

assuming sufficient smoothness, that $\rho_0 = J\rho$. This equation yields a relation between the volume element in the initial and current configuration

$$dv = \frac{\rho_0}{\rho}\, dV = J\, dV. \tag{5.39}$$

5.3.2 Balance of momentum

Equation (5.40) defines the local balance of momentum with respect to a volume element in the current configuration $\boldsymbol{\varphi}(\mathcal{B})$,

$$\operatorname{div} \boldsymbol{\sigma} + \rho\, \bar{\mathbf{b}} = \rho\, \dot{\mathbf{v}}, \qquad \sigma_{ik,i} + \rho\, \bar{b}_k = \rho\, \dot{v}_k. \tag{5.40}$$

In this equation $\boldsymbol{\sigma}$ denotes the Cauchy stress tensor. In (5.40) $\rho\, \bar{\mathbf{b}}$ defines the volume or body force (e.g. due to gravitation) and $\rho\, \dot{\mathbf{v}}$ is the inertia force term, which can be neglected in the case of a static analysis. Furthermore, the Cauchy theorem, which relates the stress vector $\mathbf{t}$ to the surface normal vector $\mathbf{n}$ is defined as

$$\mathbf{t} = \boldsymbol{\sigma}^T\, \mathbf{n}, \qquad t_i = \sigma_{ik} n_i, \qquad \left\{ \begin{array}{c} t_1 \\ t_2 \\ t_3 \end{array} \right\} = \left[\begin{array}{ccc} \sigma_{11} & \sigma_{12} & \sigma_{13} \\ \sigma_{21} & \sigma_{22} & \sigma_{23} \\ \sigma_{31} & \sigma_{32} & \sigma_{33} \end{array} \right] \left\{ \begin{array}{c} n_1 \\ n_2 \\ n_3 \end{array} \right\}. \tag{5.41}$$

Equation (5.41) is stated here in direct notation, index and matrix notation.

The local balance of angular of momentum in the absence of micropolar stresses, which is usually the case in non-magnetic materials [Truesdell and Toupin, 1960], yields the following important result

$$\boldsymbol{\sigma} = \boldsymbol{\sigma}^T, \qquad \sigma_{ik} = \sigma_{ki}, \tag{5.42}$$

which dictates the symmetry of the Cauchy stress tensor.

5.3.3 Transformation to the initial configuration, different stress tensors

The equations for the local balance of moment (5.40) and (5.42) refer to the current configuration. When a formulation of these equations related to the initial configuration $\mathcal{B}$ is needed, it is necessary to apply a *pull back* transformation. For this transformation, more stress tensors are defined, which follow from the equivalence of a force which is defined in $\mathcal{B}$ and $\boldsymbol{\varphi}(\mathcal{B})$:

$$\int_{\varphi(\partial\mathcal{B})} \boldsymbol{\sigma}\, \mathbf{n}\, da = \int_{\partial\mathcal{B}} \boldsymbol{\sigma}\, J\, \mathbf{F}^{-T} \mathbf{N}\, dA = \int_{\partial\mathcal{B}} \mathbf{P}\, \mathbf{N}\, dA. \tag{5.43}$$

Equation (5.43) defines the first Piola-Kirchhoff stress tensor $\mathbf{P}$. The transformation between the Cauchy stress tensor and the first Piola-Kirchhoff stress tensor $\mathbf{P}$ is defined as

$$\mathbf{P} = J\,\boldsymbol{\sigma}\,\mathbf{F}^{-T} \qquad P_{Ak} = J\,\sigma_{ik}\,(F_{iA})^{-1}\,. \tag{5.44}$$

The first Piola-Kirchhoff stresses are the actual stresses in terms of the area of the initial configuration. Since in equation (5.44) the spatial quantity $\boldsymbol{\sigma}$ is only multiplied on one side by $\mathbf{F}$, $\mathbf{P}$ it is a so-called *two field tensor* where one base vector lies in $\mathcal{B}$ and the other in $\boldsymbol{\varphi}\,(\mathcal{B})$. After some manipulation, it is possible to transform the local balance of momentum (5.40) to the reference configuration

$$\mathrm{Div}\,\mathbf{P} + \rho_0\,\bar{\mathbf{b}} = \rho_0\,\dot{\mathbf{v}} \tag{5.45}$$

However, when using (5.44) in the balance of angular of momentum (5.42), it can be seen that the Piola-Kirchhoff stress tensor in general is a nonsymmetric tensor: $\mathbf{P}\,\mathbf{F}^T = \mathbf{F}\,\mathbf{P}^T$.

Another stress tensor, defined in relation to the reference configuration is the second Piola-Kirchhoff stress tensor, a symmetric stress tensor, which follows from the complete *pull back* of the Cauchy stress tensor to the reference configuration $\mathcal{B}$, as shown in the following equation:

$$\begin{aligned} \mathbf{S} = \mathbf{F}^{-1}\mathbf{P} = J\,\mathbf{F}^{-1}\boldsymbol{\sigma}\,\mathbf{F}^{-T}, \\ S_{AB} = (F_{Ai})^{-1}\,P_{Bi} = J\,(F_{Ai})^{-1}\,\sigma_{ik}\,(F_{kB})^{-1}\,. \end{aligned} \tag{5.46}$$

The second Piola-Kirchhoff stress tensor $\mathbf{S}$ does not represent an experimentally measurable stress. However, it is an essential stress measure that plays a prominent role in the constitutive theory. It is "work conjugated" (duality paired) with the Green-Lagrangian strain tensor (5.20).

On the current configuration, besides the Cauchy stress tensor $\boldsymbol{\sigma}$, the Kirchhoff stress tensor $\boldsymbol{\tau}$ is often employed, which is defined as the *push forward* of the second Piola-Kirchhoff stress tensor $\mathbf{S}$ to the current configuration

$$\boldsymbol{\tau} = \mathbf{F}\,\mathbf{S}\,\mathbf{F}^T, \qquad \boldsymbol{\tau} = J\,\boldsymbol{\sigma}. \tag{5.47}$$

5.4 Weak Form of Balance of Momentum, Variational Principles

This section presents the variational formulation used for solving the boundary value problems stemming from the continuum mechanics. Numerical methods, based on variational formulations are used to obtain the solution to the problems.

5.4.1 Weak form of balance of momentum in the initial configuration

The principle of virtual work, also called the weak form of equilibrium, due to its reduced regularity requirements, is an equivalent formulation of the balance of momentum, presented on (5.40) in the current configuration and on (5.45) on the reference configuration. Since no constitutive equations enter *a priori* on the expression for the weak form, it is valid for all problem classes, including plasticity, hyperelasticity or non-conservative loading. The derivation of the weak form starts from the local equilibrium equation $\left(\operatorname{Div}\mathbf{P} + \rho_0\,\bar{\mathbf{b}} = \rho_0\,\dot{\mathbf{v}}\right)$, written on the reference configuration, which is then multiplied by a vector valued function $\boldsymbol{\eta} = \{\boldsymbol{\eta}\,|\,\boldsymbol{\eta} = \mathbf{0} \text{ on } \partial\mathcal{B}_u\}$, also called a virtual displacement or test function. Integrating over the volume of the body under consideration yields the following result

$$\int_{\mathcal{B}} \operatorname{Div}\mathbf{P}\cdot\boldsymbol{\eta}\,dV + \int_{\mathcal{B}} \rho_0\left(\bar{\mathbf{b}} - \dot{\mathbf{v}}\right)\cdot\boldsymbol{\eta}\,dV = 0. \tag{5.48}$$

Using a partial integration scheme on the first term of (5.48) and using the divergence theorem leads, with the boundary conditions, to the following weak form

$$G\left(\boldsymbol{\varphi},\boldsymbol{\eta}\right) = \int_{\mathcal{B}} \mathbf{P}\cdot\operatorname{Grad}\boldsymbol{\eta}\,dV - \int_{\mathcal{B}} \rho_0\left(\bar{\mathbf{b}} - \dot{\mathbf{v}}\right)\cdot\boldsymbol{\eta}\,dV - \int_{\partial\mathcal{B}_\sigma} \bar{\mathbf{t}}\cdot\boldsymbol{\eta}\,dA = 0. \tag{5.49}$$

In the previous expression, the gradient of $\boldsymbol{\eta}$ can also be viewed as a virtual variation $\delta\mathbf{F}$ of the deformation gradient

$$\delta\mathbf{F} = \frac{\partial}{\partial\epsilon}\left[\mathbf{F}\left(\mathbf{x} + \epsilon\,\boldsymbol{\eta}\right)\right]\Big|_{\epsilon=0}. \tag{5.50}$$

In (5.49) it is possible to exchange the first Piola-Kirchhoff stress tensor $\mathbf{P}$ with the second Piola-Kirchhoff stress tensor $\mathbf{S}$, by using the following modification

$$\mathbf{P}\cdot\operatorname{Grad}\boldsymbol{\eta} = \mathbf{S}\cdot\mathbf{F}^T\operatorname{Grad}\boldsymbol{\eta} = \mathbf{S}\cdot\frac{1}{2}\left(\mathbf{F}^T\operatorname{Grad}\boldsymbol{\eta} + \operatorname{Grad}^T\boldsymbol{\eta}\,\mathbf{F}\right) = \mathbf{S}\cdot\delta\mathbf{E}, \tag{5.51}$$

where the variation of the Green-Lagrangian strain tensor, computed according to (5.35), has been used. Note that $\delta\mathbf{E} = \frac{1}{2}\,\delta\mathbf{C}$. In (5.51) one makes use of the symmetry of $\mathbf{S}$ so that the antisymmetric part of $\mathbf{F}^T\operatorname{Grad}\boldsymbol{\eta}$ disappears in the scalar product. Using the modification presented in (5.51) it is possible to rewrite (5.49) as

$$G\left(\boldsymbol{\varphi},\boldsymbol{\eta}\right) = \int_{\mathcal{B}} \mathbf{S}\cdot\delta\mathbf{E}\,dV - \int_{\mathcal{B}} \rho_0\left(\bar{\mathbf{b}} - \dot{\mathbf{v}}\right)\cdot\boldsymbol{\eta}\,dV - \int_{\partial\mathcal{B}_\sigma} \bar{\mathbf{t}}\cdot\boldsymbol{\eta}\,dA = 0. \tag{5.52}$$

In Equation (5.52), the first term denotes the virtual internal work or the stress divergence, and the last two terms contain the virtual work of the external forces. This equation can be written in index notation as follows:

$$G(\boldsymbol{\varphi}, \boldsymbol{\eta}) = \int_{\mathcal{B}} S_{AB}\, \delta E_{AB}\, dV - \int_{\mathcal{B}} \rho_0 \left(\bar{b}_A - \dot{v}_A\right) \eta_A\, dV - \int_{\partial \mathcal{B}_\sigma} \bar{t}_A\, \eta_A\, dA = 0. \tag{5.53}$$

Providing that the solution is smooth enough, the strong form, described by (5.45), and the weak form, descrybed by (5.52), are equivalent.

5.4.2 Spatial form of the weak formulation

Previous section presented the weak form of equilibrium (5.49) written on the reference, or material configuration. The transformation of the weak form to the current configuration is achieved by using only pure geometrical operations. In order to write the weak form of equilibrium in the current configuration $\boldsymbol{\varphi}(\mathcal{B})$, it is necessary to transform the associated tensors by *push forward* operations. With the transformation of the first Piola-Kirchhoff stress tensor to the Cauchy stress tensor, as shown in (5.44), $\boldsymbol{\sigma} = \frac{1}{J}\, \mathbf{P}\, \mathbf{F}^T$, and by using (5.26) it is possible to derive

$$\mathbf{P} \cdot \operatorname{Grad} \boldsymbol{\eta} = J\, \boldsymbol{\sigma}\, \mathbf{F}^{-T} \cdot \operatorname{Grad} \boldsymbol{\eta} = J\, \boldsymbol{\sigma} \cdot \operatorname{Grad} \boldsymbol{\eta}\, \mathbf{F}^{-1} = J\, \boldsymbol{\sigma} \cdot \operatorname{grad} \boldsymbol{\eta}. \tag{5.54}$$

Furthermore, as $dv = J\, dV$ and therefor $\rho = \rho_0\, J$ is valid, it is possible to transform the weak form (5.49) into the current configuration:

$$g(\boldsymbol{\varphi}, \boldsymbol{\eta}) = \int_{\varphi(\mathcal{B})} \boldsymbol{\sigma} \cdot \operatorname{grad} \boldsymbol{\eta}\, dv - \int_{\varphi(\mathcal{B})} \rho \left(\bar{\mathbf{b}} - \dot{\mathbf{v}}\right) \cdot \boldsymbol{\eta}\, dv - \int_{\varphi(\partial \mathcal{B}_\sigma)} \bar{\mathbf{t}} \cdot \boldsymbol{\eta}\, da = 0. \tag{5.55}$$

In this equation, the result from (5.43) which shows the equivalence of a force defined in $\mathcal{B}$ and $\boldsymbol{\varphi}(\mathcal{B})$ is used to transform the stress vector $\bar{\mathbf{t}}$ into $\varphi(\mathcal{B})$. Using the symmetry of the Cauchy stress tensor enables to replace the spatial gradient of $\boldsymbol{\eta}$ by its symmetric part. Hence, with the definition

$$\nabla^S \boldsymbol{\eta} = \frac{1}{2} \left(\operatorname{grad} \boldsymbol{\eta} + \operatorname{grad}^T \boldsymbol{\eta}\right), \tag{5.56}$$

it follows that

$$g(\boldsymbol{\varphi}, \boldsymbol{\eta}) = \int_{\varphi(\mathcal{B})} \boldsymbol{\sigma} \cdot \nabla^S \boldsymbol{\eta}\, dv - \int_{\varphi(\mathcal{B})} \rho \left(\bar{\mathbf{b}} - \dot{\mathbf{v}}\right) \cdot \boldsymbol{\eta}\, dv - \int_{\varphi(\partial \mathcal{B}_\sigma)} \bar{\mathbf{t}} \cdot \boldsymbol{\eta}\, da = 0. \tag{5.57}$$

The expression for the weak form of equilibrium in the spatial configuration (5.57) has exactly the same structure as the principle of virtual work in the geometrically linear theory. The difference, however, is that all integrals, stresses and gradients have to be computed with respect to the current coordinates, which reflects the nonlinearity of (5.57) [Wriggers, 2006].

5.4.3 Minimum of total potential energy

When dealing with hyperelastic materials, a strain energy function W (see Section 5.5.1) describes the elastic energy stored in a body $\mathcal{B}$. Based on this function, the classical minimum principle of the total elastic potential can be formulated. For this the potential energy of the forces applied also have to be considered. Assuming that these forces are conservative (meaning they are path-independent) and neglecting dynamical effects, the following expression is obtained

$$\Pi\left(\boldsymbol{\varphi}\right) = \int\limits_{\mathcal{B}} \left[W\left(\mathbf{C}\right) - \rho_0\, \bar{\mathbf{b}} \cdot \boldsymbol{\varphi}\right]\, dV - \int\limits_{\partial\mathcal{B}_\sigma} \bar{\mathbf{t}} \cdot \boldsymbol{\varphi}\, dA \Longrightarrow MIN. \tag{5.58}$$

From all the possible deformation states $\boldsymbol{\varphi}$ the one that minimizes Π is the solution for the problem. The minimum can be computed by a variation of (5.58). It is related to the weak form (5.52) which can be shown by applying the directional derivative, leading to the first variation of Π:

$$\begin{aligned} \delta\Pi &= D\Pi\left(\boldsymbol{\varphi}\right) \cdot \boldsymbol{\eta} \\ &= \frac{d}{d\alpha}\, \Pi\, \left(\boldsymbol{\varphi} + \alpha\, \boldsymbol{\eta}\right)\Big|_{\alpha=0}. \end{aligned} \tag{5.59}$$

Writing the first variation of Π in explicit form one obtains

$$D\Pi\left(\boldsymbol{\varphi}\right) \cdot \boldsymbol{\eta} = \int\limits_{\mathcal{B}} \left[\frac{\partial W}{\partial \mathbf{C}} \cdot \delta\mathbf{C} - \rho_0 \bar{\mathbf{b}} \cdot \boldsymbol{\eta}\right]\, dV - \int\limits_{\partial\mathcal{B}_\sigma} \bar{\mathbf{t}} \cdot \boldsymbol{\eta}\, dA = G\left(\boldsymbol{\varphi}, \boldsymbol{\eta}\right) = 0. \tag{5.60}$$

The variation of the right Cauchy-Green tensor $\delta\mathbf{C}$ can easily be expressed in terms of the Green-Lagrange strain tensor: $2\,\delta\mathbf{C} = \delta\mathbf{E}$. The partial derivative of W with respect to $\mathbf{C}$ leads, with $2\,\partial W \,/\, \partial\mathbf{C} = \mathbf{S}$, to the second Piola-Kirchhoff stress tensor, see Equation (5.61) in Section 5.5.1. Hence (5.60) is equivalent to the weak form presented in (5.52).

Studding the construction of a minimal principle is important in several aspects, since it enables investigations regarding the existence and uniqueness of solutions. Additionally, special solution methods can be developed on the basis of a minimal principle which are efficient and reliable.

5.5 Constitutive Equations

The constitutive laws that describe the material behavior for the body in study can be arbitrary, and that does not affect the main formulation of the problem. However it is clear that the physical properties of the bodies are influenced by the general

constitutive behavior. Thus, to include a nonlinear constitutive equation valid for large deformations, finite elasticity is discuss here. Of course, it is possible to consider more complicated constitutive relations which can also be of inelastic nature, but this is not the aim of this work. The works of [Desai and Siriwardane, 1984], [Lubliner, 1990], [Khan and Huang, 1995], or [Simo and Hughes, 1998] should be consulted for example for more complex constitutive behaviors.

5.5.1 Hyperelastic Materials

This section briefly presents the hyperelastic constitutive behavior, for more detailed information, for example [Ogden, 1984] should be consulted. These can be applied to describe the constitutive behavior of rubber, foam, or any other kind of soft tissues such as muscles tissues, as shown on Chapter 6. In the case of small deformations, these constitutive equations reduce to the classical Hooke's law of linear elasticity.

For a hyperelastic material, the elastic energy stored in a body $\mathcal{B}$ is characterized by a strain energy function W. For this type of materials, the constitutive equation or response function for the second Piola-Kirchhoff stress is given by the partial derivative of the strain energy W function with respect to the right Cauchy-Green tensor, for example see [Ogden, 1984] or [Holzapfel, 2000].

$$\mathbf{S} = 2\,\frac{\partial W\left(\mathbf{C},\mathbf{X}\right)}{\partial \mathbf{C}}, \qquad S_{AB} = 2\,\frac{\partial W\left(\mathbf{C},\mathbf{X}\right)}{\partial C_{AB}} \tag{5.61}$$

This response function is objective because (5.61) represents a constitutive relation which fulfils the requirements of frame indifference [Wriggers, 2006]. In the case of a homogeneous material, the strain energy W does not depend upon $\mathbf{X}$. This section only deals with homogeneous isotropic materials. Chapter 6 presents an nonisotropic hyperelastic material behavior. The hyperelastic strain energy function W can be represented by the following isotropic tensor function

$$W\left(\mathbf{C}\right) = W\left(I_C, II_C, III_C\right), \tag{5.62}$$

where I_C, II_C and III_C are the invariants of the right Cauchy-Green train tensor. Using the chain rule and (5.62), the second Piola-Kirchhoff stresses (5.61) is obtained as

$$\mathbf{S} = 2\left[\left(\frac{\partial W}{\partial I_C} + I_C\,\frac{\partial W}{\partial II_C}\right)\mathbf{1} - \frac{\partial W}{\partial II_C}\,\mathbf{C} + III_C\,\frac{\partial W}{\partial III_C}\,\mathbf{C}^{-1}\right]. \tag{5.63}$$

where $\mathbf{1}$ is the second order identity tensor. In deriving (5.63), the following results for the derivative of invariants with respect to tensors have been used:

$$\frac{\partial I_C}{\partial \mathbf{C}} = \mathbf{1}, \qquad \frac{\partial II_C}{\partial \mathbf{C}} = I_C\,\mathbf{1} - \mathbf{C}, \qquad \frac{\partial III_C}{\partial \mathbf{C}} = III_C\,\mathbf{C}^{-1}. \tag{5.64}$$

Considering a compressible Neo-Hookean material, which is characterized by one of the simplest possible hyperelastic response function, the strain energy function W, is defined as

$$W\left(I_C, J\right) = g\left(J\right) + \frac{1}{2}\,\mu\,\left(I_C - 3\right). \tag{5.65}$$

when dealing with compressible materials, the function $g\left(J\right)$ in (5.65) has to be convex and the following growth conditions must hold:

$$\lim_{J\to+\infty} g\left(J\right) = \lim_{J\to 0^+} g\left(J\right) = +\infty \tag{5.66}$$

These conditions pose energy barriers (penalties) to the unbounded growth and to the vanishing of the volume of the deformed body; in the first case the hydrostatic pressure would grow to $+\infty$ infinite and in the second case it would grow to $-\infty$. These growth conditions are satisfied when the compressible part $g\left(J\right)$ is chosen, for example as [Ciarlet, 1988]:

$$g\left(J\right) = c\left(J^2 - 1\right) - \left(d + \mu\right)\ln J \qquad \text{with} \qquad c > 0,\, d > 0. \tag{5.67}$$

The second Piola-Kirchhoff stress tensor for the Neo-Hookian material (5.65) is now obtained using (5.63), and yields

$$\begin{aligned} \mathbf{S} &= \frac{\Lambda}{2}\left(J^2 - 1\right)\mathbf{C}^{-1} + \mu\left(\mathbf{1} - \mathbf{C}^{-1}\right), \\ S_{AB} &= \frac{\Lambda}{2}\left(J^2 - 1\right)\left(C_{AB}\right)^{-1} + \mu\left[\delta_{AB} - \left(C_{AB}\right)^{-1}\right], \end{aligned} \tag{5.68}$$

where the constants c and d have been chosen as $c = \Lambda\,/\,4$ and $d = \Lambda\,/\,2$. The material constants Λ and μ are the Lamé constants, which have to be determined by experiments.

Using the definition (5.47) and (5.61), the Kirchhoff stress can be written in terms of quantities defined in the initial configuration:

$$\boldsymbol{\tau} = 2\,\mathbf{F}\,\frac{\partial W\left(\mathbf{C}\right)}{\partial \mathbf{C}}\,\mathbf{F}^T, \qquad \tau_{ik} = 2F_{iA}\frac{\partial W\left(\mathbf{C}\right)}{\partial C_{AB}}F_{kB}. \tag{5.69}$$

Using definition (5.63), the Kirchhoff stress is obtained by the following expression

$$\boldsymbol{\tau} = 2\left[\left(\frac{\partial W}{\partial I_C} + I_C\,\frac{\partial W}{\partial II_C}\right)\mathbf{F}\,\mathbf{F}^T - \frac{\partial W}{\partial II_C}\,\mathbf{F}\,\mathbf{C}\,\mathbf{F}^T + III_C\,\frac{\partial W}{\partial III_C}\,\mathbf{F}\,\mathbf{C}^{-1}\mathbf{F}^T\right]. \tag{5.70}$$

Taking into consideration that the invariants of $\mathbf{C}$ and $\mathbf{b}$ are equal and using $\mathbf{F}\,\mathbf{C}^{-1}\mathbf{F}^T = \mathbf{1}$ it is possible to simplify (5.70), obtaining

$$\boldsymbol{\tau} = 2\left[\left(\frac{\partial W}{\partial I_b} + I_b\,\frac{\partial W}{\partial II_b}\right)\mathbf{b} - \frac{\partial W}{\partial II_b}\,\mathbf{b}^2 + III_b\,\frac{\partial W}{\partial III_b}\,\mathbf{1}\right]. \tag{5.71}$$

Comparing the expression (5.71) with (5.63) it is easy to conclude that the Kirchhoff stresses can also be derived directly in term of spatial quantities, using the following expression:

$$\boldsymbol{\tau} = 2\,\mathbf{b}\,\frac{\partial \psi\,(\mathbf{b})}{\partial \mathbf{b}}. \tag{5.72}$$

Equation (5.68) can also be transformed directly into the current configuration by the standard *push forward* operations. Noting that the Cauchy stress tensor is related to the second Piola-Kirchhoff stress tensor via the relation $\boldsymbol{\sigma} = J^{-1}\mathbf{F}\,\mathbf{S}\,\mathbf{F}^T$, see (5.46), it is possible to obtain, after some manipulation:

$$\boldsymbol{\sigma} = \frac{\Lambda}{2J}\left(J^2 - 1\right)\mathbf{1} + \frac{\mu}{J}\left(\mathbf{b} - \mathbf{1}\right), \tag{5.73}$$

$$\sigma_{ik} = \frac{\Lambda}{2J}\left(J^2 - 1\right)\delta_{ik} + \frac{\mu}{J}\left(b_{ik} - \delta_{ik}\right). \tag{5.74}$$

5.5.2 Incremental constitutive tensor

In order to derive the incremental constitutive tensor it is necessary to compute the rate of the response function (5.61). Differentiating the response function (5.61) with respect to time, one obtains the following

$$\dot{\mathbf{S}} = 2\,\frac{\partial^2 W}{\partial \mathbf{C}\,\partial \mathbf{C}}\,\left[\,\dot{\mathbf{C}}\,\right], \tag{5.75}$$

Equation (5.75) represents an incremental relation between the rate of the second Piola-Kirchhoff stress tensor $\mathbf{S}$ and the right Cauchy-Green tensor $\mathbf{C}$. Defining a fourth order incremental constitutive tensor in the following manner

$$\mathbb{C} = 4\,\frac{\partial^2 W}{\partial \mathbf{C}\,\partial \mathbf{C}}, \qquad \mathbb{C}_{ABCD} = 4\,\frac{\partial^2 W}{\partial C_{AB}\,\partial C_{CD}}, \tag{5.76}$$

it is possible to rewrite (5.75) in order to obtain

$$\dot{\mathbf{S}} = \frac{1}{2}\,\mathbb{C}\left[\,\dot{\mathbf{C}}\,\right], \qquad \dot{S}_{AB} = \frac{1}{2}\,\mathbb{C}_{ABCD}\,\dot{C}_{CD}. \tag{5.77}$$

The *push forward* of equation (5.77) to the current configuration is obtained with the Lie-derivative of the Kirchhoff stress tensor, obtaining

$$\left(\mathcal{L}_v\,\boldsymbol{\tau}\right)_{ik} = F_{iA}\,\dot{S}_{AB}\,F_{kB}, \tag{5.78}$$

Taking into account that the time derivative of the right Cauchy-Green tensors, see (5.20) and (5.36), is

$$\dot{C}_{CD} = 2\,F_{lC}\,d_{lm}\,F_{mD} \tag{5.79}$$

the relation (5.78) can be rewritten in the following form

$$(\mathcal{L}_v\,\boldsymbol{\tau})_{ik} = F_{iA}\,F_{lC}\,F_{mD}\,F_{kB}\,\mathbb{C}_{ABCD}\,d_{lm}. \tag{5.80}$$

where $\mathbf{d}$ is the symmetrical spatial velocity gradient, see (5.37). Equation (5.80) represents a *push forward* of $\mathbb{C}$ because each base vector of the incremental constitutive tensor $\mathbb{C}$ is transformed by $\mathbf{F}$, therefor it is possible to define a spatial incremental constitutive tensor $\mathfrak{c}$ as

$$\mathfrak{c}_{iklm} = F_{iA}\,F_{lC}\,F_{mD}\,F_{kB}\,\mathbb{C}_{ABCD}. \tag{5.81}$$

Using (5.81) it is possible to write (5.80) in the following compact form

$$(\mathcal{L}_v\,\boldsymbol{\tau})_{ik} = \mathfrak{c}_{iklm}\,d_{lm}, \qquad \mathcal{L}_v\,\boldsymbol{\tau} = \mathfrak{c}\,[\mathbf{d}\,]\,. \tag{5.82}$$

With (5.82), the incremental constitutive tensor for the constitutive equations (5.68), in the current configuration is obtained, by a *push forward* from the reference configuration. For the Neo-Hookean material (5.65), the response function (5.68) depends upon the deformation via the inverse of the right Cauchy-Green tensor and its determinant: $J = \sqrt{III_C}$. In order to obtain the computation of $\mathbb{C}$ using (5.76), the derivatives of J and $\mathbf{C}^{-1}$ with respect to $\mathbf{C}$ have to be computed.

Taking into account (5.64), the derivative of the Jacobian is

$$\frac{\partial J}{\partial \mathbf{C}} = \frac{1}{2}\,J\,\mathbf{C}^{-1} \tag{5.83}$$

The derivative of $\mathbf{C}^{-1}$ is obtained taking into account that $\frac{\partial}{\partial C_{CD}}\left[C_{AM}\,C^{-1}_{MB}\right] = 0$, as

$$\frac{C^{-1}_{AB}}{\partial C_{CD}} = -C^{-1}_{AC}\,C^{-1}_{BD}. \tag{5.84}$$

Since $\mathbf{C}$ is a symmetric tensor, it is only necessary to consider the symmetrical part of (5.84), and introduce the fourth order tensor $\mathbb{I}_{C^{-1}}$ which has the index notation

$$\mathbb{I}_{C^{-1}ABCD} = \frac{1}{2}\left(C^{-1}_{AC}\,C^{-1}_{BD} + C^{-1}_{AD}\,C^{-1}_{BC}\right). \tag{5.85}$$

Taking into account the definitions introduced, the constitutive tensor can now be derived. After some algebraic manipulations, it is possible to obtain

$$\begin{aligned} \mathbb{C} &= \Lambda\,J^2\,\mathbf{C}^{-1}\otimes\mathbf{C}^{-1} + \left[2\mu - \Lambda\left(J^2-1\right)\right]\mathbb{I}_{C^{-1}}, \\ \mathbb{C}_{ABCD} &= \Lambda\,J^2\,C^{-1}_{AB}\,C^{-1}_{CD} + \left[2\mu - \Lambda\left(J^2-1\right)\right]\mathbb{I}_{C^{-1}ABCD}. \end{aligned} \tag{5.86}$$

Making a *push forward* of the incremental constitutive tensor $\mathbb{C}$ to the current configuration, by using (5.81) and taking into account the following simplification

$$C^{-1}_{AC}\,C^{-1}_{BD} = F^{-1}_{pA}\,F^{-1}_{pC}\,F^{-1}_{qB}\,F^{-1}_{qD}\,F_{iA}\,F_{lC}\,F_{mD}\,F_{kB} = \delta_{pi}\,\delta_{pl}\,\delta_{qk}\,\delta_{qm} = \delta_{il}\,\delta_{km},$$

the incremental constitutive tensor in the current configuration $\boldsymbol{\varphi}(\mathcal{B})$ is then obtained as:

$$\begin{aligned} \mathfrak{c} &= \Lambda\, J^2\, \mathbf{1} \otimes \mathbf{1} + \left[\, 2\mu - \Lambda \left(J^2 - 1\right)\right] \mathbb{I}, \\ \mathfrak{c}_{iklm} &= \Lambda\, J^2\, \delta_{ik}\, \delta_{lm} + \left[\, 2\mu - \Lambda \left(J^2 - 1\right)\right] \mathbb{I}_{iklm}, \end{aligned} \tag{5.87}$$

where $\mathbf{1}$ is the second order unit tensor and $\mathbb{I}$ is a fourth order unit tensor. Both tensors are related to the current configuration. In index notation the tensor $\mathbb{I}$ has the following form

$$\mathbb{I}_{iklm} = \frac{1}{2}\left(\delta_{il}\, \delta_{km} + \delta_{im}\, \delta_{kl}\right). \tag{5.88}$$

A matrix representation of the incremental constitutive tensor in the current configuration (5.82) is preferred for a numerical treatment within the method of finite elements. For this purpose the components of the Lie derivative of the Kirchhoff stresses and the symmetrical spatial velocity gradient $\mathbf{d}$ are represented in vector form. The incremental constitutive tensor (5.87) is then a matrix which can be used to compute the incremental Kirchhoff stresses once $\mathbf{d}$ is known,

$$\mathcal{L}_v\, \boldsymbol{\tau} = \boldsymbol{D}\, \boldsymbol{d}. \tag{5.89}$$

For the case of the Neo-Hookean material, (5.89) can be explicitly writhen in the following form

$$\begin{Bmatrix} \mathcal{L}_v\tau_{11} \\ \mathcal{L}_v\tau_{22} \\ \mathcal{L}_v\tau_{33} \\ \mathcal{L}_v\tau_{12} \\ \mathcal{L}_v\tau_{23} \\ \mathcal{L}_v\tau_{31} \end{Bmatrix} = \begin{bmatrix} 2\mu+\Lambda & \Lambda J^2 & \Lambda J^2 & 0 & 0 & 0 \\ \Lambda J^2 & 2\mu+\Lambda & \Lambda J^2 & 0 & 0 & 0 \\ \Lambda J^2 & \Lambda J^2 & 2\mu+\Lambda & 0 & 0 & 0 \\ 0 & 0 & 0 & \alpha & 0 & 0 \\ 0 & 0 & 0 & 0 & \alpha & 0 \\ 0 & 0 & 0 & 0 & 0 & \alpha \end{bmatrix} \begin{Bmatrix} d_{11} \\ d_{22} \\ d_{33} \\ 2d_{12} \\ 2d_{23} \\ 2d_{31} \end{Bmatrix}. \tag{5.90}$$

$$\text{with } \alpha = \mu - \frac{1}{2}\,\Lambda\left(J^2 - 1\right).$$

For the implementation of the numerical procedures it is necessary to evaluate the incremental constitutive tensor in (5.86) in the undeformed state in the initial configuration. In the undeformed initial configuration, the deformation gradient $\mathbf{F}$ is equal to $\mathbf{1}$ and therefor, also $\mathbf{C}^{-1} = \mathbf{1}$ and $J = 1$. When the incremental constitutive tensor in (5.86) is evaluated at the undeformed state in the initial configuration, it is possible to obtain

$$\mathbb{C}_0 = \Lambda\, \mathbf{1} \otimes \mathbf{1} + 2\mu\, \mathbb{I}. \tag{5.91}$$

This equation also follows directly from (5.87) since for $\mathbf{F} = \mathbf{1}$ the initial and current configuration coincide. The constitutive tensor $\mathbb{C}_0$ is identical to the elasticity tensor of the geometrical linear theory of elasticity. Its matrix form is

$$\boldsymbol{\sigma} = \boldsymbol{D}_0\, \boldsymbol{\epsilon}. \tag{5.92}$$

For the case of the Neo-Hookean material, (5.92) can be explicitly writhen in the following form

$$\begin{Bmatrix} \sigma_{11} \\ \sigma_{22} \\ \sigma_{33} \\ \sigma_{12} \\ \sigma_{23} \\ \sigma_{31} \end{Bmatrix} = \begin{bmatrix} 2\mu+\Lambda & \Lambda & \Lambda & 0 & 0 & 0 \\ \Lambda & 2\mu+\Lambda & \Lambda & 0 & 0 & 0 \\ \Lambda & \Lambda & 2\mu+\Lambda & 0 & 0 & 0 \\ 0 & 0 & 0 & \mu & 0 & 0 \\ 0 & 0 & 0 & 0 & \mu & 0 \\ 0 & 0 & 0 & 0 & 0 & \mu \end{bmatrix} \begin{Bmatrix} \epsilon_{11} \\ \epsilon_{22} \\ \epsilon_{33} \\ 2\epsilon_{12} \\ 2\epsilon_{23} \\ 2\epsilon_{31} \end{Bmatrix}. \tag{5.93}$$

5.6 Linearization of the Equilibrium Equations

Nonlinearities on continuum mechanics can originate from a variety of phenomena. There are geometrical nonlinearities, nonlinearities stemming from the constitutive equations, or nonlinearities due to nonlinear boundary conditions, as in contact. In order to solve initial or boundary value problems, the The linearization of the associated mathematical models is necessary. The solution of the linearized problem is then obtained with a numerical method, like the Newton's method, a very efficient solution algorithm for nonlinear continuum problems, especially for numerical methods like the finite element method.

This section presents a mathematical tool which allows to obtain the linearizations of nonlinear continuum problems. These tools are applied to the kinematical relations, constitutive equations and to the weak forms. Mathematical details are omitted, but they can be found on the literature, see [Marsden and Hughes, 1983] for example.

In order to present the linearization process of the nonlinear continuum problems, the linearization of a simple example is presented. Consider a scalar valued function f which is continuous and has continuous first derivatives (C^1-continuity). Under this assumptions it is possible to express the function f in the neighborhood of $\bar{x}$ using a Taylor series expansion at $\bar{x}$:

$$f(\bar{x}+u) = \bar{f} + \bar{D}f \cdot u + R. \tag{5.94}$$

In equation (5.94) the following notation has been used: $\bar{f} = f(\bar{x})$ and $\bar{D}f = Df(\bar{x})$. The operator D denotes the derivative of f with respect to x and "." is in this case just a simple multiplication. In (5.94) u is an increment and the residual term $R = R(u)$ has the following property $\lim_{u\to 0}\frac{R}{|u|} \to 0$. Figure 5.3 depicts the geometrical interpretation of equation (5.94). With $\bar{x}$ being a fixed coordinate in (5.94), it becomes clear that (5.94) is a linear function in u, being u the independent variable and $\bar{D}f$, the tangent to the curve described by f at $\bar{x}$, which touches the curve in $\left(\bar{x}, \bar{f}\right)$.

$$f(u) = \bar{f} + \bar{D}f \cdot u \tag{5.95}$$

The linear part of $f(x)$ for $x = \bar{x}$, as given by (5.95), defines the linearization

$$L[f]_{x=\bar{x}} \equiv f(u). \tag{5.96}$$

The result presented for the one-dimensional case now be extended to scalar valued functions in three dimensions. For the three dimensional case, f is now a function of $(\mathbf{x})$ and the Taylor series expansion is

$$f(\bar{\mathbf{x}} + \mathbf{u}) = \bar{f} + \bar{D}f \cdot \mathbf{u} + R. \tag{5.97}$$

where $\bar{\mathbf{x}}$ represents a point in the three-dimensional space, $\mathbf{u}$ a vector with its origin in $\bar{\mathbf{x}}$ and the following definitions have been used:

$$\bar{f} = f(\bar{\mathbf{x}}) \qquad \text{and} \qquad \bar{D}f = Df(\bar{\mathbf{x}}) = \left.\frac{\partial f(\mathbf{x})}{\partial \mathbf{x}}\right|_{\mathbf{x}=\bar{\mathbf{x}}}, \tag{5.98}$$

where $\bar{D}f$ denotes the gradient vector of f at $\bar{\mathbf{x}}$. Equation (5.97) can now be rewritten as

$$f(\bar{\mathbf{x}} + \mathbf{u}) = \bar{f} + \operatorname{Grad} f(\bar{\mathbf{x}}) \cdot \mathbf{u} + R. \tag{5.99}$$

In Equation (5.99), the product "$\cdot$" is now a scalar product between two vectors.

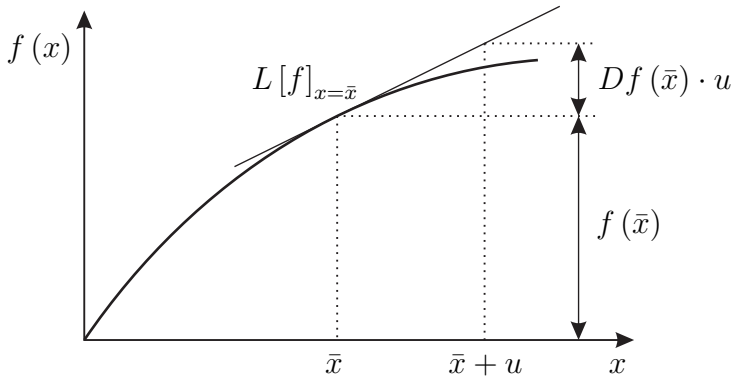

Figure 5.3: Linearization of a function $f(x)$ at $\bar{x}$.

In three dimensions, the directional derivative of f is computed at $\bar{\mathbf{x}}$ in the direction of $\mathbf{u}$. The directional derivative is defined by

$$\left.\frac{\partial}{\partial \epsilon}\left[f(\bar{\mathbf{x}} + \epsilon\,\mathbf{u})\right]\right|_{\epsilon=0}, \tag{5.100}$$

where ϵ is a scalar parameter. Here $\bar{\mathbf{x}} + \epsilon\,\mathbf{u}$ is a line in the three-dimensional space, and the directional derivative measures the increment of f in the direction of this

line in $\bar{\mathbf{x}}$. The computation of the directional derivative follows with the chain rule as

$$\frac{\partial}{\partial \epsilon}\left[f\left(\bar{\mathbf{x}}+\epsilon\,\mathbf{u}\right)\right]\Big|_{\epsilon=0} = \left[\frac{\partial f\left(\bar{\mathbf{x}}+\epsilon\,\mathbf{u}\right)}{\partial \mathbf{x}}\cdot\frac{\partial f\left(\bar{\mathbf{x}}+\epsilon\,\mathbf{u}\right)}{\partial \epsilon}\right]_{\epsilon=0} = \frac{\partial f\left(\mathbf{x}\right)}{\partial \mathbf{x}}\cdot\mathbf{u}. \tag{5.101}$$

which is equivalent to the tangent to f in $\bar{\mathbf{x}}$

$$\frac{\partial}{\partial \epsilon}\left[f\left(\bar{\mathbf{x}}+\epsilon\mathbf{u}\right)\right]\Big|_{\epsilon=0} = \bar{D}f\cdot\mathbf{u} \tag{5.102}$$

The linearization of f at $\bar{\mathbf{x}}$ is then given by the value of f and the directional derivative at $\bar{\mathbf{x}}$. The directional derivative is a linear operator, hence rules for standard derivatives like the product rule apply.

The definition of the directional derivative for functions in higher dimensional spaces is a straitforward application of the results presented. Considering the following C^1-mapping, $\mathbf{G}:\mathcal{E}\rightarrow\mathcal{F}$, where $\bar{\mathbf{x}}$ and $\mathbf{u}$ are points in the associated space:

$$\mathbf{G}\left(\bar{\mathbf{x}}+\mathbf{u}\right) = \bar{\mathbf{G}} + \bar{D}\,\mathbf{G}\cdot\mathbf{u}+\mathbf{R}. \tag{5.103}$$

Here now the "$\cdot$" is the inner product of the elements characterizing the associated space. The directional derivative is now defined as

$$\frac{d}{d\epsilon}\left[\mathbf{G}\left(\bar{\mathbf{x}}+\epsilon\,\mathbf{u}\right)\right]\Big|_{\epsilon=0} = \bar{D}\,\mathbf{G}\cdot\mathbf{u}. \tag{5.104}$$

The linear part of the mapping (5.103) at $\bar{\mathbf{x}}$ is then

$$\mathbf{L}\left[\mathbf{G}\right]_{x=\bar{x}} = \bar{\mathbf{G}} + \bar{D}\,\mathbf{G}\cdot\mathbf{u}. \tag{5.105}$$

The elements that describe the space under consideration can be scalars, vectors or tensors.

In order to simplify notation, the directional derivative $\bar{D}\,\mathbf{G}\cdot\mathbf{u}$ will also be written as $\Delta\bar{\mathbf{G}}$, were the bar denotes the evaluation of $\mathbf{G}$ at point $\bar{\mathbf{x}}$.

Tensors which refer to the current configuration are linearized by first performing a *pull back* transformation, to the reference configuration. There the linearization is computed according to the rules presented before, and then the result is transformed back to the reference configuration (*push forward* operation). Note that the *pull back* and *push forward* operations depend upon the description of the tensors, e.g. a covariant tensor has a different *pull back* than a contravariant tensor [Wriggers, 2006]. Thus for tensors $\boldsymbol{\tau}$ which refer to a covariant base (e.g. stress tensors), the directional derivative has the form

$$D\,\boldsymbol{\tau}\cdot\mathbf{u} = \mathbf{F}\left\{D\left[\mathbf{F}^{-1}\boldsymbol{\tau}\,\mathbf{F}^{-T}\right]\cdot\mathbf{u}\right\}\mathbf{F}^{T}. \tag{5.106}$$

In an analogous way, a tensor which refers to a contravariant base like a strain tensor has the directional derivative

$$D\,\mathbf{e}\cdot\mathbf{u} = \mathbf{F}^{-T}\left\{D\left[\mathbf{F}^{T}\mathbf{e}\,\mathbf{F}\right]\cdot\mathbf{u}\right\}\mathbf{F}^{-1}. \tag{5.107}$$

5.6.1 Linearization of the kinematical quantities

This section presents the linearization of the strain measures introduced previously, referring to the initial and the current configuration.

The first strain measure to be linearized is the Green-Lagrangian strain tensor (5.20), which refers to the initial configuration. Using the definition presented on (5.105), the linear part is obtained as

$$\begin{aligned} \mathbf{L}\,[\,\mathbf{E}\,]_{\varphi=\bar{\varphi}} &= \bar{\mathbf{E}} + \bar{D}\,\mathbf{E}\cdot\mathbf{u} \\ &= \bar{\mathbf{E}} + \Delta\,\bar{\mathbf{E}}, \end{aligned} \tag{5.108}$$

where the directional derivative $\bar{D}\,\mathbf{E}\cdot\mathbf{u}$ has to be computed according to (5.104)

$$\begin{aligned} \bar{D}\,\mathbf{E}\cdot\mathbf{u} &= \frac{1}{2}\,\frac{d}{d\epsilon}\left[\mathbf{F}^T\,(\bar{\boldsymbol{\varphi}}+\epsilon\,\mathbf{u})\,\mathbf{F}\,(\bar{\boldsymbol{\varphi}}+\epsilon\,\mathbf{u})-\mathbf{1}\right]\Big|_{\epsilon=0} \\ \Delta\bar{\mathbf{E}} &= \frac{1}{2}\left[\bar{\mathbf{F}}^T\,\mathrm{Grad}\,\mathbf{u}+\mathrm{Grad}^T\mathbf{u}\,\bar{\mathbf{F}}\right]. \end{aligned} \tag{5.109}$$

This result is linear in $\mathbf{u}$ and depends upon the deformation at $\bar{\boldsymbol{\varphi}}$, which is represented by $\bar{\mathbf{F}}$. When computing (5.109) at $\boldsymbol{\varphi}=\mathbf{X}$ the following linear strain tensor is obtained

$$\mathbf{L}\,[\,\mathbf{E}\,]_{\varphi=X} = \mathbf{0} + \frac{1}{2}\left[\mathrm{Grad}\,\mathbf{u}+\mathrm{Grad}^T\mathbf{u}\right]. \tag{5.110}$$

For the linearization of a strain measure refereing to the current configuration, the Almansi strain tensor, $\mathbf{e}=\frac{1}{2}\,(\mathbf{1}-\mathbf{b}^{-1})$, is used. In order to obtain the linearization it is necessary to compute in the first place the *pull back* of $\mathbf{e}$ using (5.23), and then apply the directional derivative. This result is then *pushed forward* to the current configuration

$$\begin{aligned} D\,\mathbf{e}\cdot\mathbf{u} &= \bar{\mathbf{F}}^{-T}\,\{D\,\mathbf{E}\cdot\mathbf{u}\}\,\bar{\mathbf{F}}^{-1} \\ &= \frac{1}{2}\left(\mathrm{Grad}\,\mathbf{u}\,\bar{\mathbf{F}}^{-1}+\bar{\mathbf{F}}^{-T}\mathrm{Grad}^T\mathbf{u}\right) \\ &= \frac{1}{2}\left(\overline{\mathrm{grad}}\,\mathbf{u}+\overline{\mathrm{grad}}^T\mathbf{u}\right) \\ &= \bar{\nabla}^S\Delta\,\mathbf{u}. \end{aligned} \tag{5.111}$$

The comparison of the obtained result with (5.109) shows that

$$\Delta\bar{\mathbf{E}} = \bar{\mathbf{F}}^T\,\bar{\nabla}^S\Delta\mathbf{u}\,\bar{\mathbf{F}}. \tag{5.112}$$

and therefor the linearization of the Almansi strain tensor leads to the same structure as shown in equation (5.36) for the time derivative of the Green-Lagrangian strain tensor.

5.6.2 Linearization of the constitutive equations

When dealing with inelastic constitutive equations, the linearization depends upon the algorithm which is used to integrate the evolution equations, and thus the linearization can only be computed once the integration algorithm is known. The linearization of the constitutive equations can be computed for hyperelastic response functions in an analogous way as that for the time derivatives. This section only presents the linearization of hyperelastic constitutive equations.

The response function for the second Piola-Kirchhoff stress tensor depending on the right Cauchy-Green tensor, for a hyperelastic constitutive equation is described by Equation (5.61). According to (5.105) its linearization yields

$$\begin{aligned} \mathbf{L}\left[\,\mathbf{S}\,\right]_{\varphi=\bar{\varphi}} &= \bar{\mathbf{S}} + \bar{D}\,\mathbf{S}\cdot\mathbf{u} \\ &= \bar{\mathbf{S}} + \Delta\,\bar{\mathbf{S}} \\ &= \bar{\mathbf{S}} + \left.\frac{\partial \mathbf{S}}{\partial \mathbf{C}}\right|_{\varphi=\bar{\varphi}} \left[\bar{D}\,\mathbf{C}\cdot\mathbf{u}\right]. \end{aligned} \tag{5.113}$$

This result can be reformulated with (5.76) and (5.109) as

$$\mathbf{L}\left[\,\mathbf{S}\,\right]_{\varphi=\bar{\varphi}} = \bar{\mathbf{S}} + \bar{\mathbb{C}}\left[\Delta\bar{\mathbf{E}}\right]. \tag{5.114}$$

Comparing this result with (5.113) yields

$$\Delta\bar{\mathbf{S}} = \bar{\mathbb{C}}\left[\Delta\bar{\mathbf{E}}\right]. \tag{5.115}$$

The relation (5.115) has the same structure as the incremental constitutive equation (5.77). Only the time derivatives have to be replaced by the directional derivatives.

5.6.3 Linearization of the weak form

The utilization of approximate methods is in general the only way to obtain the solution of nonlinear boundary value problems. Many of these methods, like the finite element method, are based on the variational formulation of the field equations, given for instance by the weak form or principle of virtual work. The equations for the weak form of balance presented in (5.49) or (5.52) provide the starting point for a numerical method. In order to obtain the solution of these nonlinear equations an iterative scheme has to be used, since the discretization of the weak form results in a nonlinear system of algebraic equations.

The utilization of Newton's method, among many different iterative algorithms, has been proven to often be the most efficient scheme, since it exhibits quadratic convergence near the solution point. In order to apply Newton's method to obtain the solution of the problem, it is necessary to apply a Taylor series expansion of

the nonlinear equation set at a point where the approximated solution is already known. The necessary linearization can be computed with the aid of the directional derivative.

The linearization of the weak form of equilibrium, based on equation (5.49), is first derived with respect to the initial configuration. It is assumed that the linearization is computed at a deformation state $\bar{\boldsymbol{\varphi}}$ at which the body under investigation is in equilibrium.

The linear part of the weak form of equilibrium is given by the following expression

$$L\left[\, G \,\right]_{\varphi=\bar{\varphi}} = G\left(\bar{\boldsymbol{\varphi}}, \boldsymbol{\eta}\right) + DG\left(\bar{\boldsymbol{\varphi}}, \boldsymbol{\eta}\right) \cdot \Delta\mathbf{u}. \tag{5.116}$$

were $G\left(\bar{\boldsymbol{\varphi}}, \boldsymbol{\eta}\right)$ is equal to (5.49) and $\boldsymbol{\varphi}$ is exchanged by the state $\bar{\boldsymbol{\varphi}}$. The directional derivative of G, needed to compute the linearization, is applied only to the first term in (5.49) were the assumption of conservative loading is made

$$DG\left(\bar{\boldsymbol{\varphi}}, \boldsymbol{\eta}\right) \cdot \Delta\mathbf{u} = \int_{\mathcal{B}} \left[D\mathbf{P}\left(\bar{\boldsymbol{\varphi}}\right) \cdot \Delta\mathbf{u}\right] \cdot \operatorname{Grad} \boldsymbol{\eta}\, dV; \tag{5.117}$$

all other terms do not depend upon the deformation. The linearization of the first Piola-Kirchhoff stress tensor allows to obtain, with $\mathbf{P} = \mathbf{F}\,\mathbf{S}$,

$$DG\left(\bar{\boldsymbol{\varphi}}, \boldsymbol{\eta}\right) \cdot \Delta\mathbf{u} = \int_{\mathcal{B}} \left\{\operatorname{Grad} \Delta\mathbf{u}\, \bar{\mathbf{S}} + \bar{\mathbf{F}}\left[D\mathbf{S}\left(\bar{\boldsymbol{\varphi}}\right) \cdot \Delta\mathbf{u}\right]\right\} \cdot \operatorname{Grad} \boldsymbol{\eta}\, dV. \tag{5.118}$$

The quantities labelled with a bar have to be evaluated at $\bar{\boldsymbol{\varphi}}$. For the linearization of the second Piola-Kirchhoff stresses, equation (5.115) can be used, which leads to

$$D\mathbf{S}\left(\bar{\boldsymbol{\varphi}}\right) \cdot \Delta\mathbf{u} = \bar{\mathbb{C}}\left[\Delta\bar{\mathbf{E}}\right], \tag{5.119}$$

where the last term is the linearization of the Green-Lagrangian strain tensor $\mathbf{E}$ at $\bar{\boldsymbol{\varphi}}$, see (5.109). The incremental elasticity tensor $\bar{\mathbb{C}}$ is evaluated with respect to the reference configuration using (5.76):

$$\bar{\mathbb{C}} = 4\, \frac{\partial^2 W}{\partial\mathbf{C}\, \partial\mathbf{C}}\bigg|_{\varphi=\bar{\varphi}} \tag{5.120}$$

computed at $\boldsymbol{\varphi} = \bar{\boldsymbol{\varphi}}$.

Introducing equation (5.120) into (5.118) allows to completes the linearization and to obtain the following expression:

$$DG\left(\bar{\boldsymbol{\varphi}}, \boldsymbol{\eta}\right) \cdot \Delta\mathbf{u} = \int_{\mathcal{B}} \left\{\operatorname{Grad} \Delta\mathbf{u}\, \bar{\mathbf{S}} + \bar{\mathbf{F}}\, \bar{\mathbb{C}}\left[\Delta\bar{\mathbf{E}}\right]\right\} \cdot \operatorname{Grad} \boldsymbol{\eta}\, dV. \tag{5.121}$$

By using of the trace operation and by considering the symmetry of $\bar{\mathbb{C}}$, the following compact form of (5.121) can be obtained:

$$DG\left(\bar{\boldsymbol{\varphi}}, \boldsymbol{\eta}\right) \cdot \Delta\mathbf{u} = \int_{\mathcal{B}} \left\{ \operatorname{Grad} \Delta\mathbf{u}\, \bar{\mathbf{S}} \cdot \operatorname{Grad} \boldsymbol{\eta} + \delta\bar{\mathbf{E}} \cdot \bar{\mathbb{C}} \left[\Delta\bar{\mathbf{E}}\right] \right\} dV. \tag{5.122}$$

It is important to note that symmetry exists for linearization with respect to $\boldsymbol{\eta}$ and $\Delta\mathbf{u}$. In Equation (5.122), the first term is the so-called *geometrical matrix* or *initial stress* matrix. The second term contains the initial deformations occurring in the incremental constitutive tensor $\bar{\mathbb{C}}$, the variation of the Green-Lagrangian strains defined as $\delta\bar{\mathbf{E}} = \frac{1}{2}\left(\bar{\mathbf{F}}^T \operatorname{Grad} \boldsymbol{\eta} + \operatorname{Grad}^T \boldsymbol{\eta}\, \bar{\mathbf{F}}\right)$ and its linearization, defined as $\Delta\bar{\mathbf{E}} = \frac{1}{2}\left(\bar{\mathbf{F}}^T \operatorname{Grad} \Delta\mathbf{u} + \operatorname{Grad}^T \Delta\mathbf{u}\, \bar{\mathbf{F}}\right)$. In index notation, equation (5.122) can be written as

$$DG\left(\bar{\boldsymbol{\varphi}}, \boldsymbol{\eta}\right)_A \Delta u_A = \int_{\mathcal{B}} \left\{ \Delta u_{A,B}\, \bar{S}_{BC}\, \eta_{A,C} + \delta\bar{E}_{AB}\, \bar{\mathbb{C}}_{ABCD}\, \Delta\bar{E}_{CD} \right\} dV. \tag{5.123}$$

With Equation (5.122), all relations with respect to the initial configuration, are known, and a iterative solution procedure like Newton's method can now be applied. The basis for the discretization using the finite element method for nonlinear problems in solid mechanics is now known. Equation (5.122) in the literature is also known as the *total Lagrange* formulation [Belytschko et al., 2000].

The linearization of the weak form, defined in quantities in the current configuration is obtained by a *push forward* of the linearization (5.122) to the already obtained deformations state $\bar{\boldsymbol{\varphi}}$. With the *push forward* of the Green-Lagrangian strain tensor, the second term in (5.122) can be re-written as

$$\int_{\mathcal{B}} \bar{\nabla}^S \boldsymbol{\eta} \cdot \bar{\mathbf{c}} \left[\bar{\nabla}^S \Delta\mathbf{u}\right] dV, \tag{5.124}$$

where the fourth order tensor $\bar{\mathbf{c}}$ follows from $\bar{\mathbb{C}}$ by the transformation (5.81).

The first term in (5.122) can be transformed directly with $\bar{\boldsymbol{\tau}} = \bar{\mathbf{F}}\, \bar{\mathbf{S}}\, \bar{\mathbf{F}}^T$, and expressed in terms of the Kirchhoff stresses:

$$\operatorname{Grad} \Delta\mathbf{u}\, \bar{\mathbf{S}} \cdot \operatorname{Grad} \boldsymbol{\eta} = \bar{\mathbf{F}} \operatorname{Grad} \Delta\mathbf{u}\, \bar{\mathbf{F}}^{-1} \bar{\boldsymbol{\tau}}\, \bar{\mathbf{F}}^{-1} \cdot \operatorname{Grad} \boldsymbol{\eta} = \overline{\operatorname{grad}}\, \Delta\mathbf{u}\, \bar{\boldsymbol{\tau}} \cdot \overline{\operatorname{grad}}\, \boldsymbol{\eta}. \tag{5.125}$$

Using these transformations, the linearization in terms of quantities at the current configuration state $\bar{\boldsymbol{\varphi}}$ is obtained as

$$Dg\left(\bar{\boldsymbol{\varphi}}, \boldsymbol{\eta}\right) \cdot \Delta\mathbf{u} = \int_{\mathcal{B}} \left\{ \overline{\operatorname{grad}}\, \Delta\mathbf{u}\, \bar{\boldsymbol{\tau}} \cdot \overline{\operatorname{grad}}\, \boldsymbol{\eta} + \bar{\nabla}^S \boldsymbol{\eta} \cdot \bar{\mathbf{c}} \left[\bar{\nabla}^S \Delta\mathbf{u}\right] \right\} dV. \tag{5.126}$$

By making the the transformation $d\bar{v} = \bar{J}\, dV$, the integral (5.126) can be transformed into the current configuration $\bar{\boldsymbol{\varphi}}$. The Cauchy stress tensor $\bar{\boldsymbol{\sigma}} = \frac{1}{\bar{J}}\,\bar{\boldsymbol{\tau}}$ is now used, and the incremental constitutive tensor is defined as

$$\bar{\bar{\mathfrak{C}}} = \frac{1}{\bar{J}}\,\bar{\mathfrak{C}} \tag{5.127}$$

such that the final result is obtained

$$Dg\,(\bar{\boldsymbol{\varphi}}, \boldsymbol{\eta}) \cdot \Delta\mathbf{u} = \int\limits_{\bar{\varphi}(\mathcal{B})} \left\{ \overline{\operatorname{grad}}\,\Delta\mathbf{u}\,\bar{\boldsymbol{\sigma}} \cdot \overline{\operatorname{grad}}\,\boldsymbol{\eta} + \bar{\nabla}^S\boldsymbol{\eta} \cdot \bar{\bar{\mathfrak{C}}}\left[\bar{\nabla}^S \Delta\mathbf{u}\right] \right\} dv \tag{5.128}$$

Equation (5.128) in the literature is also known as the *updated Lagrange* formulation [Bathe et al., 1975], since the deformation state $\bar{\boldsymbol{\varphi}}$ is always updated during the nonlinear incremental solution procedure.

With Equation (5.128), all relations with respect to the current configuration are known. These can now be applied within an iterative solution procedure, such as the Newton's method. The basis for the discretization using the finite element method for nonlinear problems in solid mechanics is now known.

5.6.4 Linearization of a deformation dependent load

The description of a pressure load leads to a surface load that depends upon the current deformation state. The stress vector $\mathbf{t}$ is then given in terms of the pressure p and the surface normal $\mathbf{n}$ by $\bar{\mathbf{t}} = p\,\mathbf{n}$. This leads to the necessity to add to the weak form (5.57), written in the current configuration, the following additional term

$$g\,(\boldsymbol{\varphi}, \boldsymbol{\eta}) + g_p\,(\boldsymbol{\varphi}, \boldsymbol{\eta}) = g\,(\boldsymbol{\varphi}, \boldsymbol{\eta}) + \int\limits_{\varphi(\partial\mathcal{B}_P)} p\,\mathbf{n} \cdot \boldsymbol{\eta}\, da. \tag{5.129}$$

To compute the linearization of this extra term, it is preferable to perform a *pull back* operation and transform (5.129) to the initial configuration. Two methods are possible. The first relies on the transformation of the surface normal using (5.11). This allows to obtain the expression $\int_{\partial\mathcal{B}_P} p\, J\, \mathbf{F}^{-T}\mathbf{N} \cdot \boldsymbol{\eta}\, dA$ where linearization is complicated. In the second method, a simpler procedure is used, in which the normal vector $\mathbf{n}$ is expressed by the cross product of the tangent vectors which are tangent to the convective coordinates of the surface of the body, see Figure 5.4.

The normal unit vector follows with the tangent vectors, as defined in Figure 5.4, $\mathbf{g}_\alpha\,(\alpha = 1, 2)$ as

$$\mathbf{n} = \frac{\mathbf{g}_1 \times \mathbf{g}_2}{\| \mathbf{g}_1 \times \mathbf{g}_2 \|}. \tag{5.130}$$

The tangent vectors can be computed from the deformation state using the equation $\mathbf{g}_\alpha = \boldsymbol{\varphi}_{,\alpha}$ and the area element da can be expressed by $da = \| \mathbf{g}_1 \times \mathbf{g}_2 \|\, d\theta_1 d\theta_2$ in

terms of the tangent vectors with respect to the convective coordinates. Based on these relations, the virtual work for pressure loading is

$$g_p(\boldsymbol{\varphi}, \boldsymbol{\eta}) = \int_{\theta_1} \int_{\theta_2} p\left(\boldsymbol{\varphi}_{,1} \times \boldsymbol{\varphi}_{,2}\right) \cdot \boldsymbol{\eta}\, d\theta_1 d\theta_2. \tag{5.131}$$

With the introduction of the displacement field, the tangent vectors have the form $\boldsymbol{\varphi}_{,\alpha} = (\mathbf{X} + \mathbf{u})_{,\alpha}$. Hence the linearization of (5.131) yields

$$Dg_p(\boldsymbol{\varphi}, \boldsymbol{\eta}) \cdot \Delta\mathbf{u} = \int_{\theta_1} \int_{\theta_2} p\left(\Delta\mathbf{u}_{,1} \times \boldsymbol{\varphi}_{,2} + \boldsymbol{\varphi}_{,1} \times \Delta\mathbf{u}_{,2}\right) \cdot \boldsymbol{\eta}\, d\theta_1 d\theta_2. \tag{5.132}$$

when p itself is independent of the deformation state. The linearization refers to the convected coordinates. It can be pushed forward to the current configuration, leading to

$$Dg_p(\boldsymbol{\varphi}, \boldsymbol{\eta}) \cdot \Delta\mathbf{u} = \int_{\varphi(\partial\mathcal{B}_p)} p\, \frac{\Delta\mathbf{u}_{,1} \times \boldsymbol{\varphi}_{,2} + \boldsymbol{\varphi}_{,1} \times \Delta\mathbf{u}_{,2}}{\| \boldsymbol{\varphi}_{,1} \times \boldsymbol{\varphi}_{,2} \|} \cdot \boldsymbol{\eta}\, da. \tag{5.133}$$

With this the linearization of a deformation-dependent pressure load, see (5.131), has been derived. More theoretical considerations with regard to the nonconservative nature of deformation dependent loads can be found in [Sewell, 1967], [Bufler, 1984], [Ogden, 1984] or [Simo et al., 1991].

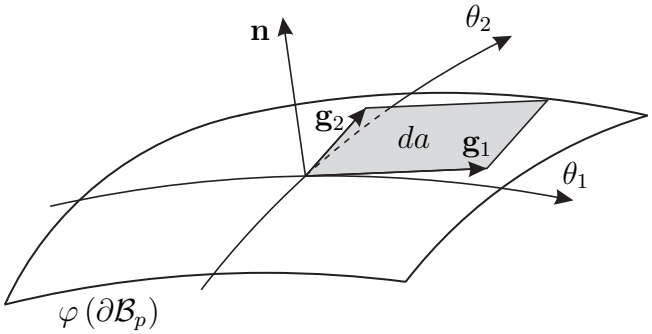

Figure 5.4: Linearization of a pressure dependent surface load.

5.7 Discretization of the Continuum

This section presents the discretization of continua undergoing large strains using isoparametric elements. This topic is discussed here only briefly. For a detailed

treatment with respect to the finite element implementations of boundary-value problems regarding large deformations, the references [Oden, 1972], [Crisfield, 1991], [Bathe, 1996], [Crisfield, 1997] or [Zienkiewicz and Taylor, 2005] and the references therein should be consulted.

Different approximations exist within the finite element method. These are geometrical approximations of the domain $\mathcal{B}$ on which the boundary value problem is defined. The associated fields, deformations or stresses also have to be approximated. Furthermore, the integrals are not evaluated exactly, since, as they are evaluated for the weak form, they have to be computed via numerical integration procedures. Collectively, these approximations are sources for errors inherent to the finite element method.

The description of the interpolations, which are the basis for a treatment using isoparametric elements, is presented here briefly. Within this framework, it is assumed that the domain $\mathcal{B}$ is discretized by n_e finite elements, which leads to the geometrical approximation $\mathcal{B}^h$:

$$\mathcal{B} \approx \mathcal{B}^h = \overline{\bigcup_{e=1}^{n_e} \Omega_e}. \tag{5.134}$$

Figure 5.5 shows the configuration of one element $\Omega_e \subset \mathcal{B}^h$, for a two-dimensional case. In Figure 5.5, $\partial\mathcal{B}^h$ denotes the boundary of the discretization $\mathcal{B}^h$, which is in general also an approximation of the function describing the real boundary $\partial\mathcal{B}$.

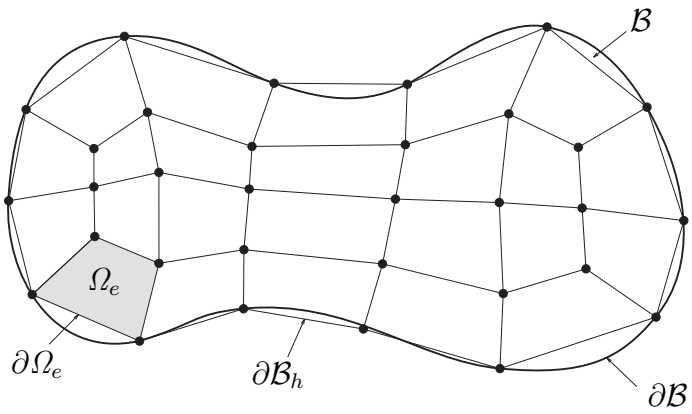

Figure 5.5: Finite element discretization of a two-dimensional body $\mathcal{B}$.

5.7.1 Isoparametric Concept

The finite element method requires the field variables to be approximated by a finite element Ω_e. The displacement field $\mathbf{u}(\mathbf{X})$ is then written as

$$\mathbf{u}_{exact}(\mathbf{X}) \approx \mathbf{u}^h(\mathbf{X}) = \sum_{I=1}^{N} N_I(\mathbf{X})\, \boldsymbol{u}_I, \tag{5.135}$$

where $\mathbf{X}$ is the position vector for a point inside Ω_e, the interpolation or basis functions which are defined on Ω_e are represented by $N_I(\mathbf{X})$, and $\boldsymbol{u}_I$ denotes the unknown nodal variables for the finite element Ω_e, which has N nodes. In the present case, $\boldsymbol{u}_I = \{u_1, u_2, u_3\}_I^T$ are the nodal variables of the displacement field.

During the development of the finite element method, many possibilities for the interpolation of the unknown functions within an element can be used. Due to its general applicability, especially when arbitrary geometries have to be discretized, the isoparametric concept is widely used. On the isoparametric approach, the geometry and field variables are approximated by the same interpolation functions, see Figure 5.6:

$$\mathbf{X}_e^h = \sum_{I=1}^{n} N_I(\boldsymbol{\xi})\, \boldsymbol{X}_I, \qquad \text{and} \qquad \mathbf{u}_e^h = \sum_{I=1}^{n} N_I(\boldsymbol{\xi})\, \boldsymbol{u}_I. \tag{5.136}$$

Equations (5.136) show that the interpolation functions $N_I(\mathbf{X})$ for an element Ω_e in $\mathcal{B}^h$ have been replaced by interpolation functions $N_I(\boldsymbol{\xi})$ defined on the reference element $\Omega_\square$, see Figure 5.6. Therefor, for each element Ω_e, a transformation

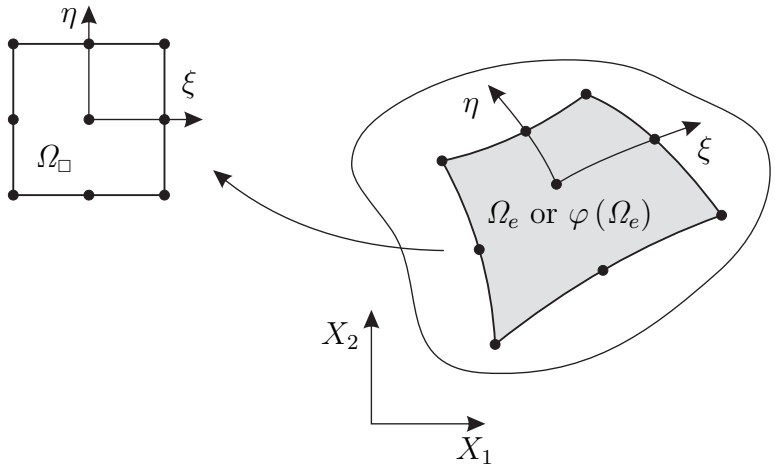

Figure 5.6: Isoparametric mapping between Ω_e and $\Omega_\square$.

exists (5.136) which relates the coordinates $\mathbf{X}_e = \mathbf{X}_e(\boldsymbol{\xi})$ to the coordinates $\boldsymbol{\xi}$ of the reference element $\Omega_\square$. Therefor, all computations are performed with respect to the reference configuration. Only in few cases do the initial and current configurations of a finite element coincide. This transformation is numerically easy to handle, and allows the transformation of arbitrary geometries into the reference element. This feature leads to the fact that, during the implementation of the method, there is almost no difference in the formulation of finite elements with respect to the current or initial configurations.

Figure 5.7 shows two different possibilities to describe deformation in continuum mechanics using the isoparametric concept. It is easy to observe that Figure 5.7 is a discrete version of Figure 5.1, where the reference configuration $\Omega_\square$ has been introduced. The kinematical relations within one element are obtained as follows

$$\boldsymbol{F}_e = \boldsymbol{j}_e \boldsymbol{J}_e^{-1} \qquad \text{and} \qquad J_e = \det \boldsymbol{F}_e = \frac{\det \boldsymbol{j}_e}{\det \boldsymbol{J}_e}, \tag{5.137}$$

which show that the deformation gradient is uniquely defined by the isoparametric

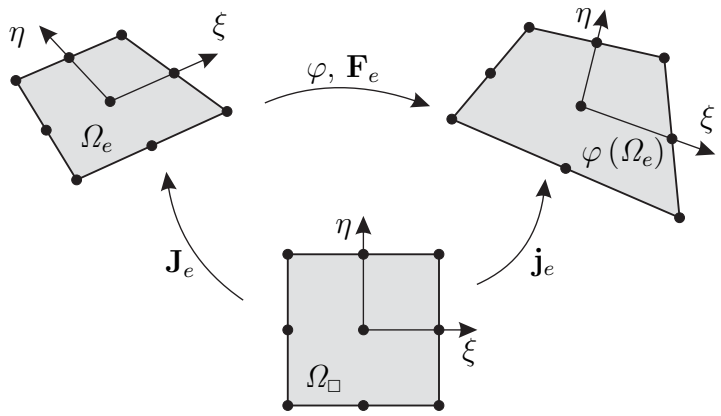

Figure 5.7: Isoparametric description of deformations.

mapping of $\Omega_\square$ onto Ω_e in the initial configuration, or onto $\varphi(\Omega_e)$ in the current configuration. In these equations, the gradients $\boldsymbol{j}_e$ and $\boldsymbol{J}_e$ are defined as follows:

$$\begin{aligned} \boldsymbol{j}_e &= \operatorname{Grad}_\xi \mathbf{x} = \frac{\partial \mathbf{x}}{\partial \boldsymbol{\xi}} = \sum_{I=1}^{n} N_{I,\xi}(\boldsymbol{\xi})\, \boldsymbol{x}_I \otimes \mathbf{E}_\xi, \\ \boldsymbol{J}_e &= \operatorname{Grad}_\xi \mathbf{X} = \frac{\partial \mathbf{X}}{\partial \boldsymbol{\xi}} = \sum_{I=1}^{n} N_{I,\xi}(\boldsymbol{\xi})\, \boldsymbol{X}_I \otimes \mathbf{E}_\xi. \end{aligned} \tag{5.138}$$

Since the derivatives $N_{I,\xi}$ are scalar quantities, they can be moved to the front of the base vectors $\mathbf{E}_\xi$. This yields the following result

$$\begin{aligned} \boldsymbol{j}_e &= \sum_{I=1}^{n} \boldsymbol{x}_I \otimes N_{I,\xi}\left(\boldsymbol{\xi}\right) \mathbf{E}_\xi = \sum_{I=1}^{n} \boldsymbol{x}_I \otimes \nabla_\xi N_I, \\ \boldsymbol{J}_e &= \sum_{I=1}^{n} \boldsymbol{X}_I \otimes N_{I,\xi}\left(\boldsymbol{\xi}\right) \mathbf{E}_\xi = \sum_{I=1}^{n} \boldsymbol{X}_I \otimes \nabla_\xi N_I, \end{aligned} \tag{5.139}$$

where $\nabla_\xi N_I$ is the gradient of the scalar function N_I with respect to the coordinates $\boldsymbol{\xi}$. With this, it is simple to compute gradients with respect to the initial or current configurations. For a vector field this reads as $\mathbf{u}^h$,

$$\begin{aligned} \operatorname{Grad} \mathbf{u}^h &= \sum_{I=1}^{n} \boldsymbol{u}_I \otimes \nabla_X N_I, \\ \operatorname{grad} \mathbf{u}^h &= \sum_{I=1}^{n} \boldsymbol{u}_I \otimes \nabla_x N_I. \end{aligned} \tag{5.140}$$

Analogous to the transformation of the derivatives between different configurations, see (5.25), it is possible to obtain

$$\nabla_\xi N_I = \boldsymbol{J}_e^T \nabla_X N_I \qquad \text{and} \qquad \nabla_\xi N_I = \boldsymbol{j}_e^T \nabla_x N_I, \tag{5.141}$$

or the inverse relations

$$\nabla_N N_I = \boldsymbol{J}_e^{-T} \nabla_\xi N_I \qquad \text{and} \qquad \nabla_x N_I = \boldsymbol{j}_e^{-T} \nabla_\xi N_I, \tag{5.142}$$

such that the gradient in (5.140) is completely defined in quantities which are defined in the reference configuration $\Omega_\square$ as

$$\begin{aligned} \operatorname{Grad} \mathbf{u}^h &= \sum_{I=1}^{n} \boldsymbol{u}_I \otimes \boldsymbol{J}_e^{-T} \nabla_\xi N_I, \\ \operatorname{grad} \mathbf{u}^h &= \sum_{I=1}^{n} \boldsymbol{u}_I \otimes \boldsymbol{j}_e^{-T} \nabla_\xi N_I. \end{aligned} \tag{5.143}$$

The only difference in the formulation of both gradients in (5.143) lies in the exchange of the gradients $\boldsymbol{j}_e$ and $\boldsymbol{J}_e$. This approach is advantageous, especially for large deformation finite element formulations.

5.7.1.1 Isoparametric interpolation functions

There exists a number of different possibilities to construct interpolation functions for isoparametric elements. The concept of the Lagrange interpolation, e.g. see [Zienkiewicz and Taylor, 2005] is used here. For a Lagrange polynomial of power $n-1$, for the one-dimensional case one obtains

$$N_I(\xi) = \prod_{\substack{J=1 \\ J \neq 1}}^{n} \frac{(\xi_J - \xi)}{(\xi_J - \xi_I)}. \tag{5.144}$$

For two-dimensional interpolations, the following product formulation is chosen

$$N_J(\xi, \eta) = N_I(\xi) N_K(\eta), \tag{5.145}$$

and for the three-dimensional interpolations,

$$N_J(\xi, \eta, \zeta) = N_I(\xi) N_K(\eta) N_L(\zeta), \tag{5.146}$$

is chosen. In these definitions, $J = 1, \ldots n^{dim}$ and $I, K, L = 1, \ldots n$ (where dim is the spatial dimension of the problem). The interpolation or shape functions are defined in the local coordinate system $\boldsymbol{\xi} = \{\xi, \eta, \zeta\}$.

Specific isoparametric shape functions for one, two and three-dimensional problems can be found in [Zienkiewicz and Taylor, 2005] or [Dhatt and Touzot, 1985], for example.

The derivatives of the different shape functions with respect to the coordinates of the initial or current configuration can be computed using (5.141). For the derivatives with respect to the coordinates of the initial configuration, for the three-dimensional case, the following is obtained

$$\nabla_X N_I = \begin{Bmatrix} N_{I,1} \\ N_{I,2} \\ N_{I,3} \end{Bmatrix} = \boldsymbol{J}_e^{-T} \begin{Bmatrix} N_{I,\xi} \\ N_{I,\eta} \\ N_{I,\zeta} \end{Bmatrix}. \tag{5.147}$$

The Jacobi matrix $\boldsymbol{J}_e$ of the element Ω_e, which is needed in this derivation, is obtained from (5.139) giving:

$$\boldsymbol{J}_e = \sum_{I=1}^{n} \boldsymbol{X}_I \otimes \nabla_\xi N_I = \begin{bmatrix} X_{1,\xi} & X_{1,\eta} & X_{1,\zeta} \\ X_{2,\xi} & X_{2,\eta} & X_{2,\zeta} \\ X_{3,\xi} & X_{3,\eta} & X_{3,\zeta} \end{bmatrix}. \tag{5.148}$$

Within this formula, the components of $\boldsymbol{J}_e$ are computed from

$$X_{m,k} = \sum_{I=1}^{n} N_{I,k} X_{m,I}, \tag{5.149}$$

where the partial derivative with respect to k stands for a derivative with respect to ξ, η or ζ.

5.7.2 Finite Element Discretization of the Weak Forms

It is possible to apply the one, two or three-dimensional shape functions to describe the interpolation for the geometry and the field variables within the weak forms, in a general way. The present section deals with this subject in a brief manner, using equations (5.52) and (5.57). The linearizations of the weak forms are also considered on this section. Following Figure 5.5, a domain is subdivided into n_e finite elements. This discretization leads to an approximation of the geometry, which affects the representation of the boundary of the domain under consideration.

An interpolation as described in (5.136) is chosen for each finite element Ω_e, which approximates the displacement field $\mathbf{u}$ and the geometry. The integrals of the weak form can then be written with the isoparametric interpolation as

$$\int_{\mathcal{B}} (\dots)\, dV \approx \int_{\mathcal{B}_h} (\dots)\, dV = \bigcup_{e=1}^{n_e} \int_{\Omega_e} (\dots)\, d\Omega = \bigcup_{e=1}^{n_e} \int_{\Omega_\square} (\dots)\, d\square. \tag{5.150}$$

In (5.150) the operator $\bigcup$ is introduced instead of a sum sign to denote the assembly process which has to be performed in order to obtain the set of nonlinear algebraic equations following from (5.150). The polynomial shape functions of the isoparametric interpolation ensures fulfillment of the inter-element continuity conditions, as well as fulfillment of the boundary conditions within the global system of equations. Since the assembly process is standard and well known, it is not described in detail here. The references [Bathe, 1982], or [Zienkiewicz and Taylor, 2005], for example, should be consulted for more details on this topic.

5.7.2.1 Total Lagrangian weak form

In order to obtain the approximation of the weak form (5.52), it is necessary to obtain the discretization of the virtual internal work $\int_{\mathcal{B}} \mathbf{S} \cdot \delta\mathbf{E}\, dV$, the inertia terms $\int_{\mathcal{B}} \rho_0\, \dot{\mathbf{v}} \cdot \boldsymbol{\eta}\, dV$ the volume loads $\int_{\mathcal{B}} \rho_0\, \bar{\mathbf{b}} \cdot \boldsymbol{\eta}\, dV$ and the surface loads $\int_{\Gamma} \bar{\mathbf{t}} \cdot \boldsymbol{\eta}\, dV$. For the virtual internal work, it is necessary to obtain the variation of the Green-Lagrangian strain tensors within the element Ω_e, see (5.150). Using (5.51) and (5.140), it is possible to obtain

$$\delta\mathbf{E}^h = \frac{1}{2} \sum_{I=1}^{n} \left[\boldsymbol{F}_e^T \left(\boldsymbol{\eta}_I \otimes \nabla_X N_I \right) + \left(\nabla_X N_I \otimes \boldsymbol{\eta}_I \right) \boldsymbol{F}_e \right], \tag{5.151}$$

where the same interpolation was used for the deformation $\boldsymbol{\varphi}$ and the variation $\boldsymbol{\eta}$. In Equation (5.151), a finite element approximation of the deformation gradient (5.7) has to be applied, which can be written with (5.140) within the element Ω_e as

$$\boldsymbol{F}_e = \sum_{K=1}^{n} \left(\mathbf{x}_K \otimes \nabla_X N_K \right). \tag{5.152}$$

For the derivation of the matrix formulation needed within the computer implementation of finite elements, index notation is necessary. For (5.151) the following is obtained

$$\delta E^h_{AB} = \frac{1}{2} \sum_{I=1}^{n} \left[F_{kA} N_{I,B} + N_{I,A} F_{kB} \right] \eta_{kI}, \tag{5.153}$$

where the different components of the deformation gradient are defined as follows $F_{kB} = \sum_{J=1}^{n} x_{kJ}\, N_{J,B}$.

Within the matrix formulation, the symmetry of the Green-Lagrangian strain tensor and its variation, can be considered. Therefor, it is possible to introduce only six components instead of the nine components of the three-dimensional strain tensor

$$\delta \boldsymbol{E} = \left\{ \begin{array}{c} \delta E_{11} \\ \delta E_{22} \\ \delta E_{33} \\ 2\,\delta E_{12} \\ 2\,\delta E_{23} \\ 2\,\delta E_{13} \end{array} \right\} = \sum_{I=1}^{n} \boldsymbol{B}_{LI}\, \boldsymbol{\eta}_I, \tag{5.154}$$

which can be approximated as a sum over the element nodes I with the matrices

$$\boldsymbol{B}_{LI} = \left[\begin{array}{ccc} F_{11}\, N_{I,1} & F_{21}\, N_{I,1} & F_{31}\, N_{I,1} \\ F_{12}\, N_{I,2} & F_{22}\, N_{I,2} & F_{32}\, N_{I,2} \\ F_{13}\, N_{I,3} & F_{23}\, N_{I,3} & F_{33}\, N_{I,3} \\ F_{11}\, N_{I,2} + F_{12}\, N_{I,1} & F_{21}\, N_{I,2} + F_{22}\, N_{I,1} & F_{31}\, N_{I,2} + F_{32}\, N_{I,1} \\ F_{12}\, N_{I,3} + F_{13}\, N_{I,2} & F_{22}\, N_{I,3} + F_{23}\, N_{I,2} & F_{32}\, N_{I,3} + F_{33}\, N_{I,2} \\ F_{11}\, N_{I,3} + F_{13}\, N_{I,1} & F_{21}\, N_{I,3} + F_{23}\, N_{I,1} & F_{31}\, N_{I,3} + F_{33}\, N_{I,1} \end{array} \right]. \tag{5.155}$$

In Equation (5.154), the index L means that the matrix $\boldsymbol{B}_{LI}$ is linear in the displacements, since $\mathbf{F}^h = 1 + \operatorname{Grad} \mathbf{u}^h$.

The stresses follow from the constitutive equation, which will be specified in the associated sections. It is important to note that the stresses have to be computed pointwise within the element, and result for instance in finite elasticity from a pure evaluation of the response function. Since also the second Piola-Kirchhoff stress tensor is symmetric, only six independent components are needed, which yields the vector $\boldsymbol{S} = \{S_{11}, S_{22}, S_{33}, S_{12}, S_{23}, S_{13}\}^T$. Taking these preliminaries into account,

the virtual internal work can be written as

$$\begin{aligned}\int_{\mathcal{B}} \delta\mathbf{E}^h \cdot \mathbf{S}^h dV &= \bigcup_{e=1}^{n_e} \int_{\Omega_e} \delta\boldsymbol{E}^T \boldsymbol{S}\, d\Omega \\ &= \bigcup_{e=1}^{n_e} \sum_{I=1}^{n} \boldsymbol{\eta}_I^T \int_{\Omega_e} \boldsymbol{B}_{LI}^T \boldsymbol{S}\, d\Omega \\ &= \bigcup_{e=1}^{n_e} \sum_{I=1}^{n} \boldsymbol{\eta}_I^T \int_{\Omega_\square} \boldsymbol{B}_{LI}^T \boldsymbol{S} \det \boldsymbol{J}_e\, d\square.\end{aligned} \tag{5.156}$$

The last term in (5.156) already reflects the evaluation of the integrals with respect to the configuration of the isoparametric reference element. To shorten the notation, the following vector is introduced

$$\boldsymbol{R}_I(\boldsymbol{u}_e) = \int_{\Omega_e} \boldsymbol{B}_{LI}^T \boldsymbol{S}\, d\Omega, \tag{5.157}$$

The virtual internal work can now be reformulated as

$$\begin{aligned}\int_{\mathcal{B}} \delta\mathbf{E}^h \cdot \mathbf{S}^h\, dV &= \bigcup_{e=1}^{n_e} \sum_{I=1}^{n} \boldsymbol{\eta}_I^T\, \boldsymbol{R}_I(\boldsymbol{u}_e) \\ &= \boldsymbol{\eta}^T \boldsymbol{R}(\boldsymbol{u}).\end{aligned} \tag{5.158}$$

In this equation $\boldsymbol{\eta}$ is the test function or virtual displacement and $\boldsymbol{R}(\boldsymbol{u})$ is the stress divergence term, also known as the residual force vector, which results from the assembly process of all the finite elements elements. In 5.158, $\delta\mathbf{E}^h$ is linear with respect to the displacement field, whereas the stress tensor $\mathbf{S}^h$ can still depend in an arbitrary nonlinear form upon the displacements.

In the weak form (5.52), the inertia term, defined by $\int_{\mathcal{B}} \rho_0 \dot{\mathbf{v}} \cdot \boldsymbol{\eta}\, dV$, is computed with interpolation of the velocity, using standard shape functions N_K for the spatial discretization,

$$\mathbf{v}(\mathbf{X}, t) = \sum_{K=1}^{n} N_K(\boldsymbol{\xi})\, \mathbf{v}_K(t). \tag{5.159}$$

The acceleration is given by derivation of the nodal values $\mathbf{v}_K(t)$, since the shape functions N_K depend only upon the spatial coordinates,

$$\dot{\mathbf{v}}(\mathbf{X}, t) = \sum_{K=1}^{n} N_K(\boldsymbol{\xi})\, \dot{\mathbf{v}}_K. \tag{5.160}$$

Inserting this result in the associated inertia term in (5.52), and applying the same discretization as in (5.151) for the variations $\boldsymbol{\eta}$, leads to

$$\begin{aligned}\int_{\mathcal{B}} \rho_0\, \boldsymbol{\eta} \cdot \dot{\mathbf{v}}\, dV &= \bigcup_{e=1}^{n_e} \int_{\Omega_e} \rho_0\, \boldsymbol{\eta}^T \dot{\mathbf{v}}\, dV \\ &= \bigcup_{e=1}^{n_e} \sum_{I=1}^{n} \sum_{K=1}^{n} \boldsymbol{\eta}_I^T \int_{\Omega_e} N_I\, \rho_0\, N_K\, d\Omega\, \dot{\mathbf{v}}_K.\end{aligned} \tag{5.161}$$

By introducing the unit matrix $\boldsymbol{I}$ and applying to the nodal velocities $\dot{\boldsymbol{v}}_K = \boldsymbol{I}\dot{\boldsymbol{v}}_K$, the following mass matrix for a nodal pair I and K of an element Ω_e is obtained

$$\boldsymbol{M}_{IK} = \int_{\Omega_e} N_I\, \rho_0\, N_K\, d\Omega\, \boldsymbol{I}, \tag{5.162}$$

The inertia term for the global system is obtained as

$$\begin{aligned}\int_{\mathcal{B}} \rho_0\, \boldsymbol{\eta} \cdot \dot{\boldsymbol{v}}\, dV &= \bigcup_{e=1}^{n_e} \sum_{I=1}^{n} \sum_{K=1}^{n} \boldsymbol{\eta}_I^T \boldsymbol{M}_{IK}\, \dot{\boldsymbol{v}}_K \\ &= \boldsymbol{\eta}^T \boldsymbol{M} \dot{\boldsymbol{v}},\end{aligned} \tag{5.163}$$

where $\boldsymbol{M}$ is the mass matrix and $\dot{\boldsymbol{v}}$ the acceleration vector after assembly of the global structure.

The loading terms are determined in an analogous way. After inserting the finite element approximations for the test function $\boldsymbol{\eta}$, the following is obtained

$$\begin{aligned}\int_{\mathcal{B}} \rho_0\, \boldsymbol{\eta} \cdot \bar{\mathbf{b}}\, dV + \int_{\Gamma_\sigma} \boldsymbol{\eta} \cdot \bar{\mathbf{t}}\, dA = &\bigcup_{e=1}^{n_e} \sum_{I=1}^{n} \boldsymbol{\eta}_I^T \int_{\Omega_e} \rho_0\, \bar{\boldsymbol{b}}\, N_I\, d\Omega + \\ &+ \bigcup_{r=1}^{n_r} \sum_{I=1}^{m} \boldsymbol{\eta}_I^T \int_{\Gamma_r} N_I\, \bar{\boldsymbol{t}}\, d\Gamma,\end{aligned} \tag{5.164}$$

where n_r are the number of loaded element boundaries and Γ_l is the element surface of an element which is subjected to a surface load defined by the stress vector $\bar{\boldsymbol{t}}$, as shown on Figure 5.8. For the interpolation function of the surface loads, a function which is reduced by one dimension can used. Therefor, the surface loads in Figure 5.8, which depicts a two-dimensional body, need as an approximation for the test function along the boundary a one-dimensional function, defined by m surface nodes (in Figure 5.8, $m = 2$ nodes). Some simplification can also be obtained here considering

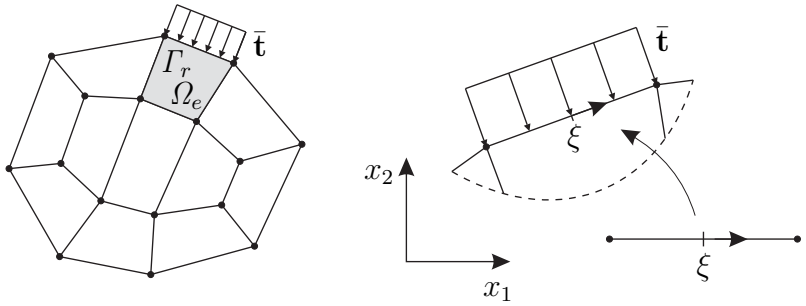

Figure 5.8: Discretization of surface loads.

$$\boldsymbol{P}_I = \int_{\Omega_e} \rho\, \bar{\mathbf{b}}\, N_I \, d\Omega \qquad \text{and} \qquad \boldsymbol{P}_I^{\sigma} = \int_{\Gamma_r} N_I\, \bar{\mathbf{t}}\, d\Gamma. \tag{5.165}$$

The following load vectors are obtained

$$\begin{aligned} \int_{\mathcal{B}} \rho\, \boldsymbol{\eta} \cdot \bar{\mathbf{b}}\, dV + \int_{\sigma} \boldsymbol{\eta} \cdot \bar{\mathbf{t}}\, dA &= \bigcup_{e=1}^{n_e} \sum_{I=1}^{n} \boldsymbol{\eta}_I^T \boldsymbol{P}_I + \bigcup_{r=1}^{n_r} \sum_{I=1}^{n} \boldsymbol{\eta}_I^T \boldsymbol{P}_I^{\sigma} \\ &= \boldsymbol{\eta}^T \boldsymbol{P}, \end{aligned} \tag{5.166}$$

where the vector $\boldsymbol{P}$ contains all the information with regard to the loads acting on the structure.

The matrix notation in (5.158), (5.163) and (5.166) yields, for the weak form (5.52),

$$\boldsymbol{\eta}^T \left[\boldsymbol{M}\dot{\boldsymbol{v}} + \boldsymbol{R}(\boldsymbol{u}) - \boldsymbol{P} \right] = 0. \tag{5.167}$$

Due to the fact that the test function $\boldsymbol{\eta}$ is arbitrary, this leads to a nonlinear system of ordinary differential equations:

$$\boldsymbol{M}\dot{\boldsymbol{v}} + \boldsymbol{R}(\boldsymbol{u}) - \boldsymbol{P} = \boldsymbol{0}. \qquad \forall \boldsymbol{u} \in \mathbb{R}^N. \tag{5.168}$$

In (5.168) all quantities are evaluated with respect to the initial configuration and N is the total number of degrees of freedoms contained in the unknown displacement vector $\boldsymbol{u}$. The acceleration vector is $\dot{\boldsymbol{v}}$ and $\boldsymbol{M}$ denotes the mass matrix.

In case that the inertia forces are zero ($\boldsymbol{M}\dot{\boldsymbol{v}} = \boldsymbol{0}$), from the system of ordinary differential equations a nonlinear algebraic system of equations which have to be solved by an iterative procedure are obtained. In general the Newton's method is applied, and hence the linearization of (5.168) is needed, which is discussed in the next section.

5.7.2.2 Linearization of the Total Lagrangian weak form

For an efficient solution of the nonlinear algebraic equation systems (5.168), Newton's method is applied which requires the linearization of (5.168). The linearization is obtained assuming that the inertia terms can be neglected. The linearization can be obtained by a direct discretization of the continuous formulation (5.122), presented here again:

$$DG\left(\bar{\boldsymbol{\varphi}}, \boldsymbol{\eta}\right) \cdot \Delta\mathbf{u} = \int_{\mathcal{B}} \left\{ \operatorname{Grad} \Delta\mathbf{u}\, \bar{\mathbf{S}} \cdot \operatorname{Grad} \boldsymbol{\eta} + \delta\bar{\mathbf{E}} \cdot \bar{\mathbb{C}} \left[\Delta\bar{\mathbf{E}}\right] \right\} dV.$$

For the first term with

$$\begin{aligned} \operatorname{Grad} \Delta\mathbf{u}^h &= \sum_{K=1}^{n} \Delta\boldsymbol{u}_K \otimes \nabla_X N_K, \\ \operatorname{Grad} \boldsymbol{\eta} &= \sum_{I=1}^{n} \boldsymbol{\eta}_I \otimes \nabla_X N_I \end{aligned} \tag{5.169}$$

the following discretization is obtained directly

$$\int_{\mathcal{B}} \operatorname{Grad} \Delta\mathbf{u}\, \bar{\mathbf{S}} \cdot \operatorname{Grad} \boldsymbol{\eta}\, dV = \bigcup_{e=1}^{n_e} \sum_{I=1}^{n} \sum_{K=1}^{n} \int_{\Omega_e} \left(\Delta\boldsymbol{u}_K \otimes \nabla_X N_K\right) \bar{\mathbf{S}} \cdot \left(\boldsymbol{\eta}_I \otimes \nabla_X N_I\right)\, d\Omega, \tag{5.170}$$

which yields, with the rules for the dyadic and scalar products and with the following definition $\Delta\boldsymbol{u}_K \cdot \boldsymbol{\eta}_I = \boldsymbol{\eta}_I^T \Delta\boldsymbol{u}_K = \boldsymbol{\eta}_I^T\, \boldsymbol{I}\, \Delta\boldsymbol{u}_K$,

$$\int_{\mathcal{B}} \operatorname{Grad} \Delta\mathbf{u}\, \bar{\mathbf{S}} \cdot \operatorname{Grad} \boldsymbol{\eta}\, dV = \bigcup_{e=1}^{n_e} \sum_{I=1}^{n} \sum_{K=1}^{n} \boldsymbol{\eta}_I^T \int_{\Omega_e} \bar{G}_{IK}\, \boldsymbol{I}\, d\Omega\, \Delta\boldsymbol{u}_K, \tag{5.171}$$

where the abbreviation

$$\bar{G}_{IK} = \left(\Delta_X N_I\right)^T\, \bar{\boldsymbol{S}}\, \nabla_X N_K \tag{5.172}$$

has been used. The matrix form of the scalar product (5.172) can be derived if the gradients are described as vectors. This leads to

$$\bar{G}_{IK} = \begin{bmatrix} N_{I,1} & N_{I,2} & N_{I,3} \end{bmatrix} \begin{bmatrix} \bar{S}_{11} & \bar{S}_{12} & \bar{S}_{13} \\ \bar{S}_{21} & \bar{S}_{22} & \bar{S}_{23} \\ \bar{S}_{31} & \bar{S}_{32} & \bar{S}_{33} \end{bmatrix} \begin{Bmatrix} N_{K,1} \\ N_{K,2} \\ N_{K,3} \end{Bmatrix}. \tag{5.173}$$

Relation (5.171) is independent from the constitutive equation, since only the stress at configuration $\bar{\boldsymbol{\varphi}}$ have to be considered. Therefor, the matrix which defined by (5.171) is often called the Initial Stress Matrix.

The second term in (5.122)

$$\int_{\mathcal{B}} \delta\bar{\mathbf{E}} \cdot \bar{\mathbb{C}} \left[\Delta\bar{\mathbf{E}}\right] dV$$

depends upon the incremental constitutive tensor $\bar{\mathbb{C}}$ which has to be evaluated at configuration $\bar{\boldsymbol{\varphi}}$, and thus is directly connected to the constitutive equation. For elastic materials this tensor has been given in Section 5.5.2 (e.g. see (5.86)). For elasto-plastic or other constitutive equations, the associated matrix formulation can be found in (5.89). Since $\Delta\bar{\mathbf{E}}$ has the same structure as $\delta\bar{\mathbf{E}}$, with (5.151) it is possible to write

$$\Delta\mathbf{E}^h = \frac{1}{2}\sum_{I=1}^{n}\left[\boldsymbol{F}_e^T\left(\Delta\boldsymbol{u}_I \otimes \nabla_X N_I\right) + \left(\nabla_X N_I \otimes \Delta\boldsymbol{u}_I\right)\boldsymbol{F}_e\right]. \tag{5.174}$$

From this relation, the matrix formulation follows with (5.155)

$$\Delta\boldsymbol{E} = \sum_{I=1}^{n}\boldsymbol{B}_{LI}\,\Delta\boldsymbol{u}_I. \tag{5.175}$$

Introduction of this relation, together with the incremental constitutive tensor $\bar{\boldsymbol{D}}$, allows to write

$$\int_{\mathcal{B}} \delta\bar{\mathbf{E}} \cdot \bar{\mathbb{C}} \left[\Delta\bar{\mathbf{E}}\right] dV = \bigcup_{e=1}^{n_e}\sum_{I=1}^{n}\sum_{K=1}^{n}\boldsymbol{\eta}_I^T\int_{\Omega_e}\bar{\boldsymbol{B}}_{LI}^T\,\bar{\boldsymbol{D}}\,\bar{\boldsymbol{B}}_{LK}\,d\Omega\,\Delta\boldsymbol{u}_k. \tag{5.176}$$

Summarizing, the following discretization can be obtained

$$\int_{\mathcal{B}}\left\{\operatorname{Grad}\Delta\mathbf{u}\,\bar{\mathbf{S}}\cdot\operatorname{Grad}\boldsymbol{\eta} + \delta\bar{\mathbf{E}}\cdot\bar{\mathbb{C}}\left[\Delta\bar{\mathbf{E}}\right]\right\}dV = \bigcup_{e=1}^{n_e}\sum_{I=1}^{n}\sum_{K=1}^{n}\boldsymbol{\eta}_I^T\,\bar{\boldsymbol{K}}_{T_{IK}}\,\Delta\boldsymbol{u}_k. \tag{5.177}$$

Here the matrix $\bar{\boldsymbol{K}}_{T_{IK}}$ denotes the "tangent matrix" because it represents the tangent to the deformation at $\bar{\boldsymbol{\varphi}}$:

$$\bar{\boldsymbol{K}}_{T_{IK}} = \int_{\Omega_e}\left[\left(\nabla_X N_I\right)^T\bar{\boldsymbol{S}}\,\nabla_X N_K + \bar{\boldsymbol{B}}_{LI}^T\bar{\boldsymbol{D}}\,\bar{\boldsymbol{B}}_{LK}\right]d\Omega. \tag{5.178}$$

It is stated for the nodal combination I, K within a finite element Ω. In this notation the submatrix $\bar{\boldsymbol{K}}_{T_{IK}}$ has the size $ndof \times ndof$, where $ndof$ is the number of degrees of freedom for one node within the finite element (in three-dimensional problems in continuum mechanics each point has three degrees of freedom, hence $ndof = 3$). Indices I and K are nodes of an element, and thus directly associated with the discretization. For example, for a ten node tetrahedron, $n = 10$, and therefor the total size of the tangent matrix $\bar{\boldsymbol{K}}_{T_e}$ for one element is $(n \cdot n_{dof}) \times (n \cdot n_{dof}) = 30 \times 30$.

5.7.2.3 Updated Lagrangian weak form

The derivation of the matrix formulation for the weak form with respect to the current configuration follows analogous to the derivation of equation (5.52), but equation (5.55) is used as a basic equation. Within the integrals, the *push forward* of the variation of the Green-Lagrangian strain tensor $\delta\mathbf{E} = \nabla^S\boldsymbol{\eta}$ is needed, see (5.56). Hence (5.56) has to be approximated. With equations (5.140), this leads to

$$\nabla^S\boldsymbol{\eta}^h = \frac{1}{2}\sum_{I=1}^{n}\left[(\boldsymbol{\eta}_I \otimes \nabla_x N_I) + (\nabla_x N_I \otimes \boldsymbol{\eta}_I)\right]. \tag{5.179}$$

As in the last section, it is advantageous to switch to index notation to derive the matrix formulation. The following is obtained

$$\left(\nabla^S\boldsymbol{\eta}\right)^h_{im} = \frac{1}{2}\sum_{I=1}^{n}\left[\eta_{iI}\,N_{I,k} + N_{I,i}\,\eta_{kI}\right]. \tag{5.180}$$

On (5.180), $N_{I,m} = \partial N_I/\partial x_m$ is the partial derivative of the shape functions with respect to the spatial coordinates x_m. These derivatives can be computed using (5.142)

$$N_{I,k} = \left\{j_e^{-1}\right\}_{1k} N_{I,\xi} + \left\{j_e^{-1}\right\}_{2k} N_{I,\eta} + \left\{j_e^{-1}\right\}_{3k} N_{I,\zeta}, \tag{5.181}$$

where $\{j_e^{-1}\}_{ik}$ are the associated components of the inverse of the Jacobi matrix $\boldsymbol{j}_e$. Equation (5.180) yields the components of $\nabla^S\boldsymbol{\eta}^h$. Due to symmetry, the vector $\left(\nabla^S\boldsymbol{\eta}^h\right)^T = [\eta_{1,1}, \eta_{2,2}, \eta_{3,3}, (\eta_{1,2}+\eta_{2,1}), (\eta_{2,3}+\eta_{3,2},), (\eta_{1,3}+\eta_{3,1})]$, which contains the components of $\nabla^S\boldsymbol{\eta}^h$, can be introduced. With this the approximation of the spatial gradient is given by

$$\nabla^S\boldsymbol{\eta}^h = \sum_{I=1}^{n}\begin{bmatrix} N_{I,1} & 0 & 0 \\ 0 & N_{I,2} & 0 \\ 0 & 0 & N_{I,3} \\ N_{I,2} & N_{I,1} & 0 \\ 0 & N_{I,3} & N_{I,2} \\ N_{I,3} & 0 & N_{I,1} \end{bmatrix} \begin{Bmatrix} \eta_1 \\ \eta_2 \\ \eta_3 \end{Bmatrix}_I = \sum_{I=1}^{n} \boldsymbol{B}_{0I}\,\boldsymbol{\eta}_I. \tag{5.182}$$

Note that matrix $\boldsymbol{B}_{0I}$ does not contain any displacements, which is indicated by the index "0".

With these preliminary remarks and the introduction of a vector $\boldsymbol{\sigma}$, defined as $\boldsymbol{\sigma} = \{\sigma_{11}, \sigma_{22}, \sigma_{33}, \sigma_{12}, \sigma_{23}, \sigma_{13}\}^T$, which contains the independent components of the

Cauchy stress tensor, the internal virtual work in (5.55) can be written as

$$\begin{aligned}\int_{\varphi(\mathcal{B})} \nabla^S \boldsymbol{\eta}^h \cdot \boldsymbol{\sigma}^h \, dv &= \bigcup_{e=1}^{n_e} \int_{\varphi(\Omega_e)} \left(\nabla^S \boldsymbol{\eta}^h\right)^T \boldsymbol{\sigma}^h \, d\omega \\ &= \bigcup_{e=1}^{n_e} \sum_{I=1}^{n} \boldsymbol{\eta}_I^T \int_{\varphi(\Omega_e)} \boldsymbol{B}_{0I}^T \, \boldsymbol{\sigma} \, d\omega \\ &= \bigcup_{e=1}^{n_e} \sum_{I=1}^{n} \boldsymbol{\eta}_I^T \int_{\Omega_\square} \boldsymbol{B}_{0I}^T \, \boldsymbol{\sigma} \, \det \boldsymbol{j}_e \, d\square.\end{aligned} \tag{5.183}$$

The last form in (5.183) already contains the reference to the isoparametric base element $\Omega_\square$. A comparison with the associated relation in (5.156) shows that both formulations distinguish each other by the $\boldsymbol{B}$-Matrix, the determinant of the isoparametric mapping (5.138) and, of course, the stress tensor. By introducing

$$\boldsymbol{r}_I\left(\boldsymbol{u}_e\right) = \int_{\varphi(\Omega_e)} \boldsymbol{B}_{0I}^T \, \boldsymbol{\sigma} \, d\omega, \tag{5.184}$$

the notation can be simplified, and for the virtual internal work one obtains

$$\begin{aligned}\int_{\varphi(\mathcal{B})} \nabla^S \boldsymbol{\eta}^h \cdot \boldsymbol{\sigma}^h \, dv &= \bigcup_{e=1}^{n_e} \sum_{I=1}^{n} \boldsymbol{\eta}_I^T \boldsymbol{r}_I\left(\boldsymbol{u}_e\right) \\ &= \boldsymbol{\eta}^T \boldsymbol{r}\left(\boldsymbol{u}\right).\end{aligned} \tag{5.185}$$

With the transformation for the volume elements $dv = J \, dV$ and the relation between the Cauchy stress tensor and the Kirchhoff stress tensor, see (5.47), which yields $\boldsymbol{\tau} = J\boldsymbol{\sigma}$, the integral representing the virtual internal work in (5.183) can can be transformed to the reference configuration:

$$\int_{\varphi(\mathcal{B})} \nabla^S \boldsymbol{\eta}^h \cdot \boldsymbol{\sigma}^h dv = \int_{\mathcal{B}} \nabla^S \boldsymbol{\eta}^h \cdot \boldsymbol{\tau}^h dV. \tag{5.186}$$

Discretization with finite elements leads to

$$\begin{aligned}\int_{\mathcal{B}} \nabla^S \boldsymbol{\eta}^h \cdot \boldsymbol{\tau}^h dV &= \bigcup_{e=1}^{n_e} \int_{\Omega_e} \left(\nabla^S \boldsymbol{\eta}^h\right)^T \boldsymbol{\tau}^h \, d\Omega \\ &= \bigcup_{e=1}^{n_e} \sum_{I=1}^{n} \boldsymbol{\eta}_I^T \int_{\Omega_e} \boldsymbol{B}_{0I}^T \, \boldsymbol{\tau} \, d\Omega \\ &= \bigcup_{e=1}^{n_e} \sum_{I=1}^{n} \boldsymbol{\eta}_I^T \int_{\Omega_\square} \boldsymbol{B}_{0I}^T \, \boldsymbol{\tau} \, \det \boldsymbol{J}_e \, d\square.\end{aligned} \tag{5.187}$$

The residual vector denoting the stress divergence term is the defined by

$$\boldsymbol{r}_I\left(\boldsymbol{u}_e\right) = \int_{\Omega_\square} \boldsymbol{B}_{0I}^T\, \boldsymbol{\tau}\, d\square. \tag{5.188}$$

The total internal work follows from (5.185).

The approximation of the inertia terms is performed according to (5.163). In the same way, (5.166), the load terms are formulated. Therefor the finite element discretization of the weak form with respect to the current configuration (5.55) can be summarized:

$$\boldsymbol{\eta}^T\left[\boldsymbol{M}\,\dot{\boldsymbol{v}} + \boldsymbol{r}\left(\boldsymbol{u}\right) - \boldsymbol{P}\right] = \boldsymbol{0}. \tag{5.189}$$

which for arbitrary values of the test function $\boldsymbol{\eta}$ yields the nonlinear ordinary differential system

$$\boldsymbol{M}\,\dot{\boldsymbol{v}} + \boldsymbol{r}\left(\boldsymbol{u}\right) - \boldsymbol{P} = \boldsymbol{0}. \tag{5.190}$$

For static problems this system reduces to a nonlinear algebraic system of equations for the unknown nodal displacements $\boldsymbol{u}$:

$$\boldsymbol{g}\left(\boldsymbol{u}\right) = \boldsymbol{r}\left(\boldsymbol{u}\right) - \boldsymbol{P} = \boldsymbol{0} \tag{5.191}$$

The vector representing the stress divergence term $\boldsymbol{r}\left(\boldsymbol{u}\right)$ can be computed in equations (5.190) or (5.191) either by (5.184) or (5.188). Both formulations are equivalent. Note that the relation (5.185) looks like the formulation in the linear theory, only the quantities $\delta\boldsymbol{e}$ and $\boldsymbol{\sigma}$ are evaluated with respect to the current configuration.

5.7.2.4 Linearization of the Updated Lagrangian weak form

The derivation of two weak forms, equations (5.185) and (5.188), which differ only in the region of integration, $\boldsymbol{\varphi}\left(\mathcal{B}^h\right)$ or $\mathcal{B}^h$ where presented on the previous section. The linearization of these forms is described in Section 5.6.3, thus is is only necessary to apply the discretization to these results.

Linearization of the weak form (5.185) follows from equation (5.128), which is given here again

$$Dg\left(\bar{\boldsymbol{\varphi}}, \boldsymbol{\eta}\right) \cdot \Delta\mathbf{u} = \int_{\bar{\varphi}(\mathcal{B})} \left\{\overline{\operatorname{grad}}\,\Delta\mathbf{u}\,\bar{\boldsymbol{\sigma}} \cdot \overline{\operatorname{grad}}\,\boldsymbol{\eta} + \bar{\nabla}^S\boldsymbol{\eta} \cdot \bar{\hat{\mathbf{c}}}\left[\nabla^S\Delta\mathbf{u}\right]\right\} dv.$$

The first term has exactly the same form as the associated term in the formulation with respect to the initial configuration. Hence the discretization is the same, and can be directly adopted from the discretization in the initial configuration, see

(5.171). Only the derivatives are now with respect to the coordinates $\bar{x}_i$ of the current configuration $\bar{\boldsymbol{\varphi}}(\mathcal{B})$. With the discretization of the gradient

$$\begin{aligned} \overline{\operatorname{grad}}\, \Delta \mathbf{u}^h &= \sum_{K=1}^{n} \Delta \boldsymbol{u}_K \otimes \bar{\nabla}_x N_K, \\ \overline{\operatorname{grad}}\, \boldsymbol{\eta}^h &= \sum_{I=1}^{n} \boldsymbol{\eta}_I \otimes \bar{\nabla}_x N_I, \end{aligned} \tag{5.192}$$

the first part of the integrals is obtained

$$\int_{\bar{\varphi}(\mathcal{B})} \overline{\operatorname{grad}}\, \Delta \mathbf{u}\, \bar{\boldsymbol{\sigma}} \cdot \overline{\operatorname{grad}}\, \boldsymbol{\eta}\, dv = \bigcup_{e=1}^{n_e} \sum_{I=1}^{n} \sum_{K=1}^{n} \boldsymbol{\eta}_I^T \int_{\bar{\varphi}(\Omega_e)} \bar{g}_{IK}\, \boldsymbol{I}\, d\Omega\, \Delta \boldsymbol{u}_k. \tag{5.193}$$

Within this term, the abbreviation

$$\bar{g}_{IK} = \left(\bar{\nabla}_x N_I\right)^T \bar{\boldsymbol{\sigma}}\, \bar{\nabla}_x N_K \tag{5.194}$$

has been used. The matrix form of the scalar product follows, as in (5.173), as

$$\bar{g}_{IK} = \left[\begin{array}{ccc} \bar{N}_{I,1} & \bar{N}_{I,2} & \bar{N}_{I,3} \end{array}\right] \left[\begin{array}{ccc} \bar{\sigma}_{11} & \bar{\sigma}_{12} & \bar{\sigma}_{13} \\ \bar{\sigma}_{21} & \bar{\sigma}_{22} & \bar{\sigma}_{23} \\ \bar{\sigma}_{31} & \bar{\sigma}_{32} & \bar{\sigma}_{33} \end{array}\right] \left\{\begin{array}{c} \bar{N}_{K,1} \\ \bar{N}_{K,2} \\ \bar{N}_{K,3} \end{array}\right\}. \tag{5.195}$$

This equation is independent from the constitutive equation, as is (5.171), since only the stresses of the configuration $\bar{\boldsymbol{\varphi}}$. enter the integral.

The second term in (5.128)

$$\int_{\bar{\varphi}(\mathcal{B})} \bar{\nabla}^S \boldsymbol{\eta} \cdot \bar{\hat{\mathbf{c}}} \left[\bar{\nabla}^S \Delta \mathbf{u}\right]\, dv$$

depends upon the incremental constitutive tensor $\hat{\mathbf{c}}$, evaluated at the current configuration $\bar{\boldsymbol{\varphi}}$, and thus directly from the constitutive equation (e.g. see Section 5.5.2, equation (5.87)). Using the same arguments as for linearization with respect to the initial configuration and (5.182), it is possible to obtain

$$\int_{\bar{\varphi}(\mathcal{B})} \bar{\nabla}^S \boldsymbol{\eta} \cdot \bar{\hat{\mathbf{c}}} \left[\bar{\nabla}^S \Delta \mathbf{u}\right]\, dv = \bigcup_{e=1}^{n_e} \sum_{I=1}^{n} \sum_{K=1}^{n} \boldsymbol{\eta}_I^T \int_{\bar{\varphi}(\Omega_e)} \bar{\boldsymbol{B}}_{0I}^T\, \bar{\boldsymbol{D}}^M\, \bar{\boldsymbol{B}}_{0K}\, d\Omega\, \Delta \boldsymbol{u}_K, \tag{5.196}$$

where all quantities in the integrals have to be evaluated at $\bar{\boldsymbol{\varphi}}$. In summary, the following discretization is obtained

$$\int_{\bar{\varphi}(\mathcal{B})} \left\{\overline{\operatorname{grad}}\, \Delta \mathbf{u}\, \bar{\boldsymbol{\sigma}} \cdot \overline{\operatorname{grad}}\, \boldsymbol{\eta} + \bar{\nabla}^S \boldsymbol{\eta} \cdot \bar{\hat{\mathbf{c}}} \left[\nabla^S \Delta \mathbf{u}\right]\right\} dv = \bigcup_{e=1}^{n_e} \sum_{I=1}^{n} \sum_{K=1}^{n} \boldsymbol{\eta}_I^T\, \bar{\boldsymbol{K}}_{T_{IK}}^M\, \Delta \boldsymbol{u}_K, \tag{5.197}$$

where matrix $\bar{\boldsymbol{K}}^{M}_{T_{IK}}$ is the tangent matrix with respect to the current configuration,

$$\bar{\boldsymbol{K}}^{M}_{T_{IK}} = \int\limits_{\bar{\varphi}(\Omega_e)} \left[\left(\bar{\nabla}_x N_I\right)^T \, \bar{\boldsymbol{\sigma}} \, \bar{\nabla}_x N_K + \bar{\boldsymbol{B}}^T_{0I} \, \bar{\boldsymbol{D}}^{M} \, \bar{\boldsymbol{B}}_{0K} \right] d\omega. \tag{5.198}$$

It is defined for the combination of nodes I, K within the element Ω_e, see also Section 5.7.2.2. The discretization of the weak form (5.188) in the current configuration follows in an analogous way. Only the final result is presented here:

$$\int\limits_{\bar{\varphi}(\mathcal{B})} \left\{ \overline{\operatorname{grad}} \, \Delta\mathbf{u} \, \bar{\boldsymbol{\tau}} \cdot \overline{\operatorname{grad}} \, \boldsymbol{\eta} + \bar{\nabla}^S \boldsymbol{\eta} \cdot \bar{\mathfrak{c}} \left[\nabla^S \Delta\mathbf{u} \right] \right\} dv = \bigcup_{e=1}^{n_e} \sum_{I=1}^{n} \sum_{K=1}^{n} \boldsymbol{\eta}^T_I \, \bar{\boldsymbol{K}}^{MR}_{T_{IK}} \, \Delta\mathbf{u}_K, \tag{5.199}$$

where matrix $\bar{\boldsymbol{K}}^{MR}_{T_{IK}}$ is the tangent matrix with respect to the current configuration:

$$\bar{\boldsymbol{K}}^{MR}_{T_{IK}} = \int\limits_{\Omega_e} \left[\left(\bar{\nabla}_x N_I\right)^T \, \bar{\boldsymbol{\tau}} \, \bar{\nabla}_x N_K + \bar{\boldsymbol{B}}^T_{0I} \, \bar{\boldsymbol{D}}^{MR} \, \bar{\boldsymbol{B}}_{0K} \right] d\Omega. \tag{5.200}$$

The matrix form $\bar{\boldsymbol{D}}^{MR}$ of the incremental constitutive tensor $\bar{\mathfrak{c}}$ can be found for a Neo-Hookean material, e.g. in (5.89). The associated form for $\bar{\boldsymbol{D}}^{M}$ results from the transformation with the Jacobi determinant J, as given in (5.127).

Chapter 6

A constitutive model for the behavior of the human pelvic floor muscles

6.1 Introduction

The soft tissues of the human body have a highly nonlinear mechanical behavior and their passive properties can frequently be described by nonlinear hyperelastic or viscoelastic constitutive relations [Fung, 1993]. Due to their structure, namely the orientation of the muscle fibers, the skeletal muscles have, definitely, a nonisotropic behavior. In addition, skeletal muscles are distinct from other soft biological tissues because of their capability of active contraction: they have the possibility of generating tension forces (stresses) when their length decreases. The justification for this can be found at the microscopic level (see Section 6.2.2): some filaments in the muscles fibers can slide with respect to each other and chemical connections can be established between such filaments at varying locations along their lengths as a result of an activation process triggered by neural electrical stimulation. This means that a part of the muscle strain in the direction of the fibers, the muscle contractile strain, is the result of a complex electro-chemical activation process. In this work this activation process will not be modelled as such in the finite element deformation analysis.

In this work, for the 3-D constitutive behavior of the pelvic floor muscles a modified form of the constitutive equation proposed earlier by Humphrey and Yin [Humphrey and Yin, 1987] for the passive deformation of cardiac muscle tissues is adopted, as presented by Martins in [Martins et al., 1998]. The non-isotropy of the the pelvic floor muscles results from the existence of muscle fibers, the direction of which is taken into account in Humphrey's model. Humphrey's model follows the

guidelines of the work of Spencer [Spencer, 1984] on fiber-reinforced incompressible hyperelastic composites, the strain energy density function in Humphrey's model is the sum of a fiber term and a term related to the embedding matrix, the latter being assumed to be isotropic. The modifications in Humphrey's model considered in this work have the objective of making it qualitatively and quantitatively compatible with the passive and active longitudinal behavior of the pelvic floor muscles. The resulting 3-D model is consistent with the 1-D models proposed by Hill [Hill, 1938] and Zajac [Zajac, 1989].

6.2 Constitutive equations

As mentioned before, the constitutive equation adopted in this work for the 3-D passive and active behavior of skeletal muscles is a modified form of the incompressible transversely isotropic hyperelastic model proposed by Humphrey and Yin [Humphrey and Yin, 1987] for passive cardiac tissues. A quasi-incompressible version of the latter model is described in Section 6.2.1. In Section 6.2.2, the microscopic structure and the operating principles of the skeletal muscles are summarized as a basis for the presentation of the 1-D models proposed by Hill [Hill, 1938] and Zajac [Zajac, 1989] for those muscles. Finally, in Section 6.2.3, the model presented in Section 6.2.1 is modified to make it compatible with the requirements and models described in Section 6.2.2.

6.2.1 Quasi-incompressible version of Humphrey's constitutive model

In this section, a quasi-incompressible version of Humphrey's constitutive model is presented. For a quasi-incompressible material, the strain energy function, per unit volume of the reference configuration, adopted by Humphrey and Yin can be written in the following form [Humphrey and Yin, 1987]:

$$U = U_I\left(\bar{I}_1^C\right) + U_f\left(\bar{\lambda}_f\right) + U_J\left(J\right). \tag{6.1}$$

The strain energy density function (6.1) is the sum of a term related to the embedding matrix, assumed isotropic, a fiber term and a term associated with the volume change. On (6.1) U_I is the strain energy stored in the isotropic matrix embedding the muscle fibers, defined as:

$$U_I = c\left\{\exp\left[b\left(\bar{I}_1^C - 3\right)\right] - 1\right\}, \tag{6.2}$$

where $\bar{I}_1^C$ is the first invariant of the right Cauchy-Green strain tensor with the volume change eliminated:

$$\bar{I}_1^C = \operatorname{tr}\bar{\mathbf{C}} = \operatorname{tr}\left(\bar{\mathbf{F}}^T\bar{\mathbf{F}}\right) = J^{-\frac{2}{3}}\operatorname{tr}\mathbf{C}, \tag{6.3}$$

$\bar{\mathbf{F}}$ being the deformation gradient with the volume change eliminated:

$$\bar{\mathbf{F}} = J^{-\frac{1}{3}}\mathbf{F}, \tag{6.4}$$

and J the volume change:

$$J = \det \mathbf{F}. \tag{6.5}$$

On (6.1) the strain energy stored in the various muscle fibers families is given by U_f and is defined as:

$$U_f = A\left\{\exp\left[a\left(\bar{\lambda}_f - 1\right)^2\right] - 1\right\}, \tag{6.6}$$

where $\bar{\lambda}_f$ represents the fiber stretch ratio in the direction $\mathbf{N}$ of the undeformed fiber:

$$\bar{\lambda}_f = \sqrt{\mathbf{N}^T\bar{\mathbf{C}}\mathbf{N}} = \sqrt{\bar{\mathbf{C}} : (\mathbf{N}\otimes\mathbf{N})}, \tag{6.7}$$

and $\otimes$ represents the tensor product. On (6.1) the portion of the strain energy associated with the volume change is given by U_J:

$$U_J = \frac{1}{D}(J-1)^2. \tag{6.8}$$

In these definitions presented here, c, b, A, a and D are constants which are defined in Section 6.2.4. As a remark, in the incompressible case $J = 1$, $\mathbf{C} = \bar{\mathbf{C}}$ and $\lambda_f = \bar{\lambda}_f$ and the Humphrey's strain energy is recovered. The strain energy density defined in (6.1) is now used to obtain the 2^{nd} Piola-Kirchhoff stress tensor $\mathbf{S}$:

$$\mathbf{S} = \frac{\partial U}{\partial \mathbf{E}} = \frac{\partial U_I}{\partial \mathbf{E}} + \frac{\partial U_f}{\partial \mathbf{E}} + \frac{\partial U_J}{\partial \mathbf{E}} = \mathbf{S}_I + \mathbf{S}_f + \mathbf{S}_J, \tag{6.9}$$

were $\mathbf{E}$ is the Green-Lagrange strain tensor, as defined in the previous chapter, in equation 5.20.

To obtain an expression for $\mathbf{S}$ it is necessary to apply the chain rule to (6.2-6.8), obtaining the following expressions:

$$\frac{\partial U_I}{\partial \mathbf{E}} = \frac{\partial U_I}{\partial \bar{I}_1^C}\frac{\partial \bar{I}_1^C}{\partial \mathbf{E}}, \tag{6.10}$$

$$\frac{\partial U_f}{\partial \mathbf{E}} = \frac{\partial U_f}{\partial \bar{\lambda}_f}\frac{\partial \bar{\lambda}_f}{\partial \mathbf{E}}, \tag{6.11}$$

$$\frac{\partial U_J}{\partial \mathbf{E}} = \frac{\partial U_J}{\partial J}\frac{\partial J}{\partial \mathbf{E}}. \tag{6.12}$$

In the expressions (6.10)-(6.12), the derivatives $\partial U_I/\partial \bar{I}_1^C$, $\partial U_f/\partial \bar{\lambda}_f$ and $\partial U_J/\partial J$ are obtained as follows:

$$U_I' = \frac{\partial U_I}{\partial \bar{I}_1^C} = bc\exp\left[b\left(\bar{I}_1^C - 3\right)\right] \tag{6.13}$$

$$U_f^{'} = \frac{\partial U_f}{\partial \bar{\lambda}_f} = 2a\left(\bar{\lambda}_f - 1\right) A \exp\left[a\left(\bar{\lambda}_f - 1\right)^2\right], \tag{6.14}$$

$$U_J^{'} = \frac{\partial U_J}{\partial J} = \frac{2}{D}\left(J - 1\right), \tag{6.15}$$

and the derivatives $\partial \bar{I}_1^C / \partial \mathbf{E}$, $\partial \bar{\lambda}_f / \partial \mathbf{E}$ and $\partial J / \partial \mathbf{E}$ necessary to define (6.10)-(6.12) are obtained by the following expressions:

$$\frac{\partial \bar{I}_1^C}{\partial \mathbf{E}} = 2J^{-\frac{2}{3}}\mathbf{1} - \frac{2}{3}\frac{1}{J}\bar{I}_1^C \frac{\partial J}{\partial \mathbf{E}}, \tag{6.16}$$

$$\frac{\partial \bar{\lambda}_f}{\partial \mathbf{E}} = J^{-\frac{2}{3}}\bar{\lambda}_f^{-1}\left(\mathbf{N} \otimes \mathbf{N}\right) - \frac{1}{3}\frac{\bar{\lambda}_f}{J}\frac{\partial J}{\partial \mathbf{E}}, \tag{6.17}$$

$$\frac{\partial J}{\partial \mathbf{E}} = J\,\mathbf{C}^{-1}, \tag{6.18}$$

where $\mathbf{1}$ is the unit 2^{nd} order tensor. With these definitions it is now possible to obtain $\mathbf{S}$ by the following expression:

$$\begin{aligned}\mathbf{S} = U_I^{'}\left(2J^{-\frac{2}{3}}\mathbf{1} - \frac{2}{3}\bar{I}_1^C\mathbf{C}^{-1}\right) + \\ + U_f^{'}\left(J^{-\frac{2}{3}}\bar{\lambda}_f^{-1}\left(\mathbf{N} \otimes \mathbf{N}\right) - \frac{1}{3}\bar{\lambda}_f\mathbf{C}^{-1}\right) + JU_J^{'}\mathbf{C}^{-1}.\end{aligned} \tag{6.19}$$

This expression can be rewritten in a form similar to the one provided by Simo [Simo, 1987]:

$$\mathbf{S} = J^{-\frac{2}{3}}\,\mathrm{DEV}\left[\frac{\partial}{\partial \bar{\mathbf{E}}}\left(U_I + U_f\right)\right] + J\frac{\partial U_J}{\partial J}\mathbf{C}^{-1}, \tag{6.20}$$

where DEV is the deviator operator in the reference configuration with the right Cauchy-Green strain tensor $\mathbf{C}$ operating as metric tensor. The definition of the DEV operator is the following:

$$\mathrm{DEV}\left[\,\cdot\,\right] = \left(\,\cdot\,\right) - \frac{1}{3}\left[\,\mathbf{C} : \left(\,\cdot\,\right)\right]\mathbf{C}^{-1}. \tag{6.21}$$

On expression 6.20, $\bar{\mathbf{E}}$ is the Green-Lagrange strain tensor with the volume change eliminated:

$$\bar{\mathbf{E}} = \frac{1}{2}\left(\bar{\mathbf{C}} - \mathbf{1}\right). \tag{6.22}$$

The expression for the 2^{nd} Piola-Kirchhoff stress tensor $\mathbf{S}$ (6.20), using the operator DEV (6.21) can easily be demonstrated, using (6.3) and the following expressions:

$$\frac{\partial U_I}{\partial \bar{\mathbf{E}}} = \frac{\partial U_I}{\partial \bar{I}_1^C}\frac{\partial \bar{I}_1^C}{\partial \bar{\mathbf{E}}}, \tag{6.23}$$

$$\frac{\partial \bar{I}_1^C}{\partial \bar{\mathbf{E}}} = 2\mathbf{1}, \tag{6.24}$$

$$\frac{\partial U_f}{\partial \bar{\mathbf{E}}} = \frac{\partial U_f}{\partial \bar{\lambda}_f} \frac{\partial \bar{\lambda}_f}{\partial \bar{\mathbf{E}}}, \tag{6.25}$$

$$\frac{\partial \bar{\lambda}_f}{\partial \bar{\mathbf{E}}} = \frac{1}{\bar{\lambda}_f} \left(\mathbf{N} \otimes \mathbf{N} \right). \tag{6.26}$$

The first term in the second member of (6.19) is obtained by applying the DEV operator to the term $\partial \bar{U}_I / \partial \bar{\mathbf{E}}$, obtaining the following result:

$$\begin{aligned} J^{-\frac{2}{3}} \mathrm{DEV} \left(\frac{\partial \bar{U}_I}{\partial \bar{\mathbf{E}}} \right) &= 2J^{-\frac{2}{3}} U_I' \mathbf{1} - \frac{2}{3} J^{-\frac{2}{3}} \left[\mathbf{C} : U_I' \mathbf{1} \right] \mathbf{C}^{-1} \\ &= \bar{U}_I' \left(2J^{-\frac{2}{3}} \mathbf{1} - \frac{2}{3} J^{-\frac{2}{3}} I_1^C \mathbf{C}^{-1} \right) \\ &= \bar{U}_I' \left(2J^{-\frac{2}{3}} \mathbf{1} - \frac{2}{3} \bar{I}_1^C \mathbf{C}^{-1} \right). \end{aligned}$$

The second term in the second member of (6.19) is obtained by applying the DEV operator to the term $\partial U_f / \partial \bar{\mathbf{E}}$, obtaining the following result:

$$\begin{aligned} J^{-\frac{2}{3}} \mathrm{DEV} \left(\frac{\partial U_f}{\partial \bar{\mathbf{E}}} \right) &= J^{-\frac{2}{3}} U_f' \bar{\lambda}_f^{-1} \left(\mathbf{N} \otimes \mathbf{N} \right) - \frac{1}{3} \frac{1}{\bar{\lambda}_f} U_f' \left[\bar{\mathbf{C}} : \left(\mathbf{N} \otimes \mathbf{N} \right) \right] \mathbf{C}^{-1} \\ &= U_f' \left(J^{-\frac{2}{3}} \bar{\lambda}_f^{-1} \left(\mathbf{N} \otimes \mathbf{N} \right) - \frac{1}{3} \bar{\lambda}_f \mathbf{C}^{-1} \right). \end{aligned}$$

Using these definitions, expression (6.20) can be rewritten in the following way:

$$\mathbf{S} = J^{-\frac{2}{3}} \, \mathrm{DEV} \left[2U_I' \mathbf{1} + U_f' \bar{\lambda}_f^{-1} \left(\mathbf{N} \otimes \mathbf{N} \right) \right] + J U_J' \mathbf{C}^{-1}. \tag{6.27}$$

The definition of the Cauchy stress tensor is an important step for the implementation of the constitutive model. Making use of (5.45), the following expression for the Cauchy stress tensor $\boldsymbol{\sigma}$ can be obtained:

$$\begin{aligned} \boldsymbol{\sigma} = \frac{1}{J} \Bigg\{ & U_I' \left[2J^{-\frac{2}{3}} \mathbf{F}\mathbf{F}^T - \frac{2}{3} \bar{I}_1^C \mathbf{F}\mathbf{C}^{-1}\mathbf{F}^T \right] + \\ & + U_f' \left[J^{-\frac{2}{3}} \bar{\lambda}_f^{-1} \mathbf{F} \left(\mathbf{N} \otimes \mathbf{N} \right) \mathbf{F}^T - \frac{1}{3} \bar{\lambda}_f \mathbf{F}\mathbf{C}^{-1}\mathbf{F}^T \right] + \\ & + J U_J' \mathbf{F}\mathbf{C}^{-1}\mathbf{F}^T \Bigg\}. \end{aligned} \tag{6.28}$$

The expression for the Cauchy stress tensor (6.28) can be simplified, by taking in consideration that:

$$\bar{\mathbf{B}} = J^{-\frac{2}{3}}\mathbf{F}\mathbf{F}^T \tag{6.29}$$

and that the following products result in the second order identity tensor $\mathbf{1}$:

$$\mathbf{F}\mathbf{C}^{-1}\mathbf{F}^T = \mathbf{F}\mathbf{F}^{-1}\mathbf{F}^{-T}\mathbf{F}^T = \mathbf{1}. \tag{6.30}$$

Taking also in account that the current muscle fiber direction $\mathbf{n}$ is given by the following expression:

$$\mathbf{n} = J^{-\frac{1}{3}}\frac{\mathbf{F}\mathbf{N}}{\bar{\lambda}_f}, \tag{6.31}$$

equation (6.28) for the Cauchy stress tensor can now be rewritten in the following form:

$$\boldsymbol{\sigma} = \frac{1}{J}\left[U_I^{'}\left(2\bar{\mathbf{B}} - \frac{2}{3}\bar{I}_1^C\mathbf{1}\right) + U_f^{'}\left(\bar{\lambda}_f\,\mathbf{n}\otimes\mathbf{n} - \frac{1}{3}\bar{\lambda}_f\mathbf{1}\right)\right] + U_J^{'}\mathbf{1}. \tag{6.32}$$

In view of (5.45) it is possible to conclude that, in the spatial description, (6.20) may be recast in the following equivalent form:

$$\boldsymbol{\sigma} = \frac{1}{J}\,\mathrm{dev}\left\{\bar{\mathbf{F}}\left[\frac{\partial}{\partial\bar{\mathbf{E}}}\left(U_I + U_f\right)\right]\bar{\mathbf{F}}^T\right\} + U_J^{'}\mathbf{1}, \tag{6.33}$$

were "dev" is now the operator deviator in the spatial configuration of the indicated argument,

$$\mathrm{dev}\,[\,\cdot\,] = (\,\cdot\,) - \frac{1}{3}\mathrm{tr}\,(\,\cdot\,)\,\mathbf{1}. \tag{6.34}$$

Using expression (6.23) to (6.26), is possible to rewrite equation (6.33),obtaining the following expression:

$$\boldsymbol{\sigma} = J^{-1}\,\mathrm{dev}\left[2U_I^{'}\bar{\mathbf{B}} + \bar{\lambda}_f U_f^{'}\,(\mathbf{n}\otimes\mathbf{n})\right] + U_J^{'}\mathbf{1}. \tag{6.35}$$

The material version of the tangent operator, which is necessary for the implementation of the constitutive model in ABAQUS (see Section 6.3), is defined as follows:

$$\mathbf{H} = \frac{\partial^2 U}{\partial\mathbf{E}\partial\mathbf{E}} = \frac{\partial\mathbf{S}}{\partial\mathbf{E}}. \tag{6.36}$$

For the definition of the material tangent operator it is necessary to obtain the differentiation of each of the three terms present in (6.9). The differentiation of the

first term yields the following result:

$$\begin{aligned}\frac{\partial \mathbf{S}_I}{\partial \mathbf{E}} &= \frac{\partial}{\partial \mathbf{E}}\left(U_I^{'}\frac{\partial \bar{I}_1^C}{\partial \mathbf{E}}\right)\\ &= U_I^{''}\left[4J^{-\frac{4}{3}}\mathbf{1}\otimes\mathbf{1}-\frac{4}{3}J^{-\frac{2}{3}}\bar{I}_1^C\left(\mathbf{1}\otimes\mathbf{C}^{-1}+\mathbf{C}^{-1}\otimes\mathbf{1}\right)+\right.\\ &\quad\left.+\frac{4}{9}\left(\bar{I}_1^C\right)^2\mathbf{C}^{-1}\otimes\mathbf{C}^{-1}\right]-\\ &\quad -U_I^{'}\left[\frac{4}{3}J^{-\frac{2}{3}}\left(\mathbf{1}\otimes\mathbf{C}^{-1}+\mathbf{C}^{-1}\otimes\mathbf{1}\right)+\right.\\ &\quad\left.+\frac{2}{3}\bar{I}_1^C\frac{\partial \mathbf{C}^{-1}}{\partial \mathbf{E}}-\frac{4}{9}\bar{I}_1^C\mathbf{C}^{-1}\otimes\mathbf{C}^{-1}\right].\end{aligned} \tag{6.37}$$

The differentiation of the second term yields the following result:

$$\begin{aligned}\frac{\partial \mathbf{S}_f}{\partial \mathbf{E}} &= \frac{\partial}{\partial \mathbf{E}}\left(U_f^{'}\frac{\partial \bar{\lambda}_f}{\partial \mathbf{E}}\right)\\ &= U_f^{''}\left[J^{-\frac{4}{3}}\bar{\lambda}_f^{-2}\left(\mathbf{N}\otimes\mathbf{N}\otimes\mathbf{N}\otimes\mathbf{N}\right)-\right.\\ &\quad\left.-\frac{1}{3}J^{-\frac{2}{3}}\left(\mathbf{N}\otimes\mathbf{N}\otimes\mathbf{C}^{-1}+\mathbf{C}^{-1}\otimes\mathbf{N}\otimes\mathbf{N}\right)+\frac{1}{9}\bar{\lambda}_f^2\mathbf{C}^{-1}\otimes\mathbf{C}^{-1}\right]-\\ &\quad -U_f^{'}\left[J^{-\frac{4}{3}}\bar{\lambda}_f^{-3}\left(\mathbf{N}\otimes\mathbf{N}\otimes\mathbf{N}\otimes\mathbf{N}\right)+\right.\\ &\quad\left.+\frac{1}{3}J^{-\frac{2}{3}}\bar{\lambda}_f^{-1}\left(\mathbf{N}\otimes\mathbf{N}\otimes\mathbf{C}^{-1}+\mathbf{C}^{-1}\otimes\mathbf{N}\otimes\mathbf{N}\right)-\right.\\ &\quad\left.-\frac{1}{9}\bar{\lambda}_f\mathbf{C}^{-1}\otimes\mathbf{C}^{-1}+\frac{1}{3}\bar{\lambda}_f\frac{\partial \mathbf{C}^{-1}}{\partial \mathbf{E}}\right].\end{aligned} \tag{6.38}$$

The differentiation of the third term yields the following result:

$$\frac{\partial S_J}{\partial \mathbf{E}} = J\left(U_J^{'}+JU_J^{''}\right)\left(\mathbf{C}^{-1}\otimes\mathbf{C}^{-1}\right)+JU_J^{'}\frac{\partial \mathbf{C}^{-1}}{\partial \mathbf{E}}. \tag{6.39}$$

In (6.37) to (6.39), $U_I^{''}$, $U_f^{''}$ and $U_J^{''}$ are the second derivatives of $U_I^{'}$, $U_f^{'}$ and $U_J^{'}$ respectively, and are defined as follows:

$$U_I^{''}=\frac{\partial U_I^{'}}{\partial \bar{I}_1^C}=b^2c\exp\left[b\left(\bar{I}_1^C-3\right)\right], \tag{6.40}$$

$$U_f^{''}=\frac{\partial U_f^{'}}{\partial \bar{\lambda}_f}=2aA\exp\left[a\left(\bar{\lambda}_f-1\right)^2\right]\left\{1+2a\left(\bar{\lambda}_f-1\right)^2\right\} \tag{6.41}$$

$$U_J^{''} = \frac{\partial U_J^{'}}{\partial J} = \frac{2}{D}. \tag{6.42}$$

In the expressions (6.37) to (6.39), it is necessary to define the derivative $\partial \mathbf{C}^{-1}/\partial \mathbf{E}$, which is obtained by the following expression:

$$\left(\frac{\partial \mathbf{C}^{-1}}{\partial \mathbf{E}}\right)_{ijkl} = \frac{\partial C_{ij}^{-1}}{\partial E_{kl}} = -\left(C_{ik}^{-1}C_{jl}^{-1} + C_{il}^{-1}C_{jk}^{-1}\right). \tag{6.43}$$

Collecting and rearranging terms, the following final form for the material tangent operator can be obtained:

$$\begin{aligned}
\mathbf{H} = {} & 4J^{-\frac{4}{3}}U_I^{''}\left(\mathbf{1}\otimes\mathbf{1}\right) - \\
& -\frac{4}{3}J^{-\frac{2}{3}}\left(U_I^{'} + \bar{I}_I^C U_I^{''}\right)\left(\mathbf{1}\otimes\mathbf{C}^{-1} + \mathbf{C}^{-1}\otimes\mathbf{1}\right) + \\
& + \left[\frac{4}{9}I_1^C\left(U_I^{'} + \bar{I}_1^C U_I^{''}\right) + \frac{1}{9}\bar{\lambda}_f\left(U_f^{'} + \bar{\lambda}_f U_f^{''}\right) + J\left(U_J^{'} + JU_J^{''}\right)\right]\left(\mathbf{C}^{-1}\otimes\mathbf{C}^{-1}\right) + \\
& + J^{-\frac{4}{3}}\bar{\lambda}_f^{-2}\left(U_f^{''} + \bar{\lambda}_f^{-1}U_f^{'}\right)\left(\mathbf{N}\otimes\mathbf{N}\otimes\mathbf{N}\otimes\mathbf{N}\right) - \\
& - \frac{1}{3}J^{-\frac{2}{3}}\left(U_f^{''} + \bar{\lambda}_f^{-1}U_f^{'}\right)\left(\mathbf{N}\otimes\mathbf{N}\otimes\mathbf{C}^{-1} + \mathbf{C}^{-1}\otimes\mathbf{N}\otimes\mathbf{N}\right) - \\
& - \left(\frac{2}{3}\bar{I}_1^C U_I^{'} + \frac{1}{3}\bar{\lambda}_f U_f^{'} - JU_J^{'}\right)\frac{\partial \mathbf{C}^{-1}}{\partial \mathbf{E}}.
\end{aligned} \tag{6.44}$$

The spatial tangent operator $\mathbf{h}$ can now be obtained through a push-forward operation:

$$\mathbf{h}_{ijkl} = \frac{1}{J}F_{im}F_{jn}F_{kp}F_{lp}H_{mnpq}. \tag{6.45}$$

Inserting (6.44) into (6.45) it is now possible to obtain the final expression for the spatial tangent operator:

$$\begin{aligned}
\mathbf{h} = {} & \frac{4}{J}U_I^{''}\left(\bar{\mathbf{B}}\otimes\bar{\mathbf{B}}\right) - \frac{4}{3}J^{-1}\left(U_I^{'} + \bar{I}_I^C U_I^{''}\right)\left(\bar{\mathbf{B}}\otimes\mathbf{1} + \mathbf{1}\otimes\bar{\mathbf{B}}\right) + \\
& + \frac{1}{J}\left[\frac{4}{9}I_1^C\left(U_I^{'} + \bar{I}_1^C U_I^{''}\right) + \frac{1}{9}\bar{\lambda}_f\left(U_f^{'} + \bar{\lambda}_f U_f^{''}\right) + J\left(U_J^{'} + JU_J^{''}\right)\right]\left(\mathbf{1}\otimes\mathbf{1}\right) + \\
& + \frac{\bar{\lambda}_f^2}{J}\left(U_f^{''} - \bar{\lambda}_f^{-1}U_f^{'}\right)\left(\mathbf{n}\otimes\mathbf{n}\otimes\mathbf{n}\otimes\mathbf{n}\right) - \\
& - \frac{1}{3}\frac{\bar{\lambda}^2}{J}\left(U_f^{''} + \bar{\lambda}_f^{-1}U_f^{'}\right)\left(\mathbf{n}\otimes\mathbf{n}\otimes\mathbf{1} + \mathbf{1}\otimes\mathbf{n}\otimes\mathbf{n}\right) + \\
& + \frac{2}{J}\left(\frac{2}{3}\bar{I}_1^C U_I^{'} + \frac{1}{3}\bar{\lambda}_f U_f^{'} - JU_J^{'}\right)\mathbb{I},
\end{aligned} \tag{6.46}$$

where $\mathbb{I}$ is the 4^{th} order unit tensor.

6.2.2 Structure, operating principles and 1-D mechanical models of the pelvic floor muscles

The muscle tissue is a complex structure with a well defined hierarchy which can be distinguished when observed at various levels of magnification [Seeley et al., 2004].

At the lowest level of magnification, it is observed that muscles are surrounded by a fibrous connective tissue, the *epimysium*, and composed of many bundles, or *fascicles*, which are in turn encased in a dense connective tissue, the *perimysium* (Fig. 6.1a).

Using a higher level of magnification (Fig. 6.1b), it is possible to observe the fascicles, composed of long cylindrical cells with many hundreds of nuclei, the *muscle fibers*, which in turn are surrounded by a loose connective tissue, the *endomysium*. Between the muscle fibers it is possible to find blood vessels and beneath the endomysium, the loose connective tissue that surrounds each muscle fiber, a thin elastic sheath with infoldings is found, the *sarcolemma*. The muscle fibers are the structural units of the muscle tissue and they range in thickness from about 10 to 100 μm and in length from about 1 to 30 cm.

Increasing the level of magnification even higher (Fig. 6.1c), it can be seen that the muscle fibers are formed by a large number of strands, the *myofibrils*, along the length of which a repeating structure is found, the *sarcomeres*, which are the functional units of the contractile system.

At the highest level of magnification (Fig. 6.1d), each sarcomere is found to be composed of thick and thin *myofilaments*, made of the proteins *myosin* and *actin*, respectively. The actin filaments are attached at one end but are free along their length to slide with respect to the myosin filaments and to make and brake chemical connections at different locations with the heads, *cross-bridges*, of the molecules of myosin. This is the process that is responsible for active contraction and force generation in the muscles (Fig. 6.1e).

This process is regulated by two additional proteins in the actin filament, the tropomyosin and the troponin and a key role on turning on and off the contractile activity is played by the calcium ion, the concentration of which, in the neighborhood of the cross-bridges, is changed as a result of electric stimuli from the neurons.

The smallest part of a muscle that can contract independently, a motor unit, is composed of a neuron and the muscle fibers stimulated by it. In large muscles each motor unit may have 1000 to 2000 muscle fibers. The degree of activation of a muscle is a result of the number of activated (recruited) motor units. Note that the fibers of each motor unit are not contiguous but are dispersed throughout the muscle; thus, even if a single motor unit were stimulated, a large portion of the muscle would appear to contract.

The longitudinal and transversal repetitive structure of the muscle and the dispersion of the motor units throughout the muscle suggest that the muscle behavior

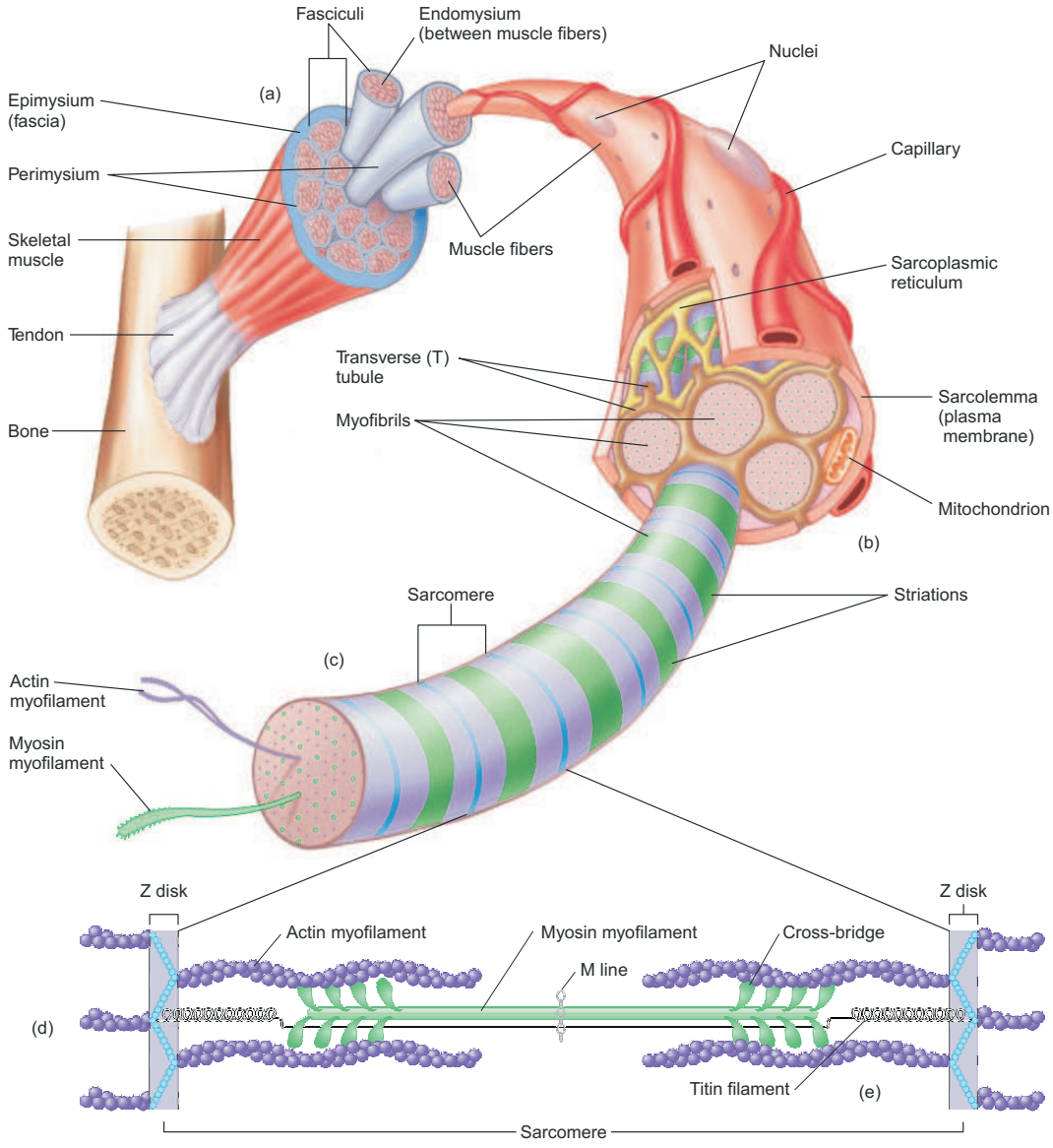

Figure 6.1: Structure of a skeletal muscle (adapted from [Seeley et al., 2004]).

is a scaled up version of the behavior of the muscle fibers which is in turn a scaled up version of the behavior of the sarcomeres.

The models proposed in the literature for the global mechanical behavior of each skeletal muscle reflect the structure and operating principles described above. A simple mechanical model was proposed by Hill in 1938 [Hill, 1938] and is still the basis for most of the currently used models. It is composed of three elements, as depicted in Fig. 6.2:

- A *contractile element* (CE), which models the active part of the muscle, freely extensible when unactivated, but capable of shortening when activated;
- A *series element* (SE), a nonlinear spring arranged in series with the contractile element, which allows a rapid change of the muscle state from inactive to active and provides an energy storing mechanism;
- A *parallel element* (PE), a nonlinear spring arranged in parallel with the two previous elements, which is responsible for the passive behavior of the muscle when it is stretched, even when the contractile element is not activated.

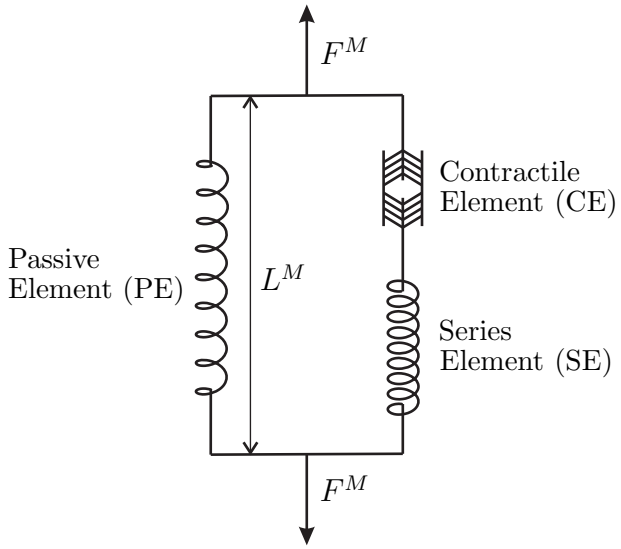

Figure 6.2: Hill's three element muscle model.

Although these interpretations are not unanimously accepted, the contractile element is generally identified with the sliding actin and myosin filaments, and the active force generated in this element is a result of the number of active cross-bridges between them. The series element is commonly associated with the intrinsic

elasticity of these myofilaments and cross-bridges and the parallel element may be related to the elasticity of the connective tissues (epimysium, perimysium and endomysium) and the sarcolemma.

From Figure 6.2 it is clear that the muscle force F^M, the forces in the contractile element, in the series element and in the parallel element, F^{CE}, F^{SE} and F^{PE}, respectively, satisfy the equilibrium equation:

$$F^M = F^{PE} + F^{SE} \tag{6.47}$$

$$F^{CE} = F^{SE} \tag{6.48}$$

On the other hand, the muscle length L^M and the lengths L^{CE}, L^{SE} and L^{PE} of those elements satisfy

$$L^M = L^{PE} \tag{6.49}$$

$$L^M = L^{SE} + L^{CE} \tag{6.50}$$

Denoting by L_0^M the *rest length of the muscle*. When fully activated at the constant length L_0^M the muscle develops a force F_0^M known as the *peak isometric muscle force*, i.e. the maximum steady-state tension force that a muscle can develop under isometric conditions; the length L_0^M is thus also known as the *optimal muscle length*. Gordon et al [Gordon and Huxley, 1966] tested this with a single skeletal fiber of a frog's skeletal muscle and concluded that if L^M/L_0^M was too small or too large, the tension would drop to zero. The maximum tension was produced when $L^M/L_0^M = 1$.

When non-activated $\left(F^{CE} = F^{SE} = 0\right)$, the muscle develops a force in the passive element (F^{PE}) that is positive for $L^M/L_0^M > 1$ (when the muscle is stretched) and that is essentially null for $L^M/L_0^M \leq 1$ (when the muscle is compressed). The evolution of F^{PE} is given by the following expression:

$$F^{PE} = F_0^M f_{PE}\left(\lambda^M\right) \tag{6.51}$$

where $\lambda^M = L^M/L_0^M$ is the muscle stretch and f_{PE} is an expression, function of λ^M.

When activated the muscle develops a force in the contractile element that is positive for $0.5 < \lambda^M < 1.5$ and that is essentially null for other values of λ^M:

$$F^{SE} = F_0^M f_{SE}\left(\lambda^M, \alpha\right) \tag{6.52}$$

where α is the activation level ranging from 0 to 1. In what concerns the series elastic element, experimental evidence characterizes it as a nonlinear spring, the stiffness of which is a function of the force F^{SE} in the same element [Zajac, 1989].

When activated, the muscle force developed in the contractile element depends on the muscle length (the muscle stretch λ^M), on the velocity of deformation of the contractile element (not considered on this work) and on the activation level.

Dividing the expressions (6.51) and (6.52) by the muscle physiological cross section area A_0, the nonlinear elastic relations for the longitudinal first Piola-Kirchhoff stresses in the parallel element and in the series element becomes:

$$T^{PE} = T_0^M f_{PE}\left(\lambda^M\right) \tag{6.53}$$

$$T^{SE} = T_0^M f_{SE}\left(\lambda^M, \alpha\right) \tag{6.54}$$

where $T_0^M = F_0^M/A_0$, is the *muscle peak stress*; this quantity may vary from muscle to muscle, particularly between "fast" and "slow" muscles and between young and old subjects [Zajac, 1989; Martins et al., 1998]: values ranging from 0.16 MPa to 1 MPa have been quoted in the literature [Crowningsfield and Brand, 1981; Zajac, 1989].

6.2.3 Constitutive model for the passive and active behavior of the human pelvic floor muscles

The model adopted for the 3-D passive and active behavior of the pelvic floor muscles is a generalization of the 3-D transversely isotropic hyperelastic model of Humphrey and Yin [Humphrey and Yin, 1987] presented in Section 6.2.1. This generalization is done in such a way that the muscle fiber term (6.6) already present in Humphrey's model is now modified to make it qualitatively and quantitatively compatible with the 1-D (longitudinal) constitutive equations (6.53) and (6.54) for the parallel and series elastic elements of the pelvic floor muscles. On the other hand, the additional (passive) elasticity given by the 3-D isotropic hyperelastic term (6.2) in Humphrey's model is tentatively kept with the same form, but with different parameter values.

The strain energy density per unit volume of the reference configuration is now given by the following expression:

$$U = U_I\left(\bar{I}_1^C\right) + U_f\left(\bar{\lambda}_f, \alpha\right) + U_J\left(J\right), \tag{6.55}$$

where U_I, and U_J, are defined in (6.2) and (6.8), respectively, and U_f is the strain energy stored in the muscle fibers which can be divided into a passive elastic part (U_{PE}) and an active part (U_{SE}) due to the contraction.

$$U_f\left(\bar{\lambda}_f, \alpha\right) = U_{PE}\left(\bar{\lambda}_f\right) + U_{SE}\left(\bar{\lambda}_f, \alpha\right). \tag{6.56}$$

For the passive strain energy, U_{PE}, it was used the expression defined in (6.6) and for the strain energy due to the contraction, the following expression, as presented in [Aulignac et al., 2004] was assumed :

$$U_{SE}\left(\bar{\lambda}_f, \alpha\right) = T_0^M \int_1^{\bar{\lambda}_f} f_{SE}\left(\lambda^M, \alpha\right) d\lambda^M. \tag{6.57}$$

where for the function $f_{SE}\left(\lambda^M, \alpha\right)$ the following expression was used:

$$f_{SE}\left(\lambda^M, \alpha\right) = \alpha \begin{cases} 1 - 4\left(\lambda^M - 1\right)^2, & \text{for } 0.5 < \lambda^M < 1.5 \\ 0 & \text{otherwise} \end{cases} \tag{6.58}$$

which means that for values of $\lambda^m > 1.5$ or $\lambda^m < 0.5$ the muscle produces no energy.

With these definitions, the second Piola-Kirchhoff stresses and the Cauchy stresses are again given by expressions (6.19) and (6.32), respectively. On these expressions $U_f^{'}$, given by (6.14), is now defined as:

$$U_f^{'} = U_{PE}^{'} + U_{SE}^{'}. \tag{6.59}$$

The expression for $U_{PE}^{'}$ is given in (6.14) and $U_{SE}^{'}$ is defined as:

$$U_{SE}^{'}\left(\bar{\lambda}_f, \alpha\right) = T_0^M f_{SE}\left(\bar{\lambda}_f, \alpha\right). \tag{6.60}$$

In what concerns the Jacobian of the constitutive model, it is again given by expression (6.44) or (6.46). The definition of $U_f^{''}$ given by (6.41), is now defined as:

$$U_f^{''} = U_{PE}^{''} + U_{SE}^{''}, \tag{6.61}$$

where $U_{PE}^{''}$ is defined in (6.41) and $U_{SE}^{''}$ is defined as:

$$U_{SE}^{''}\left(\bar{\lambda}_f, \alpha\right) = T_0^M f_{SE}^{'}\left(\bar{\lambda}_f, \alpha\right), \tag{6.62}$$

and the derivative $f_{SE}^{'}$ is defined as:

$$f_{SE}^{'}\left(\bar{\lambda}_f, \alpha\right) = \alpha T_0^M \begin{cases} -8\left(\bar{\lambda}_f - 1\right), & \text{for } 0.5 < \bar{\lambda}_f < 1.5 \\ 0 & \text{otherwise.} \end{cases} \tag{6.63}$$

6.2.4 Material parameters for the constitutive model implemented

The parameters for the material model implemented were obtained from the data produced by Janda [Janda, 2006]. In his work, Janda performed tests on three female pelvic floor fresh cadaver specimens (82, 66 and 38 years old). For the obtention of the parameters, a iterative process was used, by varying the constants b, c, A and a and running a small simulation (Figure 6.3) in accordance with the details of the tests performed by Janda. The procedure was repeated until a good fitting between the results from the FEM simulations and the results obtained by Janda was obtained. Figure 6.4 shows the experimental data obtained by Janda and the curve obtained by the finite element simulation.

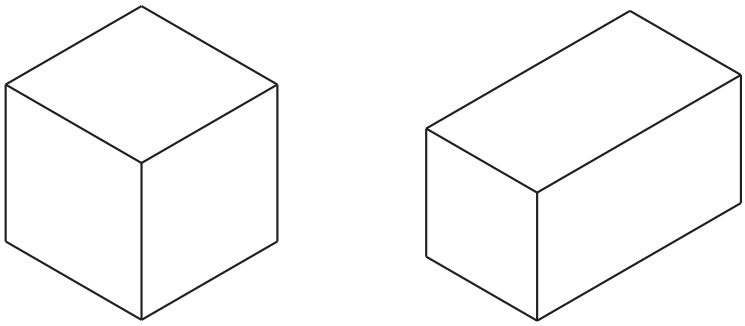

(a) Initial model

(b) Deformed model, deformation aplied in the fiber direction.

Figure 6.3: Finite element model used to obtain the material constants.

The parameters obtained that resulted in a good agreement with the experimental data are the following: $c = 1.85 \times 10^{-2}\text{N/mm}^2$, $b = 1.173$, $A = 2.80 \times 10^{-2}\text{N/mm}^2$ and $a = 0.6215$.

For the parameter D, related with the penalty condition (6.8) that ensures the incompressibility condition the value $D = 1 \times 10^{-4}\text{mm}^2/\text{N}$ was used.

The parameter T_0^M for the maximum tension produced by the muscle at resting length was considered to be $T_0^M = 0.682Pa$, in accordance with values proposed in the literature [Aulignac et al., 2004].

Figure 6.4 shows the stress/stretch relation obtained when stretching the model in the fiber direction.

6.3 Implementation in Abaqus

A standard general purpose finite element code such as ABAQUS is used to conduct the finite element simulations. The ABAQUS library of material models, although presenting a wide variety of materials, is not useful in what concerns the mechanical modeling of soft human tissues, with the possible exemption of some particular simpler cases. Nevertheless ABAQUS contains a user subroutine (UMAT) in which the user may code his own model, allowing ABAQUS to conduct simulations with complex constitutive equations, as the non-isotropic hyperelastic constitutive equation proposed in this work.

In the UMAT, given de deformation gradient, the user has to define the Cauchy stress tensor $\boldsymbol{\sigma}$ and the Jacobian matrix of the constitutive model, $d\Delta\boldsymbol{\sigma}/d\Delta\boldsymbol{\epsilon}$, were $\Delta\boldsymbol{\sigma}$ are the stress increments and $\Delta\boldsymbol{\epsilon}$ are the strain increments. Since ABAQUS / Standard is most commonly used with implicit time integration, the exact definition

of the consistent Jacobian should be used to ensure rapid convergence, this is particulary important if the material model allows large volume changes and geometric nonlinearity is considered.

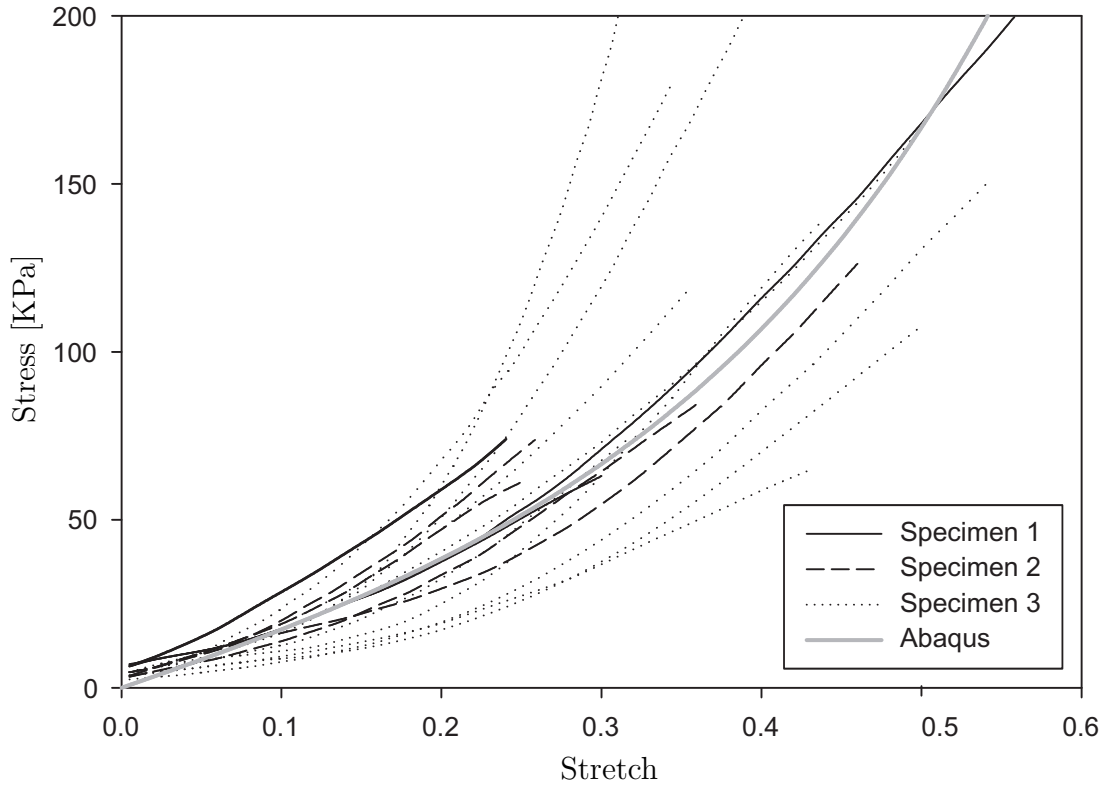

Figure 6.4: Test for the passive stretch of a cube in the in the direction of the fibers using the obtained parameters and experimental data obtained by Janda [Janda, 2006].

Chapter 7

Finite Element Simulations

7.1 Introduction

Pelvic floor dysfunctions represent an extensive problem with unknown dimensions. A study conducted by Olsen et al., based on a population under one health care system, showed that 11% of women had surgery for urinary incontinence or pelvic organ prolapse during their lifetime [Olsen et al., 1997]. Furthermore, statistics show that 30 to 40% of women suffer from some degree of incontinence in their lifetime [Kenton and Mueller, 2006]. Other study, conducted by Rortveit et al showed that the prevalence of this problem among nulliparous women ranged from 8% to 32%, increasing with age. They also showed that parity was associated with incontinence, the first delivery being the most significant [Rortveit et al., 2001].

It is still unclear whether muscle damage or neuropathy is the primary mechanism for the development of pelvic floor disorders, but some authors believe that the dysfunctions are largely caused by damage of connective tissues (ligaments and fascia) and muscles of the pelvic floor [Papa Petros, 2004]. Pregnancy and childbirth are considered particularly traumatic events leading to mechanical injury of the anal sphincter and levator ani muscles and to neuropathy of the pudendal nerves [Gregory and Nygaard, 2004]. The combined action of ligaments, fascia and muscles keeps in place and strengthens the pelvic organs, and the urethra, vagina and rectum [Papa Petros, 2004]. The normal function of the pelvic organs is thus dependent on the integrity of the pelvic floor structure. The repair of damaged ligaments/muscles should allow the cure of many of these conditions. Modern reconstructive pelvic floor surgery [Papa Petros, 2004], [Leval, 2003], [Delorme, 2001], uses polymeric or biologic tapes or meshes to reconstruct damaged suspensor ligaments or reinforce fascia tissue. The use of precise numerical models of the female pelvic cavity will, in the future, provide the tools to simulate, in a realistic manner, the pelvic floor function and the effects of its dysfunctions. And, in this manner, provide tools that

will allow surgeons to plan the surgery and perform it in a more controlled and reliable way.

During delivery, the pelvic floor experiences several changes, which cannot be measured in vivo due to clinical, technical and ethical reasons. Therefore, with this work, a biomechanical method of modeling a biologic process, in this case delivery, in order to estimate biomechanical changes (stretch, strain, etc) on tissues is presented. Knowledge of these biomechanical changes might help to explain known phenomena associated with delivery and pregnancy, like damage to the pelvic floor tissues, including the levator ani muscle. The purpose of the vaginal childbirth simulation presented is to determine the stretches and stresses induced in the pelvic floor muscles by the passage of a fetus.

To achieve these goals it is necessary to have a good geometrical description of the anatomy of the pelvic region, as well as good models of the complex mechanical behavior of the muscles and supporting structures in presence. These topics will be addressed in the following sections.

7.2 Geometrical and Finite Element Models

The construction of a 3D geometric model (such as the pelvic cavity) that can be manipulated, by numerical methods, to simulate the living human is still a challenge, namely due to the high complexity of human anatomy as recognized by several authors [DeLancey, 1999; Papa Petros, 2004]. There is also great lack of understanding of continuum biomechanics of soft biological tissues, as recognized by Humphrey [Humphrey, 2003].

One of the first attempts to model a human body was carried out in the USA, by slicing a frozen cadaver [Heinrichs, 1996] taking pictures of each slice. Although this project didn't produce any geometries, the data produced allowed many investigators to postprocess the data in order to obtain different geometrical models of the human body. The construction of a model (such as the pelvic cavity) that can be manipulated, by numerical methods, to simulate for a living human different boundary conditions is still a challenge that will probably take more than a decade to materialize, due to the high complexity of the anatomy of the human body as recognized by several authors [DeLancey, 1999; Papa Petros, 2004] and also the Open Problems regarding the Continuum biomechanics of soft biological tissues, as recognized by Humphrey [Humphrey, 2003].

Recently there have been some attempts to obtain a model for the human body [DeLancey, 1999], the pelvic floor cavity [Janda et al., 2003; Aulignac et al., 2005] and its contents [Hoyte et al., 2004; Boukerrou et al., 2004]. However at present there is not enough knowledge about the structural relationships identified by MRI imaging [Hoyte et al., 2004], to allow a precise numerical modelling to be developed

[Lien et al., 2004; Lien et al., 2005] .

In this work the Finite Element Method is used to conduct a biomechanical study of the pelvic floor muscles [Fung and Tong, 2001; Zienkiewicz and Taylor, 2005]. Using a finite element model which simulates the pelvic bones, pelvic floor muscles and fetus, the stretches and the deformations on the pelvic floor induced by the passage of the fetus, during a vaginal delivery, were measured.

A similar method as been used before to obtain the levator ani stretch during a vaginal delivery [Lien et al., 2004; Lien et al., 2005], but to our knowledge the work presented here is the first made using realistic models for the fetus and pelvic floor.

Simulation of the dynamic biomechanics of the body structures, its organs and interactions requires not only to know the physical properties of muscles, connective tissues and bone structures but also the activation mechanisms of the nervous system. Although hyperelastic constitutive models, with incorporated fiber activation, have been proposed in the past [Zahalak, 1981], reliable material coefficients and validated constitutive expressions to incorporate in the analysis are still lacking. Clinical aspects of pelvic floor disorders have been extensively studied in particular the effect of pregnancy and childbirth [Dimpfl et al., 1998; Gregory and Nygaard, 2004], however it is widely recognized that the understanding of pelvic floor components (muscles, nervous, fascia) damage and its interaction is still very limited; in particular a global perspective of the function of the pelvic floor and its anomalies is completely lacking [Gregory and Nygaard, 2004].

7.2.1 Pelvic floor Finite Element Model

The pelvic floor is composed of a group of muscles, which spreads across the inferior or the underlying surface of the pelvis. As a group, these muscles originate at the pubis, which is located anteriorly, at the frontal portion of the pelvis, just above the genitals, and extend back to the coccyx. These muscles have the form of a thick sheath, hence the name, "pelvic floor" muscles (see Chapter 2 for more details). To visualize the location and shape of these muscles see the finite element models of Figures 7.1-7.2.

Although standard 2-dimensional MRI and more recently, 3-dimensional MRI have been used to assess the anatomy of the female pelvic floor in cadavers and living women [Hoyte et al., 2004], the quality of the obtained geometric models is still reduced and therefore an alternative approach to the construction of the finite element model was used.

The finite element model of the pelvic floor used in this work was constructed using a geometrical data point-set obtained from cadaver measurements by Janda et al (Figure 7.1a). All the measurements were performed on one embalmed 72 years old female cadaver obtained for scientific research with no known pathologies of the pelvic floor [Janda et al., 2003]. The specimen was selected for having no pathology

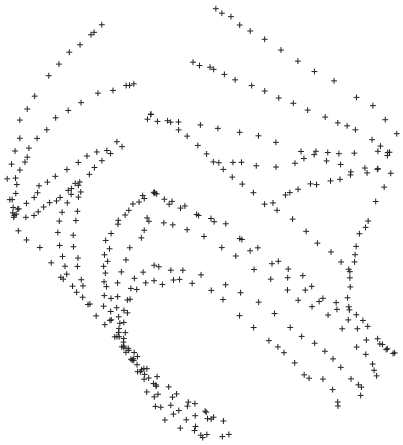

(a) Points

(b) Surfaces generated

(c) Finite element mesh.

Figure 7.1: Points, surfaces and finite element mesh.

to the pelvic floor. The cause of death was unknown and presumably not affecting the pelvic floor musculature. The result was a 3D point-set of the pelvic floor.

In Figure 7.1 the process used for the creation of the model is shown. Using the available points, lines were created, which allowed the definition of surfaces (Figure 7.1b) that were then used for the creation of the finite element mesh (Figure 7.1c). Initially a 3D model made with 4-node shell elements was obtained, which was then extruded to obtain the final 3D mesh, using 8-node hexahedral elements (volumetric elements). For the pelvic floor muscles it was assumed a constant thickness of 2mm [Aulignac et al., 2004; Aulignac et al., 2005].

In all the finite element simulations conducted, the nodes connected to the pelvic bone, ligament, and coccyx were fixed and all the others were left free.

For the childbirth simulations the finite element model of the pelvic floor was connected to a model of the pelvic skeletal structure (Figure 7.3 and Figure 7.4). To join the two models, some improvements to the initial model of the pelvic floor were made.

On Figure 7.2 the principal dimensions of the pelvic floor model are shown. These dimensions are in accordance with other models in the literature [Lien et al., 2004].

7.2.2 Pelvic girdle Finite Element Model

The pelvic girdle is the basin-shaped complex of bones that connects the trunk and legs, supports and balances the trunk, and contains and supports the intestines, urinary bladder, and internal sex organs. The pelvic girdle consists of paired hipbones, connected in front at the pubic symphysis and behind by the sacrum (see Chapter 2 for more details).

For the finite element simulations conducted in this work, the finite element model of the pelvic floor was connected to a model of the pelvic skeletal structure (Figure 7.3-7.4).

In order to join the two models, some improvements to the initial model of the pelvic floor had to be made: the Meshes 1 and 2 were added, as seen on Figure 7.5. The Mesh 1 represents the different connections between muscles of the pelvic floor and the coccyx, while the Mesh 2 represents the Arcus Tendineus, Obturator fascia and the Obturator Internus, which have a very important role in supporting the pelvic floor muscles.

The pelvic floor model attached to the pelvic girdle model is presented on Figure 7.6. The presence of the pelvic girdle finite element model has two main reasons, it helps to understand which nodes of the pelvic floor mesh will be restrained and which ones will be left free. As shown in the following sections, the pelvic floor girdle is also necessary in order to define the movements of the fetus, where the fetus cannot occupy the position of the pelvic girdle bones. After the boundary conditions are imposed and the movement of the fetus established, the pelvic girdle

(a) Points

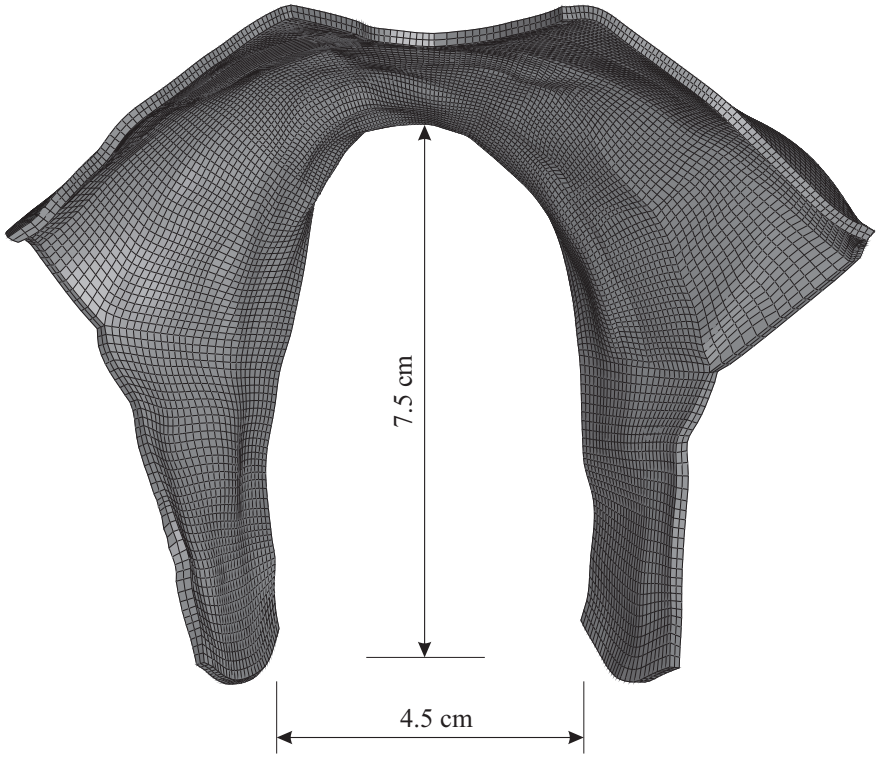

(b) Surfaces generated

Figure 7.2: Pelvic floor dimensions.

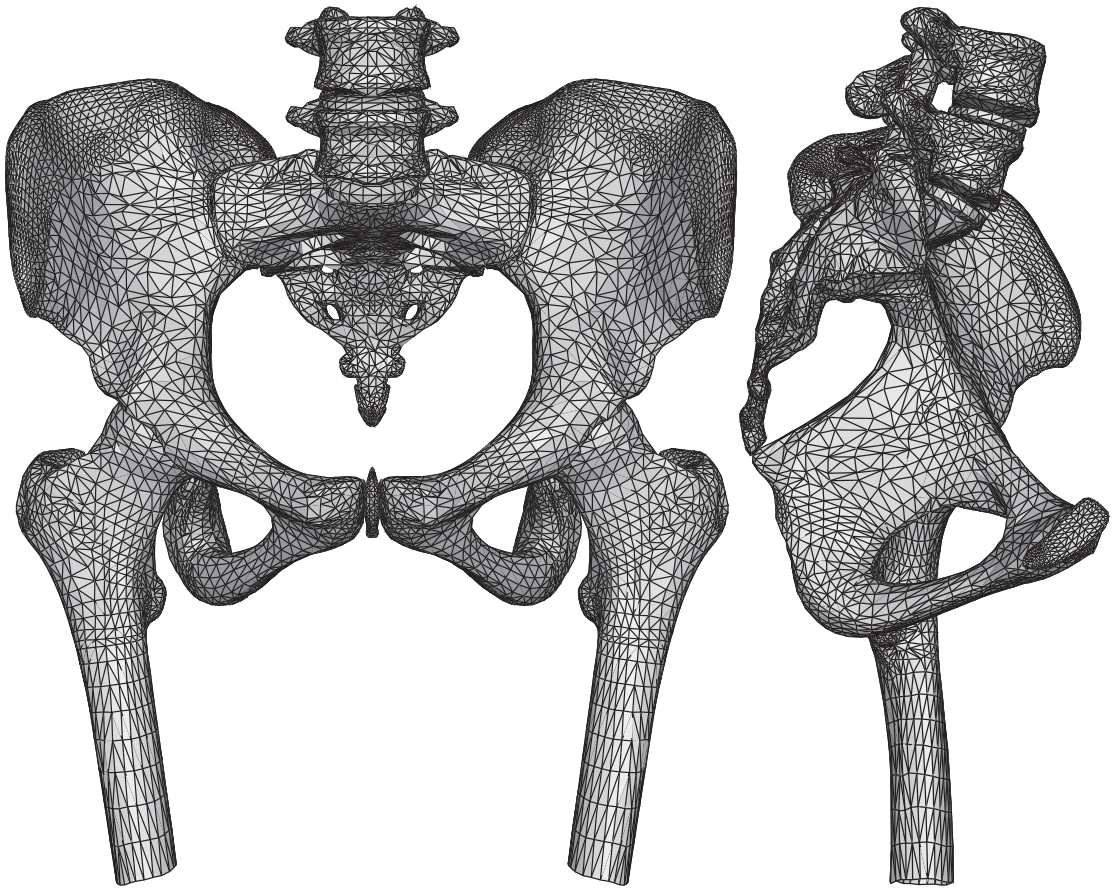

(a) Points (b) Surfaces generated

Figure 7.3: Pelvic girdle dimensions.

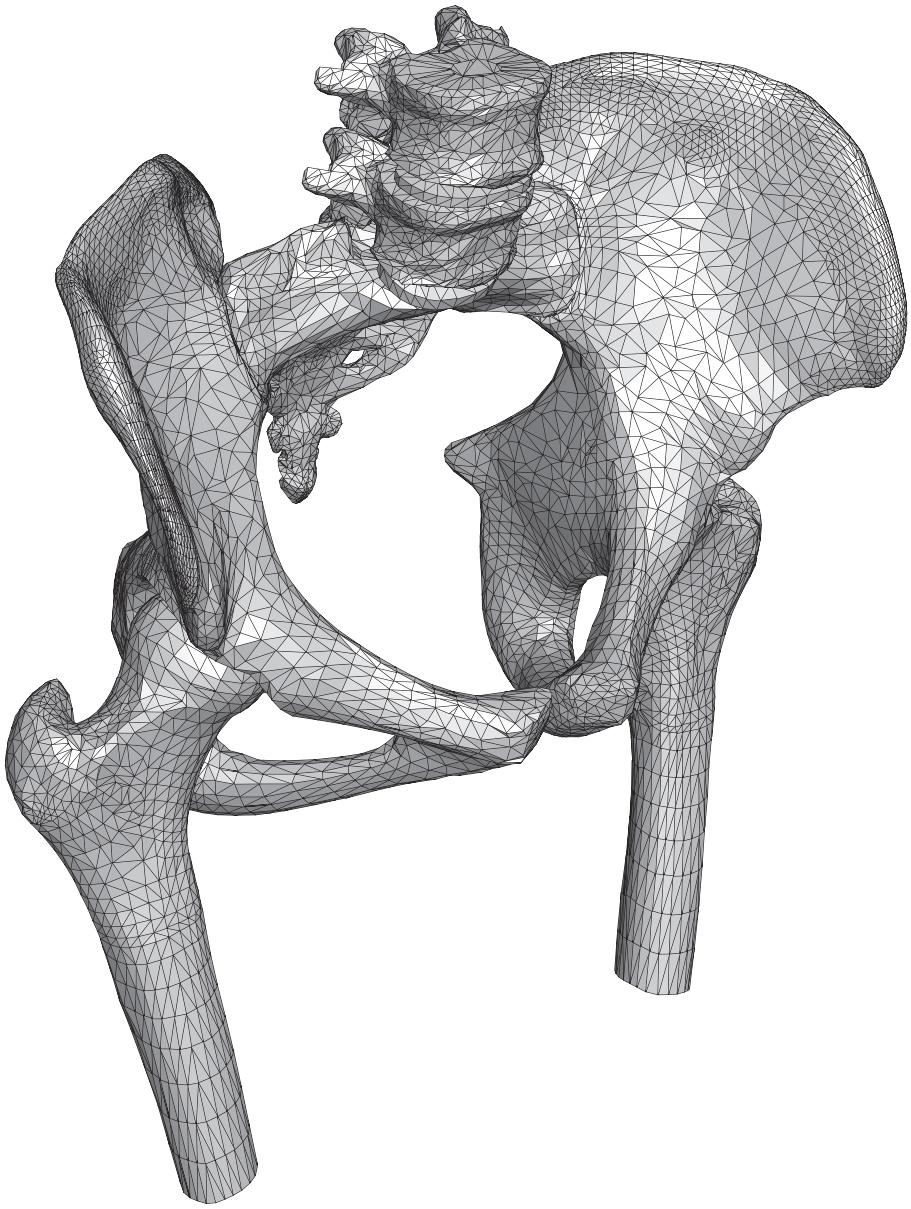

Figure 7.4: 3D view of the Finite Element model for the bones.

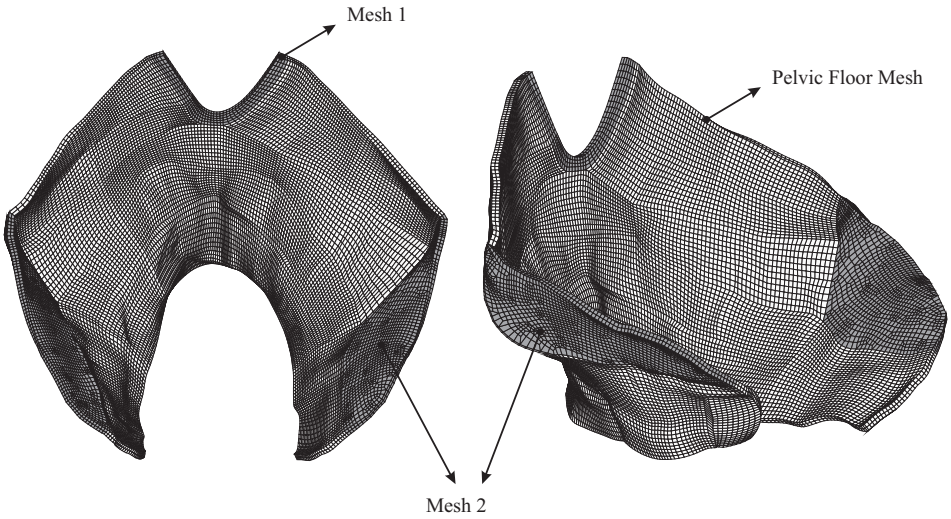

(a) Meshes added for support

(b) Modified pelvic floor

Figure 7.5: Pelvic floor model and meshes added for support.

model is removed, because its presence is no longer necessary and the computation time is faster.

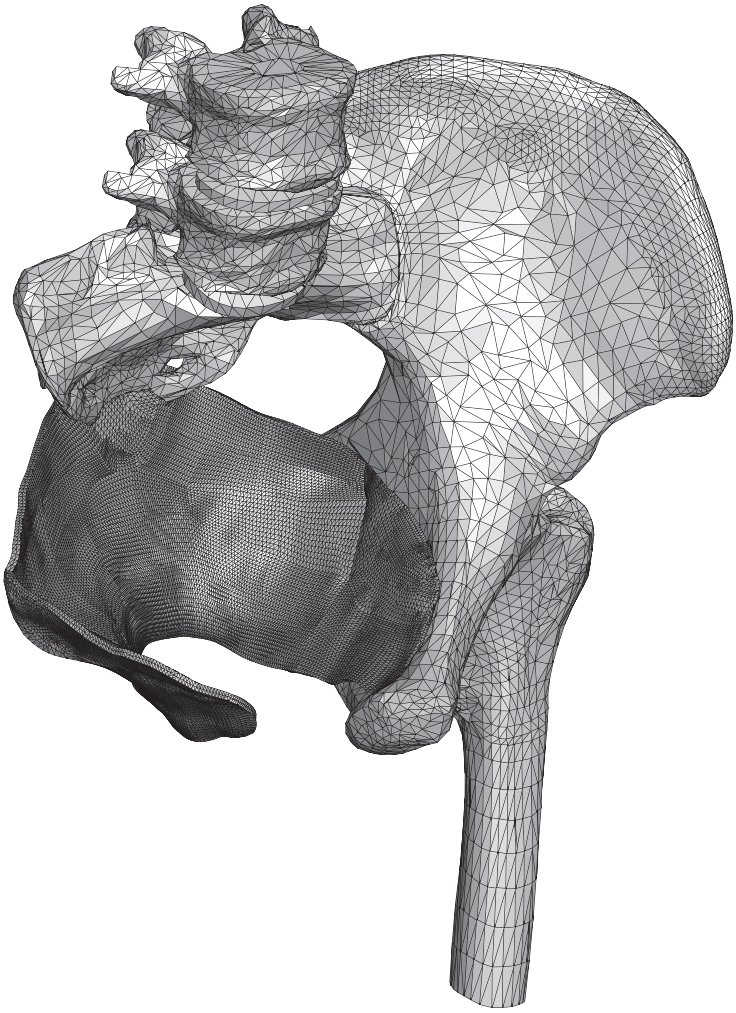

Figure 7.6: The two models joined together.

7.2.3 Fetus Finite Element Model

A fetus finite element model is necessary for the simulation of a childbirth, as presented in the following Sections. Figures 7.7 and 7.10 show the finite element model used is this work. The dimensions of the fetus model were adjusted in order for the principal obstetric dimensions for the head to be in accordance with the literature for a full-term fetus.

For the simulations of a vaginal delivery, the fetus shown in Figure 7.7 is not on a correct position. The first step applied to the fetus model was to reposition its arms and legs into a position appropriated for delivery. After a succession of simulations, using only the fetus mesh, and applying displacements to its arms and legs, the final mesh for the fetus, with the arms and legs repositioned is shown in Figure 7.8.

As the fetus head dimensions of the fetus are of major importance for the simulations conducted on the following sections, the scale of the fetus was adjusted in order to set this dimensions in accordance with the literature [Llewellyn-Jones, 2004]. Figure 7.9 shows the details of the fetus head and the principal obstetric dimensions.

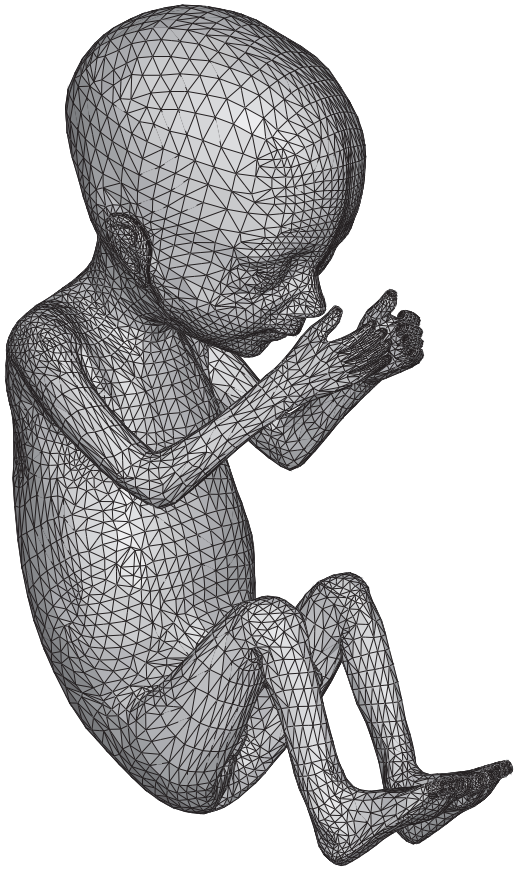

Figure 7.7: Fetus finite element model used.

The principal obstetric dimensions for the head are the following: Suboccipito-bregmatic diameter, 10 cm, Suboccipito-frontal diameter, 10.5 cm, Occipito-frontal diameter, 12.0 cm, Mento-vertical diameter, 13.0 cm and Submento-bregmatic diameter, 11.5 cm. These dimensions, shown in Figure 7.9 are in accordance with the

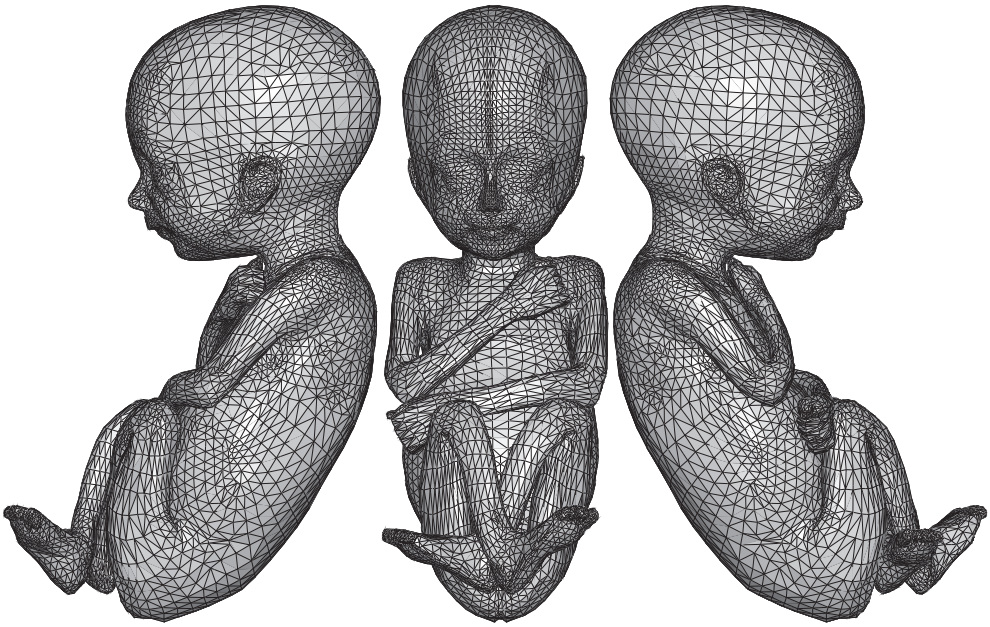

(a) Right view (b) Front view (c) Left view

Figure 7.8: Details of the fetus finite element model.

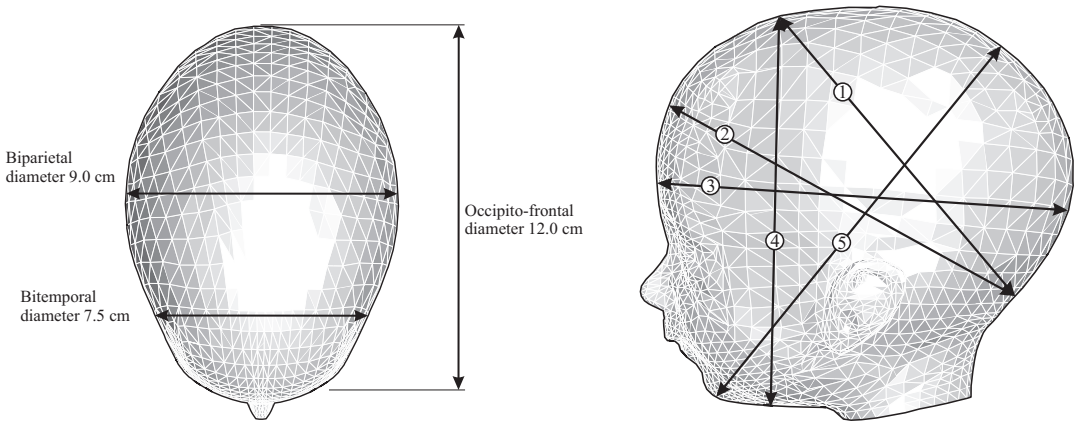

Diameter	Length	Presentation
1 Suboccipito-bregmatic	9.5 cm	Flexed vertex
2 Suboccipito-frontal	10.5 cm	Partially deflexed vertex
3 Occipito-frontal	11.5 cm	Deflexed vertex
4 Mento-vertical	13.0 cm	Brow
5 Submento-bregmatic	9.5 cm	Face

Figure 7.9: Dimension of the fetus head.

literature [Llewellyn-Jones, 2004].

In the simulations presented in the next sections, the simulations terminate after the fetus head passes the pelvic floor, therefore, the fetus head dimensions have major importance in the problem simulated.

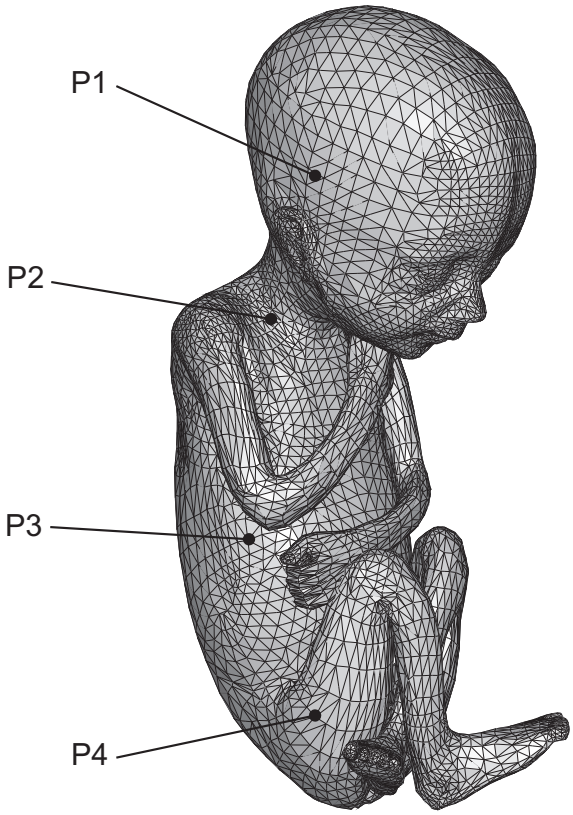

Figure 7.10: Fetus model and points used to control its movements.

The fetus finite element mesh is formed by tetrahedral elements. To control the movements of the fetus mesh the following approach was used: inside the fetus mesh, 4 groups of elements were given the properties of rigid elements and to each of these groups a reference node was assigned. Figure 7.10 shows the location of the different reference points. Therefore, by controlling the displacements and rotations of the reference nodes, the movements of the fetus are defined.

The material properties given to the remaining fetus mesh correspond to those of a material with a high stiffness, such that the fetus can be considerer rigid when compared with the pelvic floor. As the main purpose of this work is to study the behavior of the pelvic floor muscles during a vaginal delivery, using this approach will reduce the fetus deformations and facilitate the convergence of the simulation.

7.3 Numerical simulations of a childbirth delivery in vertex position

Labor is a sequence of uterine contractions that results in effacement and dilatation of the cervix and voluntary bearing-down efforts leading to the expulsion of the fetus through the vagina. Delivery is the mode of expulsion of the fetus and placenta. Labor and delivery is a normal physiologic process that most women experience without complications [DeCherney and Nathan, 2003].

Taking into account the irregular form of the birth canal and the relatively large dimensions of a grown up fetal head, it becomes evident that some of the diameters of the fetal head cannot pass trough the pelvis. Therefore, for the birth to take place, a process of adaptation and accommodation of the different dimensions of the fetal head to the different dimensions of the birth canal has to occur. The modifications in the position of the presenting part during labor are known as the mechanism of labor (see Chapter4).

The pelvic dimensions and configuration, the size of the fetus, and the strength of the contractions dictate the progress of labor. In essence, delivery proceeds along the line of least resistance, i.e., by adaptation of the smallest achievable diameters of the presenting part to the most favorable dimensions and contours of the birth canal.

The vertex position is when the baby's head is positioned to come out first, before the rest of the body, at birth. During normal labor the baby's head rotates so that the baby's face is toward the mother's back and the top of the baby's head is facing up (Figures 7.11-7.12). When this does not occur it is referred to as malposition and it may lead to difficult labor [DeCherney and Nathan, 2003]. Abnormalities of the fetal position, presentation, attitude or lie are known as malpresentations and they constitute collectively the most common cause of fetal dystocia, occurring in approximately 5% of all labors [DeCherney and Nathan, 2003].

The pelvic floor was modeled using hexahedral, eight-node elements (Abaqus C3D8H elements) and the muscle constitutive bahaviour was defined by implementing a UMAT subroutine in FORTRAN language [Hibbitt and Sorensen, 2007]. More details in the implementation can be consulted on Section 6.3. The constitutive model adopted in this work [Martins et al., 1998] for the 3D behavior of the pelvic floor muscles is a modified form of the incompressible transversely isotropic hyperelastic model proposed for passive cardiac tissues by Humphrey and Yin [Humphrey and Yin, 1987]. Mesh 1 and Mesh 2 were modeled using C3D8H elements (Figure 7.5) and the Neo-Hookean constitutive model, used in several other biomechanical studies [Peña et al., 2006] was used.

The fetus was modeled using tetrahedral elements and was considered as a deformable body, but with a very high stiffness. The movement of the fetus was

imposed by controlling the movement of several points belonging to the fetus model (Figure 7.10). All the finite element simulations were made with a non-linear analysis using the implicit version of the ABAQUS software.

The different finite element simulations presented on the following sections were made by imposing a predefined movement to the fetus, in order to obtain the stresses and strains on the pelvic floor. This methodology allows to apply different movements of the fetus during birth and to study the influence of those movements on the pelvic floor.

This problem is being intensely studied, and therefore it is possible to find in the literature some works that deals with it [Hoyte et al., 2004], [Lien et al., 2004], but to our knowledge, the simulation presented here is the first one using realistic models for the fetus body.

In this work, a vaginal delivery is shown in which different simulations were conducted. On Section 7.3.1 is shown a vaginal delivery where the fetus presents in occipito anterior position. On Section 7.3.1.1 the influence of the muscle activation on the pelvic floor, during a vaginal delivery with the fetus in occipito anterior presentation is shown. Section 7.3.1.2 shows the effect of the variation of the material parameters of the constitutive equation for the pelvic floor muscles on the results obtained. Using fetus movements that are not optimized, Section 7.3.1.3 shows the influence of the variation of the degree of rotation of the fetus head on the process of delivery.

In order to study the influence of a malposition of the fetus in the progress of delivery, a simulation of a childbirth delivery in occipito-posterior presentation is presented in Section 7.3.2. In Section 7.3.2.1 the influence of the muscle activation on the pelvic floor, during a vaginal delivery with the fetus in occipito posterior presentation is shown. Section 7.3.2.2 shows the effect of the variation of the material parameters of the constitutive equation for the pelvic floor muscles for a delivery in occipito-posterior presentation

7.3.1 Numerical modelling of childbirth delivery in occipito-anterior presentation

The mechanism of labor in vertex position consists of the following cardinal movements: engagement of the presenting part, descent of biparietal diameter of fetal head below the pelvic inlet, descent of the presenting part through the birth canal, flexion of the fetal head to present the smallest diameter of the fetal head to the maternal pelvis, internal rotation that facilitates the presentation of the optimal diameters of the fetal head to the bony pelvis, extension of the fetal head as it reach the vaginal introitus, external rotation of the fetal head after delivery to "face forward" relative to his shoulders, and finally, expulsion.

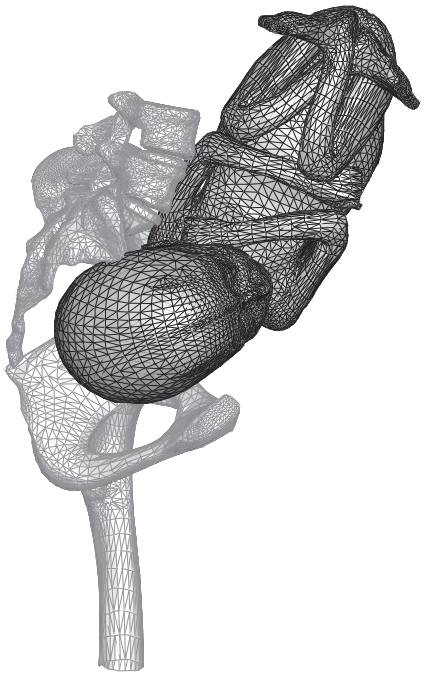

(a) Initial position

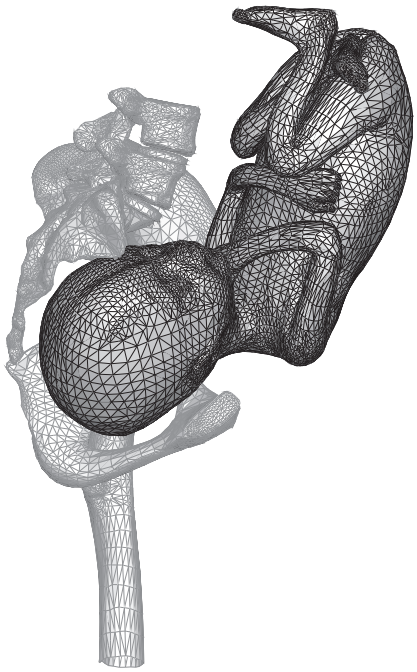

(b) Vertical displacement of 15 mm.

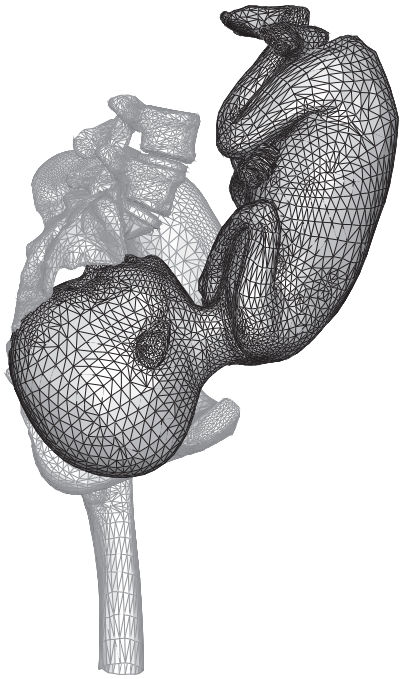

(c) Vertical displacement of 30 mm.

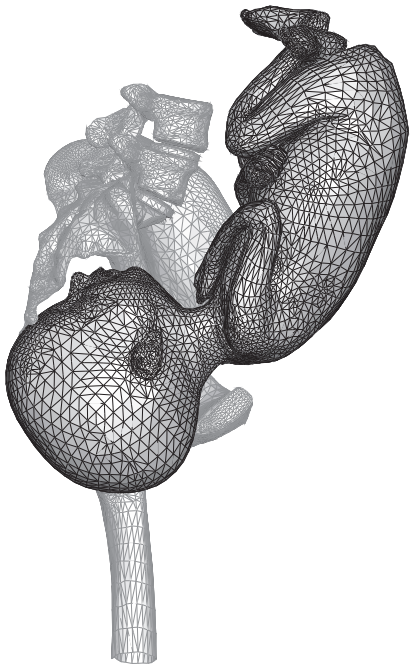

(d) Vertical displacement of 45 mm.

Figure 7.11: Fetus movements.

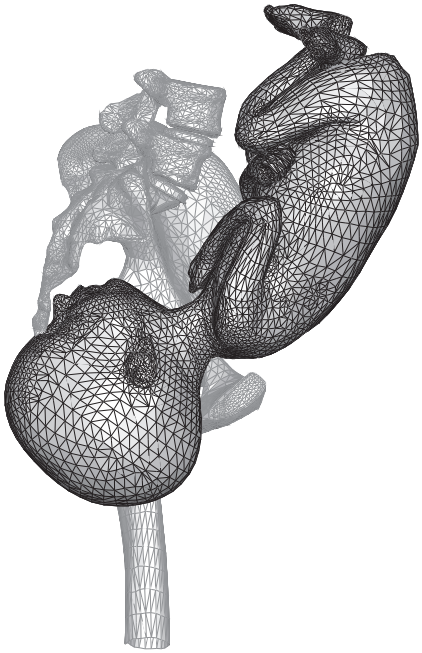

(a) Vertical displacement of 60 mm.

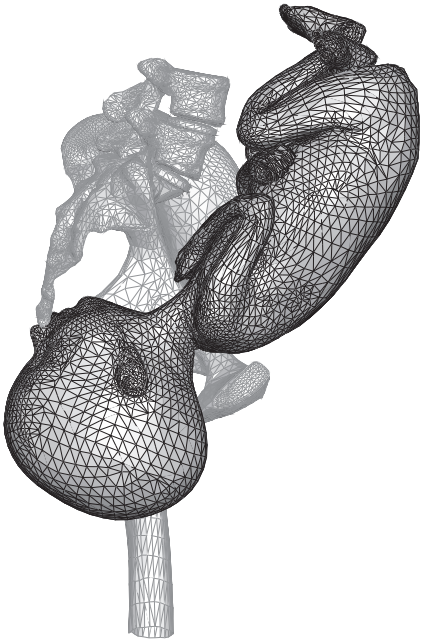

(b) Vertical displacement of 75 mm.

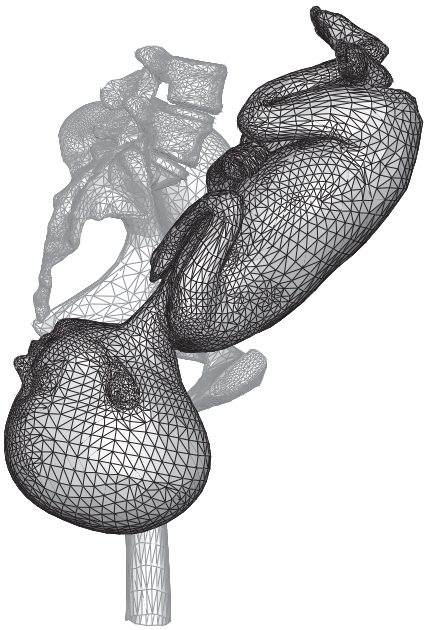

(c) Vertical displacement of 90 mm.

(d) Vertical displacement of 110 mm.

Figure 7.12: Fetus movements (continuation).

The cardinal movements refer to the movements made by the fetus during the first and second stage of labor. As the force of the uterine contractions stimulates effacement and dilatation of the cervix, the fetus moves toward the cervix. When the presenting part reaches the pelvic bones, it must make adjustments to pass through the pelvis and down the birth canal. The movements of the fetus during birth were simulated, which corresponds to the following cardinal movements: engagement of the presenting part, descent of biparietal diameter of fetal head below the pelvic inlet, descent of the presenting part through the birth canal, flexion of the fetal head to present the smallest diameter of the fetal head to the maternal pelvis, internal rotation that facilitates the presentation of the optimal diameters of the fetal head to the bony pelvis and extension of the fetal head as it reaches the vaginal introitus. The external rotation of the fetal head and expulsion were not simulated on this work. The simulation was performed using a non-linear analysis with the implicit version of the ABAQUS software.

The final step before the realization of the different simulations is the definition of the movements of the fetus. The movements of the fetus, in occipito-anterior presentation, were defined in order to present to the birth canal the smallest diameters of the fetal head at all times during birth. By using this optimization procedure, the movements of the fetus head obtained will correspond to the normal cardinal movements of the fetus, because nature in itself is an optimization process and the normal movements of the fetus are perfectly optimized.

Figures 7.11-7.12 show the sequence of movements of the fetus during birth, for different vertical displacements of the fetus head. The vertical displacement refers to the vertical displacement of the control point P1 (see Figure 7.10) which is placed inside the fetus head. Figure 7.11a shows the initial position for the fetus that corresponds to the engagement of the presenting part. Figure 7.12a shows the position of the fetus after the internal rotation, and the position of the fetus after the extension is shown in Figure 7.12d.

Controlling the fetus movements using the points presented in Figure 7.10 has proven to be a very versatile procedure, allowing to test movements of the fetus that are not optimized, as shown in the following Sections 7.3.1.3 and 7.3.2.

To process the stresses and strains obtained on the different simulations, several levels along the pelvic floor muscles were defined, as shown in Figure 7.13.

By introducing the different levels along the pelvic floor, it is now possible to present another measure of deformation, the stretch ratio. The stretch ratio is defined as the ratio between the current tissue length to the original tissue length. Measuring the length of the levels during the simulation and knowing their initial value allow us to determine the evolution of the stretch values for each path. The initial lengths for the different levels are also shown on Figure 7.13.

The definition of the different levels was made taking in attention the position of the known muscles of the pelvic floor. Levels 1 to 4 were defined on top of

the levator ani muscle and the pubococcygeal muscle. Levels 5 to 6 were defined on top of the iliococcygeal muscles. Level 7 was defined on top of the coccygeus muscles. Therefore, the results obtained for the different levels can be translated to the different muscles.

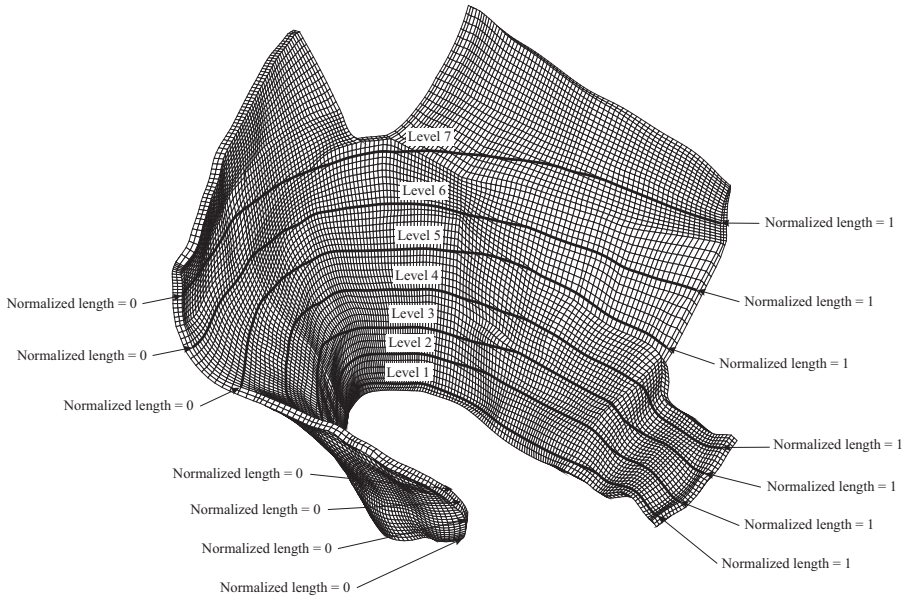

Levels	Initial Lenght	Length at 60 mm descent
Level 1	18.1 cm	22.1 cm
Level 2	19.2 cm	23.9 cm
Level 3	20.6 cm	25.1 cm
Level 4	22.1 cm	25.8 cm
Level 5	13.6 cm	16.2 cm
Level 6	13.9 cm	15.7 cm
Level 7	14.5 cm	15.8 cm

Figure 7.13: Levels used to evaluate the results.

Figure 7.14 shows the evolution of the stretch values obtained for the pelvic floor on the referenced levels, during during fetal descent. The stretch values were obtained by dividing the current length of the different levels by their original length (Figure 7.13).

The maximum value obtained for the stretch was approximately 1.63, obtained on level 1, for a vertical displacement of the fetal head of approximately 60 mm. This maximum stretch value occurs during the extension of the fetal head. The elevator ani muscle and the pubococcygeal muscle, which correspond to the levels 1 to 4

are the muscles that are subjected to the higher values of stretch. The iliococcygeal muscles (Level 5 to 6) and the coccygeus muscles (Level 7) are the muscles subjected to the lower values of stretch.

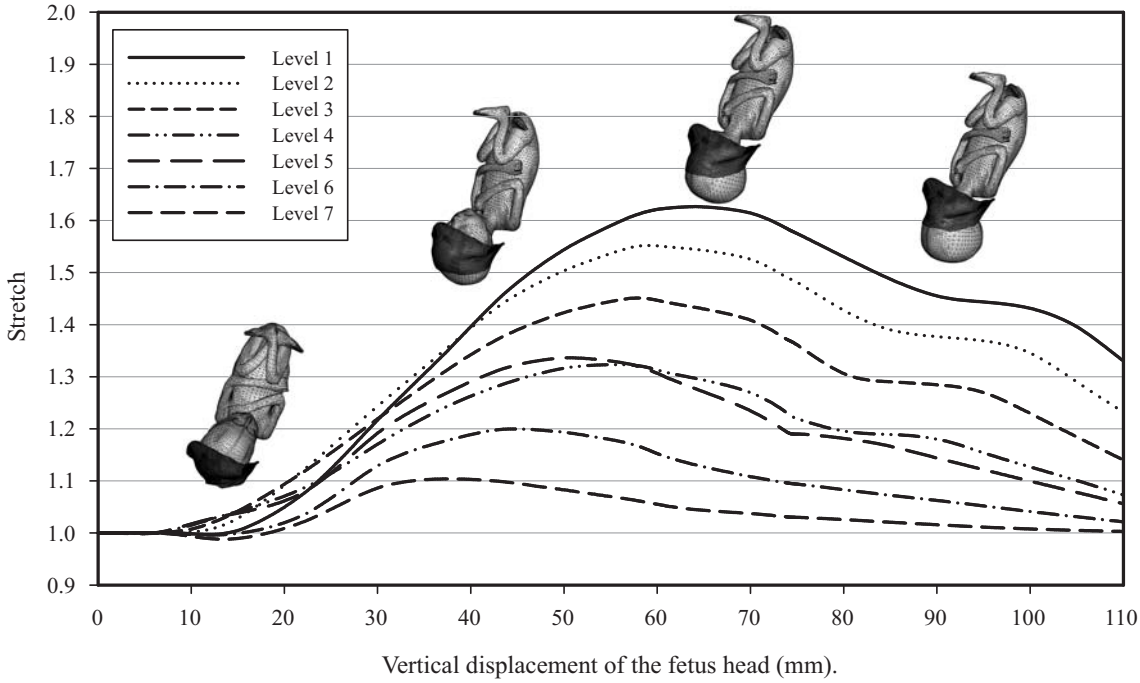

Figure 7.14: Stretch values obtained during the simulation.

Figure 7.15 shows the deformation field of the pelvic floor for a vertical displacement of the fetus head of 45, 60, 75 and 90mm. These figures clearly show the high deformations that the pelvic floor has to undergo in order to the progression of delivery to occur.

The distribution of the maximum principal stresses is shown in Figure 7.15. In the distribution of the maximum principal stresses, it can be observed that the maximum values appear on the most posterior area of the elevator ani muscle and the pubococcygeal muscle. The maximum value for the maximum principal stress, detected on the pelvic floor muscles was 1.48 MPa.

The following Figures 7.16 and 7.17 present the results obtained for the maximum principal stresses (S1) and for the logarithmic maximum principal strain (E1) along the different levels. The maximum principal strain - E1 can be defined as the ratio between the variation in length and the original tissue length. To the obtained results, the logarithmic function is applied. These results were evaluated for a fetal head descent of 30, 45, 60, 75, 90 and 105 mm. The stress and strain values are calculated for each finite element cell, along the different levels.

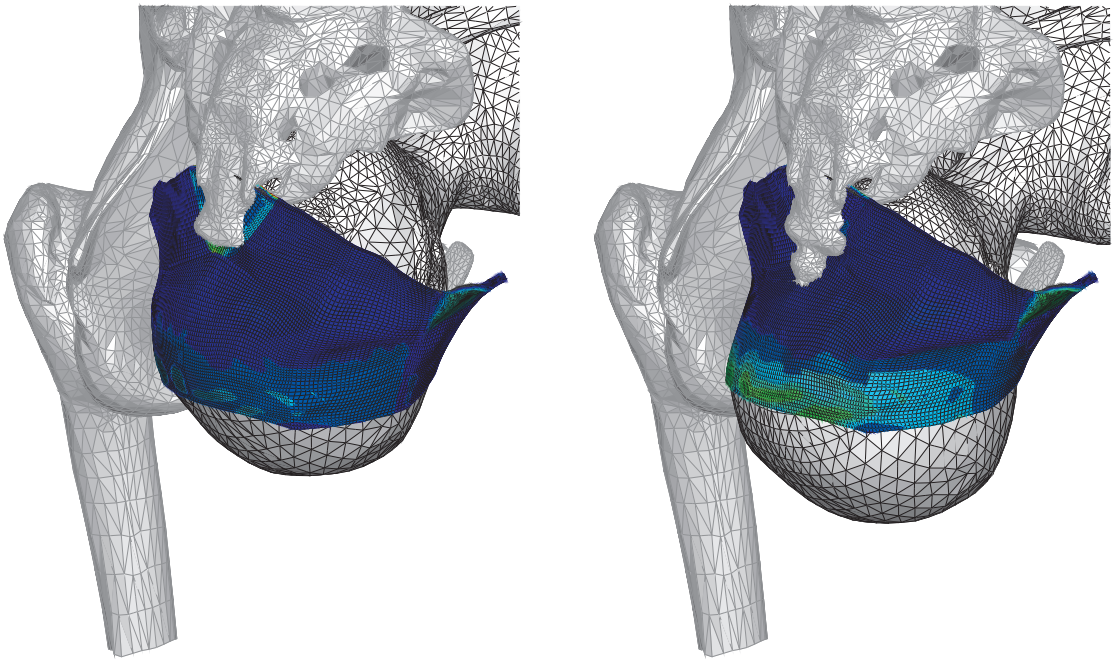

(a) Vertical displacement of 45 mm.

(b) Vertical displacement of 60 mm.

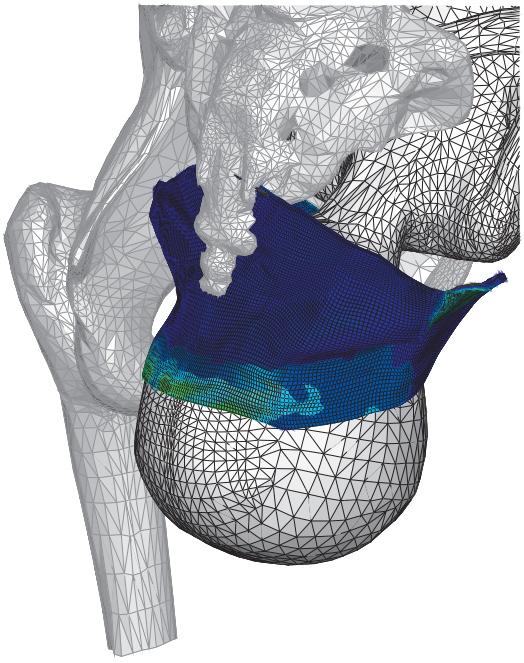

(c) Vertical displacement of 75 mm.

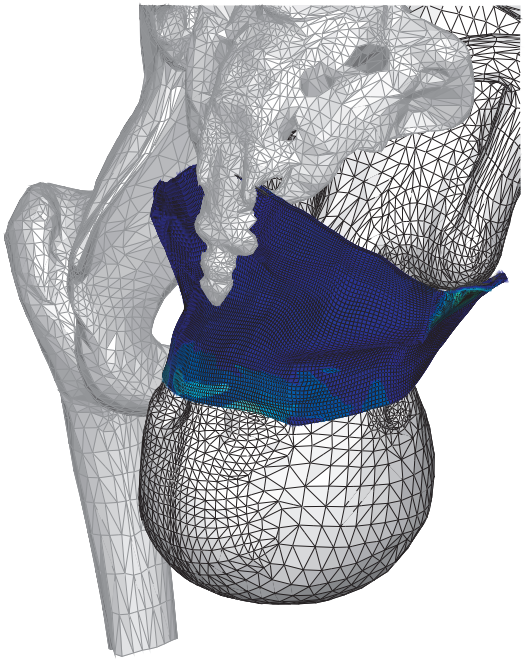

(d) Vertical displacement of 90 mm.

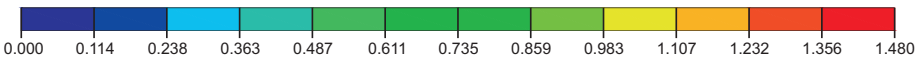

Figure 7.15: Distribution of the Maximum Principal Stresses [MPa].

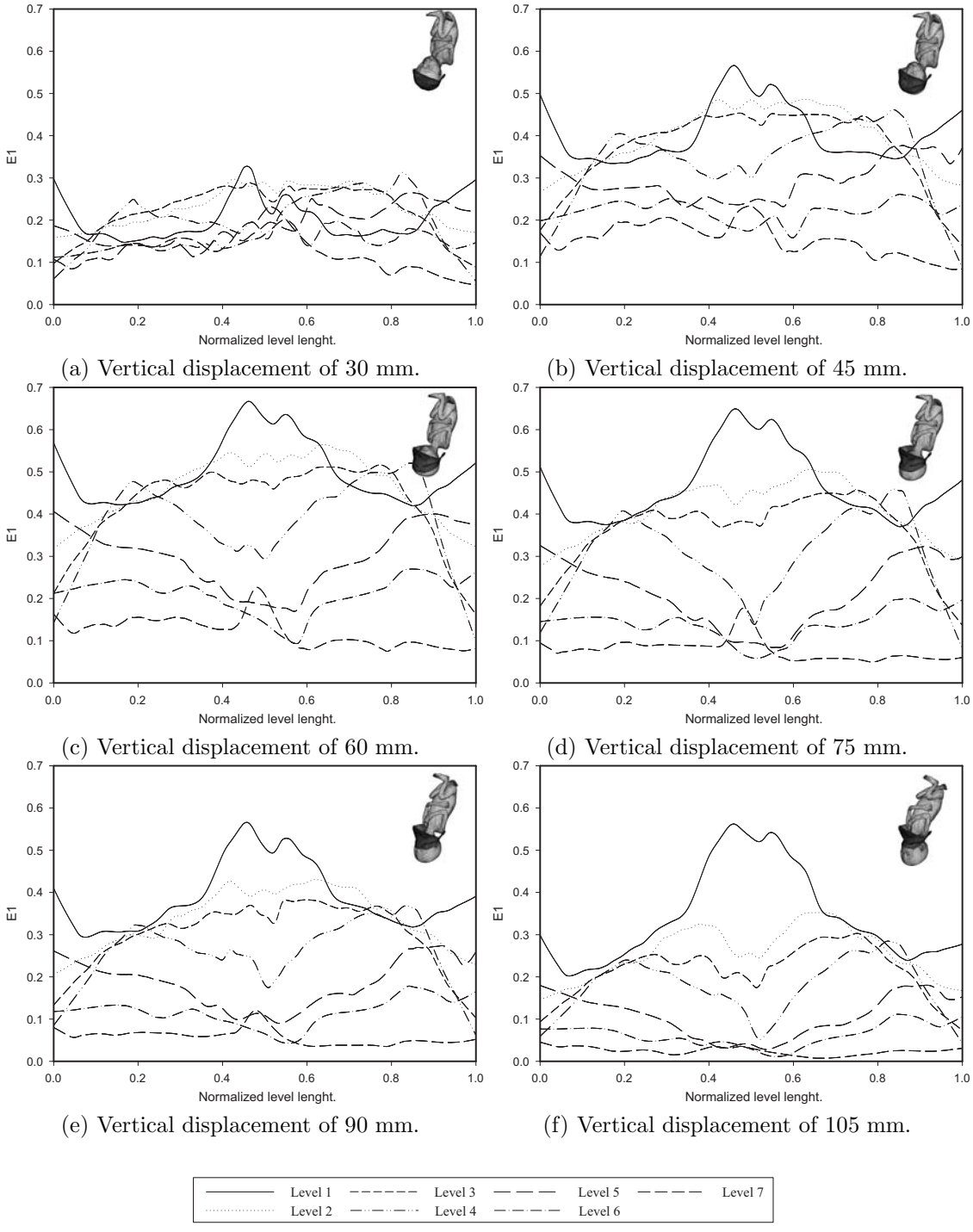

(a) Vertical displacement of 30 mm.

(b) Vertical displacement of 45 mm.

(c) Vertical displacement of 60 mm.

(d) Vertical displacement of 75 mm.

(e) Vertical displacement of 90 mm.

(f) Vertical displacement of 105 mm.

Figure 7.16: Logarithmic Maximum Principal Strain along the different levels.

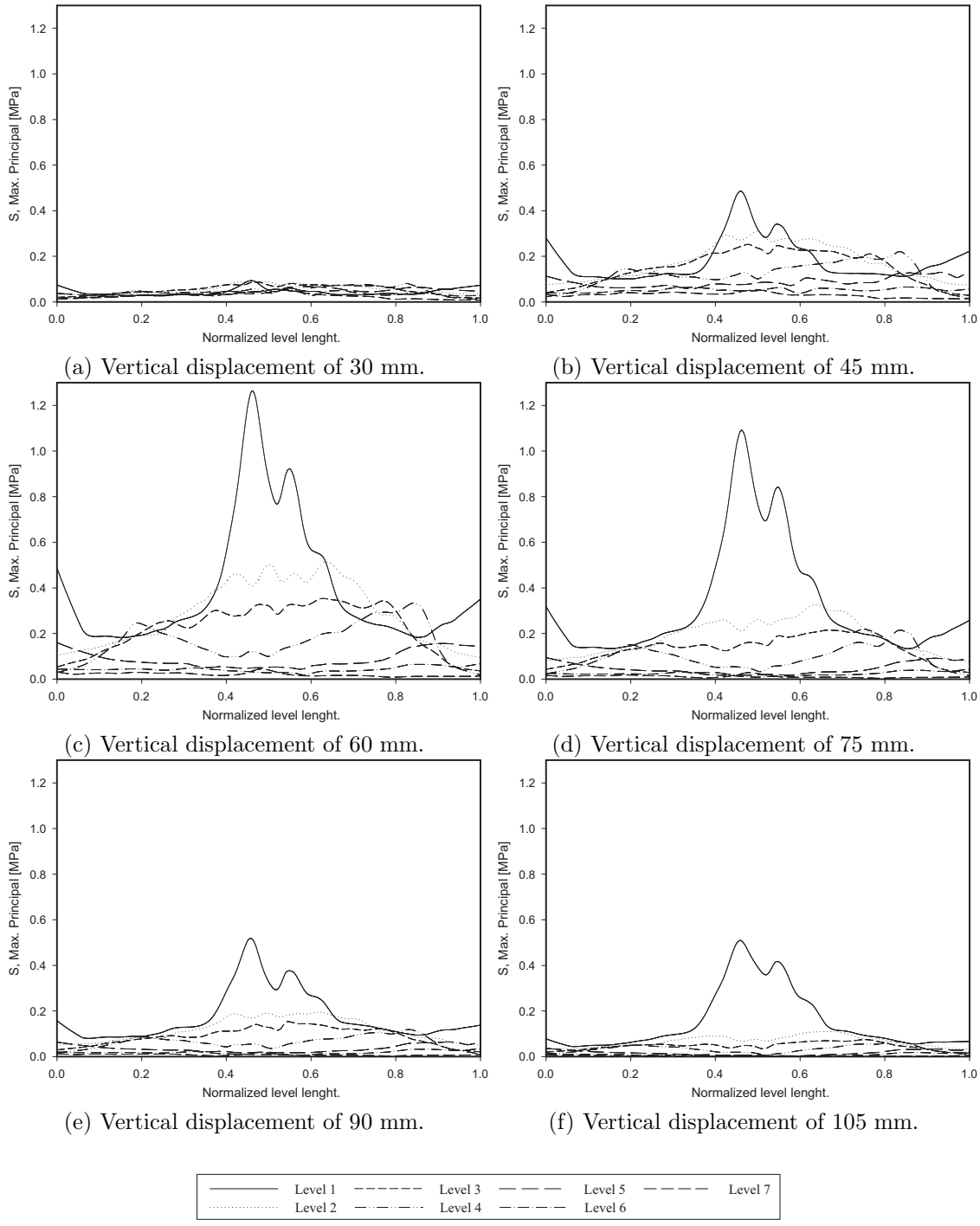

(a) Vertical displacement of 30 mm.

(b) Vertical displacement of 45 mm.

(c) Vertical displacement of 60 mm.

(d) Vertical displacement of 75 mm.

(e) Vertical displacement of 90 mm.

(f) Vertical displacement of 105 mm.

Figure 7.17: Maximum Principal Stresses along the different levels.

By presenting the different results along the different levels, the evolution of the different values can be clearly observed and also the place were the higher values are obtained.

In order to present a better comparison of the obtained results, for the different levels of Figure 7.13, only one scale varying between 0 and 1 was considered, called normalized length. For example, 0 represents one of the extremities, 0.5 represents the middle position and 1 represents the position in the opposite extremity (Figure 7.13).

Observing Figure 7.16, for the different vertical displacements of the fetal head, the maximum value of strain was obtained for a vertical displacement of 60 mm. As it is possible to observe on Figure 7.16c, a maximum value of 0.67 for the strain E1 on level 1 is obtained, for a vertical displacement of 60 mm. A close observation of the evolution of the strains along level 1 shows that high values of strain are obtained on the edges of level 1 which correspond to the points of attachment of levator ani muscle and the pubococcygeal muscle to the pelvic bones. The maximum values for the strain appear in an area that corresponds to the middle length of the levator ani muscle and the pubococcygeal muscle. By using this procedure to present the different results, it is possible to evaluate at each point of the different levels the values of strain. The stretch values presented in Figure 7.14 are more conservative, because it assumes that the deformation is equal along the different levels.

Figure 7.17 shows the evolution of the maximum principal stresses along the different levels for different vertical displacements of the fetal head. As one would expect, the evolution of the strains is closely related with the evolution of the strains (Figure 7.16), therefore the maximum value for the stress appear for roughly the same vertical displacement of the fetus head of 60 mm (Figure 7.17c). The maximum value obtained for the maximum principal stress was 1.26 MPa, on level 1. The maximum value for the stress appear on the middle length of the levator ani muscle and the pubococcygeal muscle. The extremities of level 1 also present high values of stress.

7.3.1.1 The influence of muscle activation on delivery in occipito-anterior presentation

Labor is a sequence of uterine contractions that results in effacement and dilatation of the cervix and voluntary bearing-down efforts leading to the expulsion per vagina of the products of conception. Muscle contraction plays an important role during labor [DeCherney and Nathan, 2003]. In true labor, the woman is usually aware of her contractions during the first stage. The intensity of pain depends on the fetopelvic relationships, the quality and strength of uterine contractions, and the emotional and physical status of the patient. Very few women experience no discomfort during the first stage of labor.

Contractions are often described as a cramping or tightening sensation that starts in the back and moves around to the front in a wave-like manner. Others say the contraction feels like pressure in the back. During a contraction, the abdomen becomes hard to the touch. In the childbirth process, the work of labor is done through a series of contractions. These contractions cause the upper part of the uterus (fundus) to tighten and thicken while the cervix and lower portion of the uterus stretch and relax, helping the baby pass from inside the uterus and into the birth canal for delivery [DeCherney and Nathan, 2003].

The work presented doesn't include the uterus, the largest muscle in a woman's body and the main muscle involved in the labor contractions, nevertheless it is possible to study the influence of the pelvic floor muscle activation during delivery. Although common sense dictates that the pelvic floor muscles should be relaxed during delivery, this study intends to verify the effects in the strains and stresses of an abnormal activation of the pelvic floor muscles during delivery. In order to study the effect of pelvic floor muscle activation during delivery, three simulations were conducted with different values of muscle activation α (Equation 6.52). The simulations were run with $\alpha = 0.05$, $\alpha = 0.10$ and $\alpha = 0.15$, where α is the activation level ranging from 0 to 1.

Figure 7.18a shows the results obtained for the logarithmic maximum principal strain E1 along level 1, for a fetus head descent of 60 mm and for the different muscle activations. The results obtained without activation ($\alpha = 0$) are also displayed on the same figures for comparison. In order to simplify the comparison of the results, only the results along level 1 are presented on Figure 7.18a and Figure 7.18b.

Observing the results obtained for the strains, it is visible that the higher values of strain follow the same evolution for the different activations. A maximum value of 0.67 for the strain E1 on level 1 is obtained, for the different activations, for a vertical displacement of 60 mm. This is the expected result because the higher strain values depend mostly of the dimensions of the fetus head. As the geometry of the fetus head has not changed, the results for the strains are very similar.

Figure 7.18b shows the results obtained for the maximum principal stress along level 1, for a fetus head descent of 60 mm, along level 1. For a muscle activation of $\alpha = 0.15$ a maximum principal stress of 1.36 MPa was obtained, which represents an increase of 8% in relation to the non-activated simulation $\alpha = 0.00$. For a muscle activation of $\alpha = 0.10$, a maximum value of 1.32 MPa was obtained. For $\alpha = 0.05$, a maximum value of 1.28 MPa was obtained. It can be stated that the maximum values for the maximum principal stresses are strongly dependent on the degree of muscle activation. When the muscle activation increases, the muscle becomes stiffer and therefore the value for the maximum principal tensions also increases.

If a relation between maximum principal stresses and stress induced muscle injury can be formulated, then it can be concluded that as the muscle activation increases, also the risk for injury increases.

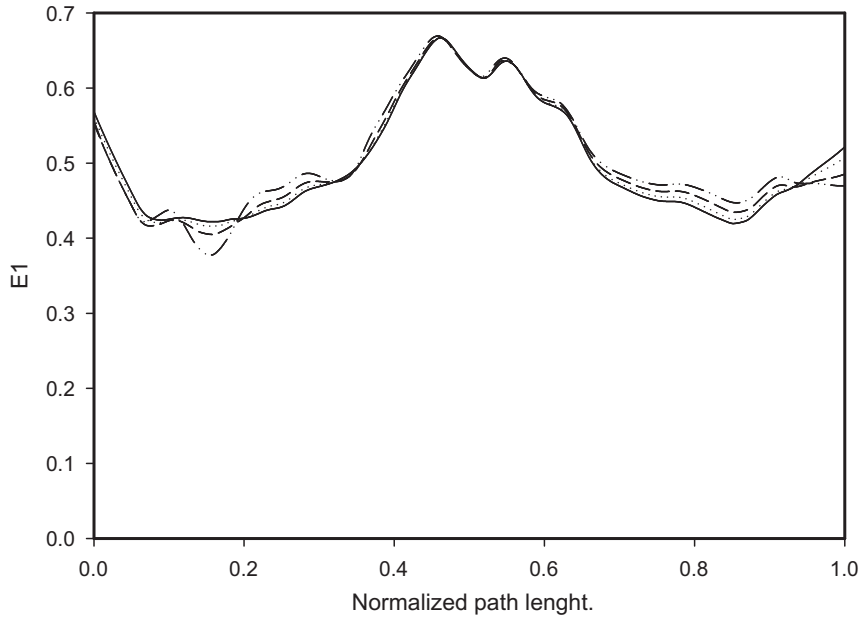

(a) Logarithmic maximum principal Strain E1.

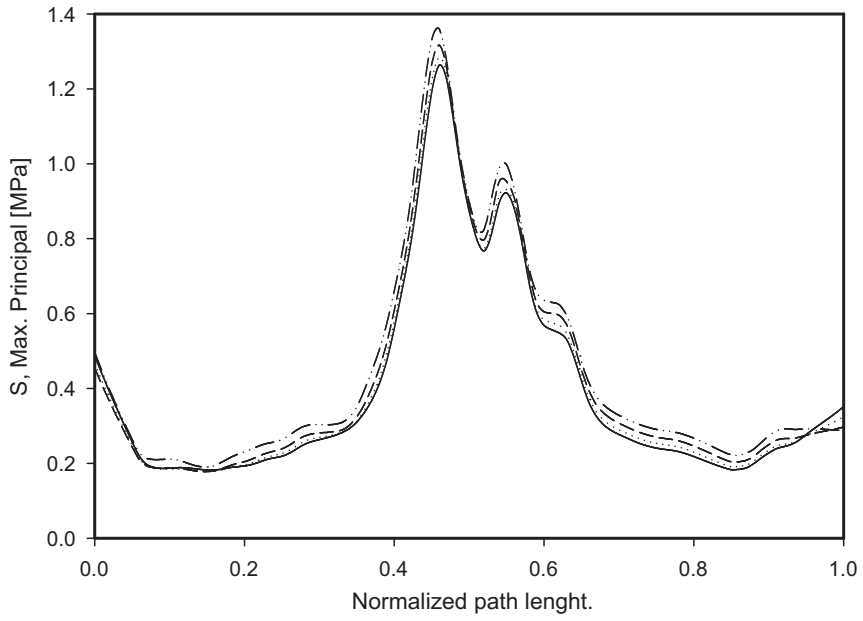

(b) Maximum Principal Stress.

Figure 7.18: Logarithmic maximum principal strain and maximum principal stresses for a fetus presenting in occipito-anterior presentation, for a fetus head descent of 60 mm, along level 1.

7.3.1.2 The influence of different material parameters on delivery in occipito-anterior presentation

Currently there is a common agreement that pregnancy, vaginal delivery, and aging are the main causes of damage to the pelvic floor, thereby initiating the development of incontinence and prolapse immediately or later in life [Snooks et al., 1984; Dimpfl et al., 1998]. Although the damage caused by vaginal delivery may lead to relaxation of the pelvic floor in most and/or weakening of contractile forces in some women [Peschers et al., 1996], it is still unclear whether this damage is of direct myogenic, neurogenic, or connective tissue origin.

From a mechanical point of view, age and parity alters the behavior of the pelvic floor muscles, and therefore, between different subjects, substantial differences in the mechanical behavior can be expected, as observed in [Janda, 2006]. In order to study the effect of the possible variability of the mechanical behavior of the pelvic floor muscles, and its influence on the obtained results, two new sets of constitutive parameters were introduced (Figure 7.19).

The procedure used to obtain the material parameters used on the simulations is described on Section 6.2.4. Figure 7.19 shows the data obtained by Janda [Janda, 2006]. All measurements were performed on three female pelvic floor fresh cadaver specimens (82, 66 and 38 years old). It can be observed that a great variability exists on the results obtained, between the different specimens and even for the same specimen. Figure 7.19 also clearly shows the nonlinear and elastic behavior of the pelvic floor muscles.

In order to verify the influence of the utilization of different material behaviors on the obtained results, two new simulations of a fetus delivery, in occipito-anterior presentation, with two new sets of material properties were conducted. To the initial material parameters, obtained on Section 6.2.4, two new sets of material parameters were introduced. The first set shows a response that is stiffer than that of the original constants used. The stress/strain behavior for the pelvic floor muscles with this set of parameters is shown in Figure 7.19 with curve Abq. Mat 2. Figure 7.19 also shows the pelvic floor behavior with the initial set of parameters (Abq. Mat. 1). The behavior of the second new set of parameters, a softer behavior, is shown in the same Figure, with curve Abq. Mat. 3.

The constitutive parameters for Abaqus Material 1 are $c = 1.85 \times 10^{-2}\text{N/mm}^2$, $b = 1.173$, $A = 2.80 \times 10^{-2}\text{N/mm}^2$ and $a = 0.6215$, for Abaqus Material 2 $c = 2.00 \times 10^{-2}\text{N/mm}^2$, $b = 1.75$, $A = 4.20 \times 10^{-2}\text{N/mm}^2$ and $a = 0.6215$, and for Abaqus Material 3 $c = 1.30 \times 10^{-2}\text{N/mm}^2$, $b = 1.173$, $A = 1.96 \times 10^{-2}\text{N/mm}^2$ and $a = 0.6215$.

For all the different materials used, for the parameter D the value $D = 1 \times 10^{-4}\text{mm}^2/\text{N}$ was used and for the parameter T_0^M for the maximum tension produced by the muscle at resting length was considered to be $T_0^M = 0.682Pa$, in accordance

with values proposed in the literature [Aulignac et al., 2004].

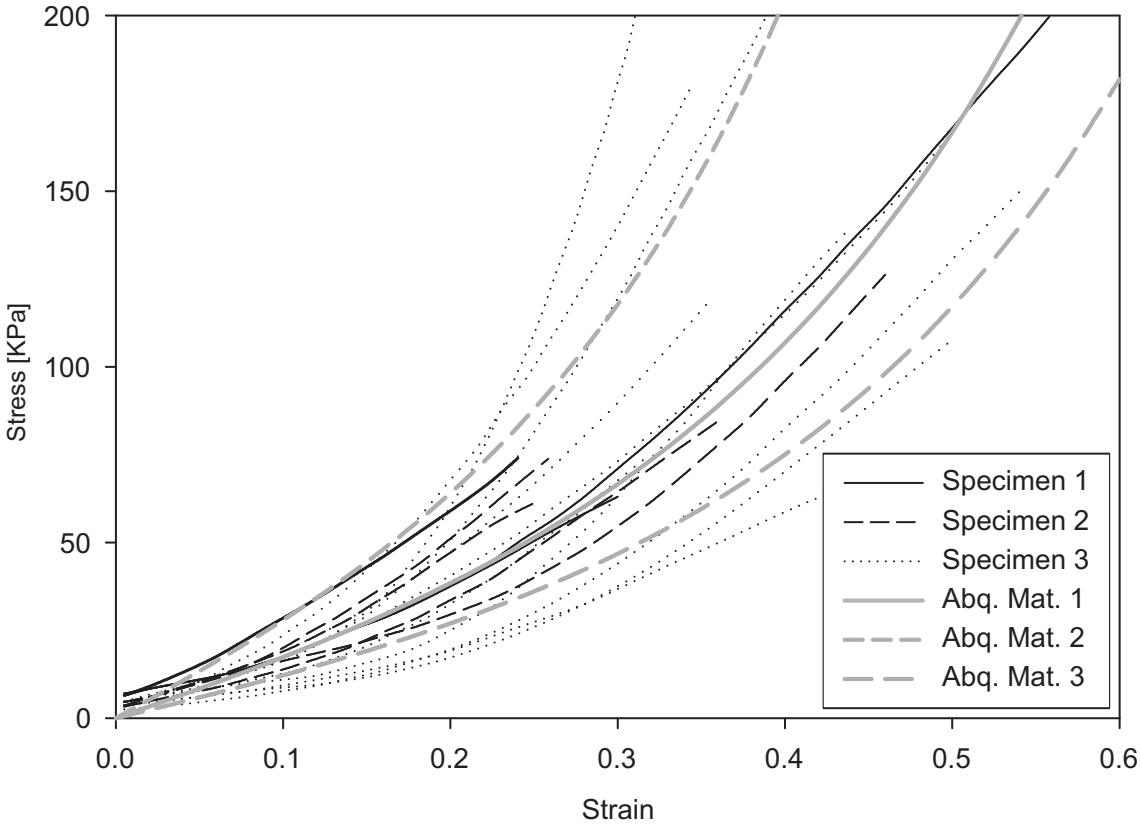

Figure 7.19: Uniaxial stress-strain response for passive material properties of the pelvic floor muscles.

Figure 7.20 shows the evolution of the logarithmic maximum principal strain obtained during the new simulations, with the different material parameters. In Figure 7.20it can be observed that of the logarithmic maximum principal strain along level 1 is approximately the same for the three different pelvic floor muscle behaviors. As discussed on the previous section, this is the expected result because the higher strain values depend mostly of the dimensions of the fetus head. As the geometry of the fetus head has not changed, the results for the strains are very similar. The small differences verified for the different vertical displacements between the Abaqus Material 1 and the remaining materials sets, are due to different relative displacements between the pelvic floor muscles and the fetus head. During the finite element simulation, when the fetus head passes trough the pelvic floor, the pelvic floor finite element mesh tends to slip on the fetus head. With different material parameters, this occurs for different fetus head vertical displacements. Nevertheless

the obtained results are very close between them. The maximum values obtained for E1 (logarithmic maximum principal strain) was 0.67 for The Abaqus Material 1 and 3, for the Abaqus Material 2, the maximum value was 0.64.

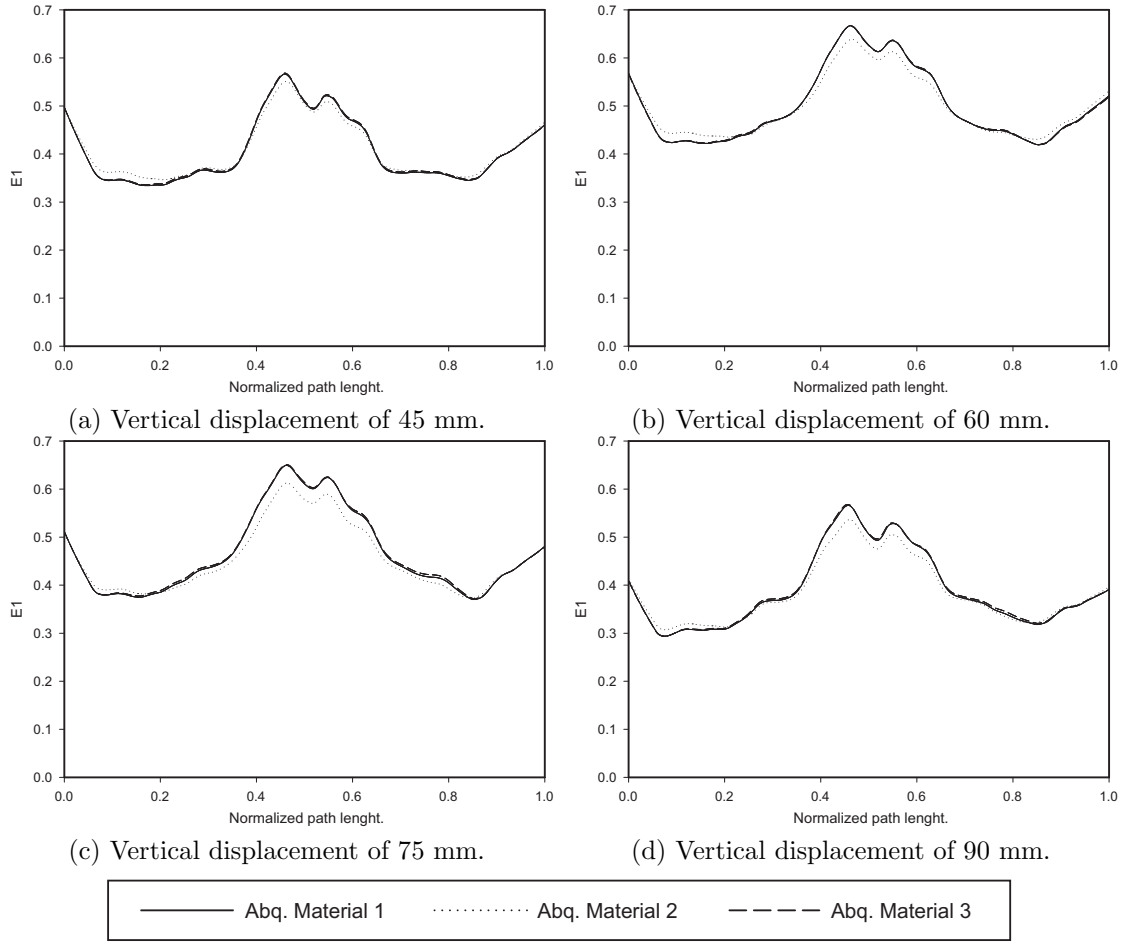

(a) Vertical displacement of 45 mm.

(b) Vertical displacement of 60 mm.

(c) Vertical displacement of 75 mm.

(d) Vertical displacement of 90 mm.

Figure 7.20: Logarithmic Maximum Principal Strain along level 1, for the different material parameters and for different fetus head displacements.

Figure 7.21 shows the evolution of the maximum principal stress along level 1 for a vertical displacement of the fetus head of 45, 60, 75 and 90 mm. Contrary to the strain values obtained, which are very close together, the stress values obtained present considerable differences between the different parameter sets. The maximum values for the maximum principal stress were obtained for a vertical displacement of 60 mm. Using the first set of material parameters (Abq. Material 1) a maximum value of 1.26 MPa was obtained, using the second set of parameters (Abq. Material 2) a value of 3.50 MPa was obtained and for the third parameter set (Abq. Material

3), a value of 0.89 MPa was obtained. A difference of almost 300% exists between the maximum values obtained with the different materials. This differences on the obtained results occur due to the exponential behavior of the constitutive model used. For larger strains, a small increment in the strains will translate in a large increment in the stresses.

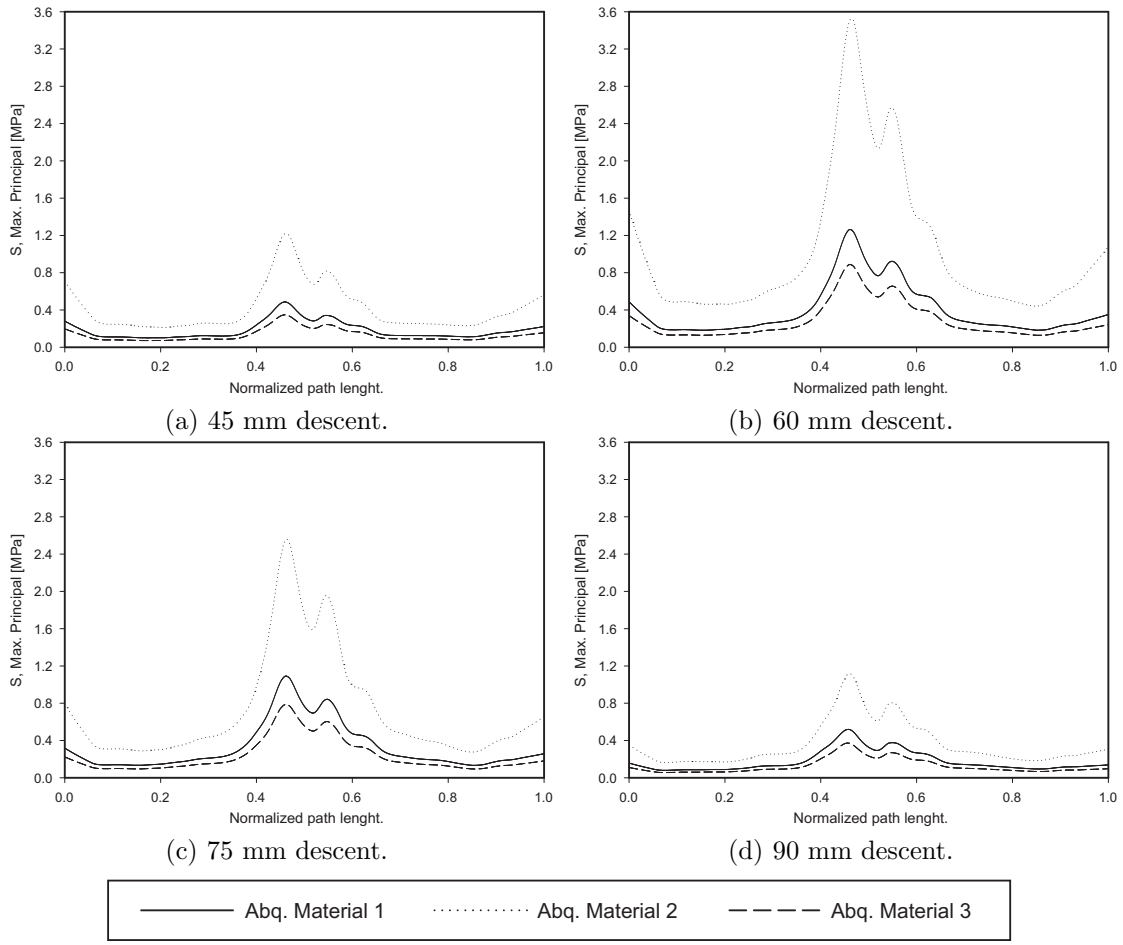

(a) 45 mm descent.

(b) 60 mm descent.

(c) 75 mm descent.

(d) 90 mm descent.

Figure 7.21: Maximum Principal Stress along level 1, for the different material parameters and for different fetus head displacements.

The finite element simulations presented on this section clearly show that the utilization of a representative set of parameters for a given subject is essential in order to obtain correct results. As shown, due to the exponential behavior of the constitutive model used, although the results for the strains are very similar, the stresses obtained are substantially different.

7.3.1.3 The influence of the variation of the fetus head flexion on delivery in occipito-anterior presentation

Malpositions are abnormal positions of the vertex of the fetal head (with the occiput as the reference point) relative to the maternal pelvis. Malpresentations are all presentations of the fetus other than vertex. Abnormal presentation and position are encountered infrequently during labor. Breech and transverse presentations should be converted to cephalic presentations by external cephalic version or delivered by cesarean section. Face, brow, and compound presentations are usually managed expectantly. Persistent occiput transverse positions are managed by rotation to anterior positions and delivered as such. Occiput posterior positions can be delivered as such or rotated to occiput anterior positions. As with any position or presentation, an obstetrician should not hesitate to abandon any rotational or operative vaginal procedure and proceed to cesarean delivery if rotation or descent does not occur with relative ease [Stitely and Gherman, 2005].

The descent of the fetus through the pelvis is a prerequisite for vaginal delivery. The fetus has to undergo a series of important manoeuvres to negotiate its journey through the maternal pelvis. The pelvis has three important diameters. The pelvic inlet has a wide transverse diameter of approximately 13 cm. The mid-cavity of the pelvis is round, and contraction of the mid-pelvis is suspected if the ischial spines are prominent or the pubic arch is narrow. The pelvic outlet has a wide anterior-posterior diameter. The fetal manoeuvres that occur during the mechanism of labour to allow the fetus to traverse the pelvic diameters in the optimal position are described below. Not all fetuses follow this pattern, as it is dependant on the presenting part. The commonest situation is with the fetus in a longitudinal lie with a cephalic presentation and a well-flexed attitude. In these circumstances, the vertex (the area bounded by the anterior edge of the posterior fontanelle, the two parietal eminences and the posterior edge of the anterior fontanelle) hits the pelvic floor first and rotates anteriorly, resulting in an occipito-anterior position with the occiput as the denominator.

Engagement of the fetal head occurs in the weeks before the onset of labour in nulliparous women, but often not until the onset of labour in multiparous women. It occurs secondary to the descent of the presenting part. The head is engaged when the widest diameter of the presenting part (the biparietal diameter in a cephalic presentation) has passed the pelvic brim or inlet. Once engaged, the head is fixed in the pelvis and is no more than two to three-fifths palpable per abdomen.

Descent of the fetal head occurs progressively during labour secondary to contraction and retraction of the myometrium.

Flexion of the fetal neck ensures that smaller diameters of the fetal head present that can negotiate the pelvis more easily. With moderate flexion, the suboccipitofrontal diameter leads (approximately 10 cm), but with good flexion this converts

to the suboccipitobregmatic diameter (9.5 cm).

Internal rotation of the fetal head occurs during descent, when the vertex is pushed down onto the anterior slope of the pelvic floor by the uterine contractions. With a well-flexed vertex presentation, the leading part of the fetal head (the occiput) rotates anteriorly from a transverse position (appropriate for the pelvic inlet) into an anteroposterior position, to pass the ischial spines (appropriate for the pelvic outlet). The fetal shoulders remain in the transverse diameter at this point so they can enter the pelvis through the widest pelvic diameter, resulting in a degree of rotation of the fetal neck. The occiput passes under the subpubic arch and distends the perineum.

The degree of flexion of the fetus body parts (body, head, and extremities) to each other is known as attitude. It is the resistance to the descent of the fetus down the birth canal, which causes the head to flex or bend so that the chin approaches the chest. The most common attitude in vertex presentation is a complete flexion. In vertex presentation, there is complete flexion of the fetus head when the fetus "chin is on his chest." This allows the smallest cephalic diameter to enter the pelvis, which gives the fewest mechanical problems with descent and delivery.

A moderate flexion or military attitude in vertex presentation is when the fetus head is only partially flexed or not flexed. It gives the appearance of a military person at attention. A larger diameter of the head would be coming through the passageway.

In vertex presentation, When the fetus head is extended or bent backwards, it is called a poor flexion or marked extension. This would be called a brow presentation. It is difficult to deliver because the widest diameter of the head enters the pelvis first. This type of cephalic presentation may require a cesarian delivery if the attitude cannot be changed.

In vertex position, when the fetus head is extended all the way back, allowing the face or chin to present first in the pelvis, this is known as hyperextended. If there is adequate room in the pelvis, the fetus may be delivered vaginally.

In order to study the influence of the fetal head flexion on the evolution of the delivery, a series of simulations, varying the degree of flexion of the fetal head were conducted. Figure 7.22a shows the definition of the angle β, used to define the amount of flexion of the fetus head. The angle β was defined as the angle between a vertical line an a line passing trough the fetus eyes and upper portion of the fetus ear, as shown in Figure 7.22a. Figure 7.22b shows the fetus head extended by the maximum degree used in the simulations, with $\beta = 54.4^{\circ}$. Figure 7.22c shows the fetus head at the most flexed position, with $\beta = 14.3^{\circ}$.

The maximum and minimum values of β were obtained by varying the rotation of the fetus head, maintaining the vertical displacement at 30 mm. By verifying the appearance of interference between the fetus head and the pelvic girdle bones and the fetus chin and chest, the maximum and minimum values were defined. The

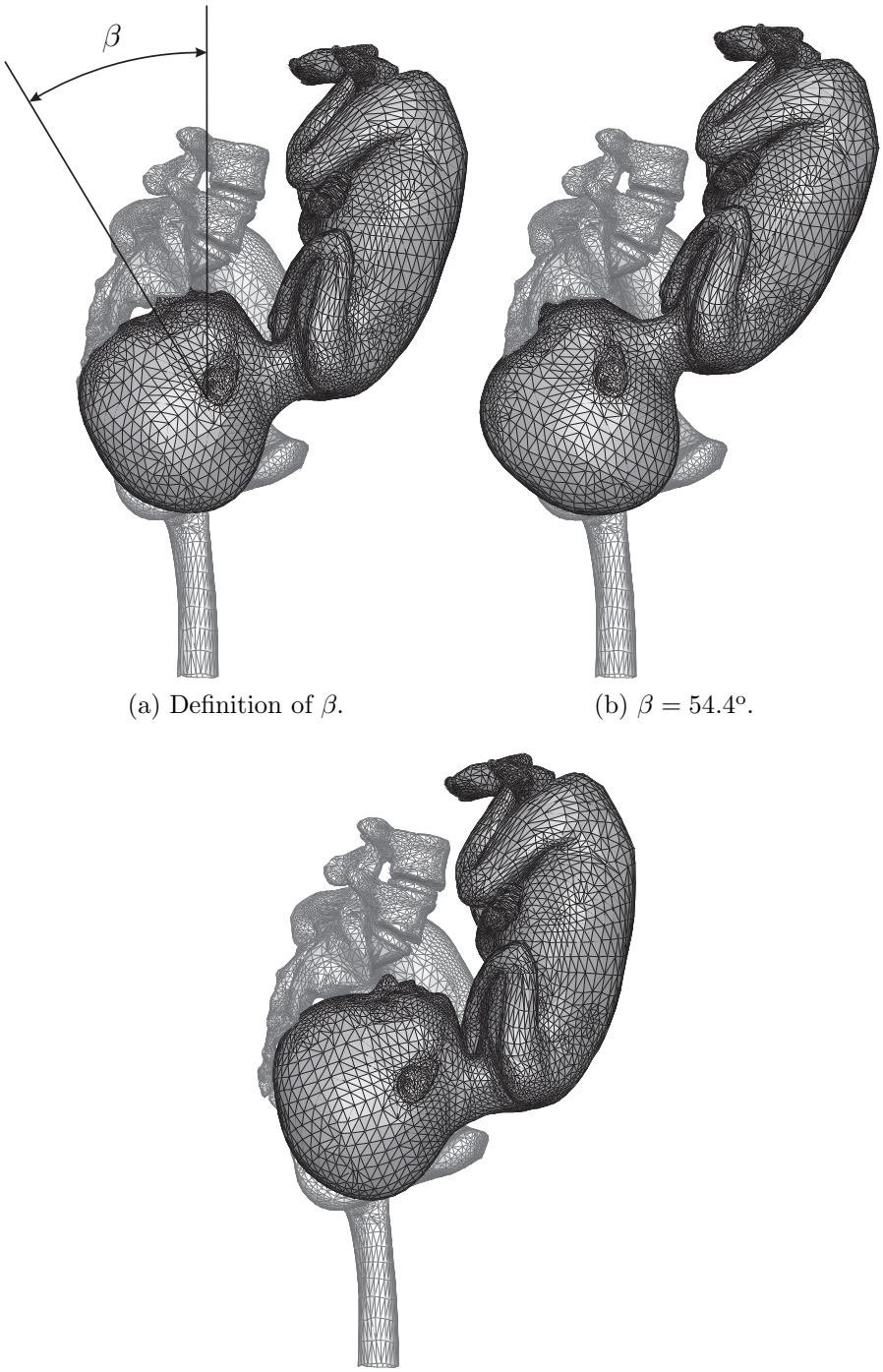

(a) Definition of β.

(b) $\beta = 54.4^{\circ}$.

(c) $\beta = 14.3^{\circ}$.

Figure 7.22: Variation of the fetus fetus head flexion at 30 mm of vertical displacement.

remaining of the fetus movements were obtained as described in Section 7.3.1.

Figure 7.23 shows the stretch values obtained during the simulation, calculated using level 1, for different fetus head rotations. It is clearly visible on Figure 7.23 that when the flexion of the fetus head is reduced (increasing β), the maximum value for the stretch is higher. The smaller values for the maximum stretch, calculated using level 1, are obtained when the fetus presents with its head at the most flexed position. When the fetus head is in complete flexion ($\beta = 14.3^{o}$), the maximum stretch obtained during delivery, for level 1 was 1.58. When the fetus head presents in extension ($\beta = 54.4^{o}$), the maximum stretch values obtained was 1.65, which represents an increase of approximately 5%. Observing the stretch values obtained when varying the fetus head flexion, it becomes clear that the fetus movements presented on Section 7.3.1 are not the most optimized ones (maximum stretch value of 1.63 obtained).

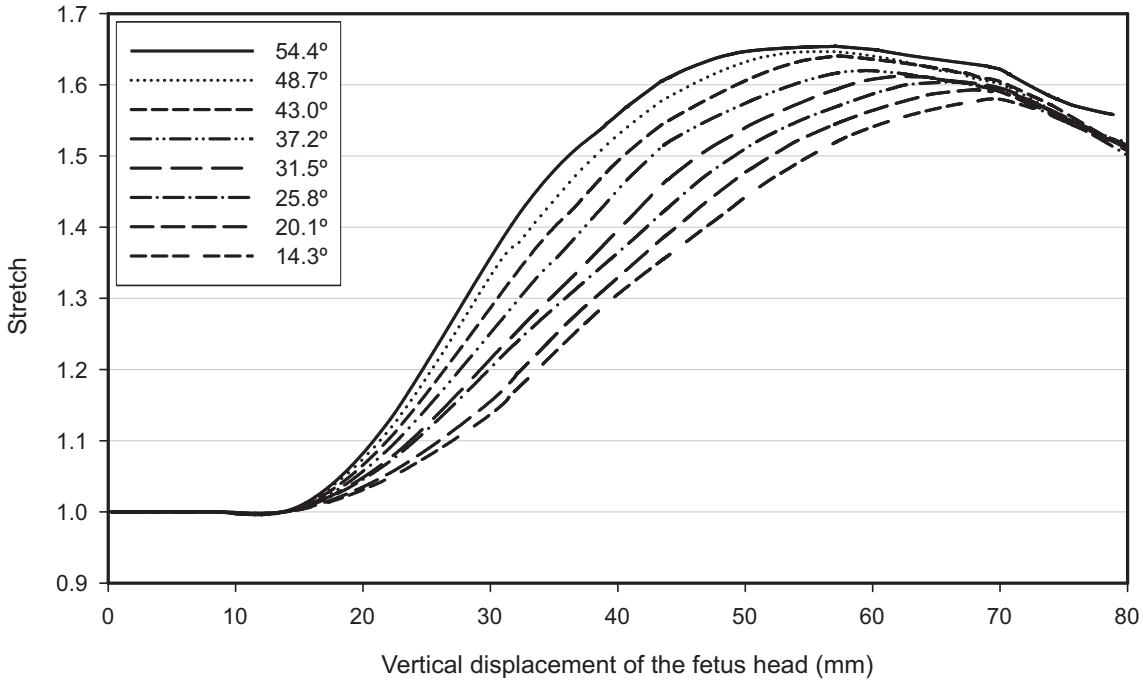

Figure 7.23: Stretch values obtained during the simulation, calculated using level 1, for different fetus head rotations.

Figure 7.24 shows the evolution of the maximum principal stresses along level 1, for a vertical fetus head displacement of 60 mm. Figure Figure 7.24 is in accordance with Figure 7.23. It is possible to observe that when the fetus presents in complete flexion ($\beta = 14.3^{o}$), the evolution of the maximum principal stresses will be the most favorable. The maximum value for the maximum principal stresses along level 1 was

1.52 MPa, obtained when the fetus presents with the head extended ($\beta = 54.4^o$). When the fetus presents with its head in complete flexion ($\beta = 14.3^o$) the maximum value for the maximum principal stress is 0.98 MPa. Once again, the most situation is when the fetus head is in complete flexion, with is chin touching his chest.

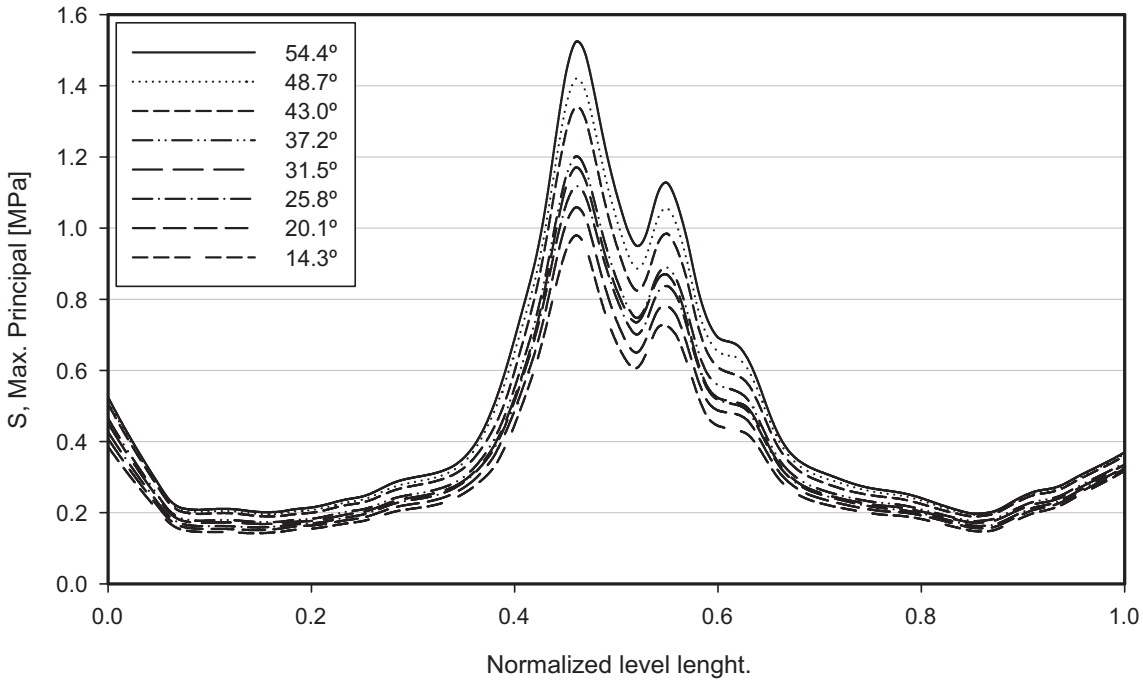

Figure 7.24: Maximum Principal Stresses along level 1, at 60 mm of vertical displacement, for different fetus head rotations.

The finite element simulation presented in this section serves two purposes. It shows that the complete flexion of the fetus head is the most favorable position during birth. The stretches and stresses obtained were smaller when the fetus head is well flected, as shown in Figure 7.22c. This section also shows some of the capabilities of the presented model in simulating deliveries in non-optimum positions. With future developments, the proposed model could become a valuable tool, aiding the obstetrician in the delivery room.

Next section continues to shows some more capabilities of the presented model, where the commonest malposition during delivery is simulated, the occipito-posterior presentation.

7.3.2 Numerical modelling of childbirth delivery in occipito-posterior presentation

Labor and delivery is a normal physiologic process that the majority of women experience without complications, nevertheless, complications can occur during delivery. Malpositions are abnormal positions of the vertex of the fetal head (with the occiput as the reference point) relative to the maternal pelvis, being the occipito-posterior presentation the commonest malposition. Malpresentations are all presentations of the fetus other than vertex [DeCherney and Nathan, 2003].

In the vast majority of deliveries near term the fetus presents by the head, with the best fit into the lower pelvis in the occipito-anterior position. The fetal head engages in the left (less commonly, right) occipito-anterior position and then undergoes a short rotation to be directly occipitoanterior in the midcavity. Sometimes, although the head is presenting, it may be not in an occipito-anterior but in an occipito-posterior or transverse position. In a few cases the head is greatly extended so that the brow or even the face can present.

In the occipito-posterior presentation, the head engages in the left or right occipito-transverse position, and the occiput rotates posteriorly, rather than into the more favorable occipito-anterior position. The reasons for the malrotation are often unclear. A flat sacrum or a head that is poorly flexed may be responsible; alternatively, poor uterine contractions may not push the head down into the pelvis strongly enough to produce correct rotation; epidural analgesia might sometimes relax the pelvic floor to an extent that the fetal occiput sinks into it rather than being pushed to rotate in an anterior direction. The diagnosis is determined clinically by vaginal examination.

The best management is to await events, preparing the woman and staff for a long labor. Progress should be monitored by abdominal and vaginal assessment, and the mother's condition should be watched closely. Good pain relief with an epidural and adequate hydration are required.

The mother may have an urge to push before full dilation, but the midwife should discourage this. If the occiput comes directly into the posterior position (face to pubis) a vaginal delivery is possible if the pelvic diameters are reasonable [Chamberlain and Steer, 1999].

The current Section 7.3.2 presents a delivery of a fetus that presents in occipito-posterior presentation. The first step to conduct the finite element simulation is to define the fetus movements. Figures 7.25 and 7.26 show the sequence of movements of the fetus during birth in occipito-posterior presentation, for different vertical displacements of the fetus head. The vertical displacement refers to the vertical displacement of the control point P1 (see Figure 7.10) which is placed inside the fetus head.

Figure 7.25a shows the initial position for the fetus that corresponds to the

engagement of the presenting part. The process to obtain the movements of the fetus in occipito-posterior presentation is similar to the one used for the occipito-anterior presentation (Section 7.3.1). The definition of the fetus movements is an optimization process, where one is trying to minimize the diameter of the fetus head that is presented to the birth canal. It is clearly visible on Figures 7.25 and 7.26 that the process of optimization is harder for an occipito-posterior presentation. The fetus head has reduced freedom of movements, because the rotation of the fetus head is limited by the fetus chin touching the fetus chest. Once the movements of the fetus are defined, the finite element simulations including the pelvic floor can be conducted.

The levels introduced on Figure 7.13 are used again in order to study the results obtained. Levels 1 to 4 were defined on top of the elevator ani muscle and the pubococcygeal muscle, levels 5 to 6 were defined on top of the iliococcygeal muscles and level 7 was defined on top of the coccygeus muscles. Therefore, the results obtained for the different levels can be translated to the different muscles.

Figure 7.27 shows the evolution of the stretch values obtained for the pelvic floor on the referenced levels, during during fetal descent. The stretch values were obtained by dividing the current length of the different levels by their original length (Figure 7.13). The maximum value obtained for the stretch was approximately 1.73, obtained on level 1, for a vertical displacement of the fetal head of approximately 60 mm. The elevator ani muscle and the pubococcygeal muscle, which correspond to the levels 1 to 4 are the muscles that are subjected to the higher values of stretch. The iliococcygeal muscles (Level 5 to 6) and the coccygeus muscles (Level 7) are the muscles subjected to the lower values of stretch. The stretch value obtained for an occipito-posterior presentation represents an increase of approximately 6.1% when compared to the occipito-anterior presentation.

Figure 7.28 shows the deformation field of the pelvic floor for a vertical displacement of the fetus head of 45, 60, 75 and 90mm. These figures clearly show the high deformations that the pelvic floor has to undergo in order to the progression of delivery to occur. The distribution of the maximum principal stresses is also shown in Figure 7.28. In the distribution of the maximum principal stresses, it can be observed that the maximum values appear on the most posterior area of the elevator ani muscle and the pubococcygeal muscle. The maximum value for the maximum principal stress, detected on the pelvic floor muscles was 3.06 MPa, wish represents an increase of almost 110% when compared with the delivery in occipito-anterior presentation.

Figure 7.29 shows the evolution of the logarithmic maximum principal strain along the different levels, for different vertical displacements of the fetal head. As it is possible to observe on Figure 7.29c, a maximum value of 0.74 for the strain E1 on level 1 was obtained, for a vertical displacement of 60 mm, which represents an increase of approximately 10% when compared with the delivery in occipito-anterior

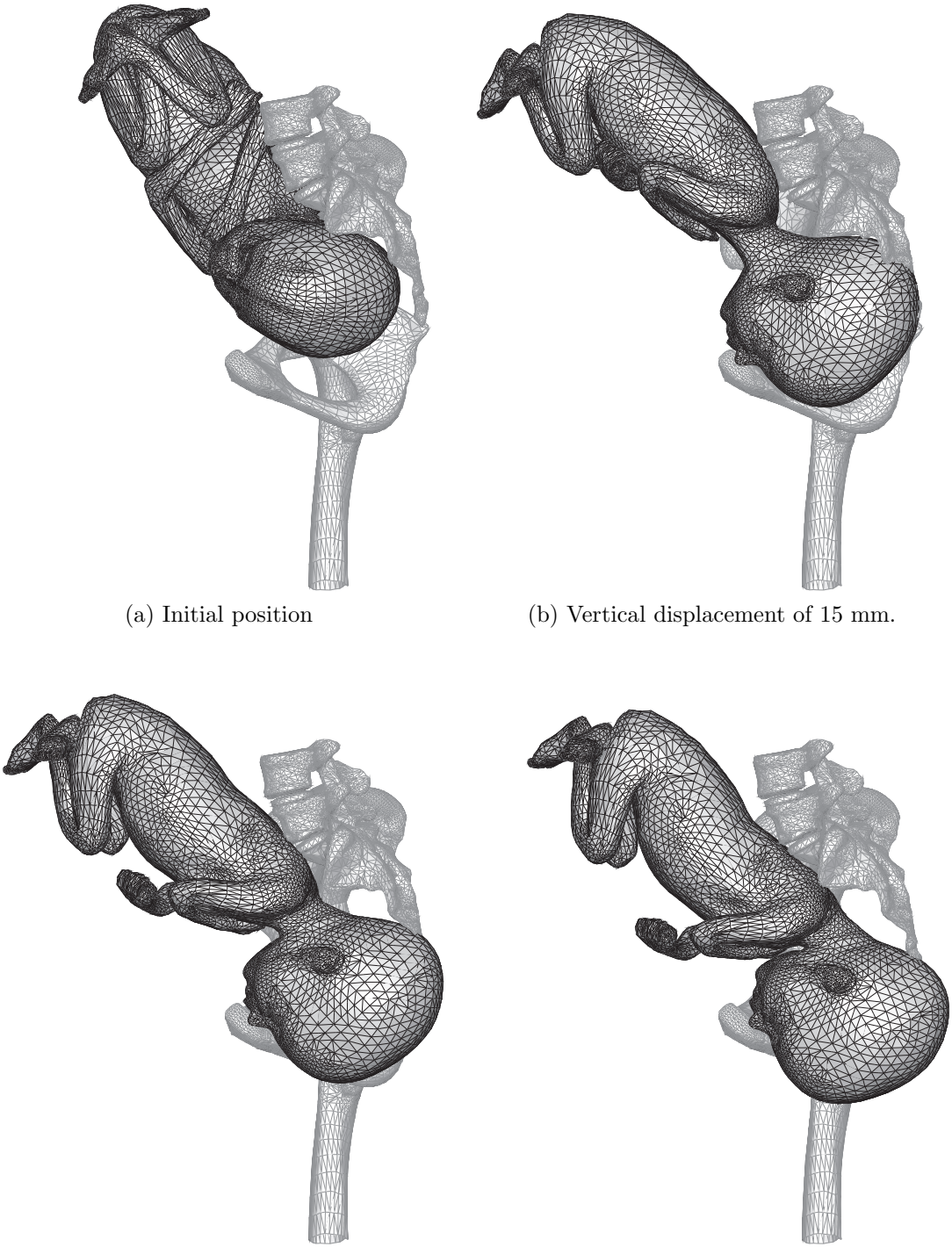

(a) Initial position

(b) Vertical displacement of 15 mm.

(c) Vertical displacement of 30 mm.

(d) Vertical displacement of 45 mm.

Figure 7.25: Fetus movements in occipito-posterior presentation.

(a) Vertical displacement of 60 mm.

(b) Vertical displacement of 75 mm.

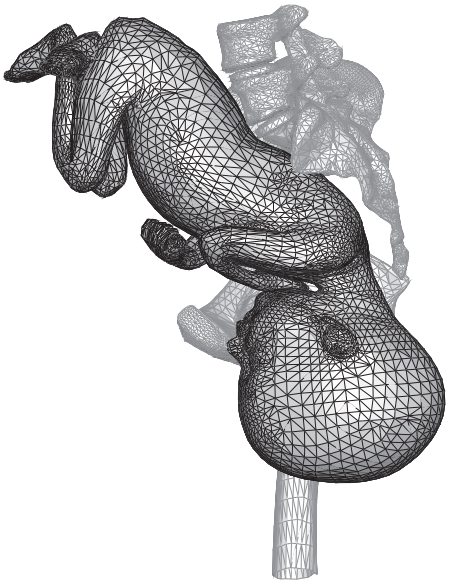

(c) Vertical displacement of 90 mm.

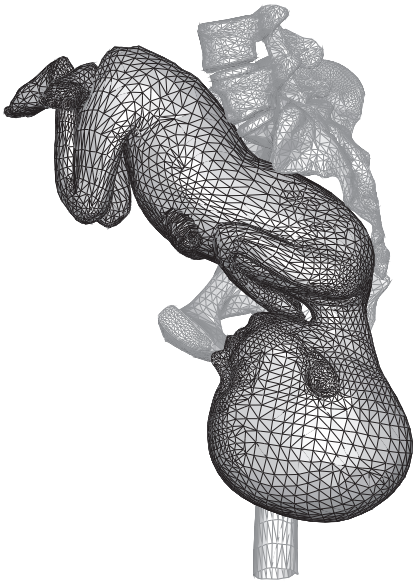

(d) Vertical displacement of 110 mm.

Figure 7.26: Fetus movements in occipito-posterior presentation (continuation).

presentation. A close observation of the evolution of the strains along level 1 shows that the higher values of strain appear on the middle of level 1, which corresponds to the middle length of the levator ani muscle and the pubococcygeal muscle. It can be observed that the extremities of level 1 also present high values of strain, which correspond to the points of attachment of levator ani muscle and the pubococcygeal muscle to the pelvic bones. By using this procedure to present the different results, it is possible to evaluate at each point of the different levels the values of strain. The stretch values presented in Figure 7.27 are more conservative, because it assumes that the deformation is equal along the different levels.

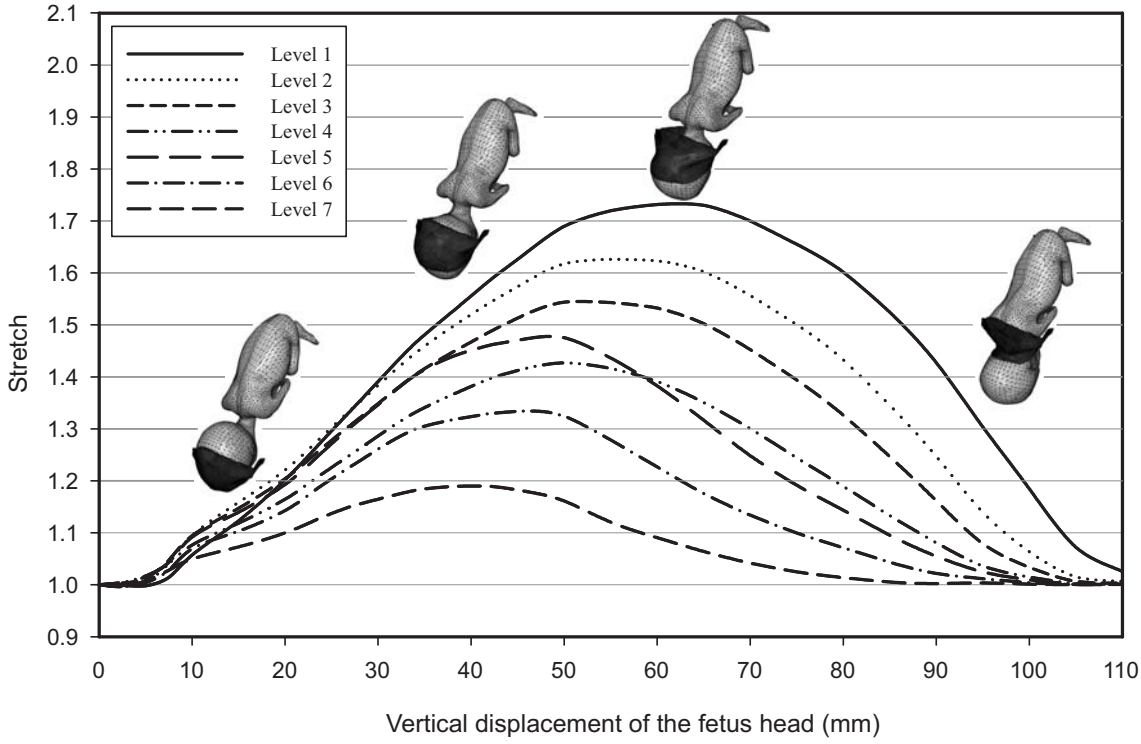

Figure 7.27: Stretch values obtained during the simulation with the fetus in occipito-posterior presentation.

Figure 7.30 shows the evolution of the maximum principal stresses along the different levels for different vertical displacements of the fetal head. As one would expect, the evolution of the strains is closely related with the evolution of the strains (Figure 7.29), therefore the maximum value for the stress appear for roughly the same vertical displacement of the fetus head of 60 mm (Figure 7.30c). The maximum value obtained for the maximum principal stress was 1.69 MPa, on level 1. The maximum value for the stress appear on the middle length of the levator ani muscle

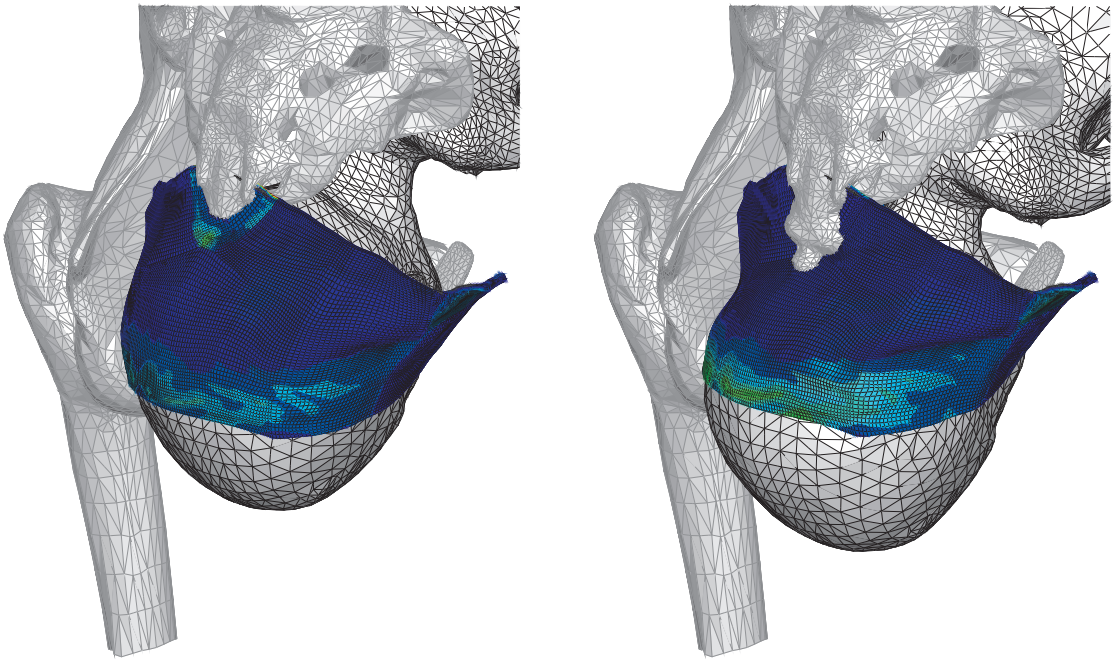

(a) Vertical displacement of 45 mm.

(b) Vertical displacement of 60 mm.

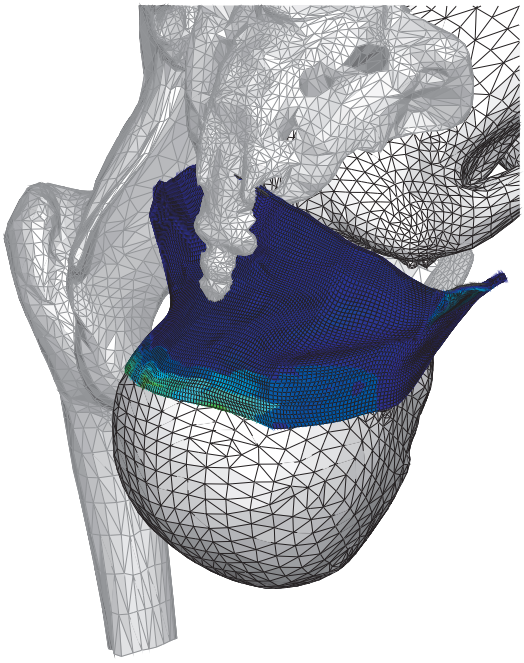

(c) Vertical displacement of 75 mm.

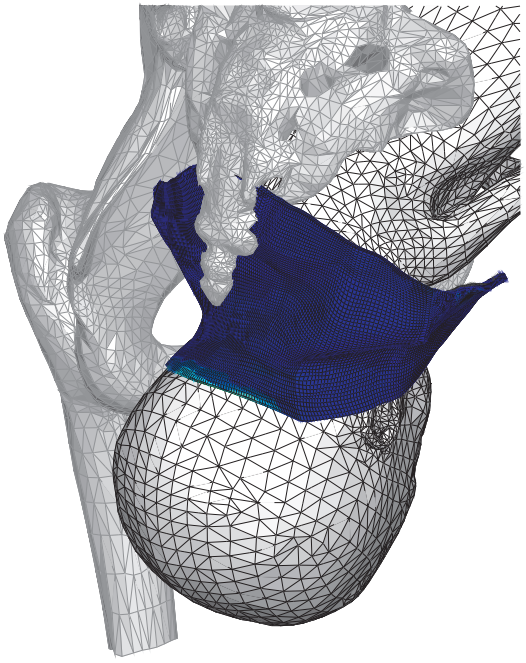

(d) Vertical displacement of 90 mm.

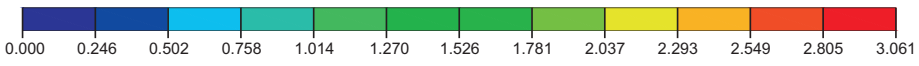

Figure 7.28: Distribution of the Maximum Principal Stresses [MPa].

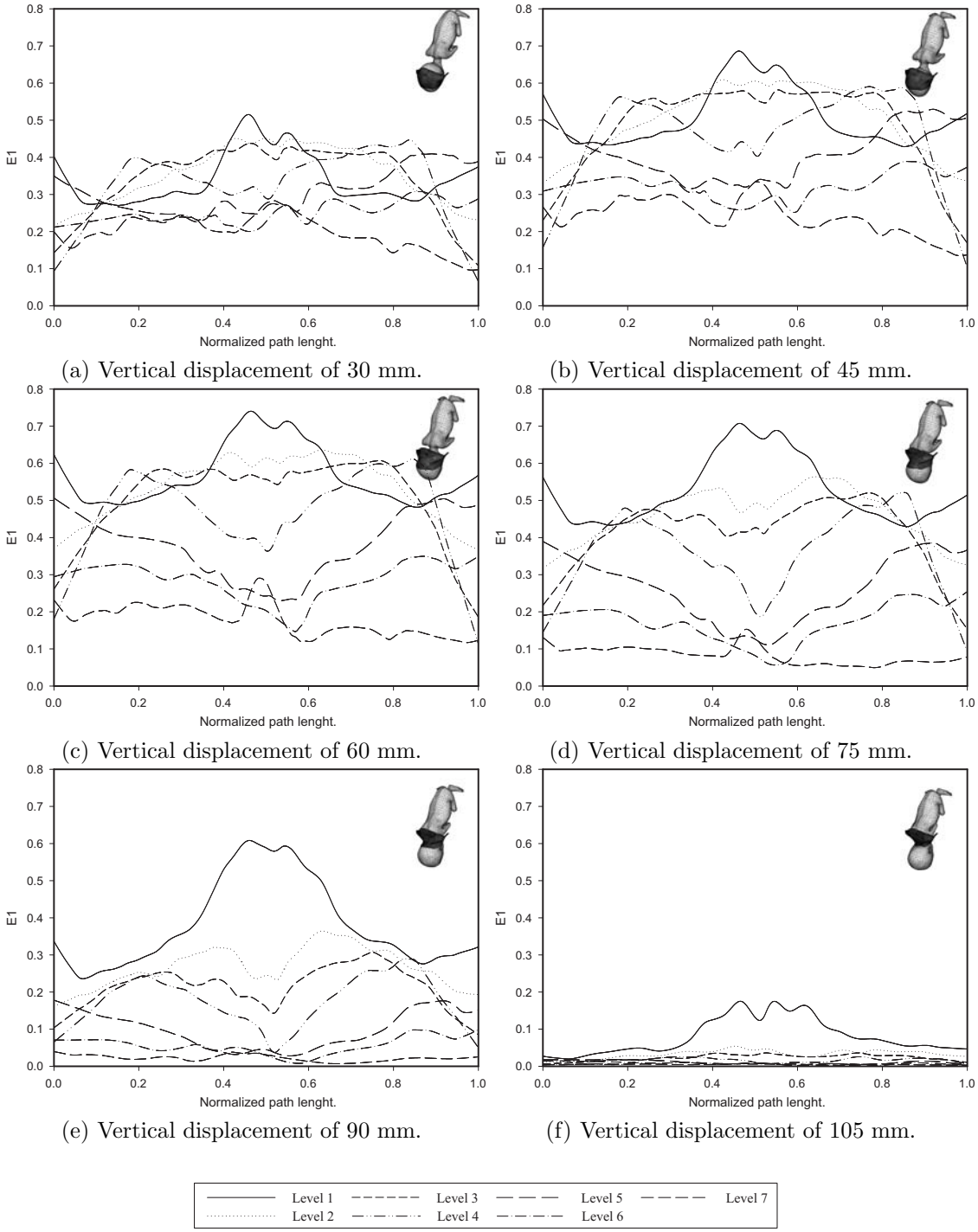

(a) Vertical displacement of 30 mm.

(b) Vertical displacement of 45 mm.

(c) Vertical displacement of 60 mm.

(d) Vertical displacement of 75 mm.

(e) Vertical displacement of 90 mm.

(f) Vertical displacement of 105 mm.

Figure 7.29: Logarithmic Maximum Principal Strain along the different levels for a fetus in occipito-posterior presentation.

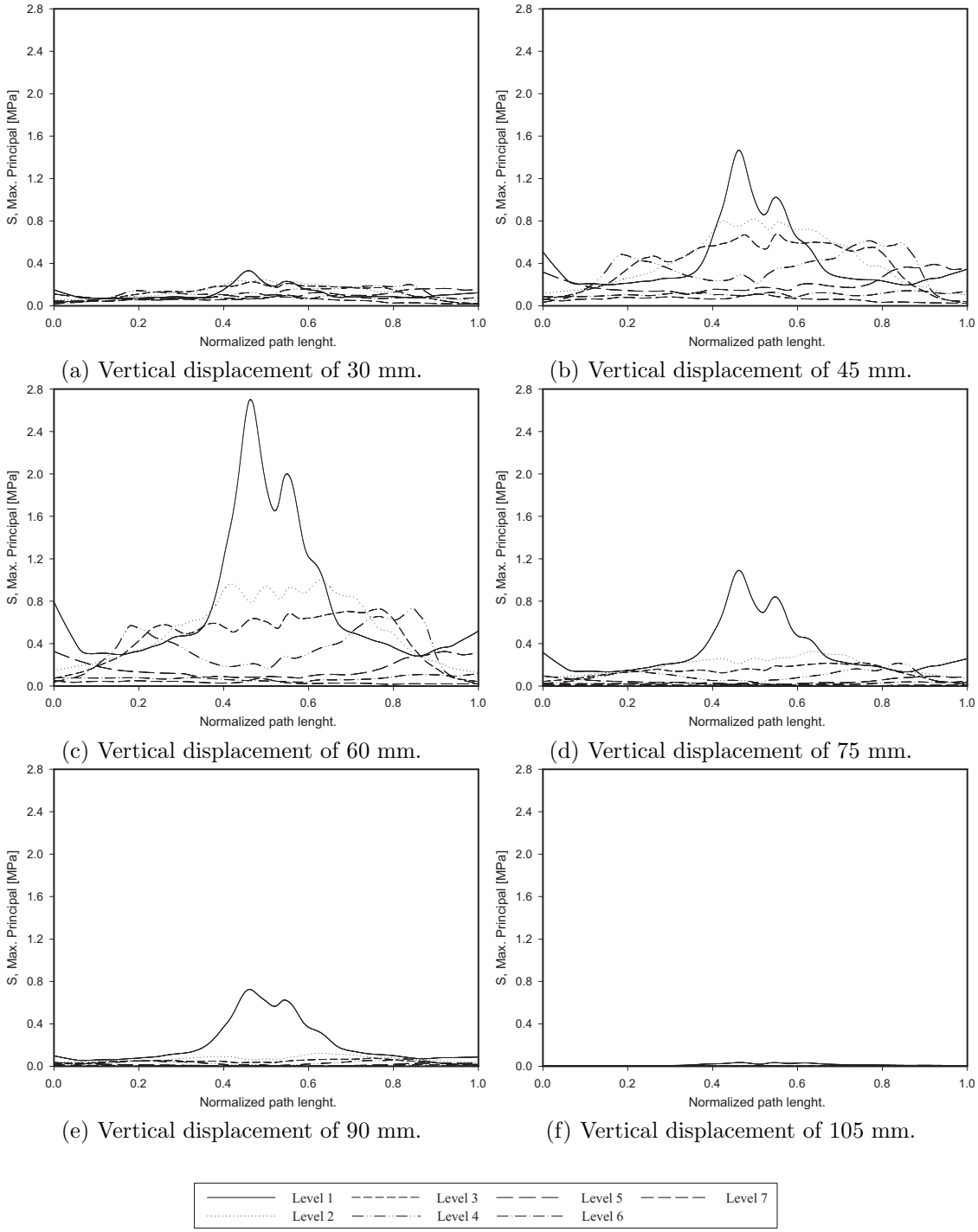

(a) Vertical displacement of 30 mm.

(b) Vertical displacement of 45 mm.

(c) Vertical displacement of 60 mm.

(d) Vertical displacement of 75 mm.

(e) Vertical displacement of 90 mm.

(f) Vertical displacement of 105 mm.

Figure 7.30: Maximum Principal Stresses along the different levels for a fetus in occipito-posterior presentation.

and the pubococcygeal muscle. The extremities of level 1 also present high values of stress. The maximum value for the maximum principal stress, in occipito-posterior presentation represents an increase of approximately 34% when compared to the occiput-anterior presentation (1.26 MPa).

The finite element simulation of a fetus delivery in occipito-posterior presentation clearly shows that this is not the optimum position for delivery. The stretches, strains and stresses obtained clearly show that a delivery in occipito-posterior presentation increases the risk for stress related injuries to the pelvic floor muscles.

7.3.2.1 The influence of muscle activation on delivery in occipito-posterior presentation

In order to study the influence of muscle activation on the strains and stresses that appear on the pelvic floor muscles, when the fetus presents in occipito-posterior presentation, the finite element simulation presented in the previous Section 7.3.2 was rerun again, using the muscle activation parameter α with the values $\alpha = 0.05$, $\alpha = 0.10$ and $\alpha = 0.15$.

Figure 7.31a shows the results obtained for the logarithmic maximum principal strain E1 along level 1, for a fetus head descent of 60 mm and for the different muscle activations. The results obtained without activation ($\alpha = 0$) are also displayed on the same figures for comparison. In order to simplify the comparison of the results, only the results along level 1 are presented on Figure 7.31a and Figure 7.31b.

Observing the results obtained for the strains, it can be observed than once again, for the different activations, the strain values follow approximately the same evolution along level 1. This coincidence is almost identical for the higher values of strain (Figure 7.31a), existing only small differences on the extremities of level 1. A maximum value of 0.74 for the strain E1 on level 1 is obtained, for the different activations, for a vertical displacement of 60 mm. Once again this is the expected result because the higher strain values depend mostly of the dimensions of the fetus head. As the geometry of the fetus head has not changed, the results for the strains are very similar.

Figure 7.31b shows the results obtained for the maximum principal stress along level 1, for a fetus head descent of 60 mm, along level 1. For a muscle activation of $\alpha = 0.15$ a maximum principal stress of 2.80 MPa was obtained, which represents an increase of 4% in relation to the non-activated simulation $\alpha = 0.00$ (2.69 MPa). The maximum values for the maximum principal stresses increases when the degree of muscle activation is increased. When the muscle activation increases, the muscle becomes stiffer and therefore the value for the maximum principal tensions also increases. It is interesting to note that when the fetus presents in occipito-posterior presentation, the difference between the different maximum values for the stresses is about 4%. When the fetus is on occipito-anterior presentation, the variation

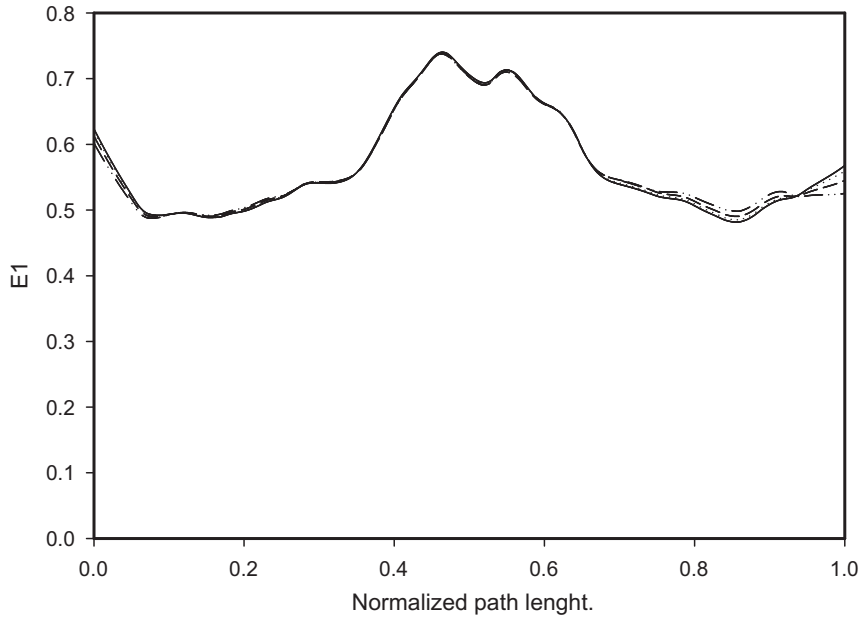

(a) Logarithmic maximum principal Strain E1.

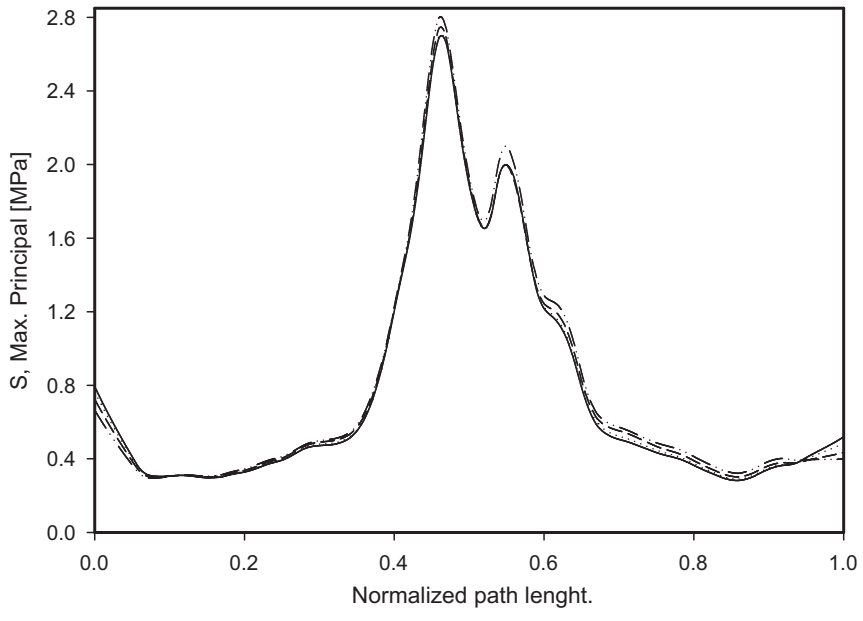

(b) Maximum Principal Stress.

Figure 7.31: Logarithmic maximum principal strain and maximum principal stresses for a fetus presenting in occipito-posterior presentation, for a fetus head descent of 60 mm, along level 1.

is approximately 8%. Nevertheless, the values obtained for an occipito-posterior presentation are greatly higher then the ones obtained for a occipito-anterior presentation.

If a relation between maximum principal stresses and stress induced muscle injury can be formulated, then it can be concluded that as the muscle activation increases, also the risk for injury increases.

7.3.2.2 The influence of different material parameters on delivery in occipito-posterior presentation

In order to verify the influence of the utilization of different material behaviors on the obtained results, two new simulations of a fetus delivery, in occipito-posterior presentation, with two new sets of material properties were conducted. The material parameters used on the new simulations are described on Section 7.3.1.2. The procedure used to obtain the material parameters used on the simulations is described on Section 6.2.4.

To the initial material parameters, obtained on Section 6.2.4, two new sets of material parameters were introduced. The first set shows a stiffer response that the original constants used. The stress/strain behavior for the pelvic floor muscles with this set of parameters is shown in Figure 7.19 with curve Abq. Mat 2. Figure 7.19 also shows the pelvic floor behavior with the initial set of parameters (Abq. Mat. 1). The behavior of the second new set of parameters, a softer behavior, is shown in the same Figure, with curve Abq. Mat. 3.

The constitutive parameters for Abaqus Material 1 are $c = 1.85 \times 10^{-2}\text{N/mm}^2$, $b = 1.173$, $A = 2.80 \times 10^{-2}\text{N/mm}^2$ and $a = 0.6215$, for Abaqus Material 2 $c = 2.00 \times 10^{-2}\text{N/mm}^2$, $b = 1.75$, $A = 4.20 \times 10^{-2}\text{N/mm}^2$ and $a = 0.6215$, and for Abaqus Material 3 $c = 1.30 \times 10^{-2}\text{N/mm}^2$, $b = 1.173$, $A = 1.96 \times 10^{-2}\text{N/mm}^2$ and $a = 0.6215$.

For all the different materials used, for the parameter D the value $D = 1 \times 10^{-4}\text{mm}^2/\text{N}$ was used and for the parameter T_0^M for the maximum tension produced by the muscle at resting length was considered to be $T_0^M = 0.682Pa$, in accordance with values proposed in the literature [Aulignac et al., 2004].

Figure 7.32 shows the evolution of the logarithmic maximum principal strain obtained during the new simulations, with the different material parameters. In Figure 7.32 it can be observed that the logarithmic maximum principal strain follows approximately the same evolution along level 1, for the three different pelvic floor muscle behaviors. The simulation using Abaqus Material 2 (stiffer behavior) produces slight smaller strains along level 1, for the different vertical displacements presented. This observation doesn't necessarily means that the simulation made using Abaqus Material 2 produced smaller strains during the entire simulation, but instead, the higher values of strain for this simulation doesn't appear for the same

vertical displacement of the fetus head. In order to simplify the presentation of the results, only the results for 45, 60, 75 and 90 mm are presented. The maximum values obtained for E1 (logarithmic maximum principal strain) was 0.74 for The Abaqus Material 1 and 3, for the Abaqus Material 2, the maximum value was 0.70.

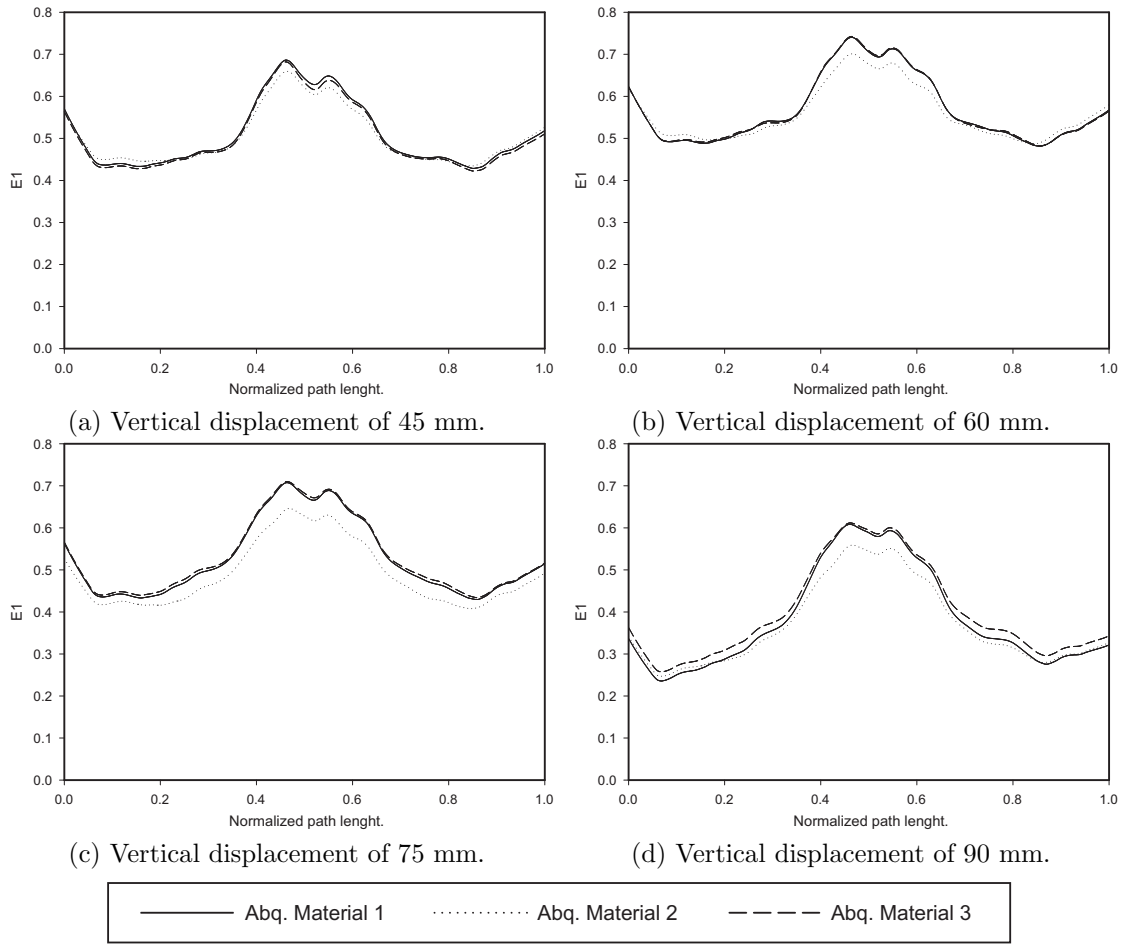

(a) Vertical displacement of 45 mm.

(b) Vertical displacement of 60 mm.

(c) Vertical displacement of 75 mm.

(d) Vertical displacement of 90 mm.

Figure 7.32: Logarithmic Maximum Principal Strain along level 1, using different material parameters and for a fetus on occipito-posterior presentation.

Figure 7.33 shows the evolution of the maximum principal stress along level 1 for a vertical displacement of the fetus head of 45, 60, 75 and 90 mm. Contrary to the strain values obtained, which are very close together, the stress values obtained present considerable differences between the different parameter sets. The maximum values for the maximum principal stress were obtained for a vertical displacement of 60 mm. Using the first set of material parameters (Abq. Material 1) a maximum value of 2.69 MPa was obtained, using the second set of parameters (Abq. Material

2) a value of 8.16 MPa was obtained and for the third parameter set (Abq. Material 3), a value of 1.95 MPa was obtained. A difference of almost 320% exists between the maximum values obtained with the different materials. This differences on the obtained results occur due to the exponential behavior of the constitutive model used. For larger strains, a small increment in the strains will translate in a large increment in the stresses.

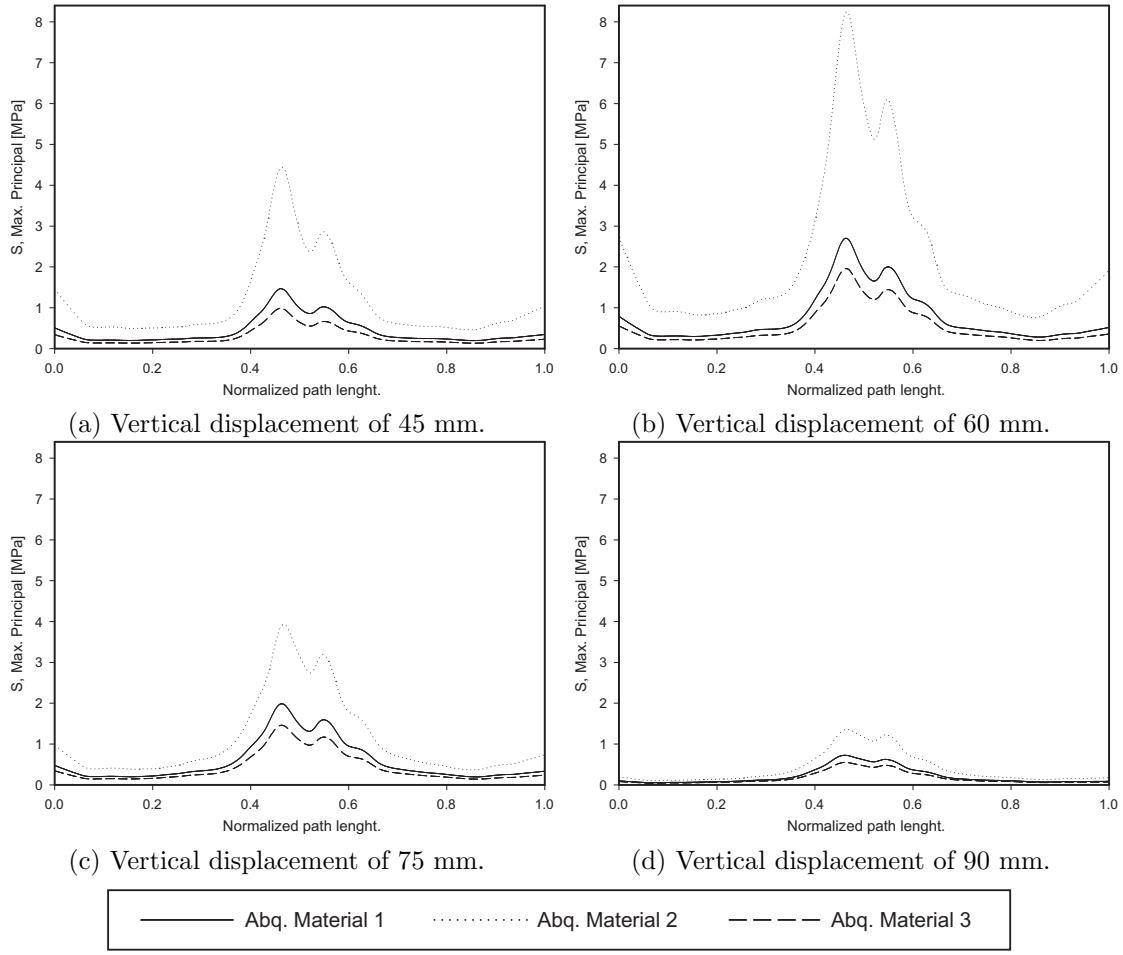

(a) Vertical displacement of 45 mm.

(b) Vertical displacement of 60 mm.

(c) Vertical displacement of 75 mm.

(d) Vertical displacement of 90 mm.

Figure 7.33: Maximum Principal Stress along level 1, using different material parameters and for a fetus in occipito-posterior presentation.

The finite element simulations presented on this section clearly show that the utilization of a representative set of parameters for a given subject is essential in order to obtain correct results. As shown, due to the exponential behavior of the constitutive model used, although the results for the strains are very similar, the stresses obtained are substantially different. The high values of maximum principal

stress obtained with Abaqus Material 2 (8.16 MPa) also mean that the inclusion of a damage model on the constitutive behavior of the pelvic floor muscles is important as a future development of the presented work.

7.4 Discussion of the results

Chapter 7 presents the different simulations conducted in this work. All simulations presented were for vaginal deliveries in vertex position.

Section 7.3.1 shows a vaginal delivery were the fetus presents in occipito-anterior position. A maximum stretch of 1.63 was obtained using level 1. Using the different levels to evaluate the evolution of the logarithmic maximum principal strain and maximum principal stress, a maximum of 0.67 was obtained for the strains and 1.26 MPa for the stresses, both maxima were obtained along level 1. The influence of muscle activation on delivery in a occipito-anterior presentation is studied on Section 7.3.1.1. The different simulations with muscle activation showed that the evolution of the logarithmic maximum principal strain is approximately the same along the different levels and for the different activations. The simulations with muscle activation also showed that the maximum values for the maximum principal stresses are strongly dependent on the degree of muscle activation. For a muscle activation of $\alpha = 0.15$ a maximum principal stress of 1.36 MPa along level 1 was obtained, which represents an increase of 8% in relation to the non-activated simulation $\alpha = 0.00$. The effect of the variation of the material parameters of the constitutive equation for a delivery in occipito-anterior presentation is studied on Section 7.3.1.2. Two new sets of parameters were introduced and the simulations repeated. The obtained results show that the logarithmic maximum principal strains are again very similar, varying between 0.67 and 0.64. The opposite is verified in relation to the maximum principal strains obtained, where values between 3.50 and 0.89 MPa were obtained, which represents a variation of 300% on the results. The final study conducted with the fetus in occipito-anterior presentation is presented on Section 7.3.1.3. This study shows the influence of the variation of the degree of rotation of the fetus head on the process of delivery. It is shown that the most favorable position is when the fetus is at the most flexed position and that when the flexion of the fetus head is reduced, the maximum value for the stretch is higher. A variation between 1.58 and 1.65 for the stretches was obtained, when varying the fetus head flexion, which represents a variation of approximately 5%. A variation between 0.98 and 1.52 MPa was obtained for the maximum principal stresses, which represent a variation of approximately 55%.

Section 7.3.1 shows a vaginal delivery were the fetus presents in occipito-posterior position. A maximum stretch of 1.73 was obtained using level 1, which represents an increase of approximately 6.1% when compared to the occipito-anterior presenta-

tion. Using the different levels to evaluate the evolution of the logarithmic maximum principal strain and maximum principal stress, a maximum of 0.74 was obtained for the strains and 1.69 MPa for the stresses, both maximums were obtained along level 1. These values represent an increase of 10% and 34% when compared to the occipito-anterior presentation. The influence of muscle activation on delivery in a occipito-anterior presentation is studied on Section 7.3.2.1. The different simulations with muscle activation showed once again the evolution of the logarithmic maximum principal strain is approximately the same along the different levels and for the different activations. The simulations with muscle activation also showed that the maximum values for the maximum principal stresses are strongly dependent on the degree of muscle activation. For a muscle activation of $\alpha = 0.15$ a maximum principal stress of 2.80 MPa along level 1 was obtained, which represents an increase of 4% in relation to the non-activated simulation $\alpha = 0.00$. This value also represents an increase of approximately 105% when compared to the occipito-anterior presentation (1.36 MPa), with the same activation $\alpha = 0.15$. The final study conducted with the fetus in occipito-posterior presentation is presented on Section 7.3.2.2. The effect of the variation of the material parameters of the constitutive equation for a delivery in occipito-posterior presentation is studied on this section. Using the two new sets of parameters previously introduced, the simulations were repeated. The obtained results show that the logarithmic maximum principal strains are again very similar, varying between 0.70 and 0.74. The opposite is verified in relation to the maximum principal strains obtained, were values between 1.95 and 8.16 MPa were obtained, which represent a variation of approximately 320% on the results. The maximum values obtained also represent an increase of approximately 130%, when compared to the occipito-anterior presentation, with the same material parameters.

The different simulations conducted show that the pelvic floor muscles have to undergo large strains and stresses in order to delivery to occur. The different results clearly show that the occipito-anterior presentation is more favorable, resulting in lower stresses and strains. Simulations also show that the when the attitude, in vertex presentation is a complete flexion, when the fetus chin is on his chest, the mechanical problems with descent and delivery are reduced. Simulations also showed that a correct characterization of the properties of the pelvic floor muscles is essential. The utilization of parameters that do not correctly characterize a given individual tissues can produce wrong results. The utilization of constitutive models that correctly characterize the pelvic floor muscles, subjected to large strains is also important, and therefor the future inclusion of a damage model on the constitutive model is an important development. The conducted simulations also show that the consideration of the muscle activation during delivery is an important aspect that must be taken into account, as the results show.

Chapter 7 presented a finite element model capable of simulating a vaginal delivery, with the fetus in vertex presentation. This chapter shows only some of the

capabilities of the presented model, which with future developments, could become a valuable tool, aiding the obstetrician in the delivery room.

Chapter 8

Conclusions

8.1 Conclusions

In Chapter 7 the different simulations conducted in this work were presented. All simulations presented were for vaginal deliveries in vertex position.

Initial investigations on the mechanisms responsible for contraction-induced injury, using nongravid, passive striated appendicular muscles, obtained a stretch value of 1.5 for the maximum non-injurious stretch as presented in the following references [Brooks et al., 1995; Lien et al., 2004]. The maximum stretch ratio of 1.63 found in this study for the occipito-anterior position, and the stretch ratio of 1.73, for the occipito-posterior position, both exceeds this largest non-injurious stretch (1.5 stretch ratio). If injury can be caused by fiber stretch exceeding a maximum permissible value, it may be concluded that a risk exists for injury of the muscles of the pelvic floor during the second stage of labor.

The stretch values obtained in this work are lower than the ones obtained in a similar work by Lien et al [Lien et al., 2004; Lien et al., 2005]. The maximum stretch value obtained by Lien et al in their work was 2.73 for the iliococcygeal muscle and 2.50 for the pubococcygeal muscle. On their work, Lien et al also considered a medial pubococcygeal muscle, passing between the vagina and anus, for which the stretch value obtained was 3.26. The presence of this muscle was not obtained in Janda's cadaver measurements [Janda, 2006], and therefore was also not considered in this work. The differences obtained for the stretch values on the iliococcygeal muscle and pubococcygeal muscle could be explained by the fact that in the work by Lien et al, a sphere was used to represent the fetus head, which could have induced higher stretches on the pelvic floor. The difference verified in the present work, between the maximum stretch value for the occipito-anterior position and the occipito-posterior positions, clearly shows the importance in considering a realistic geometry for the fetus head.

The problem studied here is very complex, and any methodology used will be prone to have limitations and to criticism. In order to properly interpret our findings, it is necessary to consider the limitations involved in this work [Parente et al., 2008].

In relation with the data (namely geometry and mechanical properties) of the pelvic floor used, some doubts can be formulated, as the absence of information about any vaginal delivery.

It was assumed that the stretch was uniform along the levels considered, which is not true because it can vary locally along and across a muscle band, especially if thickness varies, leading to a conservative estimate of muscles strains. Time-dependent material property effects on tissue stretch were not considered. Although these may affect the tissue stresses [Lien et al., 2004], they will not affect our estimates of the maximum average tissue stretch because they do not affect the inherent geometric difference between the sizes of the prelabor urogenital hiatus and fetal head.

During the last weeks of pregnancy, the pelvic floor experiences several changes in order to facilitate the delivery, which might lessen the maximal stretches. These modifications were not considered on this study [DeCherney and Nathan, 2003].

During delivery, the fetal head configuration changes, in order to reduce the volume of the skull [Llewellyn-Jones, 2004] and facilitate its passage through the birth canal. The occipital bone is displaced under the two parietal bones during childbirth, reducing the size of the posterior fontanelle, which is called moulding. During moulding, the parietal bones may also slip under each other. This effect was not considered on this study.

A multitude of variables such as variations in maternal pelvic shape, fetal head shape, the degree of moulding during delivery, symphyseal diastasis, types of episiotomies, and presenting orientation may affect the maximum muscle stretch ratios, thus affecting the final results.

The present numerical simulation shows that the muscles of the pelvic floor are submitted to high deformations during the passage of the fetus head.

During a vaginal delivery, the elevator ani muscle and the pubococcygeus muscle are the muscles that are subjected to the largest values of stretch and strain. These muscles are the ones at greater risk for a stretch related injury.

The present work showed a non-invasive procedure which can be used in the future to estimate the damage that a vaginal delivery can induce on a specific pelvic floor.

8.2 Future Work

In Chapter 7 a finite element model capable of simulating a vaginal delivery, with the fetus in vertex presentation. This thesis shows only some of the capabilities

of the presented model, which with future developments, could become a valuable tool, aiding the obstetrician in the delivery room.

The future development of the present work should address some of the limitations presented on the previous section. The different improvements that are needed to the present model should enable it to become a tool that could be adjusted to a specific women/fetus that presents to the clinician.

The first and one of the hardest complexities where improvements are needed is on the production of the geometrical models necessary to perform the numerical simulations. In order that the work presented here becomes a valuable tool for the clinician, the results produced by it should be available in useful time. Therefore, the creation of the geometries should be an optimized process, based on the information obtained by Magnetic Resonance Imaging (MRI), for example.

The characterization of the mechanical properties of the tissues of the pelvic cavity, in a labouring woman, is in itself an enormous challenge, that needs to be addressed.

In the work presented on this thesis, the fetus was considered deformable, but with a very high stiffness. In is necessary to characterize the mechanical properties of the fetus and take them into account in the simulation. Other variables, like the moulding of the fetus head, and the symphyseal diastasis are also variables that need to be taken into account.

A multitude of variables such as variations in maternal pelvic shape, fetal head shape, the degree of moulding during delivery, types of episiotomies, and presenting orientation may affect the maximum muscle stretch ratios, thus affecting the final results.

The utilization of constitutive models that correctly characterize the pelvic floor tissues, subjected to large strains, in a labouring woman, is also important, and therefore the future inclusion of a damage model on the constitutive model is an important development.

In the future, with some improvements, this model could provide the tools to simulate, in a realistic manner, the pelvic floor function and the effects of its dysfunctions, as well as the effects of a vaginal delivery on the tissues of the pelvic cavity, and in this manner, become a valuable tool in a hospital.

Bibliography

[Abrams et al., 2002] Abrams, P., Cardozo, L., Fall, M., Griffiths, D., Rosier, P., Ulmsten, U., van Kerrebroeck, P., Victor, A., and Wein, A. (2002). The standardisation of terminology of lower urinary tract function: Report from the standardisation sub-committee of the international continence society. *Neurourology and urodynamics*, 21:167–178.

[Aggazzotti et al., 2000] Aggazzotti, G., Pesce, F., Grassi, D., Fantuzzi, G., Righi, E., De Vita, D., Santacroce, S., and Artibani, W. (2000). Prevalence of urinary incontinence among institutionalized patients: a cross sectional epidemiologic study in a midsized city in northern italy. *Urology*, 56:245–249.

[Argyris and Kelsey, 1960] Argyris, J. and Kelsey, S. (1960). *Energy Theorems and Structural Analysis*. Butterworths, London.

[Aulignac et al., 2004] Aulignac, D., Martins, J., and Pires, E. (2004). Physical modeling of the pelvic floor muscles using shell elements. In *European Congress on Computational Methods in Applied Sciences and Engineering ECCOMAS 2004. Book of Abstracts*, volume II, page 110. Finland. Full paper in CD-Rom.

[Aulignac et al., 2005] Aulignac, D., Martins, J., Pires, E., Mascarenhas, T., and Natal Jorge, R. (2005). A shell finite element model of the pelvic floor muscles. *Computer Methods in Biomechanics and Biomedical Engineering*, 8:339–347.

[Bannister et al., 1997] Bannister, J., Abouzekry, L., and Read, N. (1997). Effect of aging on anorectal function. *Scandinavian Journal of Gastroenterology*, 28:353–357.

[Bathe, 1982] Bathe, K. (1982). *Finite Element Procedures in Engineering Analysis*. Prentice-Hall, Englewood Cliffs, New Jersey.

[Bathe, 1996] Bathe, K. (1996). *Finite Element Procedures*. Prentice-Hall, Englewood Cliffs, New Jersey.

[Bathe et al., 1975] Bathe, K., Ramm, E., and Wilson, E. (1975). Finite element formulation for large deformation analysis. *International Journal for Numerical Methods in Engineering*, 9:353–386.

[Belytschko et al., 2000] Belytschko, T., Liu, W., and Moran, B. (2000). *Nonlinear Finite Elements for Continua and Structures*. Wiley.

[Bidmead and Cardozo, 1998] Bidmead, J. and Cardozo, L. (1998). Pelvic floor changes in the older woman. *British Journal of Urology*, 82(suppl):18–25.

[Bonet and Wood, 1997] Bonet, J. and Wood, R. (1997). *Nonlinear Continuum Mechanics for Finite Element Analysis*. Cambridge University Press.

[Boukerrou et al., 2004] Boukerrou, M., Lambaudie, E., Dubois, P., and Cosson, M. (2004). Etude préliminaire d'un modèle mécanique de cavité vaginale. *ITBM-RBM*, 25(1):3–14.

[Brieger et al., 1997] Brieger, G., Mongelli, M., Hin, L., and Chung, T. (1997). The epidemiology of urinary dysfunction in chinese women. *International Urogynecology Journal and Pelvic Floor Dysfunction*, 8:191.

[Brooks et al., 1995] Brooks, S., Zerba, E., and Faulkner, J. (1995). Injury to muscle fibres after single stretches of passive and maximally stimulated muscles in mice. *The Journal of Physiology*, 488(2):459–69.

[Brown et al., 2002] Brown, J., Waetjen, L., Subak, L., Thom, D., Van den Eeden, S., and Vittinghoff, E. (2002). Pelvic organ prolapse surgery in the united states, 1997. *American Journal of Obstetrics & Gynecology*, 186:712–716.

[Brown et al., 2000] Brown, S., Sawaya, G., Thom, H., and Grady, D. (2000). Hysterectomy and urinary incontinence: a systematic review. *Lancet*, 356:535–539.

[Bufler, 1984] Bufler, H. (1984). Pressure loaded structures under large deformations. *Zeitschrift für angewandte Mathematik und Mechanik*, 64:287–295.

[Burgio et al., 1996] Burgio, L., Locher, L., Zyczynski, H., Hardin, M., and Singh, K. (1996). Urinary incontinence during pregnancy in racially mixed sample: characteristics and predisposing factors. *International Urogynecology Journal and Pelvic Floor Dysfunction*, 7:69–73.

[Caldwell and Moloy, 1933] Caldwell, W. and Moloy, H. (1933). Anatomical variations in the female pelvis and their effect in labor with a suggested classification. *American Journal of Obstetrics & Gynecology*, 26:479–505.

[Chadwick, 1999] Chadwick, P. (1999). *Continuum Mechanics, Concise Theory and Problems.* Dover Publications, Mineola.

[Chamberlain and Steer, 1999] Chamberlain, G. and Steer, P. (1999). Unusual presentations and positions and multiple pregnancy. *British Medical Journal*, 318:1192–1194.

[Cheater and Castleden, 2000] Cheater, M. and Castleden, M. (2000). Epidemiology and classification of urinary incontinence. *Clinical obstetrics and gynecology*, 14:183.

[Chiaffarino et al., 1999] Chiaffarino, F., Chatenoud, L., Dindelli, M., Meschia, M., Buonaguidi, A., Amicarelli, F., Surace, m., Bertola, E. Di Cintio, E., and Parazzini, F. (1999). Reproductive factors, family history, occupation and risk of urogenital prolapse. *European Journal of Obstetrics & Gynecology and Reproductive Biology*, 82:63–67.

[Chiarelli et al., 1999] Chiarelli, P., Brown, W., and McElduff, P. (1999). Leaking urine: prevalence and associated factors in australian women. *Neurourology and urodynamics*, 18(567-577).

[Ciarlet, 1988] Ciarlet, P. (1988). *Mathematical Elasticity I: Three-dimensional Elasticity.* Elsevier.

[Crawford, 1975] Crawford, J. (1975). Computer monitoring of fetal heart rate and uterine pressure. *American Journal of Obstetrics & Gynecology*, 21:342–350.

[Crisfield, 1991] Crisfield, M. (1991). *Non-linear Finite Element Analysis of Solids and Structures, volume 1.* Wiley, Chichester.

[Crisfield, 1997] Crisfield, M. (1997). *Non-linear Finite Element Analysis of Solids and Structures, volume 2.* Wiley, Chichester.

[Crowningsfield and Brand, 1981] Crowningsfield, R. and Brand, R. (1981). A physiologically based criterion of muscle force prediction in locomotio. *J. Biomech.*, I4:793–801.

[Cunningham et al., 2005] Cunningham, G., Leveno, K., Bloom, S., Hauth, J., Gilstrap, L., and Wenstrom, D. (2005). *Williams Obstetrics.* McGraw-Hill, 22th edition edition.

[D'Alfonso et al., 2006] D'Alfonso, A., Iovenitti, P., and Carta, G. (2006). Urinary disorders during pregnancy and postpartum: our experience. *Clinical and experimental obstetrics & gynecology*, (33):23–25.

[Davila and Neimark, 2002] Davila, G. and Neimark, M. (2002). The overactive bladder: prevalence and effects on quality of life. *Clinical obstetrics and gynecology*, 45:173–181.

[Davila, 2001] Davila, G. (2001). Informed consent for obstetrics management: a urogynecologic perspective. *International Urogynecology Journal and Pelvic Floor Dysfunction*, 2:289–291.

[Davila and Ghoniem, 2003] Davila, G. and Ghoniem, G. (2003). Pelvic floor dysfunction: the importance of a multidisciplinary approach. *Clinics in Colon and Rectal Surgery*, 16:3–4.

[Davila et al., 2006] Davila, G., Ghoniem, G., and Wexner, S. (2006). *Pelvic Floor Dysfunction, A Multidisciplinary Approach*. Springer-Verlag.

[DeCherney and Nathan, 2003] DeCherney, A. and Nathan, L. (2003). *Current Obstetric & Gynecologic Diagnosis & Treatment*. McGraw-Hill, 9 edition.

[DeLancey, 1999] DeLancey, J. (1999). Structural anatomy of the posterior pelvic compartment as it relates to rectocele. *American Journal of Obstetrics & Gynecology*, 180(4):815–823.

[Delome, 2001] Delome, E. (2001). La bandelette trans-obturatrice: un procédé mini-invasif pour traiter l'incontinence urinaire d'effort de la femme. *Progrès en Urologie*, 11:1306–1313.

[Delorme, 2001] Delorme, E. (2001). La bandelette trans-obturatrice: un procédé mini-invasif pour traiter l'incontinence urinaire d'effort de la femme. *Progrès en Urologie*, 11:1306–1313.

[Desai and Siriwardane, 1984] Desai, C. and Siriwardane, H. (1984). *Constitutive Laws for Engineering Materials*. Prentice-Hall, Englewood Cliffs, New Jersey.

[Dhatt and Touzot, 1985] Dhatt, G. and Touzot, G. (1985). *The Finite Element Method Displayed*. Wiley, Chichester.

[Dimpfl et al., 1998] Dimpfl, T., Jaeger, C., Mueller-Felber, W., Anthuber, C., Hirsch, A., Brandmaier, R., and Schuessler, B. (1998). Myogenic changes of the levator ani muscle in premenopausal women: The impact of vaginal delivery and age. *Neurourology and Urodynamics*, 17(3):197–205.

[Diokno et al., 1986] Diokno, C., Broke, M., and Herzog, R. (1986). Prevalence of urinary incontinence and other urological symptoms in the noninstitutional elderly. *Journal of Urology*, 136:1022.

[Doghri, 2000] Doghri, I. (2000). *Mechanics of Deformable Solids Linear, Nonlinear, Analytical and Computational Aspects*. Springer Verlag, Berlin.

[Ellis, 2006] Ellis, H. (2006). *Clinical Anatomy*. Blackwell Publishing, 11th edition edition.

[Eringen, 1962] Eringen, A. (1962). *Nonlinear Theory of Continuous Media*. New York: McGraw-Hill.

[Felt-Bersma and Cuesta, 2001] Felt-Bersma, R. and Cuesta, M. (2001). Rectal prolapse, rectal intussusception, rectocele, and solitary rectal ulcer syndrome. *Gastroenterology Clinics of North America*, 30:199–218.

[Foldspang et al., 1992] Foldspang, A., Mommsen, S., Lam, G., and Elving, L. (1992). Parity as a correlate of adult female urinary incontinence prevalence. *Journal of Epidemiology and Community Health*, 46:595–600.

[Friedman, 1967] Friedman, E. (1967). *Labor. Clinical Evaluation and Management*. Appleton-Century-Crofts.

[Fultz et al., 1999] Fultz, N., Herzog, A., Raghunathan, T., Wallace, R., and Diokno, A. (1999). Prevalence and severity of urinary incontinence in older african american and caucasian women. *The journals of gerontology. Series A, Biological sciences and medical sciences*, 54:M299–M303.

[Fung, 1993] Fung, Y. (1993). *Biomechanics. Mechanical propeties of living tissues*. Springer-Verlag.

[Fung and Tong, 2001] Fung, Y. and Tong, P. (2001). *Classic and computational solid mechanics*. World Scientific.

[Gabbe et al., 2007] Gabbe, S., Niebyl, J., and Simpson, J. (2007). *Obstetrics: Normal and Problem Pregnancies*. Elsevier, 5th ed edition.

[Giebel et al., 1998] Giebel, G., Lefering, R., Troidl, H., and Blochl, H. (1998). Prevalence of fecal incontinence: what can be expected? *International Journal of Colorectal Disease*, 13:73–77.

[Glia et al., 1998] Glia, A., Lindberg, G., Nilsson, L.H. Mihocsa, L., and Akerlund, J. (1998). Constipation assessed on the basis of colorectal physiology. *Scandinavian Journal of Gastroenterology*, 33:1273–1279.

[Gonzalez-Argente et al., 2001] Gonzalez-Argente, F., Jain, A., Nogueras, J., Davila, G., Weiss, E., and Wexner, S. (2001). Prevalence and severity of urinary incontinence and pelvic genital prolapse in females with anal incontinence or rectal prolapse. *Diseases of the Colon and Rectum*, 44:920–926.

[Gordon and Huxley, 1966] Gordon, A. and Huxley, A. (1966). The variation in isometric tension with sarcomere length in vertebrate muscle fibers. *J. Physiology (London)*, 185:170–182.

[Gregory and Nygaard, 2004] Gregory, W. and Nygaard, I. (2004). Childbirth and pelvic floor disorders. *Clinical Obstetrics and Gynecology*, 47(2):394–403.

[Hanretty, 2003] Hanretty, K. (2003). *Obstetrics Illustrated*. Churchill Livingstone, 6th edition edition.

[Heinrichs, 1996] Heinrichs, W. (1996). 3D female pelvic organ models: Comparison of the visible human female with a reproductive age pelvis. In R.A. Banvard, editor, *The Visible Human Project Conference Proc*. Marylan, USA.

[Hibbitt and Sorensen, 2007] Hibbitt, K. and Sorensen (2007). *Abaqus Theory Manual, Version 6.7*. Dassault Systems.

[Hill, 1938] Hill, A. (1938). The heat of shortening and the dynamic constants of muscle. *Proc. R. Sot. Biol.*, I26:136–195.

[Holzapfel, 2000] Holzapfel, G. (2000). *Nonlinear Solid Mechanics: A Continuum Approach for Engineering*. Wiley.

[Howarth and Botha, 2005] Howarth, G. and Botha, D. (2005). Amniotomy plus intravenous oxytocin for induction of labour. *The Cochrane Database of Systematic Reviews*.

[Hoyte et al., 2004] Hoyte, L., Jakab, M., Warfield, S., Shott, S., Flesh, G., and Fielding, J. (2004). Levator ani thickness variations in symptomatic and asymptomatic women using magnetic resonance-based 3-dimensional color mapping. *American Journal of Obstetrics & Gynecology*, 191(3):856–861.

[Humphrey, 2003] Humphrey, J. (2003). Continuum biomechanics of soft biological tissues. *Proceedings: Mathematical, Physical and Engineering Sciences*, 459(2029):3–46.

[Humphrey and Yin, 1987] Humphrey, J. and Yin, F. (1987). On constitutive relations and finite deformations of passive cardiac tissue: A pseudostrain-energy function. *Journal of biomechanical engineering*, 109(4):298–304.

[Jackson et al., 1996] Jackson, S., Avery, N., Tarlton, J., Eckford, S., Abrams, P., and Bailey, A. (1996). Changes in metabolism of collagen in genitourinary prolapse. *Lancet*, 347:1658–1661.

[Janda, 2006] Janda, S. (2006). *Biomechanics of the pelvic floor musculature*. Ph.D. thesis, Technische Universiteit Delft.

[Janda et al., 2003] Janda, S., Van der Helm, F., and Blok, S. (2003). Measuring morphological parameters of the pelvic floor for finite elements modelling purposes. *Journal of Biomechanics*, 36(6):749–757.

[Johnson et al., 1989] Johnson, J., Sonnenberg, A., and Koch, T. (1989). Clinical epidemiology of chronic constipation. *Journal of Clinical Gastroenterology*, 11:525–536.

[Kent, 2001] Kent, M. (2001). *Human Anatomy*. McGraw-Hill, 6th edition edition.

[Kenton and Mueller, 2006] Kenton, K. and Mueller, E. (2006). The global burden of female pelvic floor disorders. *British Journal of Urology International*, 98:1–5.

[Khan and Huang, 1995] Khan, A. and Huang, S. (1995). *Continuum theory of plasticity*. Wiley, Chichester,New York.

[Khullar et al., 1998] Khullar, V., Damiano, R., and Toozs-Hobson, P.C.L. (1998). Prevalence of faecal incontinence among women with urinary incontinence. *British Journal of Obstetrics and Gynaecology*, 105:1211–1213.

[Lai et al., 1993] Lai, W., Rubin, D., and Krempl, E. (1993). *Introduction to Continuum Mechanics*. Pergamon Pr.

[Langer et al., 2003] Langer, R., Lipshitz, Y., Halperin, R., Pansky, M., Bukovsky, I., and Sherman, D. (2003). Prevention of genital prolapse following burch colposuspension: comparison between two surgical procedures. *International Urogynecology Journal and Pelvic Floor Dysfunction*, 14:13–16.

[Lara and Nacey, 1994] Lara, C. and Nacey, J. (1994). Ethnic differences between maori, pacific island and european new zealand women in prevalence and attitudes to urinary incontinence. *The New Zealand medical journal*, 107:374–376.

[Lepert, 1995] Lepert, P. (1995). Anatomy and physiology of cervical ripening. *Clinical Obstetrics and Gynecology*, 38:267–279.

[Leval, 2003] Leval, J. (2003). Novel surgical technique for the treatment of female stress urinary incontinence: transobturator vaginal tape inside-out. *European Urology*, 44:724–730.

[Lieberman et al., 2005] Lieberman, E., Davidson, K., Lee-Parritz, A., and Shearer, E. (2005). Changes in fetal position during labor and their association with epidural analgesia. *Obstetrics & Gynecology*, 105:974–982.

[Lien et al., 2004] Lien, K., Mooney, B., DeLancey, J.O., and Ashton-Miller, J. (2004). Levator ani muscle stretch induced by simulated vaginal birth. *The American College of Obstetricians and Gynecologists*, 103(1):31–40.

[Lien et al., 2005] Lien, K., Morgan, D., DeLancey, J.O., and Ashton-Miller, J. (2005). Pudendal nerve stretch during vaginal birth: A 3d computer simulation. *American Journal of Obstetrics & Gynecology*, 192(5):1669–76.

[Llewellyn-Jones, 2004] Llewellyn-Jones, D. (2004). *Fundamentals of Obstetrics and Gynaecology*. Elsevier Health Sciences.

[Lubliner, 1990] Lubliner, J. (1990). *Plasticity Theory*. MacMillan, London.

[MacArthur et al., 1997] MacArthur, C., Bick, D., and Keighley, M. (1997). Faecal incontinence after childbirth. *British Journal of Obstetrics and Gynaecology*, 104:46–50.

[Mader, 2004] Mader, S. (2004). *Understanding Human Anatomy & Physiology*. McGraw-Hill, 5th edition edition.

[Malvern, 1969] Malvern, L. (1969). *Introduction to the Mechanics of a Continuous Medium*. Prentice-Hall, Englewood Cliffs, New Jersey.

[Mant et al., 1997] Mant, J., Painter, R., and Vessey, M. (1997). Epidemiology of genital prolapse: observations from the oxford family planning association study. *British Journal of Obstetrics and Gynaecology*, 104:579–585.

[Marsden and Hughes, 1983] Marsden, J. and Hughes, T. (1983). *Mathematical Foundations of Elasticity*. Prentice-Hall, Englewood Cliffs, New Jersey.

[Martins et al., 1998] Martins, J., Pires, E., Salvado, R., and Dinis, P. (1998). A numerical model of passive and active behaviour of skeletal muscles. *Computer methods in applied mechanics and engineering*, 151(3-4):419–433.

[Meschia et al., 1999] Meschia, M., Bruschi, F., Amicarelli, F., Pifarotti, P., Marchini, M., and Crosignani, P. (1999). The sacrospinous vaginal vault suspension: critical analysis of outcomes. *International Urogynecology Journal and Pelvic Floor Dysfunction*, 10:155–159.

[Meschia et al., 2002] Meschia, M., Buonaguidi, A., P., P., Somigliana, E., Spennacchio, M., and Amicarelli, F. (2002). Prevalence of anal incontinence in women with symptoms of urinary incontinence and genital prolapse. *Obstetrics & Gynecology*, 100:719–723.

[Milsom et al., 1993] Milsom, I., Ekelund, P., Molander, U., Arvidsson, L., and Areskoug, B. (1993). The influence of age, parity, oral contraception, hysterectomy and menopause on the prevalence of urinary incontinence in women. *Journal of Urology*, 149:1459–1462.

[Moalli et al., 2003] Moalli, P., Jones, I., Meyn, L., and Zyczynski, H. (2003). Risk factors associated with pelvic floor disorders in women undergoing surgical repair. *Obstetrics & Gynecology*, 101:869–874.

[Mommsen and Foldspang, 1994] Mommsen, S. and Foldspang, A. (1994). Body mass index and adult female urinary incontinence. *World Journal of Urology*, 12:319–322.

[Moore and Dalley, 2006] Moore, K. and Dalley, A. (2006). *Clinically Oriented Anatomy*. Lippincott Williams & Wilkins, 5th edition edition.

[Nakanishi et al., 1997] Nakanishi, N., Tatara, K., Naramura, H., Fujiwara, H., Takashima, Y., and Fukuda, H. (1997). Urinary and fecal incontinence in a community-residing older population in japan. *Journal of the American Geriatrics Society*, 45:215–219.

[Neil et al., 1981] Neil, M., Parks, A., and Swash, M. (1981). Physiological studies of the anal sphincter musculature in faecal incontinence and rectal prolapse. *British Journal of Surgery*, 68:531–536.

[Nelson et al., 1995] Nelson, R., Norton, N., Cautley, E., and Furner, S. (1995). Community based prevalence of anal incontinence. *JAMA: the journal of the American Medical Association*, 274:559–561.

[Netter, 2006] Netter, F. (2006). *Atlas of Human Anatomy*. Saunders, 4th edition edition.

[Nygaard and Lemke, 1996] Nygaard, I. and Lemke, J. (1996). Urinary incontinence in rural older women: prevalence, incidence and remission. *Journal of the American Geriatrics Society*, 44:1049.

[Oden, 1972] Oden, J. (1972). *Finite Elements of Nonlinear Continua*. McGraw-Hill, New York.

[Ogden, 1984] Ogden, R. (1984). *Non-Linear Elastic Deformations*. Ellis Horwood and John Wiley, Chichester.

[Olsen et al., 1997] Olsen, A., Smith, V., Bergstrom, J., Colling, J., and Clark, A. (1997). Epidemiology of surgically managed pelvic organ prolapse and urinary incontinence. *Obstetrics & Gynecology*, 89:501–6.

[Papa Petros, 2004] Papa Petros, P. (2004). *The Female Pelvic Floor, Function, Dysfunction and Management According to the Integral Theory*. Springer.

[Parente et al., 2008] Parente, M., Natal Jorge, R., Mascarenhas, T., Fernandes, A., and Martins, J. (2008). Deformation of the pelvic floor muscles during a vaginal delivery. *International Urogynecology Journal and Pelvic Floor Dysfunction*, 19:65–71.

[Peña et al., 2006] Peña, E., Calvo, B., Martinez, M., Palanca, D., and Doblare, M. (2006). Why lateral meniscectomy is more dangerous than medial meniscectomy. a finite element study. *Journal of Orthopaedic Research*, 24:1001–1010.

[Peet and Castleden, 1995] Peet, S. and Castleden, C. (1995). The prevalence of urinary and fecal incontinence in hospitals and residential and nursing homes for older people. *British medical journal*, 311:1063.

[Peschers et al., 1996] Peschers, U., Schär, G., Anthuber, C., DeLancey, J., and Schüssler, B. (1996). Changes in vesical neck mobility following vaginal delivery. *Obstetrics & Gynecology*, 88:1001–1006.

[Pollak et al., 2003] Pollak, J., Chong, D., Bratter, J., Pietro, P., and Davila, G. (2003). C-section versus vaginal delivery: what do patients want? *International Urogynecology Journal and Pelvic Floor Dysfunction*, 14(suppl):S53.

[Rashid and Basson, 1996] Rashid, Z. and Basson, M. (1996). Association of rectal prolapse with colorectal cancer. *Surgery*, 119:51–55.

[Rekers et al., 1992] Rekers, H., Drogendijk, C., Valkenburg, H., and Riphagen, F. (1992). Urinary incontinence in women from 35 to 79 years of age: prevalence and consequences. *European Journal of Obstetrics & Gynecology and Reproductive Biology*, 43:229–234.

[Rhodes et al., 1999] Rhodes, J., Kjerulff, K., Langenberg, P., and Guzinski, G. (1999). Hysterectomy and sexual functioning. *JAMA, the journal of the American Medical Association*, 282:1934–1947.

[Rortveit et al., 2001] Rortveit, G., Hannestad, Y., Daltveit, A., and Hunskaar, S. (2001). Age- and type-dependent effects of parity on urinary incontinence. the norwegian epincont study. *Obstetrics & Gynecology*, 98:1004–10.

[Sarrel, 1990] Sarrel, P. (1990). Sexuality and menopause. *Obstetrics & Gynecology*, 75:26S–30S.

[Scanlon and Sanders, 2007] Scanlon, V. and Sanders, T. (2007). *Essentials of Anatomy and Physiology*. F. A. Davis Company, 5th edition edition.

[Seeley et al., 2004] Seeley, R., Stephens, T., and Tate, P. (2004). *Anatomy and Physiology*. McGraw-Hill, 6th edition edition.

[Sewell, 1967] Sewell, M. (1967). On configuration-dependent loading. *Archives of Rational Mechanics*, 23:321–351.

[Simo et al., 1991] Simo, J., Taylor, R., and Wriggers, P. (1991). A note on finite element implementation of pressure boundary loading. *Communications in Applied Numerical Methods*, 7:513–525.

[Simo, 1987] Simo, J. (1987). On a fully three-dimensional finite strain viscoelastic damage model: Formulation and computational aspects. *Comp. Meth Appl. Mech. and Engng.*, (60):153–173.

[Simo and Hughes, 1998] Simo, J. and Hughes, T. (1998). *Computational Inelasticity*. Springer.

[Smilen et al., 1998] Smilen, S., Saini, J., Wallach, S., and Porges, R. (1998). The risk of cystocele after sacrospinous ligament fixation. *American Journal of Obstetrics & Gynecology*, 179:1465–1472.

[Snooks et al., 1984] Snooks, S., Setchell, M., Swash, M., and Henry, M. (1984). Injury to innervation of pelvic floor sphincter musculature in childbirth. *Lancet*, 2:546–550.

[Snooks et al., 1990] Snooks, S., Swash, M., Mathers, S., and Henry, M. (1990). Effect of vaginal delivery on the pelvic floor: a five year follow-up. *British Journal of Surgery*, 77:1358–1360.

[Sobotta et al., 2001] Sobotta, J., Putz, R., Pabst, R., and Bedoui, S. (2001). *Sobotta Atlas of Human Anatomy*. Lippincott Williams & Wilkins, 13th edition edition.

[Spellacy et al., 1985] Spellacy, W., Miller, S., Winegar, A., and Peterson, P. (1985). Macrosomia-maternal characteristics and infant complications. *Obstetrics & Gynecology*, 66:158–161.

[Spencer, 1984] Spencer, A. (1984). *Continuum Theory of the Mechanics of Fibre-reinforced Composites*. Springer-Verlag, New York.

[Standring, 2004] Standring, S. (2004). *Gray's Anatomy: The Anatomical Basis of Clinical Practice*. Churchill Livingstone, 39th edition edition.

[Stewart et al., 2001] Stewart, W., Herzog, R., Wein, A., and Abrams, P. (2001). Prevalence and impact of overactive bladder in the usa: results from the noble program. *Neurourology and Urodynamics*, 20.

[Stitely and Gherman, 2005] Stitely, M. and Gherman, R. (2005). Labor with abnormal presentation and position. *Obstetrics and Gynecology Clinics of North America*, 32:165–179.

[Sultan et al., 1993] Sultan, A., Kamm, M., Bartram, C., and Hudson, C. (1993). Anal sphincter trauma during instrumental delivery. *International Journal of Gynecology & Obstetrics*, 43:263–270.

[Sultan et al., 1993] Sultan, A., Kamm, M., Hudson, C., Thomas, J., and Bartram, C. (1993). Analsphincter disruption during vaginal delivery. *The New England Journal of Medicine*, 329:1905–1911.

[Sultan et al., 1994] Sultan, A., Kamm, M., Hudson, C., and Bartram, C. (1994). Third degree obstetric anal sphincter tears: risk factors and outcomes of primary repair. *British Medical Journal*, 38:887–891.

[Surrenti et al., 1995] Surrenti, E., Rath, D., Pemberton, J., and Camilleri, M. (1995). Audit of constipation in a tertiary referral gastroenterology practice. *American Journal of Gastroenterology*, 90:1471–1475.

[Swash et al., 1985] Swash, M., Henry, M., and Snooks, S. (1985). Unifying concept of pelvic floor disorders and incontinence. *Journal of the Royal Society of Medicine*, 78:906–911.

[Talley et al., 1993] Talley, N., Weaver, A., Zinsmeister, A., and Melton, L. (1993). Functional constipation and outlet delay: a population-based study. *Gastroenterology*, 105:781–790.

[Talley et al., 1996] Talley, N., Fleming, K., Evans, J., O'Keefe, E., Weaver, A., Zinsmeister, A., and L.J., M. (1996). Constipation in an elderly community:

a study of prevalence and potential risk factors. *American Journal of Gastroenterology*, 91:19–25.

[Truesdell and Toupin, 1960] Truesdell, C. and Toupin, R. (1960). *The classical field theories*. Springer.

[Viktrup et al., 1992] Viktrup, L., Lose, G., Rolff, M., and Farfoed, K. (1992). The symptom of stress incontinence caused by pregnancy or delivery in primiparas. *Obstetrics & Gynecology*, 79:945–949.

[Virtanen and Makinen, 1993] Virtanen, H. and Makinen, J. (1993). Retrospective analysis of 711 patients operated on for pelvic relaxation in 1983-1989. *International Journal of Gynecology & Obstetrics*, 42:109–115.

[Vongsangnak et al., 1985] Vongsangnak, V., Varma, J., and Smith, A. (1985). Reappraisal of thiersch's operation for complete rectal prolapse. *Journal of the Royal College of Surgeons of Edinburgh*, 30:185–187.

[Weber et al., 1995] Weber, A., Walters, M., Schover, L., and Mitchinson, A. (1995). Sexual function in women with uterovaginal prolapse and urinary incontinence. *Obstetrics & Gynecology*, 85:483–487.

[Weber et al., 2004] Weber, A., Buchsbaum, G., Chen, B., Clark, A., Damaser, M., Daneshgari, F., Davis, G., DeLancey, J.O., Kenton, K., Weidner, A., and Word, R. (2004). Basic science and translational research in female pelvic floor disorders: Proceedings of an nih-sponsored meeting. *Neurourology and Urodynamics*, 23(4):288–301.

[Wood et al., 1998] Wood, J., Amos, L., and Rieger, N. (1998). Third degree anal sphincter tears: risk factors and outcome. *The Australian and New Zealand Journal of Obstetrics and Gynaecology*, 38:414–417.

[Wriggers, 2006] Wriggers, P. (2006). *Computational Contact Mechanics*. Springer, 2 edition.

[Wright, 2005] Wright, J. (2005). Endoanal ultrasound. *Surgery (Oxford)*, 23:168–170.

[Zahalak, 1981] Zahalak, G. (1981). A distribution-moment approximation for kinetic theories of muscular contraction. *Mathematical Biosciences*, 55:89–114.

[Zajac, 1989] Zajac, F. (1989). Muscle and tendon: Properties, models, scaling and application to biomechanics and motor control, crc crit. rev. *Biomed. Engrg.*, 17:359–411.

[Zienkiewicz and Taylor, 2005] Zienkiewicz, O. and Taylor, R. (2005). *The finite element method for solid and structural mechanics*. Elsevier, 6 edition.